A COMPARATIVE STUDY OF DC–DC CONVERTERS' EFFECTS ON THE OUTPUT CHARACTERISTICS OF DIRECT ETHANOL FUEL CELLS AND NiCd BATTERIES

by

FLORIAN MIŞOC

B.Sc., University of Bucharest, 1989
M.Sc., Pittsburg State University, 1999

AN ABSTRACT OF A DISSERTATION

submitted in partial fulfillment of the requirements for the degree

DOCTOR OF PHILISOPHY

Department of Electrical and Computer Engineering
College of Engineering

KANSAS STATE UNIVERSITY
Manhattan, Kansas

2007

Abstract

Characterized by variable impedances, DC power sources normal operation, reliability, and life-time is negatively affected by the sequential switching within any DC power system. The impedances of Nickel-Cadmium (NiCd) storage batteries and Direct Ethanol Fuel Cells (DEFC) vary nonlinearly; therefore, existing DC power system models, that employ averaging of the sequential switching process, are inaccurate in describing the system output voltage.

In this research, Fourier-series models of DC–DC converters are developed and evaluated, through numerical computations and computer simulations. Both NiCd-DC converter and DEFC-DC converter power systems are experimentally evaluated over a selected switching frequency range. Input voltage and output voltage characteristics of two types of DEFC-DC converter systems (Nickel-mesh and Nickel-foam electrode assembly) are determined. Experimental results are compared to computer simulations, thus validating the Fourier-series models.

Experimental results show a correlation between the DC converter switching frequency and the output of the DC power system. Sequential switching operation, along with the type of DC converter employed, are factors determining the maximum power transfer of the system. The models developed in this work are flexible over a large switching frequency range, and for any desired duty cycle. Correction factors, accounting for the source-converter impedance matching, are easily implemented in Fourier-series models. The research demonstrates the advantages of Fourier-series models, as compared to both large-signal and small-signal models, with regard to accuracy and ease of implementation to any DC–DC converter-driven power system.

A COMPARATIVE STUDY OF DC–DC CONVERTERS' EFFECTS ON THE OUTPUT CHARACTERISTICS OF DIRECT ETHANOL FUEL CELLS AND NiCd BATTERIES

by

FLORIAN MIŞOC

B.Sc., University of Bucharest, 1989
M.Sc. Pittsburg State University, 1999

A DISSERTATION

submitted in partial fulfillment of the requirements for the degree

DOCTOR OF PHILOSOPHY

Department of Electrical and Computer Engineering
College of Engineering

KANSAS STATE UNIVERSITY
Manhattan, Kansas

2007

Approved by:

Major Professor
Medhat M. Morcos

Copyright

Abstract

Characterized by variable impedances, DC power sources normal operation, reliability, and life-time is negatively affected by the sequential switching within any DC power system. The impedances of Nickel-Cadmium (NiCd) storage batteries and Direct Ethanol Fuel Cells (DEFC) vary nonlinearly; therefore, existing DC power system models, that employ averaging of the sequential switching process, are inaccurate in describing the system output voltage.

In this research, Fourier-series models of DC–DC converters are developed and evaluated, through numerical computations and computer simulations. Both NiCd-DC converter and DEFC-DC converter power systems are experimentally evaluated over a selected switching frequency range. Input voltage and output voltage characteristics of two types of DEFC-DC converter systems (Nickel-mesh and Nickel-foam electrode assembly) are determined. Experimental results are compared to computer simulations, thus validating the Fourier-series models.

Experimental results show a correlation between the DC converter switching frequency and the output of the DC power system. Sequential switching operation, along with the type of DC converter employed, are factors determining the maximum power transfer of the system. The models developed in this work are flexible over a large switching frequency range, and for any desired duty cycle. Correction factors, accounting for the source-converter impedance matching, are easily implemented in Fourier-series models. The research demonstrates the advantages of Fourier-series models, as compared to both large-signal and small-signal models, with regard to accuracy and ease of implementation to any DC–DC converter-driven power system.

Table of Contents

List of Figures

List of Tables

Acknowledgements

I am thankful to my Heavenly Father and the Lord Jesus Christ, for granting me the health, wisdom, and power, to perform this research, and complete my doctoral program. It is by His grace, that I am who I am, and I am where I am.

I take this opportunity to thank my major professor, Dr. Medhat M. Morcos for his guidance, support and constant encouragement throughout my doctoral program. Dr. Morcos' technical expertise and teaching enthusiasm has been, and will always be an inspiration in my future endeavors.

I am grateful to my committee members, Dr. Bharat V. Ratra, Dr. Anil Pahwa, Dr. Steven K. Starrett, and Dr. Shie-Shien Yang, for their time and effort, and for giving me the privilege to serve on my doctoral committee. I am especially thankful to the committee members for the suggestions given in the preparation of my dissertation.

I would like to express my appreciation to Dr. James Lookadoo of Pittsburg State University, for granting me access to specialized equipment, and for guiding me through the experimental data collection. I am equally appreciative to the help provided by Dr. Junxiao "Charlie" Wu of the Center for Advanced Vehicular Systems, Mississippi State University. Their expert advice has been instrumental in the successful completion of this research.

Special thanks are due to my high school professors, at Grupul Şcolar Industrial Zarneşti, George Căfădaru, Mihai Paiu, Ioan Mureşan, Ioan Busuioc, and Gheorghe Bucur for their commitment and professionalism that inspired me, opening my academic and professional horizons.

Last, but not least, I am grateful to my wife Gladys, for her kindness, and patience, on this important step in my life. Her constant support and encouragement was instrumental in completing this work. I would like to thank my parents and my grandparents, for their unwavering love and care.

Florian Mişoc

Manhattan, Kansas

October, 2007

Dedication

This research is dedicated in the memory of my late father, Cristea Mişoc. In spite of financial hardships and social restrains of Romania's communist regime, my father has provided for me a proper learning and living environment. His continuous efforts and instruction time, has consolidated my understanding of Mathematics and Sciences, positively impacting my academic and professional achievements. My father's example of ethical conduct, at work and in the community, has been–and will always be–a beacon toward achieving the highest levels of education and social conduct, based on Christian moral principles. I take this opportunity to remember my father, Cristea Mişoc, for his kindness, tolerance, and above all, his dedication to helping others, through great personal sacrifice. His short life is an exemplary model of how a father should be.

CHAPTER 1 - Introduction

DC power systems applications range from high level power, found in maritime equipment, to the low level power, used in wireless communication systems. From its early implementation for residential power, to aerospace applications, DC power systems underwent substantial transformations, resulting in lighter, more reliable, and more efficient power systems in use today. From the voltaic pile to the space shuttle Hydrogen fuel cell, DC power sources have evolved, as new materials and techniques were employed. Increased complexity of electrochemical reactions governing the operation of DC power sources, interfacing power electronics circuitry to regulate the flow of power is essential, thus achieving greater output voltage flexibility and efficiency.

1.1 Applications of DC System Models

DC power systems have been developed and implemented first by Thomas Edison in the Nineteenth century, through a simple DC power network of a limited range, as electric power for residential use, mainly illumination. The invention of the automobile prompted the implementation of a DC power system for the auxiliary equipment operation of a motor vehicle. The DC power system for residential and industrial applications was quickly replaced by the more versatile AC power system developed by Nicola Tesla. However, the DC power system developed for the automobile is still in use today. With ever increase of electric power demand, and cost associated with its distribution, DC power systems are becoming more popular, especially in remote locations, and/or applications requiring electric power storage, i.e., storage batteries.

Fuel cells are devices that convert, through an electrochemical process, chemical energy into electrical energy. This energy conversion process has been used to power

electric systems in NASA space programs, and it is currently under development for vehicular applications, and as cogeneration to the power grid.

Fuel cell operation principle has been discovered by William Grove in 1842. However, fuel cell technology has been considered first during the late 1960s at NASA's laboratories, for the space program. In recent years, other government sponsored agencies such as National Renewable Energy Laboratories, Los Alamos National Laboratories, and Oak Ridge National Laboratories, have actively participated in the study and development of fuel cell technology. In conjunction with U.S. government sponsored agencies, many private companies are investing financial and human resources into fuel cells development and commercialization. Companies like General Motors and Honda, have already developed fuel-cell powered vehicles (GM), or currently are commercializing vehicles (Honda scooter) powered by fuel cells.

1.2 Collaboration with the Industry

The research presented in this dissertation has been conducted in collaboration with Kansas NASA-EPSCoR program and the Kansas Space Grant Consortium for unmanned aerial vehicle. The research main goal is to determine the optimal DC power system scheme to power a remotely operated aerial vehicle and its auxiliary research equipment, i.e., small power RADAR, communication system, etc. The use of aerial vehicle future will be the exploration of planet Mars via low altitude unmanned flights. From the multiple choices for power sources, Direct Ethanol Fuel Cells are considered due to their high power densities.

1.3 Fourier-Series Models

Mathematical models of DC–DC converters; buck, boost, and buck-boost, are developed using the Fourier series decomposition method. Each type of DC–DC

converter is mathematically reduced to a set of s-domain equations, from which their transfer functions can be derived. Unlike large-signal models and small-signal models, Fourier-series models developed can accurately describe the transient operation of a DC–DC converter, from the first duty cycle until the steady-state operation.

The DC–DC converter operation consists of sequential switching, generating voltage square waves in some point of the electrical circuit, which is a source of nonlinearity. Power-electronics interfaced circuits; DC–DC converters in particular, are inherently nonlinear due to the sequential switching governing the power conversion process. However, a good approximation of the sequential switching is to consider any square wave as a sum of sinusoids, according to Fourier series theory. Thus, a square wave, of any frequency and duty cycle, can be represented with great accuracy as a sum of sinusoids with variable amplitudes and distinct phase angles. By estimating the pulse voltage generated through sequential switching as a sum of sinusoidal waves, the entire system can be considered linear, time–invariant, thus it is possible to determine system's stability, controllability, and observability.

Fourier-series models of DC–DC converters are only an approximation of the physical circuit. Their accuracy is dependent on the number of harmonics considered for the input voltage-source and/or current-source, and on the accurate modeling of each element in the circuit, mainly circuit losses associated with each device.

1.4 The Research

The present research investigates the output characteristics of Direct Ethanol Fuel-Cell (DEFC) systems interfaced to DC–DC converters, as compared to Nickel-Cadmium battery systems. Fourier-series models of DC–DC converters were developed to aid in the analysis of the experimental results, and to accurately predict system stability, controllability, and observability. The models of DC power systems developed in this research, allow the user to edit change to the model parameters, i.e., load resistance, capacitance, inductance, etc, as they apply to physical DC power systems. The

Fourier-series models presented in this research offer the advantage of AC and DC analysis simultaneously, thus a comprehensive view of the system characteristics is obtained. The analysis is further enhanced through MATLAB numerical computing.

Based on power electronics principles, the sequential switching within DC–DC converters is approximated by Fourier-series representation. Thus, the averaging method of sequential switching is no longer used. Mode 1 (*on*) and mode 2 (*off*) systems, for continuous conduction mode (CCM), are uniquely represented by a single set of state-space matrices, particular to each type of DC–DC converter. Several data sets, describing the input-output characteristics of NiCd-DC converter, and DEFC-DC converter, were compiled and used to determine the electrochemical coefficient for state-space representation of each DC power system. Comparison of experimental data and MATLAB simulations shows good agreement, over a predetermined switching frequency range, and hence, the proposed DC–DC converter models.

In Chapter 2, literature pertaining to fuel cell classification and applications is reviewed. Dynamic models of PEM fuel cells and thermodynamic properties are documented. The electrochemistry characteristic to fuel cells and their complex impedance are investigated.

DC–DC converters are characterized by nonlinearities of semiconductor devices in their circuitry, and with sequential switching operation. Modeling of power electronics circuits, and/or systems interfaced to power electronics, is difficult, and requires a certain degree of approximation. Large-signal models and small-signal models of DC–DC converters are currently used, offering a global view of the converter characteristics. Due to nonlinearities within the system, sub-harmonics of relatively large magnitudes occur within portions of the circuit. Current mathematical models do not predict such occurrences, although experimental data reveal these unwanted phenomena.

Theoretical background concerning the operation of PEM fuel cells, the electrochemistry of NiCd batteries, and Direct Ethanol Fuel Cells, is presented in Chapter 3. Extensive information is presented on the Gibbs free energy theory, governing DEFC energy conversion. Differential equations describing the output voltage and inductor current for continuous conduction mode are presented. Characteristics and operation regimes of DC–DC converter controlled switches, bipolar junction transistor (BJT) and

metal oxide semiconductor field effect transistor (MOSFET), are presented. Linearization of nonlinear systems is largely employed whenever an approximate state-space representation of the system suffices the desired application. The method of linearization is briefly explained.

Sequential switching generates periodic waveforms of voltages and currents within the system network. Any periodic waveform can be accurately described by an infinite sum of sinusoidal waves, of well determined amplitudes and phase angles. Thus, a square-wave voltage, or a triangular-wave current, can be represented with great accuracy by a sum of finite number of sinusoidal waves.

In Chapter 4, the small signal models of DC–DC converters are presented. Averaged switch method is investigated for all three types of converters (buck, boost, and buck-boost), and the state space representations of the averaged systems are derived. Analytical derivation is performed to linearized the nonlinear system about an operating point. DC operating point transfer function is deduced, and the AC component characteristic is derived. For a global representation of DC power systems, the linearization method could be sufficiently accurate. Thus, the modeling technique is largely used by many power electronics engineers. Oversizing the low-pass filter capacitor at the output end reduces significantly the ripple ratios present in the output voltage, thus a desired DC output voltage is obtained.

Small signal models of DC–DC converters are particularly useful in applications requiring sudden changes of duty cycle, as a response of system load dynamics. It is this type of applications that will, most likely, continue to use the small signal modeling. Limitations associated with sub-harmonics phenomena during duty cycle transition, will continue to restrict the range of applications for the averaged switch model.

Chapter 5 presents the development steps of all three types of converters. All converters are assumed to operate in continuous conduction mode (CCM), thus each converter would be operating in two sequential modes: *on* mode and *off* mode. Each converter mode is described by a set of first-order differential equations. Then, an equivalent state-space representation is developed. Careful consideration is given to the free wheeling diode operation. Its function is emulated by equaling an element of state-space matrix to zero. The input voltage and/or current are described by their respective

Fourier-series equivalents. S-domain expression of inductor currents are derived for each converter.

In Chapter 6, numerical values are attributed to each DC–DC converter component. State-space representations derived in Chapter 5 are implemented in MATLAB code. Simulations of transient and steady-state operation regimes are performed for three distinct duty cycles, 50%, 65%, and 80%, and at three switching frequencyes, 200 Hz, 500 Hz, and 1 kHz. The average outputs of all three models, resulted from MATLAB simulation are in agreement with the expected theoretical values, for ideal source DC power systems. Routh stability tests show that all three Fourier-series models are stable.

Chapter 7 presents the experimental results verifying the Fourier-series models for NiCd battery powered DC source, and DEFC mesh and foam DC powered sources. Experiments were conducted at Pittsburg State University, Pittsburg, KS, and at Mississippi Valley state University, Itta Bena, MS. Limited by the available equipment, measured output voltages were accurate within 1 mV. Experimental results have been used to determine the limitations of the NiCd battery model, and the need for an improved model of the PEM fuel cell.

Chapter 8 presents the conclusions of the research, and lists possible enhancement to the Fourier-series models developed in this work.

1.5 Impact of the Research

The Fourier-series models developed in this work, are instrumental in DC power system design for NASA EPSCoR program, and will be used by ACTA-nanotech Corporation in the DEFC power systems design. Results obtained from DC–DC converter interface to NiCd batteries and direct ethanol fuel cells (DEFC) show a correlation between converter switching frequency and the DC source power output, for a chosen duty cycle operation. In applications requiring maximum power output the choice of duty cycle and switching frequency can be more accurately made.

Applications employing storage batteries, as those used in this research, may require high efficiency. Knowledge on the battery response to sequential switching is instrumental for determining the optimal operation parameters, and/or system design changes.

Fuel cell applications can accommodate either high efficiency at low power transfer, or high power transfer at low efficiency. Those features can be implemented for a given fuel cell-DC power system by simply adjusting the switching frequency of the DC−DC converter while maintaining the duty cycle constant. One such application is vehicular systems, where the amount of power varies widely.

CHAPTER 2 - Literature Review

DC power systems have gained popularity in stationary and mobile applications, and led to further development of power electronics in the last two decades. DC power systems operation consists of sequential switching, thus requiring a mathematical representation, as an approximation of the physical system, for the design and analysis of power system.

This chapter highlights the contributions reported in the literature related to the research topic of this dissertation. Fuel cell classification and applications are surveyed, describing the electrochemical characteristics of electrolyte membranes and the dynamics governing the electrochemical process. Electrical model describing the polymer electrolyte membrane fuel cell (PEMFC) dynamic characteristics is presented. Large-signal models and small-signal models of DC–DC converters are introduced, and electronic chaos and sub-harmonic effects in the context of DC converter driven fuel cells are presented.

2.1 Classification and Applications of Fuel Cells

Fuel cell classification is generally done based on the fuel cell electrolyte. Electrolyte type determines fuel cell operating temperature, materials used for fuel cell fabrication, type of fuel and oxidant used in the electrochemical reaction, and the operating characteristics of a fuel cell. Because of the differences in some of the operating characteristics, different types of fuel cells are suited for different applications [1].

2.1.1 Polymer Electrolyte Membrane Fuel Cell

Polymer electrolyte membrane fuel cell, commonly known as proton exchange membrane (PEM) fuel cell, employs a solid polymer electrolyte. The membrane is made of Teflon-like material, and is an excellent conductor for protons, yet a great insulator for electrons. The main advantage of PEM fuel cell is its high power density, higher than any other fuel cell type, with the exception of alkaline fuel cells. There are a number of benefits from the use of solid electrolyte; lower corrosion is associated with the use of solid electrolyte, and no liquid management is required, as is the case for liquid electrolytes. The solid electrolyte allows low operating temperatures (between 70^0C and 90^0C) of fuel-cell, which is beneficial in applications where a quick start is required. PEM fuel cells are preferred, due to their long life characteristic, for different application fields [2].

A significant disadvantage of PEM fuel cells is the cost of Platinum catalyst (or Pt-Pd catalyst), which is a key component for the PEM. The amount of Platinum used in PEM fuel cells has been decreased in the last decade, through membrane optimization. However, further reduction of the amount of catalyst used in the PEM fuel cells is needed in order to lower the overall cost to a range competitive with internal combustion engines or other current technologies. Carbon-monoxide contamination is another disadvantage of the PEM fuel-cells, which can be compensated by careful design [3]. Some PEMFCs operate with fuels other than Hydrogen, i.e., Methanol, Formic Acid, and Ethanol. PEMFCs are used in a variety of applications, stationary or mobile power sources. Since their quick start-up, they are well suited for vehicular applications, while low operating temperatures allow their use in portable applications, in some cases replacing the battery power source system.

2.1.2 Alkaline Fuel Cells

Alkaline fuel cells (AFC) use a liquid solution of Potassium-Hydroxide as an electrolyte. This electrolyte is retained in a matrix, allowing protons to penetrate through it, while the electrons do not. The limiting reaction in any fuel cell is the cathode reaction, due to the longer reaction time as compared with the anode reaction. In AFCs, the cathode reaction is much faster than in other types of fuel cells, enhancing the overall performance of the AFC [2]. The low operating temperature in the same range as PEMFCs (between 70^0C and 90^0C), gives AFC a quick-start characteristic.

Very intolerant to Carbon-Dioxide, AFCs are not operated with normal outside air as oxidant, requiring an auxiliary system to remove the Carbon-Dioxide from the intake air. Another disadvantage of AFCs, is the limited life of the electrolyte and its corrosive nature, increasing the cost of alkaline fuel cells. Research is currently conducted into evaluating possible less expensive catalysts, such as Carbon and metal oxide electrodes that can lower the AFCs' cost.

2.1.3 Phosphoric Acid Fuel Cells

Phosphoric acid fuel cells (PAFC) employ a liquid phosphoric acid as electrolyte. Similar to the alkaline fuel cells, the electrolyte (phosphoric acid) is placed in a Teflon matrix, retaining the acid in a well defined region of the fuel cell. The operating temperature range for PAFC is between 175 and 200^0C, twice the operating temperature of PEM-FC and AFC, and cannot exceed 210^0C, the melting temperature for the Teflon matrix. One of the main advantages of the PAFC is that it is very tolerant to impurities in the reformed hydrocarbon fuels, making PAFCs a less expensive alternative. This type of fuel cell has been under development for more than 20 years, its cost was decreased and its efficiency improved.

High operating temperature allows the PAFCs to be interfaced with cogeneration systems, thus increasing the overall system efficiency up to 85 %. One main disadvantage

shared by PAFCs and PEMFCs is the very expensive catalyst used, which keeps the price of fuel cells in the high range. Other disadvantages of PAFC are its relatively low current and power density, and the excessively large size and weight of the system. Used in vehicular applications, PAFCs are tolerant to fuel impurities; however, they require a warm-up time to achieve peak power operation [4].

2.1.4 Solid Oxide Fuel Cells

Solid oxide fuel cells (SOFC) are high-temperature fuel cells, using an electrolyte made of Yttria-stabilized Zirconia, a solid ceramic material. The high operating temperature (600 to 1000^0C) gives SOFC the advantage of a high efficiency over low-temperature fuel cells, and the ability to use a large variety of inexpensive catalysts. High operating temperature allows SOFCs to use more types of fuels, without the use of a reformer. However, the high operating temperature determines some disadvantages; a long start-up time and premature deterioration (breakdown) of the fuel cell components. Due to those factors, SOFCs are restricted, at this time, to medium and large-scale power generation applications.

2.1.5 Molten Carbonate Fuel Cells

Molten carbonate fuel cells (MCFC) use a molten carbonate salt mixture, usually Lithium-Carbonate and Potassium-Carbonate, as their electrolyte. MCFC is a high-temperature fuel cell (600 to 1000^0C), exhibiting the same advantages and disadvantages of the SOFCs. The only economical applications of MCFCs are large scale power generation, in the order of 250 kW to 2 MW [2].

2.2 Dynamic Model using Circuit Equivalent of PEM Fuel Cell

A dynamic model and model validation for PEM fuel cells was performed using MATLAB-SIMULINK and PSpice environments, both approaches modeling the fuel cell as an electric circuit. Steady-state response and transient response have been considered for the dynamic modeling [5].

Previous studies of steady-state fuel cells characteristics [6]–[11], and dynamic modeling of fuel cells [12]–[14], were based mainly on empirical equations and/or the electrochemical reactions inside the fuel cell.

2.2.1 Double-layer Equivalent Circuit

In the mathematical approach, the following assumptions are made to simplify the analysis [6]–[8], [15]:

- One-dimensional treatment.
- Ideal and uniformly distributed gases.
- Constant gas pressure and constant gas flow in the fuel cell's channels.
- Humidified Hydrogen fuel cell is used and the oxidant is humidified air.
- A ratio of 1:2 of anode water pressure versus cathode water pressure is assumed.
- Fuel cell operates at a constant temperature of 100 ^{o}C.
- The electrochemical reaction product (H_2O) is in liquid phase.
- The overall specific heat capacity of the stack is assumed to be constant.
- Individual cells' parameters can be lumped together to represent a fuel cell stack.

In a PEM fuel cell the membrane is coated with an electrically conductive material which acts as a catalyst for the electrochemical reaction. Platinum (Pt) and Platinum-alloy are the most use materials for this purpose. Both conductive plates are separated by the partially-conductive Proton Exchange Membrane, which allows only

positive ions (H^+) flow, thus presenting a capacitive property of the fuel cell assembly. The only path for electron flow is assured by the membrane metallic coating and the external electrical circuit. Two charged layers of opposite polarity are formed across the boundary between the porous cathode and the membrane [15], [16]. Those layers, commonly known as electrochemical double-layer, can store electric energy thus behaving like a large capacitor. In the equivalent electrical circuit of the double-layer, the capacitance resulted from the double-layer charging effect is very large, due to the porous nature of the PEM, and can reach values of several Farads [15], [17].

2.2.2 Thermodynamic properties equivalent circuit

In practice, fuel cells work in conjunction with power electronics (DC–DC converters, DC–AC converters, voltage regulators, etc.), thus an equivalent electrical circuit for the fuel cell was developed, simulating the fuel cell's thermodynamic properties [5].

During transient operation conditions, the fuel cell temperature will vary. This temperature gradient can be determined by the heat transfer equation [18].

2.2.3 Internal potential equivalent circuit

The internal potential of fuel cell is a function of load current and temperature, and is modeled as two series-connected parameter-controlled voltage sources. Both parameter-controlled voltage sources are series connected with the standard reference potential E_0, represented as an independent voltage source.

MATLAB-SIMULINK and PSpice models were compared with a 500W SR-12 Avista Lab PEM fuel cell [5]. The following conclusions were drawn:

a. Increasing the load current from 1.1 A to 20.5 A, in 0.2 A increments and periods of 40 seconds each, the power versus current curves obtained experimentally agree with the theoretical values and with the computer simulations.

b. Temperature response of the PEM fuel cell stack was measured during the same ramp conditions as in "a", with an increase rate of 5 mA/s [5]. Experimental data and the computer simulations are in agreement within 3.5 K, in the worst case.

c. Dynamic properties of the PEM fuel cell stack are mainly influenced by the double-layer charging effects, fuel and oxidant flow, and thermodynamic characteristics inside the fuel cell [19]. The time constant for fuel cell equivalent electric circuit is relatively small (of the order of 1 second) for a large capacitance. This is due to the low value of double-layer resistance (< 0.05 Ω), when the fuel cell operates in the linear region [5]. However, the double-layer capacitance is large (in the order of several Farads), thus affecting fuel cell transient response. For a step input load-current, the voltage drops simultaneously to a certain value, and then decays exponentially to its steady-state value.

In the same time, the fuel and oxidant flow rate cannot follow the load-current change, thus accounting to a flow change delay of few tens of seconds to as much as few hundreds of seconds. The thermodynamic inertia of the fuel cell accounts for response delay in the order of minutes. Therefore, the transient response of the PEM fuel cell is dominated by its thermodynamic characteristics and by fuel and oxidant flow rate, over the long time operation [5].

2.2.4 Electrochemical impedance of PEM fuel cells

The frequency dependence of fuel cell impedance is a function of the double-layer capacitance [20], and is different for planar catalyst model than the porous catalyst model [21]. In addition, the oxygen reduction reaction occurring in the fuel cell involves an adsorption step giving rise to an inductive behavior at low frequencies (around 0.6 Hz) [22]. The impedance response of PEM fuel cells is a combination of the responses of the

anode and cathode half-cells, with time constants of different values and frequency dependent [20].

2.3 Transient Performance of Fuel Cell System

Fuel cell systems are considered the replacement of internal combustion engine for mobile applications, thus reducing (and possibly eliminating) the dependency on fossil fuels in the near future [23]. For automotive applications, fuel cells' transient behavior is one of the key requirements: constant optimal temperature, membrane hydration, and partial pressures of the reactants. In this way, the degradation of fuel cell stack voltage is avoided, while maintaining high efficiency and extending fuel cell stack life [23]. To form a "fuel cell engine," a fuel cell stack needs to be integrated with other components: Hydrogen supply system, air supply system, cooling system, and humidification system.

The power output of a fuel-cell stack depends on current drawn from the stack, and on stack output voltage. The fuel cell voltage is a function of: current, reactants partial pressures, fuel cell temperature, and membrane's (PEM) humidity. The water used in the humidifier, stored in the water tank at ambient temperature, is used to hydrate the membrane and to remove most the heat generated by the fuel cell stack [23]. This is accomplished by the cooling system, which re-circulates de-ionized water through the fuel cell stack. Since fuel cell stack output voltage varies significantly, direct connection to traction motors is not suitable, thus power conditioners are needed to interface fuel cell stacks with the loads (traction motors) [24]. It is assumed that multiple cathode and anode volumes of the multiple fuel cells connected to form a stack are lumped together as a single stack-anode and stack-cathode volumes, thus simplifying the analysis. The fuel cell stack model contains four subsystems models: stack voltage model, anode flow model, cathode flow model, and membrane hydration model. It is also assumed that fuel cell stack temperature is perfectly controlled by the cooling system, and maintained at optimal value of 80^0C.

2.3.1 Model of transient behavior of PEM fuel cell

Variations of temperature, current and humidity have shown related variation in the output voltage of a PEM fuel cell [25]. An increased conductivity, due to increased membrane humidity [26], [27], results in a decrease of the membrane's internal resistance and output voltage variations [28]. Current variations, dependent on loads and power demands in most applications, determine a nonlinear output voltage response, with variations dependent on fuel cell operating temperature [28]. Since a fuel cell model can not take into account all parameters involved in the transient response, a mathematical model is limited to a particular PEM manufacturer model, and even different between cells in a stack [29]. The response of porous electrodes [30] and non-uniform ionic conductivity [31] properties can be used for an improved impedance model.

Fuel cells are mainly characterized by their steady-state current/voltage responses, while information obtained from transient responses is valuable for property measurements. Some transient techniques used are: potential stepping, potential sweeping, current interrupt, and electrochemical impedance spectroscopy [32]–[36].

2.4 Voltage Model of Fuel Cell Stack

The stack voltage is calculated as function of stack current, cathode pressure, reactant partial pressures, fuel cell temperature, and membrane humidity. All fuel cells are series-connected, thus the stack voltage, v_{st}, is calculated by multiplying the cell voltage, v_{fc}, by the number of cells, n, in the stack:

$$v_{st} = n \cdot v_{fc} \tag{2.1}$$

The stack current, I_{st}, is equal to the cell current; the cell current density is:

$$i_{fc} = \frac{I_{st}}{A_{fc}} \tag{2.2}$$

The fuel cell voltage is found using a combination of empirical and physical equations [29]:

$$v_{fc} = E - v_{act} - v_{conc} - v_{ohm} \tag{2.3}.$$

The open circuit voltage, E, is calculated from the energy balance between chemical energy in the reactants and electrical energy as [6]:

$$E = 1.229 - 0.85 \cdot 10^{-3}\left(T_{high} - T_{low}\right) + 4.3085 \cdot 10^{-5} \cdot T_{high} \cdot \left[\ln\left(p_{H_2}\right) + \frac{1}{2}\ln\left(p_{O_2}\right)\right] \tag{2.4}$$

Activation overvoltage, v_{act}, is calculated using an approximation of Tafel equation:

$$v_{act} = v_0 + v_a \cdot \left(1 - e^{-c_1 \cdot i}\right) \tag{2.5}$$

Concentration overvoltage, v_{conc}, resulting from the change in reactants concentrations, is expressed by an approximate equation:

$$v_{conc} = i \cdot \left(c_2 \cdot \frac{i}{i_{\max}}\right)^{c_3} \tag{2.6}.$$

where, c_1, c_2, c_3, and $i_{\max}$, are constants that depend on temperature and reactants partial pressures, and need to be determined experimentally.

Ohmic overvoltage, v_{ohm}, is the voltage drop due to polymer membrane resistance associated with proton transfer through the membrane, and the intrinsic resistance of anode-electrode and cathode-electrode, to the flow of electrons:

$$v_{ohm} = i \cdot R_{ohm} \tag{2.7}.$$

The fuel-cell ohmic resistance is dependent on membrane thickness, t_m, membrane conductivity, σ_m, and fuel-cell humidity, λ_m:

$$R_{ohm} = \frac{t_m}{\sigma_m} = \frac{t_m}{\left(b_{11}\lambda_m - b_{12}\right) \cdot \exp\left(b_2\left(\frac{1}{T_{low}} - \frac{1}{T_{high}}\right)\right)} \tag{2.8}.$$

The values of constants b_{11}, b_{12}, and b_2, are determined empirically, and are unique to each type of polymer used for membrane fabrication. No sufficient experimental data is available to verify the voltage degradation function of membrane water content [23]. Oversaturated conditions cause condensation and liquid formulation inside the anode and/or cathode, in effect causing further fuel cell voltage degradation [23].

A number of fundamental problems must be overcome to improve PEM fuel cells performance: (1) identify key parameters for fuel cell performance and examine how to optimize stack and system design; (2) identify critical issues, such as the effects of start-up and shut-down, transient response; and, (3) examine performance under extreme conditions, such as sub-freezing temperatures.

2.5 Nonlinear Dynamics of Power Electronics

Power electronics are the link between electric power generation and electric power consumer, therefore power converters cannot be viewed outside their interface with power sources (generators, batteries, fuel cells, etc.) and loads (heaters, electric motors, etc.). Power electronics, in general, and power converters, in particular, are integral part of the whole electrical system, thus influencing the operation and characteristics of the system, aiming to achieve three goals:

1) Convert electrical energy from one form to another.
2) Achieve high conversion efficiency, minimizing losses through wasteful heat.
3) Reduce the size of power converters and the equipment they interface with.

2.5.1 Chaos phenomena in power converters

First mentioned by Van der Pol in 1927 [37], [38], chaotic effects in electronic circuits are often occurrences in DC–DC converters and other control systems

incorporating a pulse-width modulator [39], [40]. First mentioned in a 1984 conference paper [41], chaos in controlled DC–DC converter was later analyzed and further expanded to other power electronics systems [42]. Electronic chaos was further investigated, and other causes were identified [43]. Later those ideas were developed, mainly concerned with chaos prediction and experimental validation for DC–DC converters [44]–[48].

In the construction of any power converter there are two basic component groups:

a) Switching components, ideally lossless, characterized by $v = 0$ for the *on* mode, and $i = 0$ for the *off* mode, therefore displaying zero energy dissipation: $p = v \cdot i = 0$. Active switches such as transistors turn *on–off–on–off*, in response to a controlling signal. Passive switches (diodes) exhibit high nonlinear $v - i$ characteristic.

b) Reactive components, such as inductors and capacitors, are characterized by their energy storage capabilities, properly described by: $v_L(t) = L \cdot \left({}^{di}/_{dt} \right)$ for inductors, and $i_C(t) = C \cdot \left({}^{dv}/_{dt} \right)$ for capacitors.

2.5.2 Continuous conduction mode

During each functional cycle, *on–off*, *on–off*, electric energy is "pumped around" through the circuit, implying the existence of nonlinearity [37]. Sources of nonlinearity in electronic circuits are semiconductor devices (switches) intrinsic properties, inductors induced nonlinearity, and nonlinearity associated with control circuits (comparators, PWMs, etc.).

Nonlinear dynamics in power electronics induce chaotic effects in the entire circuit, complex and initially unpredictable characteristic. In an *R-L-D* circuit, a transformer connected to a rectifier diode, the transformer leakage inductance resonates with the diode nonlinear capacitance resulting in a chaotic transient when excited by the

switches. A tuned circuit involving a saturating inductor has a similar chaotic effect. Ferro-resonance in the power system can cause excessive voltages and currents [49].

2.5.3 Discontinuous conduction mode

In discontinuous mode (DCM) the converter has three modes of operation, represented by three separate circuits, all derived from the converter circuit. From a typical buck converter circuit, shown in Fig. 2.1, three mode circuits are derived.

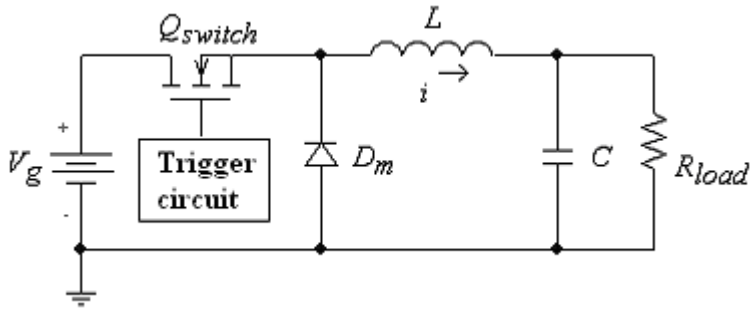

Figure 2.1: Typical buck converter circuit

Mode 1: Transistor Q_{switch} conducts for a fraction $k(t)$ of each switching cycle.

Mode 2: Diode D_m conducts for a period of time, until current $i = 0$.

Mode 3: Both transistor Q_{switch} and diode D are *off*.

The differential equation describing the discontinuous conduction mode (DCM) is of first order (unlike the continuous conduction mode: second-order differential equation). This is expected, since the inductor does not enter into long-run dynamics of the system, therefore, current $i = 0$ at both the beginning and end of each cycle.

Since a first-order system, having a pole at $s = -1/\tau$, with proportional control has a phase grater than 90^0, it is expected to exhibit good stability. However, less stability of the system was observed at high frequencies, since another pole is present in the differential equation describing the system [49].

The continuous-conduction mode model does not account for the switching frequency, since operation over a single cycle is considered. The conventional analysis, using the averaging method, predicts stability for all input voltages, whereas in reality sub-harmonics and chaos are possible.

2.6 Mathematical Models for DC–DC Converters

DC–DC converters are nonlinear dynamic systems. Such systems may be stable in the vicinity of an operating point, but may not be stable when undergoing a large perturbation [50]. Conventional methods of modeling DC–DC converter circuits consists of taking an average over a switching cycle, thus linearizing the circuit over an operating point [51]. State-space averaging operates on the state-space representation of the system [52], while other methods using "injected/absorbed currents" treat the switch-diode combination in isolation from the circuit [53]. The aim of all these methods is to replace the nonlinear, time-varying dynamical system with an averaged, linearized system. Since the linearization is implemented only over an operating point, changes in load impedance, switching frequency, or other parameters, make the linearization inaccurate.

2.6.1 Large-signal model for DC–DC converters

The output voltage of a DC–DC switching converter is controlled by the duty ratio of the active switch. The active switch (transistor) and the diode are nonlinear components, and can be modeled as controlled current-source for the switching transistor, and as a controlled voltage-source for the diode [54], [55].

Analysis of dynamic characteristics for current-programmed DC–DC converters is very complicated due in part to the feedback control loops. The procedure for developing a large-signal averaged circuit model for current-programmed converters consists in six main steps [56]:

1) A large-signal averaged circuit model of the switch converter is developed, having the duty ratio as control variable.
2) The expression of the rising slope of inductor current for each power mode is developed.
3) The duty ratio k is expressed as function of the control current, inductor current, and other circuit variables.
4) In the large-signal model, the duty ratio is substituted with its equivalent expression found in Step 3, thus the average transistor current, and average voltage across diode are expressed in terms of control current.
5) The active switch (transistor) is replaced by the controlled current-source, and the diode is replaced by the controlled voltage-source.
6) All other components remain unchanged, thus the large-signal model is concluded.

Those steps are followed for developing large-signal models for boost, buck-boost, and Cúk converters.

Large-signal averaged circuit model of the current-programmed DC–DC switching converter is obtained by: (a) replacing the active switch with a controlled current-source (dependent on the current command, supply voltage, and other circuit variables), having the same value as the averaged current flowing through the active switch; (b) replacing the diode with a controlled voltage-source (also dependant the current command, supply voltage, and other circuit variables), having a value equal to the averaged voltage across the diode, and (c) keeping the rest of the switching converter unchanged. Large-signal averaged circuit models, gives the designer a global view of the system dynamics, and a clear understanding of the system limitation to achieve robust control, presenting the following advantages [56]:

- Reduction of mathematical derivations needed to obtain the large-signal dynamic characteristics of the system.
- Parasitic parameters (inductor's winding-resistance, capacitor equivalent series-resistor), can be easily evaluated for the large-signal model.

However, the large-signal models considered are suitable only for cases when the supply voltage and control signal change slowly (as compared to the switching period [53].

2.6.2 Small-signal model for DC–DC converters

In the small-signal models of DC–DC converters, the main focus is on determining the transfer function governing the converter operation. The converter is considered as a nonlinear, time-dependent system, linearized through averaging method about a selected operating point [57].

State-space (small-signal) method is referred to as the switch averaging method, where the converter is switching between two time-invariant modes of operation: *on*-time and *off*-time [58]. Both modes of operation for the buck converter; *on*-mode and *off*-mode, can be represented as a linear, time-invariant system, which is the starting point for the state-space averaging method, where a single, linear, time-invariant representation of the system is derived. Since continuous conduction operation is assumed, two systems must be considered. Thus, two state-space representations need to be derived in the first step [59]. The buck converter is represented as switching between two different linear, time-invariant systems during a switch period. Thus, the buck converter behaves like a linear, time-varying system. Averaging the two linear systems with respect to their time span during the switching period, a nonlinear, time-varying system is obtained, which is an approximation of the two linear, time-invariant systems. Assuming that the operating point is an equilibrium point, the system is accurately described by its state-space DC model and by its state-space AC model [59].

Large-signal and small-signal models are suited for steady-state operation with little or no variations over the operating point. However, transient operating conditions of the system are not accurately described by either large-signal model or small-signal model. The fuel cell/DC–DC converter model for the space-shuttle power system, assumes a value of 4 Farads of capacitance at the fuel cell output terminals. However, this is valid only if the fuel cell is acting as a source. There is no mathematical model or data determining on how much energy the fuel cell could absorb when presented with a transient from an external source without damage or reduced life [60]. Testing the

shuttle–space station system 120 Vdc–28 Vdc power supply, with a flight fuel cell from the shuttle, was scheduled for early summer, 2006. During those tests, fuel cell source impedance measurements were conducted at various load conditions for small signal stability verifications. Test for large signal stability, by applying transients, would then follow [60]. NASA and Boeing are interested in an electrical model at the output terminals under steady-state and transient operating conditions. The power system is designed by Boeing to accommodate bidirectional flow of power, via a buck-boost bidirectional DC–DC converter.

CHAPTER 3 - Theoretical Background

Storage batteries and fuel cells are devices that convert chemical energy into electrical energy. This energy conversion process can be applied to power vehicles, electric appliances, electronic devices, or can be applied to the power grid via power electronics systems.

This chapter presents the theoretical foundation needed to accomplish the work of this dissertation. Characteristics and design consideration of DC power systems are first presented for resistive and inductive loads. Two types of DC power sources and their energy conversion processes are discussed; storage battery and fuel cells. Models of DC–DC converters and their steady-state characteristics are investigated. Finally, Fourier-series decomposition theory is presented, as it pertains to sequential switching mechanisms characteristic to power electronics.

3.1 DC Power Systems

In general, a power system is comprised of four main elements: power-source, control system, load, and electrical lines, and is equally valid for AC systems and DC systems [61]. The power source for DC power systems can be any type of battery, solar cells or fuel cells, which can generate electrical power at a nominal voltage and current, for a given amount of time. A DC power system block diagram is presented in Figure 3.1, where each block has a set of characteristics that are expressed mathematically [62].

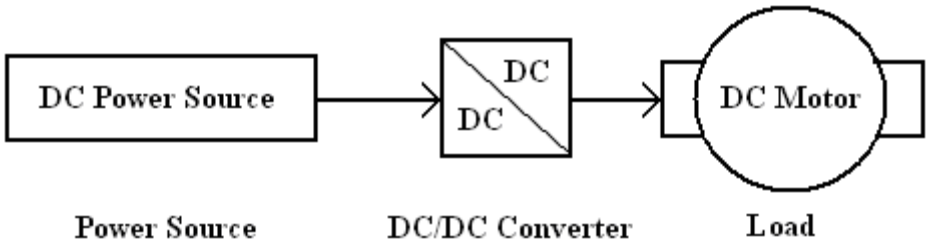

Figure 3.1: DC Power System block diagram

AC power systems are in general characterized by an inductive reactance, since most elements of the system are inductive in nature. Conversely, DC power systems are characterized by resistive elements working in conjunction with inductive and capacitive elements [62]. Therefore, at start up, DC power systems have one of the three type of responses; over-damped, critically damped, and under-damped, based on the system design and operation requirements [63], [64].

3.2 Electric model of storage battery

Denoting the anode reactants by *A*, and the cathode reactants by *K*, the electrochemical processes occurring at anode and cathode are described by:

$$A \rightarrow \left(A^{+}\right) + e^{-} \tag{3.1}$$

$$K + \left(A^{+}\right) + e^{-} \rightarrow P \tag{3.2}$$

where *P* represents the electrochemical reaction products, including the generated heat. Combining the anode and cathode processes (3.1) and (3.2), the equation describing the electrochemical reaction in a storage battery is derived.

$$A + K = P + electric - current \tag{3.3}$$

Considering the density of charge transport through the electrolyte ρ, the electric field *E*, and the current density due to charge transport *J*, the state continuity equation is:

$$\nabla \cdot J + \frac{d\rho}{dt} = 0 \tag{3.4}$$

For stationary material motion, i.e., electrolyte, the current density and the density of charge are:

$$J = \sigma \cdot E \tag{3.5}$$

$$\rho = \nabla \cdot \varepsilon E \tag{3.6}$$

From Equations (3.4) and (3.5), the continuity equation is:

$$\nabla \cdot E + \frac{d}{dt}\left(\nabla \cdot \varepsilon E\right) = 0 \tag{3.7}$$

Thus, the continuity equation for a storage battery is:

$$\sigma E = \frac{-d}{dt}\left(\varepsilon E\right) \tag{3.8}$$

Relaxation time constant τ, is defined as:

$$\tau = \frac{\varepsilon}{\sigma} \quad , \tag{3.9}$$

The solution of continuity Equation (3.7), with initial conditions $E(t=0) = E_0/a$, describes the transient behavior of the decaying electric field.

$$E = \frac{E_0}{a} \cdot e^{\left(-\frac{t}{\tau}\right)} \tag{3.10}$$

Thus, the expression in (3.10) resembles a parallel *RC* circuit, describing the storage battery capacitance *C* and its dielectric loss *R*, as shown in Fig. 3.2.

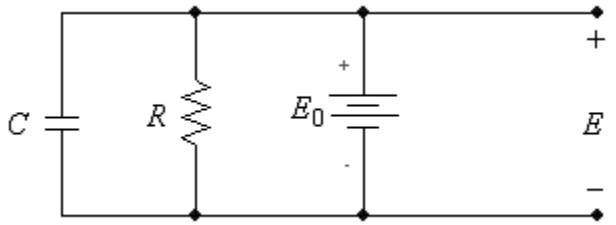

Figure 3.2: Equivalent circuit of storage battery

The lumped-parameter circuit, shown in Fig. 3.2, can be represented mathematically in the s-domain as:

$$E(s) = E_0 \cdot \frac{\tau}{1 + s \cdot \tau} = E_0 \cdot \frac{RC}{1 + s \cdot RC} = E_0 \cdot \frac{1}{s + \left(\frac{1}{RC}\right)} \tag{3.11}$$

The Nickel-Cadmium (NiCd) battery, consists of a nickel-plated, woven mesh cathode, while the anode is a cadmium-plated net. The electrolyte used is potassium-hydroxide (KOH), acting only as an ion conductor, and does not contribute significantly to the battery electrochemical reaction. NiCd batteries present good performance in high discharge and low temperature operation. The electrochemical reactions occurring at the anode and cathode generate a potential difference of 0.81 V, and 0.49 V, respectively, with an overall open-circuit voltage of 1.3 V. The respective reactions at the anode and cathode are:

$$Cd + 2 \cdot OH^{-} \rightarrow Cd(OH)_2 + 2e^{-} \tag{3.12}$$

$$NiO_2 + 2 \cdot H_2O \rightarrow Ni(OH)_2 + 2 \cdot OH^{-} \tag{3.13}$$

The chemical reaction describing the operation of a NiCd battery is:

$$Cd + NiO_2 + 2 \cdot H_2O \rightarrow Cd(OH)_2 + Ni(OH)_2 \tag{3.14}$$

3.4 Fuel Cell Principle of Operation

Fuel cells operation is based on electrochemical principles. The recombination reaction of gaseous hydrogen and oxygen, producing water vapor, is the foundation of the process. Of recent interest is the ethanol-oxygen electrochemical reaction, due in part to the unsophisticated fuel storage system. Direct ethanol fuel cell (DEFC) reactants are liquid ethanol and gaseous oxygen, while the reaction products are liquid water and gaseous carbon dioxide. The oxy-reduction process occurs naturally, and is governed by the migration of charged particles toward regions of lower electrochemical energy [1].

3.4.1 Fuel cell electrochemical reactions

In hydrogen-oxygen reaction-based fuel cells, water vapor is the final product, and has a lower electrochemical energy than the reactants, thus causing the charged particles in each of the two reactants to move toward each other [1], [2], and [15].

$$2H_2 + O_2 \Rightarrow 2H_2O \tag{3.15}$$

The hydrogen-oxygen reaction generates two electrons per reacting Hydrogen molecule.

Separating the hydrogen-oxygen reactants with an electrolyte (or an electrolytic membrane), which conducts protons and insulates electrons, the following phenomenon occurs: protons from the hydrogen atoms will move through the electrolytic membrane, while hydrogen electrons will not. These electrons will tend to recombine with the protons on the other side of the membrane to reach electrical neutrality and stability. When a path for electrons is added to the system, connecting the two sides of the membrane, the electrons will travel through it. The movement of electrons through the external circuit is controlled to generate electric energy, as shown in Fig. 3.3.

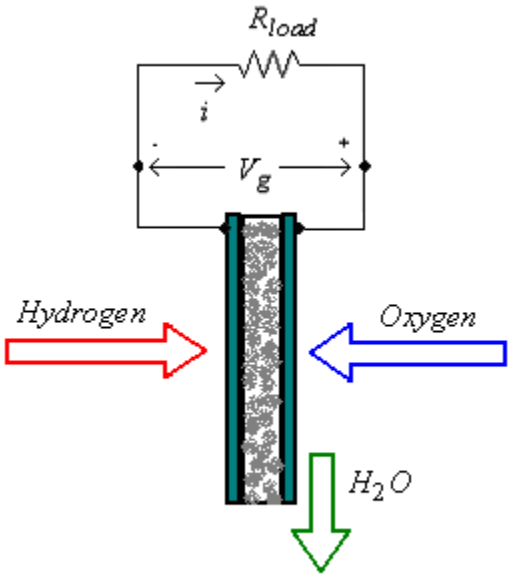

Figure 3.3: PEM fuel cell operation

The electrochemical reaction occurring in the system is broken down into two half reactions; the oxidation half-reaction, and the reduction half-reaction [15].

The oxidation half reaction, presented in (3.3), is the dissociation of hydrogen atoms into protons and electrons, and takes place at the anode side of the electrolytic membrane.

$$2H_2 \Rightarrow 4H^+ + 4e^- \tag{3.16}$$

After the dissociation, the protons will move through the electrolytic membrane, while the electrons are free to move through the external electric circuit connecting the anode and the cathode.

The reduction half-reaction occurs at the cathode, and is expressed by (3.4).

$$O_2 + 4H^+ + 4e^- \Rightarrow 2H_2O \tag{3.17}$$

The oxygen atoms bond to the protons flowing through the membrane and the electrons coming from the external circuit, forming water. Compared to partial oxidation internal reforming process, direct oxidation has two main advantages: higher electric efficiency, and elimination of nitrogen-fuel contamination.

Since direct hydrocarbon fuel-cell advantages were reported only in single cell applications, it is intuitive to implement DC–DC converter driven fuel-cell stack systems in future applications [21]. Direct ethanol fuel cells generate twelve electrons per reacting ethanol molecule.

$$C_2H_5OH + 3O_2 = 3H_2O + 2CO_2 + 12e^- + 12^+ \tag{3.18}$$

The movement of those charged particles can be used to generate electricity, which is the controlled flow of electrons, presented in Figure 3.4.

Direct ethanol fuel cells are less expensive to manufacture and operate, thus reducing the risks associated with the pressurized and/or cryogenic storage of hydrogen fuel. Instead, liquid solution of 10 – 20% ethanol is used to operate the cell. The reactants are separated by an anionic membrane similar to PEM membrane.

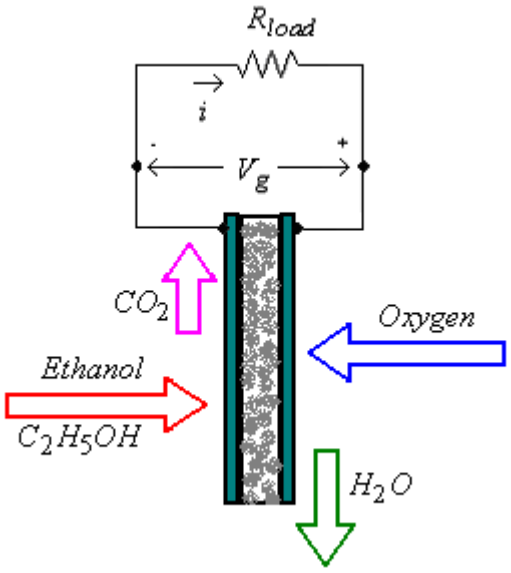

Figure 3.4: Direct Ethanol fuel cell operation

The reduction reaction at anode is described by:

$$C_2H_5OH + 3H_2O = 2CO_2 + 12e^- + 12H^+ \tag{3.19}$$

At the cathode, the oxidation reaction is described by:

$$3O_2 + 12H^+ + 12e^- = 6H_2O \tag{3.20}$$

The Electric Power generated by any type of fuel cell is expressed mathematically by:

$$P_{cell} = I_{load} \cdot V_{out} \tag{3.21}$$

where power P_{load} is expressed in Watts, current I_{load} is expressed in Amps, and voltage V_{out} is expressed in Volts.

One measure of electric current is *current density; i*, defined as:

$$i = \frac{I}{A} \tag{3.22}.$$

where A is the area of fuel cell in m^2, and the current density i is expressed in Amp/m^2.

3.4.2 Gibbs free energy

Known as Gibbs Function of a thermodynamic system, Gibbs free energy is defined in terms of enthalpy *H* and entropy *S* as:

$$G = H - T \cdot S \tag{3.23}$$

Similarly, the molar Gibbs energy of formation is expressed in terms of molar enthalpy of formation and molar entropy [18]:

$$\bar{g}_f = \bar{h}_f - T \cdot \bar{s} \tag{3.24}$$

In a fuel cell, the temperature *T* is constant, while the change in molar enthalpy and molar entropy determines the change in molar Gibbs free energy:

$$\Delta\bar{g}_f = \Delta\bar{h}_f - T \cdot \Delta\bar{s} \tag{3.25}$$

where Δh_f is the difference between products' molar enthalpy and the reactants' molar enthalpy [15]:

$$\Delta\bar{h}_f = 3\left(\bar{h}_f\right)_{H_2O} + 2\left(\bar{h}_f\right)_{CO_2} - \left(\bar{h}_f\right)_{C_2H_5OH} - 3\left(\bar{h}_f\right)_{O_2} \tag{3.26}$$

Similarly, Δs_f is the difference between products' molar entropy and reactants' molar entropy [15]:

$$\Delta\bar{s}_f = 3\left(\bar{s}_f\right)_{H_2O} + 2\left(\bar{s}_f\right)_{CO_2} - \left(\bar{s}_f\right)_{C_2H_5OH} - 3\left(\bar{s}_f\right)_{O_2} \tag{3.27}$$

Since twelve atoms of hydrogen and six atoms of oxygen participate in the formation reaction of six molecules of water, and one molecule of ethanol is consumed, twelve electrons are generated by each ethanol-oxygen reaction. Therefore, the voltage across the fuel cell is the change in molar Gibbs free energy (negative) for the reaction divided by the electric charge flowing through the external circuit, for the reaction to take place:

$$V = \frac{-\Delta\bar{g}_f}{12 \cdot F} \tag{3.28}$$

where *F* is Faraday's constant; *F* = 96486 Coulomb/mol.

Theoretically, the maximum possible voltage that could be obtained from a PEM fuel cell is the result of converting all the waste heat into useful work [1], [15]:

$$V_{\max} = \frac{-\Delta\bar{h}_f}{12 \cdot F} \tag{3.29}$$

Therefore, for a given load current, the efficiency of a PEM fuel cell is given by the ratio of actual cell voltage to the maximum voltage:

$$\eta = \frac{V}{V_{\max}} = \frac{\Delta\bar{g}_f}{\Delta\bar{h}_f} \tag{3.30}$$

In the electrochemical reaction, the partial pressure of reactants and products along with temperature reaction has an influence on the reaction speed and fuel cell efficiency. The change in Gibbs free energy under any pressure is related to the change in Gibbs free energy at standard pressure P^0 by the following equation [10]:

$$\Delta\bar{g}_f = \Delta\bar{g}_f^0 - R \cdot T \cdot \ln\left(\frac{P_{C_2H_5OH} \cdot P_{O_2}^3}{P^2{}_{CO_2} \cdot P^3{}_{H_2O} \cdot \left(P^0\right)^6}\right) \tag{3.31}$$

Substituting this expression of Gibbs free energy into the relation for output voltage, the PEM fuel cell output voltage as related to reactants and products partial pressures is [10]:

$$V = V^0 + \frac{R \cdot T}{12 \cdot F} \cdot \ln\left(\frac{P_{C_2H_5OH} \cdot P_{O_2}^3}{P^2{}_{CO_2} \cdot P^3{}_{H_2O} \cdot \left(P^0\right)^6}\right) \tag{3.32}$$

where $\boldsymbol{V^0}$ is the PEM fuel cell output voltage at standard pressure P^0.

For a single fuel cell, the following losses need to be considered when estimating efficiency, output voltage, and load current

- Activation losses, given by the Butler-Volmer equation, and approximated by the Tafel equation for almost the entire range of operation for a PEM fuel cell:

$$V_{activation} = \frac{R \cdot T}{12 \cdot \alpha \cdot F} \cdot \ln\left(\frac{i}{i_0}\right) \tag{3.33}$$

- Ohmic losses, due to the electric resistance of electrodes and positive-ion *(H_2)* flow in the electrolyte (PEM), directly proportional to the current density:

$$V_{ohmic} = i \cdot r \tag{3.34}$$

For practical applications, a number of fuel cells electrically connected in series, anode-to-cathode, is employed with the goal of achieving a desired operating voltage, suited for the system operation. This assembly is called fuel cell stack. However, fuel cells are not ideal voltage sources; therefore the total voltage collected at the output of fuel cell stack is less than the sum of the individual fuel cell voltages.

For a direct ethanol fuel cell, whose opened circuit voltage is 0.91V, an approximate efficiency value could be found by multiplying the voltage by 80 [15]:

$$\eta = 0.91 \cdot 80 = 72.8\% \tag{3.35}$$

Interfacing the fuel cell stack to power electronics, such as DC–DC converters, provides the fuel cell power system with a high degree of output voltage flexibility [62].

3.5 DC–DC Converters

Power electronics, in general, and power converters, in particular, are integral part of the whole electrical system, thus influencing its operation and dynamic characteristics [62], [64]. Sequential switching is a technique used in DC–DC converters operation to transfer energy from source to load, and implies the existence of nonlinearities [58]. Main sources of nonlinearities in power electronics circuits are: intrinsic properties of semiconductor devices (switches), inductor nonlinearity, and nonlinearity associated with control circuits. Thus, nonlinear dynamics of power electronics can induce chaotic effects in the entire circuit, with undesired and unpredictable characteristics [65], [66].

The block diagram in Fig. 3.5 represents a DC–DC converter, and is characterized by input voltage V_{in} and input current I_{in}, and by output voltage V_{out} and load current I_{load}.

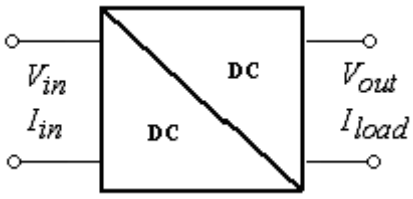

Figure 3.5: DC–DC converter block diagram

High frequency switching DC–DC converters are most often used as interfaces between DC systems of different voltage levels, or they can be used as interfaces between DC and AC systems [67].

The voltage difference ($V_{out} - V_{in}$) must be a voltage drop across a series element of the converter, connected between the input and output terminals. The current difference ($I_{in} - I_{load}$) follows a path assured by the shunt element of the converter. Therefore, the minimal DC–DC converter topology can be represented by two elements: series element and shunt element, such that the power input is theoretically equal to the power delivered by the converter to the load [67]. Using semiconductor switches at its input port, and low-pass filters at output port, a DC–DC converter can be represented as shown in Fig. 3.6.

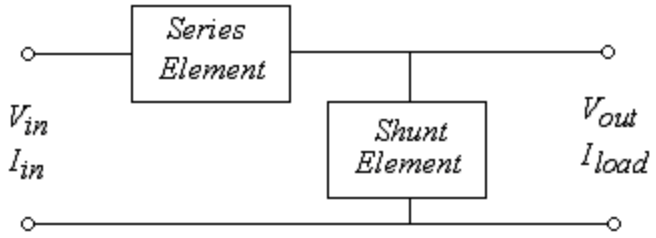

Figure 3.6: DC–DC converter implementation

3.5.1 DC buck converter

A buck converter is the DC analogous of an AC step-down transformer; its output average voltage is lower than its input voltage. Unlike a transformer, a buck converter has the flexibility of varying output voltage, by simply modifying the duty cycle of the square wave triggering the semiconductor switch. Thus, the circuit operation of the buck converter, shown in Fig. 3.7, is divided into two modes. Mode 1, transistor Q_{switch} is switched *on*, the input current flows through inductor *L*, filter capacitor *C*, and the load R_{load}. Mode 2, transistor Q_{switch} is turned *off*. Intuitively, the corresponding voltage applied to the buck converter reactive components (inductor L, and capacitor C), is a square wave.

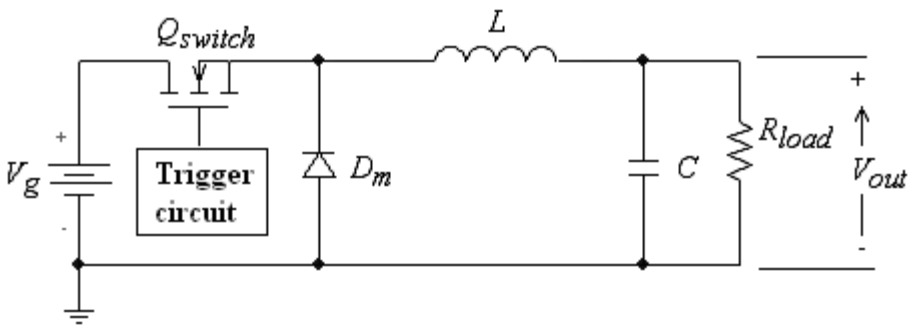

Figure 3.7: DC Buck converter circuit diagram

The average output voltage of a DC buck converter, under continuous conduction requirements, is:

$$V_{out} = k \cdot V_g \tag{3.36}$$

The peak-to-peak ripple current for a buck converter is:

$$\Delta I = \frac{V_g \cdot k \cdot (1-k)}{f \cdot L} \tag{3.37}$$

The peak-to-peak ripple output voltage (which is equal to the peak-to-peak voltage across the capacitor) is [67]:

$$\Delta V_{out} = \Delta V_C = \frac{V_g \cdot k \cdot (1-k)}{8 \cdot L \cdot C \cdot f^2} = \frac{\Delta I}{8 \cdot f \cdot C} \tag{3.38}$$

The values of inductor L and capacitor C, that must meet the requirements of peak-to-peak ripple current and voltage, are found from (3.19) and (3.20) [67]:

$$L = \frac{V_g \cdot k \cdot (1-k)}{f \cdot \Delta I} \tag{3.39}$$

$$C = \frac{\Delta I}{8 \cdot f \cdot \Delta V_C} \tag{3.40}$$

3.5.2 DC boost converter

The DC analogous of a step-up transformer is known as boost converter, with an output voltage exceeding the input voltage, function of the duty cycle of the controlling square wave signal. The circuit of a typical boost converter is shown in Fig. 3.8. Its operation is comprised of two modes. Mode 1 extends over the time span corresponding to turning *on* transistor Q_{switch}. The rising input current flows through transistor Q_{switch} and inductor L. Mode 2 spans over the time corresponding to the transistor Q_{switch} being turned *off*. During mode 2, the energy stored in the magnetic field of inductor L is returned to the circuit as an additional current transferred to the load. The resulting current flows through inductor L, diode D_m, filtering capacitor C, and load R_{load}. This determines an output voltage across the load higher than the voltage at the source terminals [68].

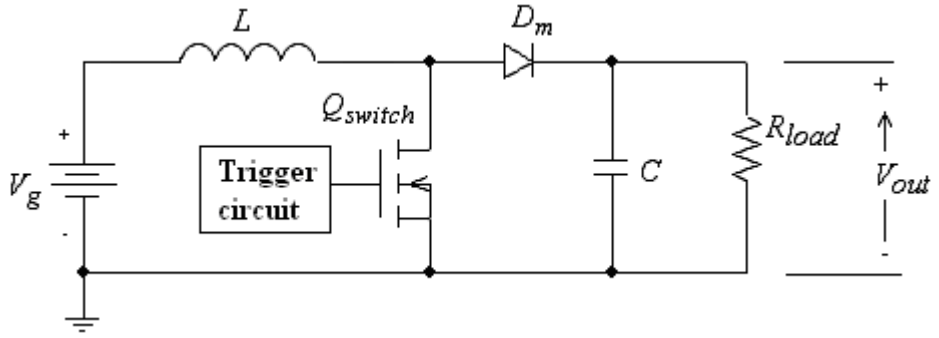

Figure 3.8: DC boost converter circuit diagram

The average output voltage of a DC boost converter, during continuous conduction mode is [67]:

$$V_{out} = \frac{V_g}{(1-k)} \tag{3.41}.$$

The peak-to-peak ripple current for a boost converter is [67], [68]:

$$\Delta I = \frac{V_g \cdot k}{f \cdot L} \tag{3.42}$$

The peak-to-peak ripple voltage across the capacitor for a boost converter, functions of average load current I_a, switching frequency f, and capacitance C, is [67], [68]:

$$\Delta V_{out} = \Delta V_C = \frac{I_a}{f \cdot C} \tag{3.43}$$

From Equations (3.25) and (3.26), the values for inductor L and capacitor C are found [67]:

$$L = \frac{V_g \cdot k}{f \cdot \Delta I} \tag{3.44}$$

$$C = \frac{I_a}{f \cdot \Delta V_C} \tag{3.45}$$

3.5.3 DC Buck-Boost Converter

With greater output voltage flexibility, the buck-boost converter can be implemented as a bidirectional DC–DC converter, provided that both solid-state switches are controllable devices. A buck-boost converter provides an output voltage that may be greater or less than the input voltage. The output voltage polarity is opposite to that of the input voltage, hence its alternate name: inverting regulator. Figure 3.9 presents the circuit of a typical buck-boost converter. The two modes of operation assume continuous current flow. During mode 1, transistor Q_{switch} is turned *on*, diode D_m is reversed biased, thus the flow of current is restricted to the portion of circuit comprised of transistor Q_{switch} and inductor L. During mode 2, transistor Q_{switch} is turned *off*, the energy stored in inductor L magnetic field is released in the form of a current, which will flow through the circuit comprised of inductor L, load-capacitor arrangement R_{load}-C, and diode D_m.

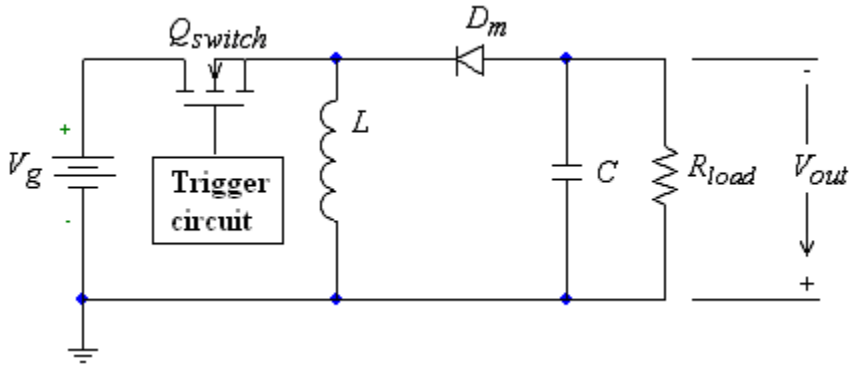

Figure 3.9: DC buck-boost converter circuit diagram

The average output voltage measured across the load is given by:

$$V_{out} = V_C = -\frac{V_g \cdot k}{(1-k)} \tag{3.46}$$

The peak-to-peak voltage ripple and current ripple respectively are:

$$\Delta I = \frac{V_g \cdot k}{f \cdot L} \tag{3.47}$$

$$\Delta V_{out} = \Delta V_C = \frac{I_a \cdot k}{f \cdot C} \tag{3.48}$$

For design purposes, the values of inductor L and capacitor C, for a given switching frequency, and with known maximum peak-to-peak ripple voltage and ripple current, are [67]:

$$L = \frac{V_g \cdot k}{f \cdot \Delta I} \tag{3.49}$$

$$C = \frac{I_a}{f \cdot \Delta V_C} \tag{3.50}$$

3.6 Solid-State Switches

Prior to the invention and development of bipolar junction transistors (BJT) and the semiconductor diode, all switching operations were performed by mechanical

switches incorporated in complex networks. Applications requiring repeated *on–of* switching were often subjected to failure, due to the material fatigue associated with mechanical switches used in pre-World War II technology [69]. A bipolar junction transistor operating in the saturation region can be modeled as a controlled-current current source, with the base current I_B and the β_{DC} of the transistor as the controlling parameters. Thus the magnitude of the current-source is equal to the transistor's collector current; $I_C = \beta_{DC} I_B$. Ideally, the current-source has infinite internal impedance [69]. In the common-emitter topology, presented in Fig. 3.10, the collector current I_C is controlled solely by the base current I_B.

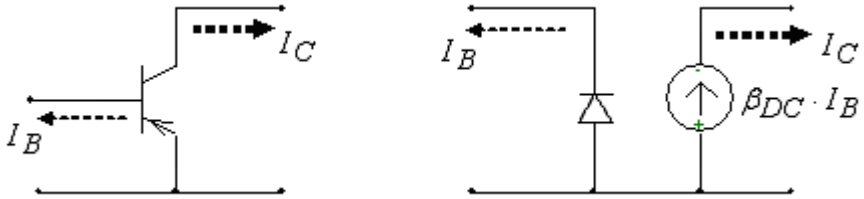

Figure 3.10: DC equivalent of BJT

Like the bipolar junction transistor operating in saturation mode, the MOSFET can be represented as a controlled current-source, as shown in Fig. 3.11. All silicon switching devices (diode, IGBT, MOSFET, GTO, etc.) are characterized by a *turn-on* time and a *turn-off* time, determining a measurable slope for the leading and trailing edges of the square wave[64].

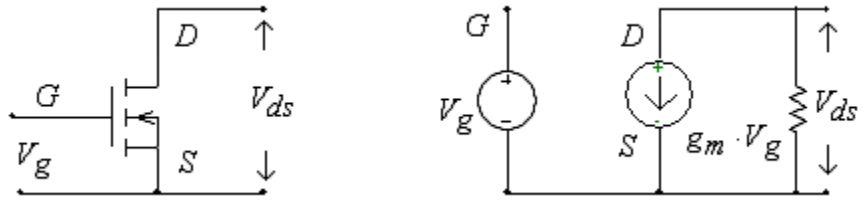

Figure 3.11: DC equivalent of E-MOSFET

The DC equivalent circuit of the MOSFET is a voltage-controlled current source. For the enhancement type MOSFET, the controlling voltage is the voltage applied at the gate terminal with respect to the source terminal. The process of controlling the source-drain current is somewhat different for the depletion-type MOSFET, since the conducting

channel is already fabricated into the silicon crystal. The scaling factor g_m is known as the transistor's transconductance [70].

3.7 Linearization of Nonlinear Systems

A linear system is one that satisfies the homogeneity and additivity conditions. Considering the action of a system by the symbol *S*, the response (or output) of the system function of the input *u*, is:

$$y = S(u). \tag{3.51}$$

A homogenous system is one for which:

$$S(a \cdot u) = a \cdot S(u), \tag{3.52}$$

and additive system is one for which:

$$S(u_1 + u_2) = S(u_1) + S(u_2), \tag{3.53}$$

for all $a = constant$, u_1 and u_2.

Many physical systems are described by nonlinear models. The voltage-current characteristics of most electronic devices are nonlinear, on-off relay controllers are the most common example [71]. The correlation between transfer function pole and zero locations and time response behavior is generally invalid. The stability of a nonlinear system is not a simple function of eigenvalue locations, instead the stability of equilibrium points must be investigated, which can be a multitude of stable and unstable equilibrium points [71]. A periodically excited nonlinear system is not restricted to outputs of the same frequency as the input, yielding sub-harmonics and/or higher-order harmonics and even continuous spectra (electronic chaos) as part of the nonlinear system output [72]. Stability, controllability, and observability cannot be tested on a global basis by using rank tests [73]. Many nonlinear systems with small nonlinearities can be approximated by an equivalent linear model, obtained by linearizing about a known nominal solution or operating point [74].

Considering a nonlinear system described by:

$$\begin{cases} \dot{x} = f(x,u,t) \\ y = h(x,u,t) \end{cases}. \tag{3.54}$$

A nominal solution $x_n(t)$, $u_n(t)$, and $y_n(t)$ of the system in (3.53) is known. The difference between the nominal vector functions and some small perturbed functions $x(t)$, $u(t)$, and $y(t)$ are defined as [71]:

$$\begin{aligned} \Delta x &= x(t) - x_n(t) \\ \Delta u &= u(t) - u_n(t) \\ \Delta y &= y(t) - y_n(t) \end{aligned}. \tag{3.55}$$

Then the system state-space representation can be written:

$$\begin{cases} \dot{x}_n + \Delta\dot{x} = f(x_n + \Delta x, u_n + \Delta u, t) = f(x_n, u_n, t) + \left[\frac{\partial f}{\partial x}\right]_n \Delta x + \left[\frac{\partial f}{\partial u}\right]_n \Delta u + \ldots\ldots \\ y_n + \Delta y = h(x_n + \Delta x, u_n + \Delta u, t) = h(x_n, u_n, t) + \left[\frac{\partial h}{\partial x}\right]_n \Delta x + \left[\frac{\partial h}{\partial u}\right]_n \Delta u + \ldots\ldots \end{cases} \tag{3.56}$$

For sufficiently small perturbations, the higher-order terms can be neglected, leaving only the linear equations [71]:

$$\begin{cases} \Delta\dot{x} = \left[\frac{\partial f}{\partial x}\right]_n \Delta x + \left[\frac{\partial f}{\partial u}\right]_n \Delta u \\ \Delta y = \left[\frac{\partial h}{\partial x}\right]_n \Delta x + \left[\frac{\partial h}{\partial u}\right]_n \Delta u \end{cases}. \tag{3.57}$$

If the nominal solution is an equilibrium point, and the nominal input and its variation are zero;

$$\begin{aligned} x_n(t) &= x_{equil} = const. \\ u_n(t) &= 0 = \Delta u(t) \end{aligned} \tag{3.58}$$

Then, the stability of the equilibrium point is governed by the differential equation:

$$\Delta\dot{x} = \left[\frac{\partial f}{\partial x}\right]_n \Delta x \tag{3.59}$$

The Jacobian matrix $\left[\frac{\partial f}{\partial x}\right]$ is constant and its eigenvalues determine the system stability about the equilibrium point [71]:

- If all eigenvalues have negative real parts, the equilibrium point is asymptotically stable, for sufficiently small perturbations.

- If one or more eigenvalues have positive real parts, the equilibrium point is unstable.
- If one or more of the eigenvalues are on the $j\omega$-axis and all other are in the left-half plane, no conclusion about stability can be drawn from the linear model.

3.8 Fourier-Series Approximation

An arbitrary periodical signal can be represented with great accuracy as a sum of sinusoids with variable amplitudes and variable phase angles. The general expression of an arbitrary current waveform *i(t)*, is given by the expression [75]:

$$i(t) = C_0 + \sum_{n=1}^{\infty} C_n \sin(n\omega_1 t + \varphi_n). \tag{3.60}$$

The term C_0 is the bias term, and has a constant value; its value is given by the equation below. For symmetrical waves, this term will be zero.

$$C_0 = \frac{1}{T}\int_0^T i(t)dt \tag{3.61}$$

All amplitudes, including the amplitude of the fundamental sinusoid, are derived from the expressions below, with the integration over a time equal to one period of the signal.

$$C_n = \sqrt{{A_n}^2 + {B_n}^2} \tag{3.62}$$

$$A_n = \frac{2}{T}\int_0^T i(t)\cos(n\omega_1 t)dt \tag{3.63}$$

$$B_n = \frac{2}{T}\int_0^T i(t)\sin(n\omega_1 t)dt \tag{3.64}$$

The phase angle of each harmonic is different, although its value can be repetitive, and is determined by [75]:

$$\varphi_n = \tan^{-1}\left(\frac{A_n}{B_n}\right) \tag{3.65}$$

It is impractical to consider an infinite number of sinusoidal terms, therefore a finite number of harmonics is normally used. Using the correlation function;

$$c_n = \frac{1}{\sqrt{E_g \cdot E_f}} \cdot \int_0^T f(t) g(t) dt \,, \tag{3.66}$$

a level of approximation is numerically determined [75]. The function *f(t)* represents the signal waveform, while *g(t)* represents the Fourier-series approximation of *f(t)*. A value of the correlation function equal to zero indicates no correlation between the original function and its approximated Fourier-series representation, while a value close to 1, is an indication of a good approximation.

CHAPTER 4 - Small Signal Models of DC–DC Converters

Mathematical models of DC–DC converters have been developed to aid the design and analysis of DC power systems. In 1970s, the unified large signal model was developed, and was aimed to describe quantitatively the average voltages and currents the semiconductor switches in a DC converter are subjected to. This global view did not provide sufficient insights on the stresses exerted on the semiconductor devices during sequential switching. Numerous methods of analysis and computer simulations were lately developed in an attempt to closely describe the transient conditions associated with sequential switching of DC converters.

In Chapter 4, the small signal model for three DC–DC converters, buck, boost, and buck-boost, are developed using the averaged switch method, combined with the piecewise circuit analysis. The power source is assumed ideal, i.e., the voltage source under consideration is characterized by zero impedance and constant voltage.

4.1 Averaged Switch Method

Conventional methods of modeling a DC–DC converter circuit consist of taking an average over a switching cycle, thus linearizing the circuit over an operating point. In continuous conduction mode, two modes of operation are present, thus two state-space representations are used in describing the system. State-space averaging refers to the state-space representations of the system; *on* mode and *off* mode for continuous conduction mode (CCM), while other methods using "injected/absorbed-currents" treat the switch-diode combination in isolation from the circuit. In discontinuous mode (DCM) the converter has three modes of operation, represented by three separate circuits, and three distinct state-space representations are used in the averaging method. In the small-

signal models of DC–DC converters described in this chapter, the main focus is on determining the transfer function governing the converter operation, and is limited to continuous conduction mode (CCM) analysis.

4.2 Averaged-Switch Model of DC Buck Converter

The buck converter in Fig. 3.7 is a nonlinear, time-dependent system, and its operation is described by the two modes, illustrated in Fig. 4.1 (a) and (b). The system is linearized through switch averaging method about a selected operating point, and with respect to the transistor duty cycle *k*.

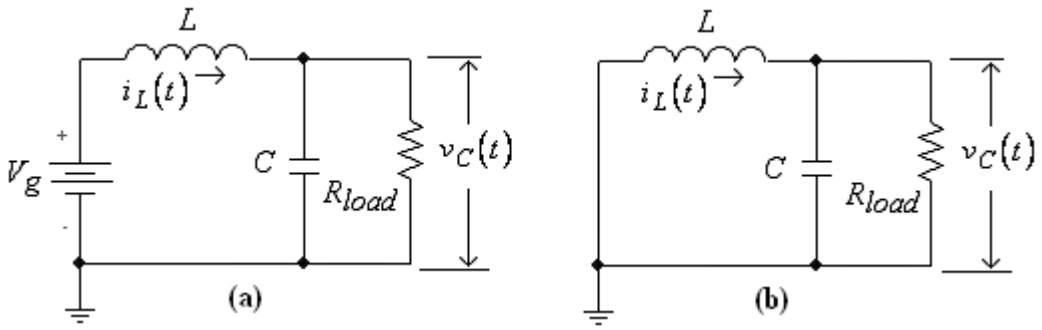

Figure 4.1: Buck converter, (a) mode 1, (b) mode 2

4.2.1 State-space representations of buck converter

Mode 1 of operation is described by two differential equations derived from the circuit in Fig. 4.1 (a), and consistent with transistor Q_{switch} being turned *on*:

$$\begin{cases} \dfrac{di_L(t)}{dt} = 0 \cdot i_L(t) - \left(\dfrac{1}{L}\right) v_C(t) + \left(\dfrac{1}{L}\right) V_g \\ \dfrac{dv_C(t)}{dt} = \dfrac{1}{C} i_L(t) - \left(\dfrac{1}{R_{load} C}\right) v_C(t) + 0 \cdot V_g \end{cases} \tag{4.1}$$

The state-space representation for mode 1 (transistor is *on*) is given by:

$$\begin{cases} \dot{x} = A_1 \cdot x(t) + B_1 \cdot u(t) \\ y = C_1 \cdot x(t) + D_1 \cdot u(t) \end{cases}. \tag{4.2}$$

where the variable vector, input vector, output vector, and duty cycle respectively, are:

$$x(t) = \begin{bmatrix} i_L(t) \\ v_C(t) \end{bmatrix} \tag{4.3}$$

$$u(t) = \begin{bmatrix} v_g(t) \end{bmatrix} \tag{4.4}$$

$$y = v_{out}(t) \tag{4.5}$$

$$k = \frac{t_{on}}{T}. \tag{4.6}$$

The corresponding state-space representation for mode 1 is:

$$\begin{bmatrix} \dot{i}_L(t) \\ \dot{v}_C(t) \end{bmatrix} = \begin{bmatrix} 0 & -1/L \\ 1/C & -1/R_{load}C \end{bmatrix} \cdot \begin{bmatrix} i_L(t) \\ v_C(t) \end{bmatrix} + \begin{bmatrix} 1/L \\ 0 \end{bmatrix} \cdot \begin{bmatrix} V_g \end{bmatrix}$$
$$y = \begin{bmatrix} 0 & 1 \end{bmatrix} \cdot \begin{bmatrix} i_L(t) \\ v_C(t) \end{bmatrix} + \begin{bmatrix} 0 \end{bmatrix} \cdot \begin{bmatrix} V_g \end{bmatrix} \tag{4.7}$$

During mode 2, transistor Q_{switch} is turned *off*, and the voltage across diode is zero, as illustrated in Fig. 4.1 (b). Mode 2 is described by a set of differential equations, consistent with the transistor Q_{switch} being turned *off*:

$$\begin{cases} \dfrac{di_L(t)}{dt} = 0 \cdot i_L(t) - \left(\dfrac{1}{L}\right) v_C(t) + 0 \cdot V_g \\ \dfrac{dv_C(t)}{dt} = \dfrac{1}{C} i_L(t) - \left(\dfrac{1}{R_{load}C}\right) v_C(t) + 0 \cdot V_g \end{cases} \tag{4.8}$$

The state-space representation of mode 2 is obtained from mode 1 state-space representation, by setting all coefficients of V_g to zero:

$$\begin{cases} \dot{x} = A_2 \cdot x(t) + B_2 \cdot u(t) \\ y = C_2 \cdot x(t) + D_2 \cdot u(t) \end{cases} \tag{4.9}$$

$$\begin{bmatrix} i_L(t) \\ \dot{v}_C(t) \end{bmatrix} = \begin{bmatrix} 0 & -1/L \\ 1/C & -1/R_{load}C \end{bmatrix} \cdot \begin{bmatrix} i_L(t) \\ v_C(t) \end{bmatrix} + \begin{bmatrix} 0 \\ 0 \end{bmatrix} \cdot \begin{bmatrix} V_g \end{bmatrix}$$
$$y = \begin{bmatrix} 0 & 1 \end{bmatrix} \cdot \begin{bmatrix} i_L(t) \\ v_C(t) \end{bmatrix} + \begin{bmatrix} 0 \end{bmatrix} \cdot \begin{bmatrix} V_g \end{bmatrix} \tag{4.10}$$

Therefore, comparing the two state-space representations of modes 1 and 2, only matrices B_1 and B_2 are different, the other matrices remaining unchanged:

$$A_2 = A_1,\ C_2 = C_1,\ D_2 = D_1, \text{ and } B_2 = \begin{bmatrix} 0 \\ 0 \end{bmatrix} \neq B_1 \tag{4.11}$$

4.2.2 Averaged state-space representation

The two linear systems are averaged with respect to their time span during the switching period [6]:

$$\begin{cases} \dot{x} = \left[k(t) \cdot A_1 + \left(1 - k(t)\right) A_2\right] \cdot x(t) + \left[k(t) \cdot B_1 + \left(1 - k(t)\right) \cdot B_2\right] \cdot u(t) \\ y = \left[k(t) \cdot C_1 + \left(1 - k(t)\right) C_2\right] \cdot x(t) + \left[k(t) \cdot D_1 + \left(1 - k(t)\right) \cdot D_2\right] \cdot u(t) \end{cases} \tag{4.12}$$

This system representation, is an approximation of the time-varying system, in which a new input variable is introduced: duty cycle *k(t)*. Thus, a new input vector *u'(t)* is defined:

$$u'(t) = \begin{bmatrix} u(t) \\ k(t) \end{bmatrix} = \begin{bmatrix} v_g(t) \\ k(t) \end{bmatrix} \tag{4.13}$$

The nonlinear, time-invariant system obtained, with state vector *x(t)*, input vector *u'(t)*, and output *y(t)* is written in a general format as:

$$\begin{cases} \dot{x} = f\left(x(t), u'(t)\right) \\ y(t) = g\left(x(t), u'(t)\right) \end{cases} \tag{4.14}$$

Defining the deviations from an operating point, a straight forward linearization is applied:

$$\begin{aligned} x(t) &= X + \hat{x}(t) \\ u'(t) &= U' + \hat{u}'(t) \\ y(t) &= Y + \hat{y}(t) \end{aligned} \tag{4.15}$$

In which, capital letters are used to denote the DC values (operating point), while hat-variables (^) are used to denote deviation (or perturbation signals), generally AC values.

4.2.3 Linearization of buck converter representation

The following variables are defined for the time transistor Q_{switch} is OFF:

$$k'(t) = 1 - k(t) \quad \text{and} \quad k' = 1 - k \tag{4.16}$$

The equations for operating point, DC output voltage, value are:

$$\begin{cases} 0 = A \cdot X + B \cdot U \\ Y = C \cdot X + D \cdot U \end{cases}. \tag{4.17}$$

For the DC operating point state-space representation, the input vector U is the DC component of vector $u(t)$ in (4.4).

$$u(t) = U + \hat{u}(t) = \left[v_g(t)\right] = \left[V_g\right] + \left[\hat{v}_g(t)\right] \tag{4.18}$$

Matrices **A**, **B**, **C**, and **D** in Equation (4.17), are given by the relations:

$$A = k \cdot A_1 + k' \cdot A_2 \tag{4.19}$$

$$B = k \cdot B_1 + k' \cdot B_2 \tag{4.20}$$

$$C = k \cdot C_1 + k' \cdot C_2 \tag{4.21}$$

$$D = k \cdot D_1 + k' \cdot D_2 \tag{4.22}$$

The equations for operating point in (4.22) are rewritten as:

$$\begin{bmatrix} 0 \\ 0 \end{bmatrix} = \begin{bmatrix} 0 & \frac{-1}{L} \\ \frac{1}{C} & \frac{-1}{R_{load}C} \end{bmatrix} \cdot \begin{bmatrix} I_L \\ V_C \end{bmatrix} + \begin{bmatrix} \frac{k}{L} \\ 0 \end{bmatrix} \cdot \begin{bmatrix} V_g \end{bmatrix}$$

$$Y = \begin{bmatrix} 0 & 1 \end{bmatrix} \cdot \begin{bmatrix} I_L \\ V_C \end{bmatrix} + \begin{bmatrix} 0 \end{bmatrix} \cdot \begin{bmatrix} V_g \end{bmatrix} \tag{4.23}$$

Expanding the system representation (4.22), the following DC equations are derived:

$$\begin{cases} 0 = -\frac{V_C}{L} + k \cdot \frac{V_g}{L} \\ 0 = \frac{I_L}{C} - \frac{V_C}{R_{load}C} \\ Y = V_{out} = V_C \end{cases} \tag{4.24}$$

Therefore, the voltage across capacitor *C*, and the output voltage V_{out} are:

$$V_C = R_{load} \cdot I_L \tag{4.25}$$

$$V_{out} = k \cdot V_g \tag{4.26}$$

The ratio of capacitor voltage to source voltage defines the buck converter voltage gain. The voltage across the diode during the duty cycle *k*, is equal to the source voltage V_g, and zero otherwise. Therefore, the load voltage is equal to the average voltage across the diode.

4.2.4 AC Component of buck converter output voltage

The output voltage, measured across capacitor *C*, has two components; DC output voltage and AC output component (output ripple). Extrapolating the method used for the DC output voltage, the output ripple for steady-state operation, with constant source voltage V_g, and constant duty cycle *k*, cannot be determined. The averaged state space representation takes an average over the converter operation, thus only average quantities i.e. DC load voltage, determined through this method are useful. The AC component of the output voltage is determined from the two modes of operation, for continuous

conduction mode. The analysis can be performed only for the steady state operation, after the desired output DC voltage has been reached. The corresponding s-domain circuits for the two modes of operation are shown in Fig. 4.2 (a) and (b).

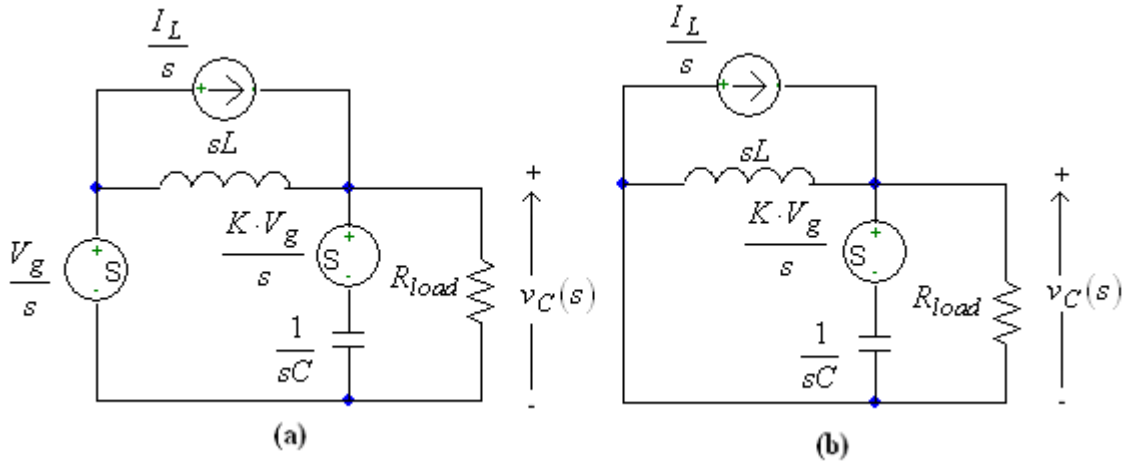

Figure 4.2: Buck converter in the s-domain, (a) mode 1, (b) mode 2

For mode 1, the s-domain expression of the output voltage is derived through superposition method:

$$v_{C-on}(s) = v'_C(s) + v''_C(s) + v'''_C(s) \tag{4.27}$$

Each one of the three terms of equation (4.27) is determined to be:

$$v'_C(s) = \frac{R_{load} \cdot V_g}{s \cdot \left(s^2 (R_{load} LC) + sL + R_{load}\right)} \tag{4.28}$$

$$v''_C(s) = \frac{(R_{load} L) \cdot I_L}{s \cdot \left(s^2 R_{load} LC + sL + R_{load}\right)} \tag{4.29}$$

$$v'''_C(s) = \frac{s^2 R_{load} LC \cdot K \cdot V_g}{s \cdot \left(s^2 R_{load} LC + sL + R_{load}\right)} \tag{4.30}$$

The expression for the AC output voltage component for mode 1, during steady-state is:

$$v_{C-on}(s) = \frac{\left(s^2 R_{load} LC \cdot k + L \cdot k + R_{load}\right)}{s \cdot \left(s^2 R_{load} LC + sL + R_{load}\right)} \cdot V_g \tag{4.31}$$

The s-domain expression of the AC output voltage during mode 2 is determined through superposition method. Only two sources are present, thus the output voltage during mode 2 is described by two terms:

$$v_{C-off}(s) = v'_C(s) + v''_C(s) \tag{4.32}$$

The AC output voltage component during mode 2 is a decaying voltage described by:

$$v_{C-off}(s) = \frac{\left(s^2 R_{load} LC + L\right)}{s \cdot \left(s^2 R_{load} LC + sL + R_{load}\right)} \cdot k \cdot V_g \tag{4.33}$$

The poles of Equations (4.31) and (4.33) are numerically identical, while the corresponding zeros are different for the two equations. Finding the numerical values of poles, zeros, and gains allows for piecewise graphical representation of one cycle *on-off*, during steady-state operation.

4.3 Averaged-Switch Model of DC–DC Boost Converter

The boost converter in Fig. 3.8 is assumed to operate in continuous conduction mode, with zero voltage drop across switching transistor Q_{switch} and diode D_m. The operation over a switching cycle is nonlinear, time-dependent, and is described by two sets of differential equations, particular to each mode of operation. The two modes over a switching cycle are illustrated in Fig. 4.3 (a) and (b).

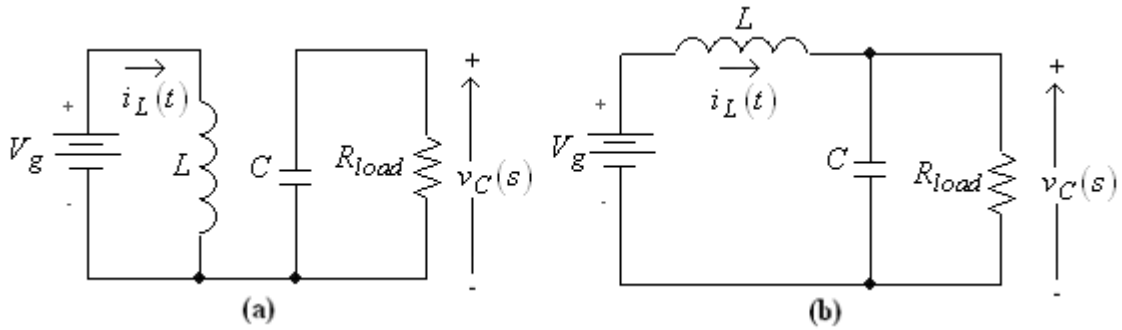

Figure 4.3: Boost converter, (a) mode 1, (b) mode 2

4.3.1 State-space representation of boost converter

During mode 1, transistor Q_{switch} is turned *on*, thus the current flows only through the inductor and the switching transistor, since the diode is reverse biased. During this mode, capacitor voltage $v_C(t)$ is decaying, as the capacitor discharges through the load resistor. The circuit is presented in Fig. 4.2 (a), and is described by the set of differential equations:

$$\begin{cases} \dfrac{di_L(t)}{dt} = 0 \cdot i_L(t) + 0 \cdot v_C(t) + \dfrac{1}{L} V_g \\ \dfrac{dv_C(t)}{dt} = 0 \cdot i_L(t) - \left(\dfrac{1}{RC}\right) v_C(t) + 0 \cdot V_g \end{cases} \tag{4.34}$$

Thus the state-space representation in condensed format is:

$$\begin{cases} \dot{x} = A_1 \cdot x(t) + B_1 \cdot u(t) \\ y = C_1 \cdot x(t) + D_1 \cdot u(t) \end{cases} \tag{4.35}$$

The system in (4.49) is expanded in matrix for as:

$$\begin{bmatrix} \dot{i}_L(t) \\ \dot{v}_C(t) \end{bmatrix} = \begin{bmatrix} 0 & 0 \\ 0 & -1/R_{load}C \end{bmatrix} \cdot \begin{bmatrix} i_L(t) \\ v_C(t) \end{bmatrix} + \begin{bmatrix} 1/L \\ 0 \end{bmatrix} \cdot \begin{bmatrix} V_g \end{bmatrix}$$
$$y = \begin{bmatrix} 0 & 1 \end{bmatrix} \cdot \begin{bmatrix} i_L(t) \\ v_C(t) \end{bmatrix} + \begin{bmatrix} 0 \end{bmatrix} \cdot \begin{bmatrix} V_g \end{bmatrix} \tag{4.36}$$

During mode 2, transistor Q_{switch} is turned *off*, thus the equivalent circuit for this mode is represented as in Fig. 4.2 (b). The differential equations describing the boost converter during mode 2 are:

$$\begin{cases} \dfrac{di_L(t)}{dt} = 0 \cdot i_L(t) + \dfrac{-1}{L} \cdot v_C(t) + \dfrac{1}{L} V_g \\ \dfrac{dv_C(t)}{dt} = \dfrac{1}{C} \cdot i_L(t) - \left(\dfrac{1}{RC}\right) v_C(t) + 0 \cdot V_g \end{cases} \tag{4.37}$$

The corresponding state-space representation of the system is:

$$\begin{cases} \dot{x} = A_2 \cdot x(t) + B_2 \cdot u(t) \\ y = C_2 \cdot x(t) + D_2 \cdot u(t) \end{cases} \tag{4.38}$$

In expanded format, the system representation in (4.52) is:

$$\begin{bmatrix} \dot{i}_L(t) \\ \dot{v}_C(t) \end{bmatrix} = \begin{bmatrix} 0 & -1/L \\ 1/C & -1/R_{load}C \end{bmatrix} \cdot \begin{bmatrix} i_L(t) \\ v_C(t) \end{bmatrix} + \begin{bmatrix} 1/L \\ 0 \end{bmatrix} \cdot \begin{bmatrix} V_g \end{bmatrix}$$

$$y = \begin{bmatrix} 0 & 1 \end{bmatrix} \cdot \begin{bmatrix} i_L(t) \\ v_C(t) \end{bmatrix} + \begin{bmatrix} 0 \end{bmatrix} \cdot \begin{bmatrix} V_g \end{bmatrix} \tag{4.39}$$

From the expanded representations in (4.50) and (4.53), it may be observed that:

$B_2 = B_1$, $C_2 = C_1$, $D_2 = D_1$, and

$$A_2 = \begin{bmatrix} 0 & -1/L \\ 1/C & -1/R_{load}C \end{bmatrix} \neq \begin{bmatrix} 0 & 0 \\ 0 & -1/R_{load}C \end{bmatrix} = A_1 \tag{4.40}$$

4.3.2 Averaged state-space representation

Considering the two state-space representations in (4.47) and (4.50), and following the same procedure of switch averaging for the buck converter, the averaged state-space representation of the system is given by:

$$\begin{cases} \dot{x} = \left[k(t) \cdot A_1 + \left(1 - k(t)\right) A_2\right] \cdot x(t) + \left[k(t) \cdot B_1 + \left(1 - k(t)\right) \cdot B_2\right] \cdot u(t) \\ y = \left[k(t) \cdot C_1 + \left(1 - k(t)\right) C_2\right] \cdot x(t) + \left[k(t) \cdot D_1 + \left(1 - k(t)\right) \cdot D_2\right] \cdot u(t) \end{cases} \tag{4.41}$$

Using capital letters to denote the DC values (operating point), and hat-variables (^) to denote deviation (or perturbation signals), generally AC values, the state-space vectors are described by:

$$\begin{aligned} x(t) &= X + \hat{x}(t) \\ u'(t) &= U + \hat{u}'(t) \\ y(t) &= Y + \hat{y}(t) \end{aligned} \tag{4.42}$$

4.3.3 Linearization of boost converter representation

The linearization of the averaged boost converter model follows an identical procedure as performed for the buck converter model. The results of linearization are presented. The equations for operating point values are:

$$\begin{cases} X = A^{-1} \cdot B \cdot U \\ Y = \left(-C \cdot A^{-1} \cdot B + D \right) \cdot U \end{cases} \tag{4.43}$$

Matrices **A**, **B**, **C**, and **D** are:

$$A = k \cdot A_1 + k' \cdot A_2 = \begin{bmatrix} 0 & k'/L \\ k'/C & -1/R_{load}C \end{bmatrix} \tag{4.44}$$

$$B = k \cdot B_1 + k' \cdot B_2 = \begin{bmatrix} 1/L \\ 0 \end{bmatrix} \tag{4.45}$$

$$C = k \cdot C_1 + k' \cdot C_2 = \begin{bmatrix} 0 & 1 \end{bmatrix} \tag{4.46}$$

$$D = k \cdot D_1 + k' \cdot D_2 = \begin{bmatrix} 0 \end{bmatrix} \tag{4.47}$$

Since: $A' = A$, $B' = \begin{bmatrix} B & B_k \end{bmatrix}$, $C' = C$, $D' = \begin{bmatrix} D & D_k \end{bmatrix}$, and;

$$B_k = (A_1 - A_2)X + (B_1 - B_2)U = \begin{bmatrix} 0 & -1/L \\ -1/C & 0 \end{bmatrix} \cdot \begin{bmatrix} I_L \\ V_C \end{bmatrix} + 0 \cdot U = \begin{bmatrix} -V_C/L \\ -I_L/L \end{bmatrix} \tag{4.48}$$

$$D_k = (C_1 - C_2)X + (D_1 - D_2)U = 0 \cdot X + 0 \cdot U = \begin{bmatrix} 0 \end{bmatrix}, \tag{4.49}$$

Matrices B' and D' are:

$$B' = \begin{bmatrix} 1/L & -V_C/L \\ 0 & -I_L/L \end{bmatrix} \tag{4.50}$$

$$D' = \begin{bmatrix} 0 & 0 \end{bmatrix} \tag{4.51}$$

The following DC equations, for the operating point, are derived by expanding the system representation:

$$\begin{cases} 0 = A \cdot X + B \cdot U \\ Y = C \cdot X + D \cdot U \end{cases} \Rightarrow \begin{bmatrix} 0 \\ 0 \end{bmatrix} = \begin{bmatrix} 0 & k'/L \\ k'/C & -1/R_{load}C \end{bmatrix} \cdot \begin{bmatrix} I_L \\ V_C \end{bmatrix} + \begin{bmatrix} 1/L & -V_C/L \\ 0 & -I_L/L \end{bmatrix} \cdot \begin{bmatrix} V_g \\ k \end{bmatrix} \quad (4.52)$$

$$\begin{cases} 0 = k' \cdot \dfrac{V_C}{L} + \dfrac{V_g}{L} - k \cdot \dfrac{V_C}{L} \\ 0 = k' \cdot \dfrac{I_L}{C} + \dfrac{V_C}{R_{load}C} - k \cdot \dfrac{I_L}{L} \end{cases} \quad (4.53)$$

The voltage across capacitor C is equal to output voltage V_{out}:

$$V_C = \left(k' \cdot R_{load} + \frac{k \cdot R_{load} \cdot C}{L} \right) \cdot I_L \quad (4.54)$$

$$V_{out} = \frac{1}{(1-k)} \cdot V_g \quad (4.55)$$

4.3.4 AC component of boost converter output voltage

Assuming continuous conduction mode of operation, the AC output voltage component for the boost converter is determined as a piece-wise function. Each of the two expressions for the AC component of output voltage is found from the s-domain circuit characteristic for mode 1 (*on-mode*), and mode 2 (*off-mode*). The corresponding s-domain circuits for the two modes are shown in Fig. 4.4 (a) and (b).

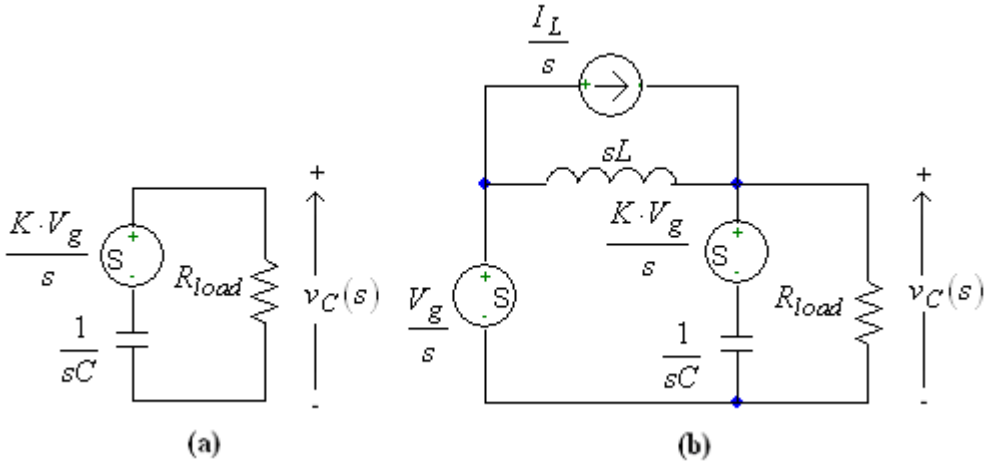

Figure 4.4: Boost converter in the s-domain, (a) mode 1, (b) mode 2

During mode 1, transistor Q_{switch} is *on*, thus the voltage source and the energy stored in the magnetic field of the inductor have no effects on the output voltage $v_C(s)$. The expression for the AC component of output voltage during mode 1 is a decaying voltage:

$$v_{C-on}(s) = \frac{R_{load} \cdot k \cdot V_g}{sR_{load} + \left(\frac{1}{C}\right)} \tag{4.56}$$

During mode 2, transistor Q_{switch} is *off*. The circuit describing this mode is shown in Fig. 4.4 (b). The AC component of output voltage is described by a sum of three terms, according to the superposition principle:

$$v_{C-off}(s) = v'_C(s) + v''_C(s) + v'''_C(s) \tag{4.57}$$

The three terms of Equation (4.57) are:

$$v'_C(s) = \frac{R_{load} \cdot V_g}{s \cdot \left(s^2 (R_{load} LC) + sL + R_{load}\right)} \tag{4.58}$$

$$v''_C(s) = \frac{(R_{load} L) \cdot I_L}{s \cdot \left(s^2 R_{load} LC + sL + R_{load}\right)} \tag{4.59}$$

$$v'''_C(s) = \frac{s^2 R_{load} LC \cdot k \cdot V_g}{s \cdot \left(s^2 R_{load} LC + sL + R_{load}\right)} \tag{4.60}$$

The expression of the AC component of output voltage is:

$$v_{C-off}(s) = \frac{\left(s^2 R_{load} LC \cdot k + L \cdot k + R_{load}\right)}{s \cdot \left(s^2 R_{load} LC + sL + R_{load}\right)} \cdot V_g \tag{4.61}$$

4.4 Averaged Switch Model of DC Buck-Boost Converter

Known as indirect converter, DC Buck-Boost converter is characterized by an output voltage with inverted polarity. Two modes describe its operation in the continuous

conduction mode. Fig. 4.5 (a) and (b) presents the circuit diagrams for the two modes of operation, mode 1 (*on* mode), and mode 2 (*off* mode).

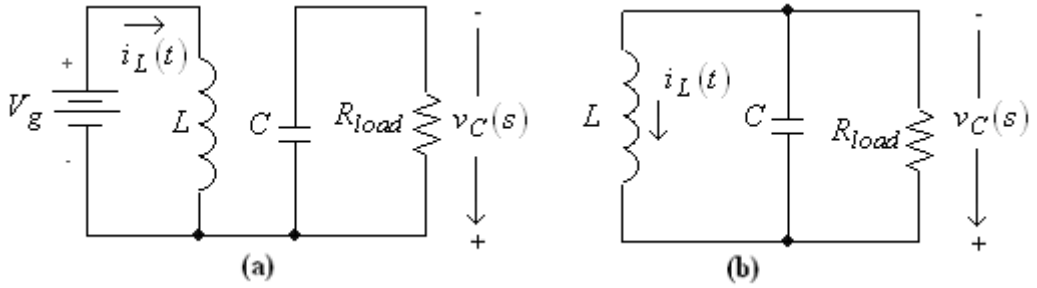

Figure 4.5: Buck-boost converter, (a) mode 1, (b) mode 2

4.4.1 State-space representation of buck-boost converter

Mode1 is described mathematically by the set of differential equations:

$$\begin{cases} \dfrac{di_L(t)}{dt} = 0 \cdot i_L(t) + 0 \cdot v_C(t) + \dfrac{1}{L} V_g \\ \dfrac{dv_C(t)}{dt} = 0 \cdot i_L(t) - \left(\dfrac{1}{R_{load} C} \right) v_C(t) + 0 \cdot V_g \end{cases} \tag{4.62}$$

The corresponding state-space representation for mode 1 of the buck-boost converter is:

$$\begin{bmatrix} \dot{i}_L(t) \\ \dot{v}_C(t) \end{bmatrix} = \begin{bmatrix} 0 & 0 \\ 0 & -1/R_{load} C \end{bmatrix} \cdot \begin{bmatrix} i_L(t) \\ v_C(t) \end{bmatrix} + \begin{bmatrix} 1/L \\ 0 \end{bmatrix} \cdot \left[v_g(t) \right]$$

$$y = \begin{bmatrix} 0 & 1 \end{bmatrix} \cdot \begin{bmatrix} i_L(t) \\ v_C(t) \end{bmatrix} + [0] \cdot \left[v_g(t) \right] \tag{4.63}$$

During mode 2, switching transistor is turned *off*, thus the equivalent circuit for the buck-boost converter is presented in Fig. 4.5 (b). The differential equations describing the system are:

$$\begin{cases} \dfrac{di_L(t)}{dt} = 0 \cdot i_L(t) - \dfrac{1}{L} \cdot v_C(t) + 0 \cdot V_g \\ \dfrac{dv_C(t)}{dt} = \dfrac{1}{C} \cdot i_L(t) - \left(\dfrac{1}{R_{load} C} \right) v_C(t) + 0 \cdot V_g \end{cases} \tag{4.64}$$

The corresponding state-space representation for buck-boost converter during mode 2 is:

$$\begin{bmatrix} \dot{i}_L(t) \\ \dot{v}_C(t) \end{bmatrix} = \begin{bmatrix} 0 & 1/L \\ 1/C & -1/R_{load} C \end{bmatrix} \cdot \begin{bmatrix} i_L(t) \\ v_C(t) \end{bmatrix} + \begin{bmatrix} 0 \\ 0 \end{bmatrix} \cdot \begin{bmatrix} v_g(t) \end{bmatrix}$$
$$y = \begin{bmatrix} 0 & 1 \end{bmatrix} \cdot \begin{bmatrix} i_L(t) \\ v_C(t) \end{bmatrix} + \begin{bmatrix} 0 \end{bmatrix} \cdot \begin{bmatrix} v_g(t) \end{bmatrix} \tag{4.65}$$

4.4.2 Averaged state-space representation

From the state-space representation of mode 1 (*on* mode) and mode 2 (*off* mode) described by (4.63) and (4.65), and following the same procedure applied to buck and boost converters, the averaged state-space representation of buck-boost converter system is obtained:

$$\begin{cases} \dot{x} = \left[k(t) \cdot A_1 + \left(1 - k(t)\right) A_2 \right] \cdot x(t) + \left[k(t) \cdot B_1 + \left(1 - k(t)\right) \cdot B_2 \right] \cdot u(t) \\ y = \left[k(t) \cdot C_1 + \left(1 - k(t)\right) C_2 \right] \cdot x(t) + \left[k(t) \cdot D_1 + \left(1 - k(t)\right) \cdot D_2 \right] \cdot u(t) \end{cases} \tag{4.66}$$

Employing the same notation for the state-space vectors, where capital letters denote DC values (operating points), and hat-variables (^) to denote deviation (or perturbation signals), generally AC values, the general expressions of state-space vectors are:

$$\begin{aligned} x(t) &= X + \hat{x}(t) \\ u'(t) &= U + \hat{u}'(t) \\ y(t) &= Y + \hat{y}(t) \end{aligned} \tag{4.67}$$

The averaged state-space representation is:

$$\begin{cases} \begin{bmatrix} \dot{i}_L(t) \\ \dot{v}_C(t) \end{bmatrix} = \begin{bmatrix} 0 & (1-k)/L \\ (1-k)/C & -1/R_{load}C \end{bmatrix} \cdot \begin{bmatrix} i_L(t) \\ v_C(t) \end{bmatrix} + \begin{bmatrix} k/L \\ 0 \end{bmatrix} \cdot u(t) \\ y = \begin{bmatrix} 0 & 1 \end{bmatrix} \cdot \begin{bmatrix} i_L(t) \\ v_C(t) \end{bmatrix} + [0] \cdot u(t) \end{cases} \tag{4.68}$$

4.4.3 Linearization of buck-boost converter representation

The equations describing the system about an operating point (DC output voltage) are:

$$\begin{cases} 0 = A \cdot X + B \cdot U \\ Y = C \cdot X + D \cdot U \end{cases} . \tag{4.69}$$

Matrices **A**, **B**, **C**, and **D** in (4.69) are derived as:

$$A = k \cdot A_1 + k' \cdot A_2 \tag{4.70}$$

$$B = k \cdot B_1 + k' \cdot B_2 \tag{4.71}$$

$$C = k \cdot C_1 + k' \cdot C_2 \tag{4.72}$$

$$D = k \cdot D_1 + k' \cdot D_2 \tag{4.73}$$

For the DC operating point state-space representation, the input vector U is the DC component of vector $u(t)$.

$$u(t) = U + \hat{u}(t) = \left[v_g(t) \right] = \left[V_g \right] + \left[\hat{v}_g(t) \right] \tag{4.74}$$

The equations for operating point in (4.22) are rewritten as:

$$\begin{bmatrix} 0 \\ 0 \end{bmatrix} = \begin{bmatrix} 0 & \frac{1}{L} \\ \frac{(1-k)}{C} & \frac{-1}{R_{load}C} \end{bmatrix} \cdot \begin{bmatrix} I_L \\ V_C \end{bmatrix} + \begin{bmatrix} \frac{k}{L} \\ 0 \end{bmatrix} \cdot \left[V_g \right]$$

$$Y = \begin{bmatrix} 0 & 1 \end{bmatrix} \cdot \begin{bmatrix} I_L \\ V_C \end{bmatrix} + [0] \cdot \left[V_g \right] \tag{4.75}$$

Expanding the system representation (4.22), the following DC equations are derived:

$$\begin{cases} 0 = (1-k)\dfrac{V_C}{L} + k \cdot \dfrac{V_g}{L} \\ 0 = \dfrac{(1-k)\cdot I_L}{C} - \dfrac{V_C}{R_{load} C} \\ Y = V_{out} = V_C \end{cases} \tag{4.76}$$

Therefore, the voltage across capacitor C, and the output voltage V_{out} are:

$$V_C = (1-k)\cdot R_{load} \cdot I_L \tag{4.77}$$

$$V_{out} = \frac{-k \cdot V_g}{(1-k)} \tag{4.78}$$

The ratio of capacitor voltage to source voltage defines the buck converter voltage gain. The voltage across the diode during the duty cycle k, is equal to the source voltage V_g, and zero otherwise. Therefore, the load voltage is equal to the average voltage across the diode.

4.2.4 AC component of buck-boost converter output voltage

The AC component of buck-boost converter is of reverse polarity as compared with buck and/or boost converter. The method of deriving the mathematical expression of the AC component is similar to that of buck and boost converter. Using the averaged state-space representation to determine the AC component would lead to an erroneous result, thus the averaged switch method is limited to a global representation of the DC output component. From the s-domain equivalent circuit of mode 1, shown in Fig. 4.6 (a), the output voltage expression is found through voltage divider method.

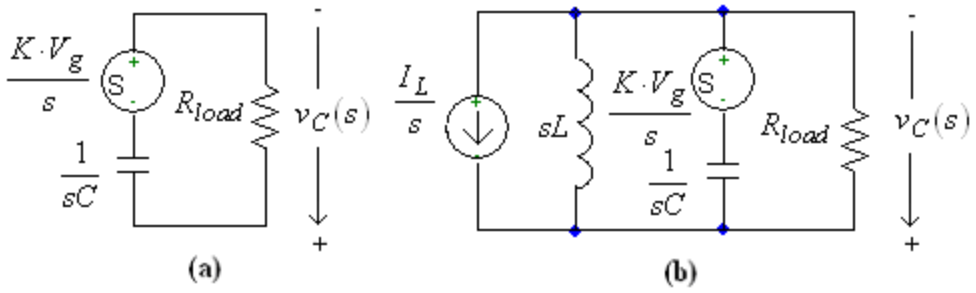

Figure 4.6: Buck-boost in the s-domain, (a) mode 1, (b) mode 2

The voltage source and the energy stored in inductor magnetic field do not contribute to the output voltage value during mode 1. Thus the AC output voltage is a decaying voltage described by:

$$v_{C-on}(s) = \frac{-R_{load} \cdot k \cdot V_g}{sR_{load} + \left(\frac{1}{C}\right)} \tag{4.79}$$

The AC output voltage component is of reverse polarity as compared with the input voltage polarity for the buck-boost converter. The AC component of output voltage during mode 2, shown in Fig. 4.6 (b), has negative polarity with respect to the input voltage polarity, and is expressed as:

$$v_{C-off}(s) = v'_C(s) + v''_C(s) \tag{4.80}$$

Expanding the expression for the AC voltage in (4.80), the AC component of output voltage during mode 2 is:

$$v_{C-off}(s) = \frac{\left(-s^2 R_{load} LC - L\right)}{s \cdot \left(s^2 R_{load} LC + sL + R_{load}\right)} \cdot k \cdot V_g \tag{4.81}$$

All three converters share similar expression for matrix *A* in one of their operating modes.

Matrix *A* corresponding to the *off*-mode for buck converter is identical to the *off*-mode matrix *A* for boost converter. Meanwhile, the *off*-mode matrix *A* of the buck-boost converter is similar to the homologous matrices for buck and boost converters. The only exception is element a_{12} being of opposite sign to similar elements for buck and boost converters. This is a consequence of the reverse polarity of the output voltage, as

compared with the input voltage. Since the buck and boost converters have output voltages of the same polarity as the input voltages, their *off*-mode matrices *A* are identical.

4.5 Averaged Switch Models of DC Power Systems

DC power sources are integral part of DC–DC converter circuits. Thus, the DC source characteristics affect the average output voltage of the power system, and the magnitude of the output voltage ripple. First order approximation of DC power sources consists of an ideal voltage source series connected to a resistor, emulating the power source internal resistance, r_i.

Mode 1, (*on*), of a buck converter, with first order approximation of its DC power source, is shown in Fig 4.7.

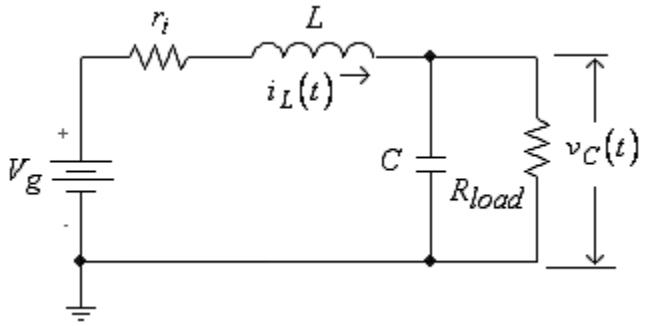

Figure 4.7: Mode 1 of buck converter

The power-source internal resistance determines a change in the differential equations describing the system.

$$\begin{cases} \dfrac{di_L(t)}{dt} = \left(\dfrac{-r_i}{L}\right) i_L(t) - \left(\dfrac{1}{L}\right) v_C(t) + \left(\dfrac{1}{L}\right) V_g \\ \dfrac{dv_C(t)}{dt} = \dfrac{1}{C} i_L(t) - \left(\dfrac{1}{R_{load}\,C}\right) v_C(t) + 0 \cdot V_g \end{cases} \tag{4.82}$$

Thus, mode 1 state-space representation is:

$$\begin{bmatrix} \dot{i}_L(t) \\ \dot{v}_C(t) \end{bmatrix} = \begin{bmatrix} -r_i/L & -1/L \\ 1/C & -1/R_{load}C \end{bmatrix} \cdot \begin{bmatrix} i_L(t) \\ v_C(t) \end{bmatrix} + \begin{bmatrix} 1/L \\ 0 \end{bmatrix} \cdot \begin{bmatrix} V_g \end{bmatrix}$$
$$y = \begin{bmatrix} 0 & 1 \end{bmatrix} \cdot \begin{bmatrix} i_L(t) \\ v_C(t) \end{bmatrix} + \begin{bmatrix} 0 \end{bmatrix} \cdot \begin{bmatrix} V_g \end{bmatrix} \tag{4.83}$$

During mode 2, switching transistor Q_{switch} is *off*, thus, the power source is disconnected from the circuit. Therefore, the state-space representation of mode 2 is identical to that of ideal source system described by (4.10).

Averaging the two linear systems over a switching cycle and expanding the system representation, the following set of DC equations is obtained:

$$\begin{cases} 0 = k \cdot \dfrac{-r_i}{L} \cdot I_L - \dfrac{1}{L} \cdot V_C + k \cdot \dfrac{1}{L} \cdot V_g \\ 0 = \dfrac{1}{C} \cdot I_L - \dfrac{1}{R_{load}C} \cdot V_C \\ Y = V_{out} = V_C \end{cases} \tag{4.84}$$

The DC voltage across the capacitor in steady-state operation is:

$$V_C = R_{load} \cdot I_L \tag{4.85}$$

Therefore, the correlation between the open-circuit voltage of the DC power source and the output voltage of the buck converter is:

$$V_C = V_{out} = \frac{k \cdot V_g}{\left(1 + \dfrac{k \cdot r_i}{R_{load}}\right)} \tag{4.86}$$

The first-order approximation of DC power source for a boost converter during mode 1 (*on* mode), is shown in Fig 4.8.

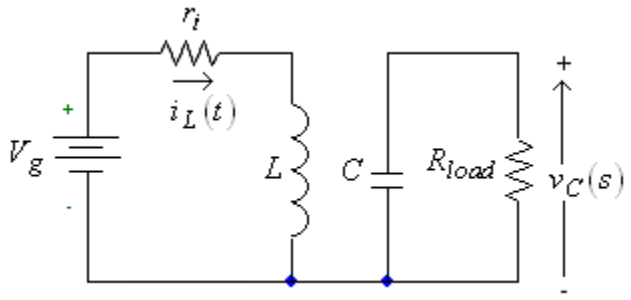

Figure 4.8: Mode 1 of boost converter

Mode 2, (*off*), of a boost converter, with first order approximation of its DC power source, is shown in Fig 4.9.

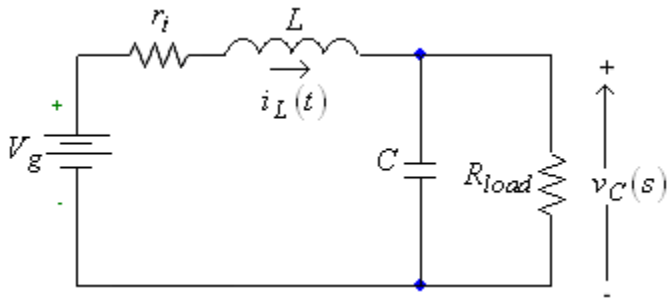

Figure 4.9: Mode 2 of boost converter

Two differential equations describe each mode. The internal resistance of the power source is considered in the state-space representation of each mode. Mode 1 is described by:

$$\begin{cases} \dfrac{di_L(t)}{dt} = \dfrac{-r_i}{L} \cdot i_L(t) + 0 \cdot v_C(t) + \dfrac{1}{L} V_g \\ \dfrac{dv_C(t)}{dt} = 0 \cdot i_L(t) - \left(\dfrac{1}{RC}\right) v_C(t) + 0 \cdot V_g \end{cases} \tag{4.87}$$

The boost converter state-space representation of mode 1 is:

$$\begin{bmatrix} \dot{i}_L(t) \\ \dot{v}_C(t) \end{bmatrix} = \begin{bmatrix} -r_i/L & 0 \\ 0 & -1/R_{load}C \end{bmatrix} \cdot \begin{bmatrix} i_L(t) \\ v_C(t) \end{bmatrix} + \begin{bmatrix} 1/L \\ 0 \end{bmatrix} \cdot \begin{bmatrix} V_g \end{bmatrix}$$
$$y = \begin{bmatrix} 0 & 1 \end{bmatrix} \cdot \begin{bmatrix} i_L(t) \\ v_C(t) \end{bmatrix} + [0] \cdot \begin{bmatrix} V_g \end{bmatrix} \tag{4.88}$$

Mode 2 is described by:

$$\begin{cases} \dfrac{di_L(t)}{dt} = \dfrac{-r_i}{L} \cdot i_L(t) - \dfrac{1}{L} \cdot v_C(t) + \dfrac{1}{L} V_g \\ \dfrac{dv_C(t)}{dt} = \dfrac{1}{C} \cdot i_L(t) - \left(\dfrac{1}{RC}\right) v_C(t) + 0 \cdot V_g \end{cases} \tag{4.89}$$

The boost converter state-space representation for mode 2 is:

$$\begin{bmatrix} \dot{i}_L(t) \\ \dot{v}_C(t) \end{bmatrix} = \begin{bmatrix} -r_i/L & -1/L \\ 1/C & -1/R_{load}C \end{bmatrix} \cdot \begin{bmatrix} i_L(t) \\ v_C(t) \end{bmatrix} + \begin{bmatrix} 1/L \\ 0 \end{bmatrix} \cdot \begin{bmatrix} V_g \end{bmatrix}$$
$$y = \begin{bmatrix} 0 & 1 \end{bmatrix} \cdot \begin{bmatrix} i_L(t) \\ v_C(t) \end{bmatrix} + [0] \cdot \begin{bmatrix} V_g \end{bmatrix} \tag{4.90}$$

Averaging the two linear time-independent systems with respect to time, over a switching cycle, the following DC system is deduced:

$$\begin{cases} 0 = \dfrac{-r_i}{L} \cdot I_L - \dfrac{k'}{L} \cdot V_C + \dfrac{1}{L} \cdot V_g \\ 0 = \dfrac{k'}{C} \cdot I_L - \dfrac{1}{R_{load}C} \cdot V_C + \dfrac{1}{L} \cdot V_g \\ Y = V_{out} = V_C \end{cases} \tag{4.91}$$

Therefore, the expression for the output voltage is given by:

$$V_{out} = \frac{R_{load} \cdot (1-k)}{r_i + R_{load} \cdot (1-k)^2} \cdot V_g \tag{4.92}$$

The first-order approximation of DC power source during mode 1 (*on* mode), for a buck-boost converter, is shown in Fig 4.10.

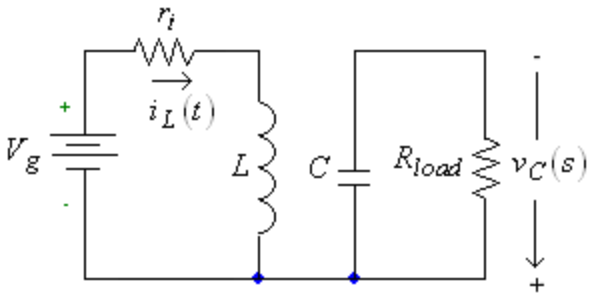

Figure 4.10: Mode 1 of buck-boost converter

The changes associated with the internal resistance of the power source are described by:

$$\begin{cases} \dfrac{di_L(t)}{dt} = \dfrac{-r_i}{L} \cdot i_L(t) + 0 \cdot v_C(t) + \dfrac{1}{L} V_g \\ \dfrac{dv_C(t)}{dt} = 0 \cdot i_L(t) - \left(\dfrac{1}{R_{load} C} \right) v_C(t) + 0 \cdot V_g \end{cases} \tag{4.93}$$

The state-space representation of mode 1 is given by:

$$\begin{aligned} \begin{bmatrix} \dot{i}_L(t) \\ \dot{v}_C(t) \end{bmatrix} &= \begin{bmatrix} -r_i/L & 0 \\ 0 & -1/R_{load} C \end{bmatrix} \cdot \begin{bmatrix} i_L(t) \\ v_C(t) \end{bmatrix} + \begin{bmatrix} 1/L \\ 0 \end{bmatrix} \cdot \left[v_g(t) \right] \\ y &= \begin{bmatrix} 0 & 1 \end{bmatrix} \cdot \begin{bmatrix} i_L(t) \\ v_C(t) \end{bmatrix} + [0] \cdot \left[v_g(t) \right] \end{aligned} \tag{4.94}$$

The first-order DC power source approximation of the buck-boost converter system is identical to that of ideal source buck-boost system. Thus, averaging the two linear systems with respect to time over a switching cycle, the corresponding DC system is obtained:

$$\begin{cases} 0 = k \cdot \dfrac{-r_i}{L} \cdot I_L + k' \cdot \dfrac{1}{L} \cdot V_C + k \cdot \dfrac{1}{L} \cdot V_g \\ 0 = k' \cdot \dfrac{1}{C} \cdot I_L - \dfrac{1}{R_{load} C} \cdot V_C \end{cases} \tag{4.95}$$

The state-space representation of the averaged system is:

$$\begin{cases} \begin{bmatrix} \dot{i}_L(t) \\ \dot{v}_C(t) \end{bmatrix} = \begin{bmatrix} k \cdot (-r_i)/L & (1-k)/L \\ (1-k)/C & -1/R_{load}C \end{bmatrix} \cdot \begin{bmatrix} i_L(t) \\ v_C(t) \end{bmatrix} + \begin{bmatrix} k/L \\ 0 \end{bmatrix} \cdot u(t) \\ y = \begin{bmatrix} 0 & 1 \end{bmatrix} \cdot \begin{bmatrix} i_L(t) \\ v_C(t) \end{bmatrix} + [0] \cdot u(t) \end{cases} \tag{4.96}$$

The average output voltage of the buck-boost converter is given by:

$$V_{out} = V_C = \frac{k \cdot (1-k) \cdot R_{load}}{k \cdot r_i + (1-k)^2 \cdot R_{load}} \cdot V_g \tag{4.97}$$

4.5.1 Output voltage of NiCd power system

The internal resistance of NiCd batteries considered in this research was determined experimentally, and was found to be $r_i = 0.05\Omega$. The open-circuit voltage for NiCd battery is 2.6V. The average output voltages for NiCd power source interfaced to buck converter are determined by:

$$V_{out} = \frac{k}{\left(1 + \frac{k \cdot r_i}{R_{load}}\right)} \cdot V_g \tag{4.98}$$

The conversion ratio changes with the load resistance as well. For consistency, all measurements, simulations, and numerical estimations applied to buck converters use the same value of load resistance; $R_{load} = 100\Omega$. The system output voltages, at duty cycles of 50%, 65%, and 80%, are recorded in Table 1.

Table 1: NiCd buck converter output voltage

Duty cycle, k (%)	Output voltage, V_{out} (V)
50	1.299
65	1.689
80	2.079

The average output voltages of boost converter driven NiCd system are determined for an internal resistance of the power source (NiCd battery), $r_i = 0.05\Omega$, and a load resistance, $R_{load} = 10\ k\Omega$.

$$V_{out} = \frac{(1-k)\cdot R_{load}}{r_i + (1-k)^2 \cdot R_{load}} \cdot V_g \tag{4.99}$$

All measurements, simulations, and numerical estimations applied to boost converters use the same value of load resistance; $R_{load} = 10\ k\Omega$. The system output voltages, at duty cycles of 50%, 65%, and 80%, are recorded in Table 2.

Table 2: NiCd boost converter output voltage

Duty cycle, k (%)	Output voltage V_{out} (V)
50	5.199
65	7.428
80	12.998

The average output voltage of boost-converter DC power system is 1 mV lower than the average output voltage of ideal power source boosts-converter system. With a load resistance of 10 kΩ, the NiCd buck-boost converter system is determined by:

$$V_{out} = \frac{k\cdot(1-k)\cdot R_{load}\cdot V_g}{k\cdot r_i + (1-k)^2 \cdot R_{load}} \tag{4.100}$$

The average output voltages of NiCd buck-boost converter at 50%, 65%, and 80% duty cycle, are recorded in Table 3.

Table 3: NiCd buck-boost converter output voltage

Duty cycle, k (%)	Output voltage, V_{out} (V)
50	2.599
65	4.828
80	10.398

At 50% duty cycle, the average output voltage is 1 mV lower than the ideal source buck-boost converter. At 65% duty cycle, NiCd buck-boost converter system exhibits identical average output voltage as ideal source buck-boost converter. Operating at 80%

duty cycle, NiCd system exhibits an average output voltage 2 mV lower than the ideal source buck-boost converter system.

4.5.2 Output voltage of DEFC power system

The measured value of DEFC-mesh internal resistance is r_i = *0.00408Ω*, while the internal resistance of DEFC-foam is r_i = *0.00815Ω*. The average output voltages for DEFC-mesh and DEFC-foam power sources, interfaced to buck converters, are determined for three duty cycles; 50%, 65%, and 80%. The open-circuit voltage of both fuel cells is 0.91V.

$$V_{out-mesh} = \frac{k}{\left(1+\frac{k \cdot r_{i-mesh}}{R_{load}}\right)} \cdot V_g \tag{4.101}$$

$$V_{out-foam} = \frac{k}{\left(1+\frac{k \cdot r_{i-foam}}{R_{load}}\right)} \cdot V_g \tag{4.102}$$

Table 4 shows the output voltages of both DEFC mesh and foam-buck converter systems.

Table 4: DEFC mesh and foam-buck converter output voltage

Duty cycle, *k* (%)	DEFC-mesh voltage (V)	DEFC-foam voltage (V)
50	0.454	0.454
65	0.591	0.591
80	0.727	0.727

Due to low values of DEFCs internal resistances, as compared to the load resistance, the output voltages are identical for all three duty cycles. However, buck-converter driven DEFC system exhibits lower average output voltage of 1mV, as compared to the ideal power source of similar system. The difference is larger for systems of lower ratio value, load resistance/power source internal resistance, R_{load} / r_i.

Boost converter systems are characterized by constant power output from DC source. Thus the internal resistance of the source is a path for electric current in both mode 1 (*on*) and mode 2 (*off*).

$$V_{out-mesh} = \frac{(1-k)\cdot R_{load}}{r_{i-mesh} + (1-k)^2 \cdot R_{load}} \cdot V_g \tag{4.103}$$

$$V_{out-foam} = \frac{(1-k)\cdot R_{load}}{r_{i-foam} + (1-k)^2 \cdot R_{load}} \cdot V_g \tag{4.104}$$

The output voltages of both DEFC mesh and foam-boost converter systems are recorded in Table 5.

Table 5: DEFC mesh and foam-boost converter output voltage

Duty cycle, *k* (%)	DEFC-mesh voltage (V)	DEFC-foam voltage (V)
50	1.819	1.819
65	2.599	2.599
80	4.549	4.549

DEFC-mesh average output voltages and DEFC-foam average output voltages, interfaced to boost converter, are identical at switching duty cycles of 50%, 65% and 80% respectively. However, lower values of average output voltages of 1 mV are observed, as compared to ideal-source boost converter.

Buck-boost driven DEFC average output voltages are determined for three duty cycles; 50%, 65%, and 80%:

$$V_{out-mesh} = \frac{k\cdot(1-k)\cdot R_{load}\cdot V_g}{k\cdot r_{i-mesh} + (1-k)^2 \cdot R_{load}} \tag{4.105}$$

$$V_{out-foam} = \frac{k\cdot(1-k)\cdot R_{load}\cdot V_g}{k\cdot r_{i-foam} + (1-k)^2 \cdot R_{load}} \tag{4.106}$$

Table 6 shows the output voltages of both DEFC mesh and foam-buck-boost converter systems.

Table 6: DEFC mesh and foam-buck-boost converter output voltage

Duty cycle (%)	DEFC-mesh voltage (V)	DEFC-foam voltage (V)
50	0.909	0.909
65	1.689	1.689
80	3.639	3.639

Buck-boost converter-driven DEFC-mesh and DEFC-foam systems exhibit an average output voltage that is 1 mV lower than that of the ideal power source buck-boost converter system. Differences of internal resistances of the two DEFCs do not result in significant differences of their average output voltages.

CHAPTER 5 - Fourier-series Models of DC–DC Converters

Mathematical models of DC–DC converters, using the Fourier-series decomposition method, are developed in this chapter. Each DC–DC converter is approximated with its equivalent DC-pulse, voltage source or current source model, in which the circuit comprised of switching transistor, free-wheeling diode, and voltage source, is replaced by a voltage source or a current source. The pulse-voltage and pulse-current waves generated by the sequential switching is further represented as a sum of sinusoidal voltages or currents, thus the DC–DC converters considered are approximated by their equivalent Fourier-series model. At steady-state operation, the Fourier-series models are compared with their corresponding small-signal models. Unlike large-signal models and small-signal models, Fourier-series models developed in this chapter, can accurately describe the transient operation of a DC–DC converter, from the first duty cycle, until, and including, the steady-state operation mode. Fourier-series models of DC–DC converter-driven DEFCs systems are developed in this chapter. The output voltage expression of DEFC system is derived.

5.1. Fourier-series model of DC–DC buck converter

DC–DC converter operation consists of sequential switching, generating voltage and current periodic waves in some point of the circuit, which is a source of nonlinearity. Power electronics interfaced circuits; DC–DC converters in particular, are inherently nonlinear due to the sequential switching governing the power conversion process. The entire system being nonlinear, the concepts of stability, controllability, and observability, normally characterizing linear, time-invariant (LTI) systems, generally do not apply.

However, a good approximation of the sequential switching is to consider any periodic wave as a sum of sinusoids, according to Fourier-series theory. Thus, an arbitrary, periodic waveform, of any frequency, can be represented with great accuracy as a sum of sinusoids with variable amplitudes and distinct phase angles:

$$
\begin{aligned}
v(t) &= C_0 + \sum_{n=1}^{\infty} C_n \sin(n\omega_1 t + \varphi_n) \\
C_0 &= \frac{1}{T}\int_0^T v(t)dt \\
C_n &= \sqrt{{A_n}^2 + {B_n}^2} \\
A_n &= \frac{2}{T}\int_0^T v(t)\cos(n\omega_1 t)dt \\
B_n &= \frac{2}{T}\int_0^T v(t)\sin(n\omega_1 t)dt \\
\varphi_n &= \tan^{-1}\left(\frac{A_n}{B_n}\right)
\end{aligned}
\tag{5.1}
$$

5.1.1. *Source-switches equivalent circuit for the buck converter*

The DC–DC buck converter circuit diagram shown in Fig. 5.1, has a MOSFET switching transistor, regulating the flow of current through inductor *L* and load *R*-*C*. The following assumptions are considered for the development of Fourier-series model of the DC–DC buck converter: The power source used is an ideal voltage source; no internal resistance and cell capacitance are considered. The voltage drop across switching transistor, in *on* mode, is assumed negligible. The free-wheeling diode is assumed ideal; zero resistance in forward-bias mode, and infinite resistance in reverse-bias mode. No copper resistance is associated with the inductor winding.

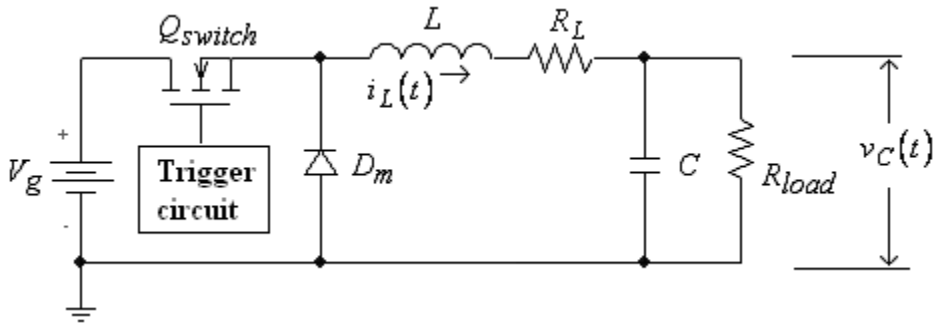

Figure 5.1: Ideal source, buck converter diagram

The voltage drop across the free-wheeling diode has a peak value equal to the source voltage, during transistor *on* mode. During *off* mode, the voltage drop across the free wheeling diode is equal to the forward bias voltage of the diode. Thus, the voltage across free wheeling diode is a square wave, with duty cycle identical to that of the switching transistor. Therefore, the buck converter source-transistor-diode circuit can be replaced with an independent pulse-voltage source. The rest of the buck converter circuit remains unchanged [76].

The maximum current of the current-source for the buck converter is determined through Ohm's law; the DC voltage V_g is divided by the total resistance of the circuit after the switching transistor has been turned *on* for a long time. This amount of time ensures that capacitor C is completely charged, and inductor L behaves like a short circuit. In practical applications, the maximum current flowing through the inductor is dependent on the duty cycle and switching frequency. The current flowing through inductor L by the sequential switching process in the converter resembles a square wave.

5.1.2. *Voltage source approximation for buck converter*

Theoretically, no intrinsic resistance in DC mode is associated with inductor L, capacitor C, voltage source, V_g, and switching transistor Q_{switch}. However, real electronic components are characterized by internal resistances and corresponding reactance. Those

values do have an effect on the inductor-current phase angles for the Fourier-series representation used in the buck converter model. Considering the DC bias of the pulse-voltage source, and its *n* harmonics, the periodic wave expression for the voltage pulse is mathematically approximated by the formula:

$$v_{pulse}(t) = C_0 + C_1 \cdot \sin(\omega_1 t + \varphi_1) + C_2 \cdot \sin(\omega_2 t + \varphi_2) + \ldots + C_n \cdot \sin(\omega_n + \varphi_n) \quad (5.2)$$

Since the buck converter circuit is comprised of resistive and reactive components, with multiple sources, the analysis can be accomplished in the s-domain. The Laplace transform of the time-domain input voltage is,

$$\begin{aligned} L\{v(t)\} = L\{C_0\} + L\{C_1 \cdot \sin(\omega_1 t + \varphi_1)\} + L\{C_2 \cdot \sin(\omega_2 t + \varphi_2)\} + \ldots. \\ + L\{C_{21} \cdot \sin(\omega_{21} + \varphi_{21})\} + \ldots + L\{C_n \cdot \sin(\omega_n + \varphi_n)\} \end{aligned} \quad (5.3)$$

A square wave voltage of amplitude 2.6 V, and duty cycle k = 65%, is approximated by a DC bias and 21 harmonics of the switching frequency, as shown in Fig. 5.2. The amplitudes of all 21 harmonics considered in the approximation are found employing the general formulae:

$$\begin{aligned} C_n &= \sqrt{{A_n}^2 + {B_n}^2} \\ A_n &= \frac{2}{T}\int_0^{kT} V_{\max} \cdot \cos\left(\frac{n \cdot 2\pi}{T} \cdot t\right) dt + \int_{kT}^{T} 0 \cdot \cos\left(\frac{n \cdot 2\pi}{T} \cdot t\right) dt = \frac{V_{\max}}{n\pi} \sin(k \cdot n \cdot 2\pi) \\ B_n &= \frac{2}{T}\int_0^{kT} V_{\max} \cdot \sin\left(\frac{n \cdot 2\pi}{T} \cdot t\right) dt + \int_{kT}^{T} 0 \cdot \sin\left(\frac{n \cdot 2\pi}{T} \cdot t\right) dt = \frac{V_{\max}}{n\pi} \left[1 - \cos(k \cdot n \cdot 2\pi)\right] \\ \varphi_n &= \tan^{-1}\left(\frac{A_n}{B_n}\right) \end{aligned} \quad (5.4)$$

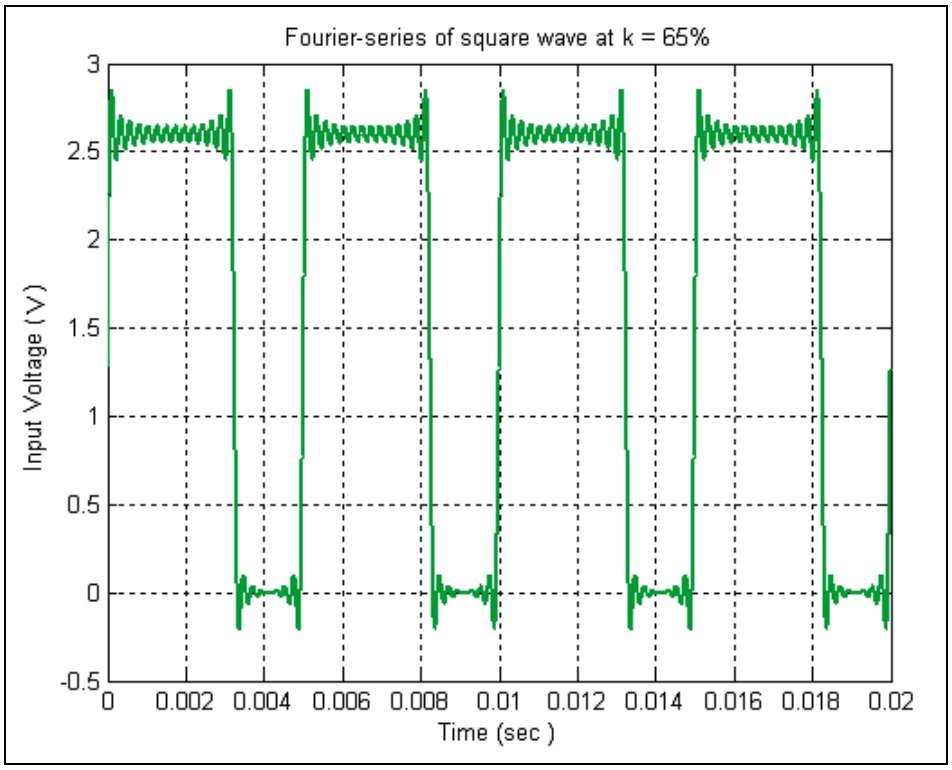

Figure 5.2: Square wave Fourier-series equivalent

During *off* time, the inductor current and free-wheeling diode current are identical. During *on* time, inductor current waveform is determined by the initial conditions associated with all reactive components in the circuit of mode 1 (*on*). The inductor current peak value is determined by the load resistance and the magnitude of the pulse voltage. The equivalent square wave representation approximated by Fourier series suffices the circuit analysis with a level of accuracy determined by the correlation function:

$$c_n = \frac{1}{\sqrt{E_g \cdot E_f}} \cdot \int_0^T f(t)g(t)dt \tag{5.5}$$

where E_g is the energy of signal *g(t)*, and E_f is the energy of signal *f(t)*. The correlation coefficient c_n has a value from –1 (for symmetrical signals) to +1 (for identical signals). For practicality purposes, a correlation coefficient $c_n = 0.99$ allows an accurate square wave representation, thus a DC–DC converter (buck or boost converter) is closely approximated by an equivalent linear, time-invariant system right from the beginning.

5.1.3. State-space representation of buck Fourier-series model

Knowing that:

$$v_{pulse}(k,t) = v_g(t) \tag{5.6}$$

$$\begin{aligned} v_L(t) &= v_g(t) - (R_L + R_{load}) \cdot i_L(t) \\ i_C(t) &= i_L(t) - \left(\frac{1}{R_{load}}\right) \cdot v_C(t) \end{aligned} \tag{5.7}$$

The differential equations governing system operation are:

$$\frac{di_L(t)}{dt} = \left(\dot{i}_L\right) = \left(\frac{-(R_L + R_{load})}{L}\right) \cdot i_L(t) + \left(\frac{1}{L}\right) \cdot v_g(t) \tag{5.8}$$

$$\frac{dv_C(t)}{dt} = \left(\dot{v}_C\right) = \left(\frac{1}{C}\right) \cdot i_{pulse}(t) - \left(\frac{1}{R_{load}C}\right) \cdot v_C(t) \tag{5.9}$$

Therefore, the state-space representation of the buck converter's Fourier model is:

$$\begin{aligned} \begin{bmatrix} \dot{i}_L \\ \dot{v}_C \end{bmatrix} &= \begin{bmatrix} -(R_L + R_{load})/L & 0 \\ 1/C & -1/R_{load}C \end{bmatrix} \cdot \begin{bmatrix} i_L(t) \\ v_C(t) \end{bmatrix} + \begin{bmatrix} 1/L \\ 0 \end{bmatrix} \cdot \left[v_g(t)\right] \\ \left[v_{out}\right] &= \begin{bmatrix} 0 & 1 \end{bmatrix} \cdot \begin{bmatrix} i_L(t) \\ v_C(t) \end{bmatrix} + [0] \cdot \left[v_g(t)\right] \end{aligned} \tag{5.10}$$

From (5.10) it is clear that state matrix *A* is nonsingular. Thus, evaluating the output voltage is accomplished by solving the system of time-domain differential equations in (5.10). The assumption is that the equivalent source voltage is accurately expressed by its Fourier-series representation. Expanding the s-domain expression for the equivalent pulse-voltage source in (5.3), the Laplace transform of the pulse voltage input would be:

$$\begin{aligned} V(s) = \frac{C_0}{s} + C_1 \cdot \frac{s \cdot (\sin\varphi_1) + \omega_1 \cdot (\cos\varphi_1)}{s^2 + {\omega_1}^2} + C_2 \cdot \frac{s \cdot (\sin\varphi_2) + \omega_2 \cdot (\cos\varphi_2)}{s^2 + {\omega_2}^2} + \ldots \\ + C_n \cdot \frac{s \cdot (\sin\varphi_n) + \omega_n \cdot (\cos\varphi_n)}{s^2 + {\omega_n}^2} = u(s) = U_s \end{aligned} \tag{5.11}$$

Therefore, the s-domain of the state-space representation for the system is,

$$\begin{cases} s \cdot X_s = A \cdot X_s + B \cdot U_s \\ Y_s = A \cdot X_s + D \cdot U_s \end{cases} \tag{5.12}$$

The set of equations are rewritten to determine the output vector Y_s:

$$\begin{cases} X_s = (sI - A)^{-1} \cdot B \cdot U_s \\ Y_s = C \cdot X_s + D \cdot U_s \end{cases} \tag{5.13}$$

The DC–DC buck converter circuit diagram, presented in Fig. 5.1, has a MOSFET switching transistor, regulating the current flow through inductor *L*, switching transistor, and the voltage source, during mode 1. During mode 2, the load current through R_{load} is generated by the collapsing magnetic field of inductor *L*. From (5.12), the expression of s-domain output vector (output voltage) is derived:

$$Y_s = C \cdot (sI - A)^{-1} \cdot B \cdot U_s + D \cdot U_s = V_C(s) \tag{5.14}$$

Expanding the equation in (5.15), the output matrix is written as:

$$Y_s = \left(\begin{bmatrix} 0 & 1 \end{bmatrix} \cdot \left(\begin{bmatrix} s(R_L + R_{load})/L & 0 \\ 1/C & \left(s + 1/R_{load}C\right) \end{bmatrix} \right)^{-1} \cdot \begin{bmatrix} 1/L & \cdots & 1/L \\ 0 & \cdots & 0 \end{bmatrix} \right) \cdot U_s \tag{5.15}$$

It is clear from (5.14) that matrix *(sI− A)* is not singular, thus it is possible to determine the s-domain expression for the output voltage. The s-domain output voltage is described by:

$$V_{out}(s) = \left(\begin{bmatrix} 0 & 1 \end{bmatrix} \cdot \frac{1}{\det(sI - A)} \cdot \begin{bmatrix} \left(s + 1/R_{load}C\right) & 0 \\ -1/C & s(R_L + R_{load})/L \end{bmatrix} \right) \cdot \begin{bmatrix} 1/L \\ 0 \end{bmatrix} \cdot U_s \tag{5.16}$$

Since the voltage across capacitor *C* is equal to the output voltage, expanding the expression in (5.16) the converter output voltage is determined. Since matrix *D* in the s-domain state-space representation is a *1xn* matrix, with all its elements equal to zero, matrix *D* is no longer relevant to the output voltage expression, thus it has been omitted from Equations (5.15) and (5.16). Determinant *det*(*sI*−*A*) in Equations (5.16) is:

$$\det(sI - A) = s(R_L + R_{load}) \cdot \left(s + \frac{1}{R_{load}C} \right) = s^2 (R_L + R_{load}) + s\left(\frac{R_L + R_{load}}{R_{load}C} \right) \tag{5.17}$$

The condensed expression of s-domain output voltage is:

$$V_C(s) = \left(\left[s(R_L + R_{load}) \left(s + \frac{1}{R_{load} C} \right) \left(\frac{-1}{C} \right) \quad s(R_L + R_{load})^2 \cdot \left(s + \frac{1}{R_{load} C} \right) \right] \right) \cdot U_s \tag{5.18}$$

The s-domain output voltage in expanded format is:

$$V_{out}(s) = \left(- \frac{(R_L + R_{load})(s^2 + s)}{R_{load} C^2} \right) \cdot \left(\frac{C_0}{s} + C_1 \cdot \frac{s(\sin\varphi_1) + \omega_1(\cos\varphi_1)}{s^2 + {\omega_1}^2} + \ldots \right.$$
$$\left. + C_n \cdot \frac{s(\sin\varphi_n) + \omega_n(\cos\varphi_n)}{s^2 + {\omega_n}^2} \right) \tag{5.19}$$

Time-domain expression for converter output voltage is determined through inverse Lapalce operation on the s-domain output voltage expression in (5.19). It is impossible to determine the time-domain analytical expression of the output voltage, without knowing the numerical values, in Equation (5.19), for converter components: duty cycle, pulse-current source value, and impedance values. For a set of converter components, any change of the duty cycle will require a re evaluation of the time-domain output voltage.

5.2. Fourier-series model of DC–DC boost converter

The Fourier-series model for DC–DC boost converter is similar to the buck converter model, with the exception of an additional coefficient C_{DC}, accounting for the continuous current flow through inductor *L*. During *on* time of operation, there are two currents; one flowing through the voltage source, inductor, diode, and the *R*-*C* load, and the other through the voltage source, inductor, and switching transistor. Since the *on* mode current can reach unacceptable values for a high duty cycle, in modeling a boost converter the internal resistances of the power source, switching transistor, and inductor are no longer negligible.

5.2.1. Source-switches equivalent circuit for the boost converter

The elementary model of DC–DC boost converter, due to its operation characteristics, is accomplished on a set of assumptions, different than that of the buck converter. The voltage-source internal resistance is not zero. There is no cell capacitance associated with the voltage source. The voltage drop across the conducting transistor and inductor ohmic resistance are nonzero. Reverse-biased diode presents an infinite resistance to the flow of current. Considering transistor Q_{switch} being *off* for a long time, and the voltage source connected to the converter circuit, there is a constant current flowing through inductor L and load resistor R_{load}. As transistor Q_{switch} is turned *on*, the current flowing through inductor L increases to a maximum value that is dependent on the combined resistance; inductor, switching transistor, and voltage source, as well as the time for which switching transistor stays *on*. Thus the energy stored in the inductor magnetic field increases from a constant value to a peak value, over the entire *on* mode. At the inductor terminal, closest to the voltage source, the flow of current is constant during *off* time, then increases to a peak value during *on* time. During *on* time, the capacitor voltage decays, thus the potential difference between the inductor terminals, when the switching transistor is turned *off*, determines a current flow from the voltage source toward the load. During *off* mode, the energy stored in the magnetic field of the inductor is released through the circuit, thus the inductor is "seen" by the load resistor and filtering capacitor, as a decaying magnitude current source. The switching transistor, in the boost converter circuit shown in Fig. 5.3, is a voltage-controlled current-source. The sub circuit transistor-diode-power source is "seen" by the inductor as periodic, variable amplitude, current source.

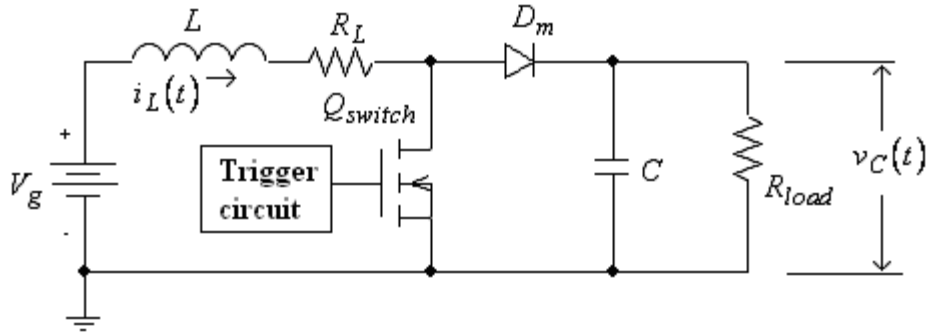

Figure 5.3: Ideal-source, boost converter

5.2.2 Voltage and current source approximation for boost converter

The inductor current is a function of the input voltage and switching frequency. The input current is determined for each duty cycle and each switching frequency. The Fourier-series expression of input current for the boost converter model is:

$$i_{pulse}(t) = C_0 + C_1 \cdot \sin(\omega_1 t + \varphi_1) + \cdots + C_n \cdot \sin(\omega_n t + \varphi_n) \tag{5.20}$$

The initial voltage (determined from the assumptions that the converter was connected to the power source for a long time) and the initial inductor current are given by:

$$V_0 = V_g$$
$$I_0 = C_0 = \left(\frac{V_g}{R_L}\right) \tag{5.21}$$

For practical applications, the number of harmonics employed for the current waveform approximation is a finite number, chosen to satisfy the correlation coefficient requirements (i.e., $c_n = 0.99$). The inductor current waveform at 65% duty cycle, during mode2, (*off*), is shown in Fig. 5.4.

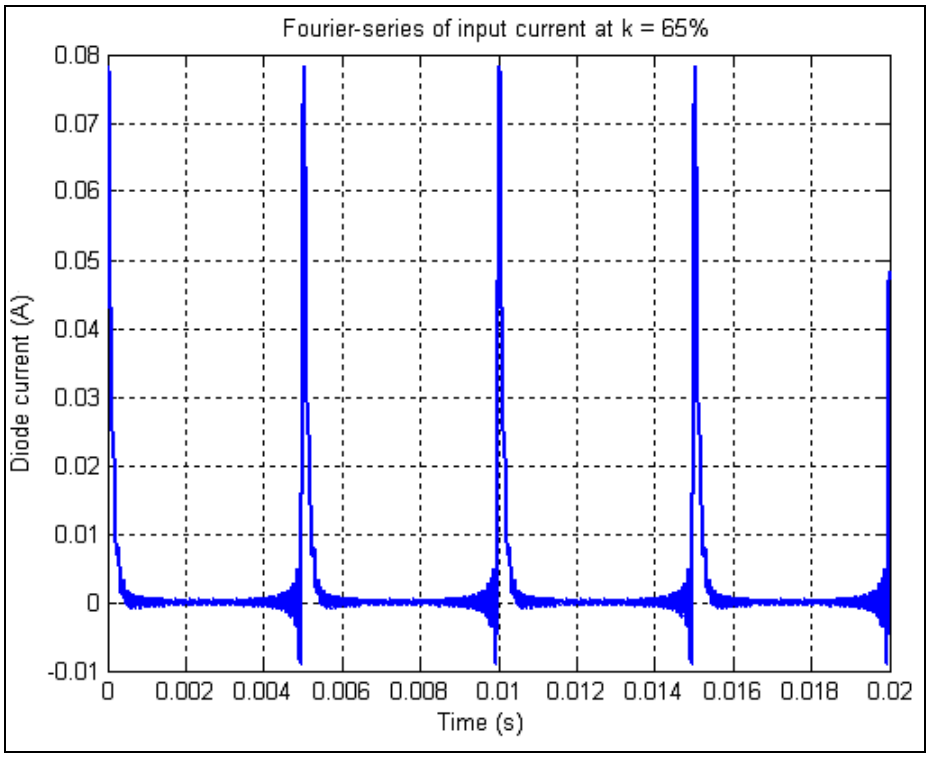

Figure 5.4: Off mode inductor current waveshape

5.2.3 State-space representation of boost Fourier-series model

The two differential equations describing the boost converter system in Fig. 5.3 are:

$$\frac{di_L(t)}{dt} = (\dot{i}_L) = \left(\frac{-R_L}{L}\right) \cdot i_L(t) + \left(\frac{k}{L}\right) \cdot v_C(t) + \left(\frac{1}{L}\right) \cdot v_g(t) \tag{5.22}$$

$$\frac{dv_C(t)}{dt} = (\dot{v}_C) = \left(\frac{-1}{R_{load}C}\right) \cdot v_C(t) + \left(\frac{1}{C}\right) \cdot i_{pulse}(t) \tag{5.23}$$

Compared to the state-space representation of the buck converter, boost converter is characterized by multiple inputs: a pulse voltage, of peak value equal to the source voltage, and a pulse current, comprised of decaying inductor currents during each *off* mode. Both (5.22) and (5.23) are first-order differential equations with nonzero initial conditions for their respective variables.

$$\begin{bmatrix} \dot{i}_L \\ \dot{v}_C \end{bmatrix} = \begin{bmatrix} -R_L/L & k/L \\ 0 & -1/R_{load}C \end{bmatrix} \cdot \begin{bmatrix} i_L(t) \\ v_C(t) \end{bmatrix} + \begin{bmatrix} 1/L & 0 \\ 0 & 1/C \end{bmatrix} \cdot \begin{bmatrix} v_g(t) \\ i_{pulse}(k,t) \end{bmatrix}$$

$$[v_{out}] = [0 \quad 1] \cdot \begin{bmatrix} i_L(t) \\ v_C(t) \end{bmatrix} + [0 \quad 0] \cdot \begin{bmatrix} v_g(t) \\ i_{pulse}(k,t) \end{bmatrix} \tag{5.24}$$

Matrices B, D, and the input vector U_s are of different dimensions as compared to the homologous matrices of the buck converter state-space representation. Input vector U_s determines the dimensions of matrices B and D, and its increased number of elements, as compared with buck converter case, is a consequence of the voltage-and-current driven system.

5.3 Fourier-series model of DC–DC buck-boost converter

DC–DC buck-boost converters have the capability to vary the output voltage from zero to a maximum value, thus combining the performances of buck and boost converters. This unique feature is accomplished by varying the duty cycle of the switching transistor from zero to a maximum value, which is determined by maximum current limitations of the electronic components. The extreme value of the duty cycle equal to 0% is of no theoretical or practical interest. On the other extreme, a duty cycle equal to 100%, or any large values, is destructive to the converter components and it should be avoided at all times.

5.3.1. Source-switches equivalent circuit for the buck-boost converter

Since switching transistor Q_{switch} can be modeled as a controlled current source, shown in Fig. 5.5(a), the buck-boost converter can be represented as an independent DC-

pulse current source, series connected with the energy-storing inductor *L*, and the capacitor-load resistance circuit *R*-*C*, shown in Fig. 5.5(b) [76].

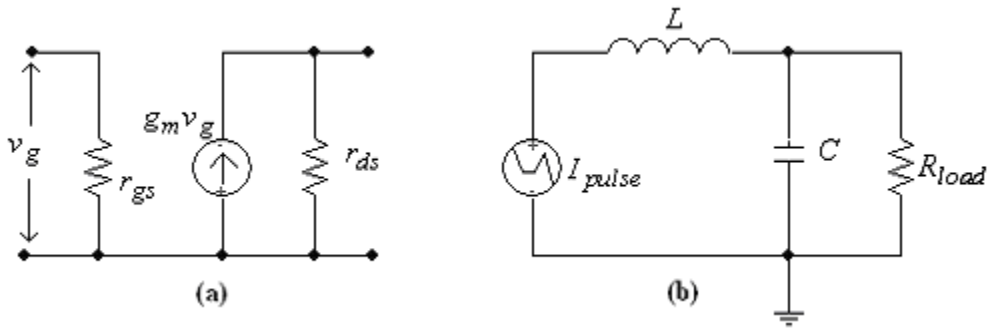

Figure 5.5: (a) **MOSFET equivalent circuit, (b) buck converter equivalent circuit**

Mode 2 of buck-boost converter is described by the same differential equation as of the boost converter, and represented by identical circuits. The circuit representing mode 2 does not include any independent power source, and is solely driven by the current generated through the collapsing magnetic field of the inductor.

The output voltage polarity, for buck-boost converter, is of opposite sign than the polarity of its input voltage, as shown in Fig. 5.6.

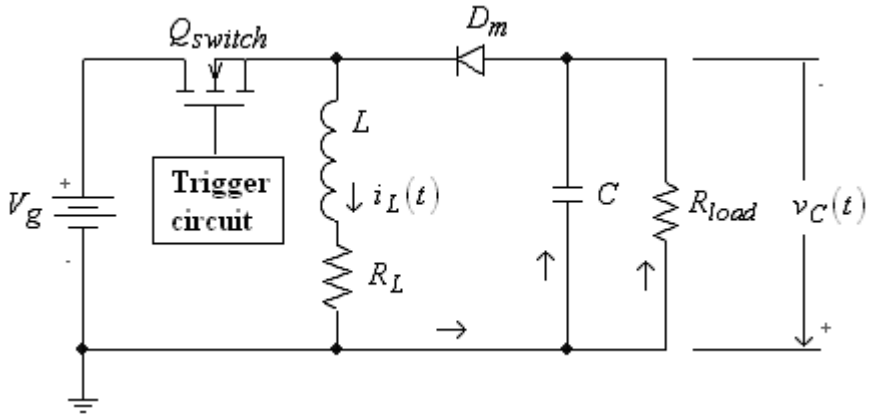

Figure 5.6: Typical buck-boost converter diagram

The inductor current follows a path dictated by the free-wheeling diode, thus the alternate name, indirect converter. Inductor current is proportional to the energy stored in

the magnetic field of the inductor, and to the inductor voltage. The current delivered to the load is due only to the collapsing magnetic field of the inductor, and is a decaying current during the *off* mode. Thus the inductor is "seen" by the load as a periodic wave, pulse-current source, with a frequency equal to the switching frequency, and a waveform determined by the voltage source characteristics, and the buck-boost components parameters.

5.3.2. Current source approximation for buck-boost converter

The input voltage expression of the buck-boost converter is instrumental in determining the peak value of inductor current at the end of mode 1. Input current expression, for the equivalent converter circuit, is determined analytically. Since the inductor current is a periodical wave, it is approximated by its Fourier-series equivalent:

$$i_{pulse}(t) = C_0 + C_1 \cdot \sin(\omega_1 t + \varphi_1) + \cdots + C_n \cdot \sin(\omega_n t + \varphi_n) \qquad (5.25)$$

The energy stored in the inductor magnetic field is equal to that of the boost converter during mode 1 (switching transistor is *on*). The inductor current and load voltage are variables of two time-domain differential equations, with zero initial conditions. Since the two modes of buck-boost converter do not share at least one component at any given time, during one cycle, the two differential equations describing the system are independent.

5.3.3. State-space representation of buck-boost Fourier-series model

The state-space representation for buck-boost converter is similar to that of the boost converter, provided the coefficients for the Fourier-series input current are determined as mentioned above. Only a finite, relevant number of harmonics are considered for practical applications. A large number of harmonics can make the analysis

cumbersome, without any added benefits to the overall system model and its state-space representation.

Two state-space variables are considered to describe the buck-boost system; inductor current $i_L(t)$, and capacitor voltage $v_C(t)$.

$$\frac{di_L(t)}{dt} = \left(\dot{i}_L\right) = \left(\frac{-R_L}{L}\right) \cdot i_L(t) + \frac{v_g(t)}{L} \tag{5.26}$$

$$\frac{dv_C(t)}{dt} = \left(\dot{v}_C\right) = \left(\frac{-1}{R_{load}C}\right) \cdot v_C(t) + \left(\frac{1}{C}\right) \cdot i_{pulse}(t) \tag{5.27}$$

The input pulse-current flow direction is determined by conditions discussed in Section 5.3.1, thus the system output voltage is:

$$v_{out}(t) = -v_C(t) \tag{5.28}$$

The buck-boost converter state-space representation in general form is:

$$\begin{bmatrix} \dot{i}_L \\ \dot{v}_C \end{bmatrix} = \begin{bmatrix} -R_L/L & 0 \\ 0 & -1/R_{load}C \end{bmatrix} \cdot \begin{bmatrix} i_L(t) \\ v_C(t) \end{bmatrix} + \begin{bmatrix} 1/L & 0 \\ 0 & 1/C \end{bmatrix} \cdot \begin{bmatrix} v_g(t) \\ i_{pulse}(t) \end{bmatrix}$$
$$\left[v_{out}\right] = \begin{bmatrix} 0 & -1 \end{bmatrix} \cdot \begin{bmatrix} i_L(t) \\ v_C(t) \end{bmatrix} + \begin{bmatrix} 0 & 0 \end{bmatrix} \cdot \begin{bmatrix} v_g(t) \\ i_{pulse}(t) \end{bmatrix} \tag{5.29}$$

Writing the input vector in its explicit form, i.e., voltage and pulse current, matrix B can be written as a nonsingular matrix. Matrix D has all its elements equal to zero. Similar to the state-space representation of boost converter, the state-space representation of buck-boost converter presents an input comprised only of pulse current, and zero input voltage. Its explicit state-space representation is:

$$\begin{bmatrix} \dot{i}_L \\ \dot{v}_C \end{bmatrix} = \begin{bmatrix} -R_L/L & 0 \\ 0 & -1/R_{load}C \end{bmatrix} \cdot \begin{bmatrix} i_L(t) \\ v_C(t) \end{bmatrix} + \begin{bmatrix} 1/L & 0 \\ 0 & 1/C \end{bmatrix} \cdot \begin{bmatrix} v_0 + v_1 \sin(\omega_1 t + \varphi_1) + \cdots \\ C_0 + C_1 \sin(\omega_1 t + \varphi_1) + \cdots \end{bmatrix}$$

$$\left[v_{out}\right] = \begin{bmatrix} 0 & -1 \end{bmatrix} \cdot \begin{bmatrix} i_L(t) \\ v_C(t) \end{bmatrix} + \begin{bmatrix} 0 & 0 \end{bmatrix} \cdot \begin{bmatrix} v_0 + v_1 \sin(\omega_1 t + \varphi_1) + \cdots \\ C_0 + C_1 \sin(\omega_1 t + \varphi_1) + \cdots \end{bmatrix} \tag{5.30}$$

Matrices A, B, C, and D for the buck-boost state-space representation are identical to that of buck converter. The analysis of buck-boost converter Fourier-series model can

be accomplished in the s-domain, where the input current is equal to the Laplace transform of $i_{pulse}(t)$ used previously in (5.10).

The s-domain representation of buck-boost Fourier-series model is:

$$\begin{cases} s \cdot X_s = A \cdot X_s + B \cdot U_s \\ Y_s = A \cdot X_s + D \cdot U_s \end{cases} \tag{5.31}$$

where X_s, U_s, and Y_s are the s-domain state-space variable vector, input vector, and output, respectively. In order to find an explicit expression for the output vector, as a function of system variables, the system of Equations (5.31) is re-written as:

$$\begin{cases} X_s = \left(sI - A\right)^{-1} \cdot B \cdot U_s \\ Y_s = C \cdot X_s + D \cdot U_s \end{cases} \tag{5.32}$$

As in the previous cases, the output vector Y_s is written in analytical form as:

$$Y_s = C \cdot \left(sI - A\right)^{-1} \cdot B \cdot U_s + D \cdot U_s = V_C(s) \tag{5.33}$$

The analytical format similarities between the s-domain representation of the buck-boost converter and that of the boost converter, allows writing the expression of the output voltage of buck-boost converter by substituting every V_g term in the boost converter s-domain, with zero.

Although the output voltage expressions of boost converter and buck-boost converter are similar, the input vector for identical duty cycles and voltage sources are different. For this reason, the Fourier-series input voltage and/or current should be carefully determined for each type of converter, and for each duty cycle, respectively. Of interest to the designing engineer is the time-domain expression of the output voltage which is done through numerical analysis.

5.4. Current waveforms and their Fourier-series approximations

Inductors are reactive components that limit the variation of current in a circuit. The inductor role in DC–DC converters is to store and release energy through the flow of

current, thus determining the current waveshape, which is different for each type of converter and for each duty cycle. Assuming continuous conduction mode of operation, the analytical expressions for the s-domain inductor currents are developed.

5.4.1 Inductor current of buck converter

During mode 1 (*on* mode), transistor Q_{switch} assures unrestricted path for inductor current flow, as shown in Fig. 4.1 (a). The s-domain equivalent circuit during mode 1 is shown in Fig 5.6. The circuit represents the steady-state operation, where there is a non-zero inductor current and capacitor voltage at the beginning of each *on-off* cycle.

Figure 5.7 shows the s-domain circuit of the buck converter, during mode 1 (*on* mode).

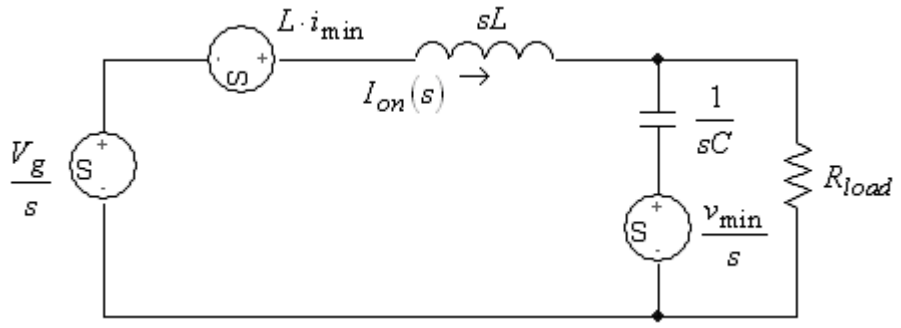

Figure 5.7: Buck converter, s-domain mode 1

The s-domain expression for inductor current is determined by superposition in the circuit of Fig. 5.5:

$$I_{on}(s) = I'(s) + I''(s) + I'''(s) \tag{5.34}$$

The corresponding partial currents are found by considering one source at the time. The expressions for the three currents are:

$$I'(s) = \frac{(R_{load} + 1) \cdot V_g}{\left(s^2 \cdot LCR_{load} + s \cdot L + R_{load}\right)} \tag{5.35}$$

$$I''(s) = \frac{-(s \cdot LC + CR_{load}) \cdot v_{\min}}{\left(s^2 \cdot LCR_{load} + s \cdot L + R_{load}\right)} \tag{5.36}$$

$$I'''(s) = \frac{(s \cdot CR_{load}) \cdot L \cdot i_{\min}}{\left(s^2 LCR_{load} + s \cdot L + R_{load}\right)} \tag{5.37}$$

The expression for inductor current during mode 1 is expanded to:

$$I_{on}(s) = \frac{(R_{load} + 1) \cdot V_g + (s \cdot CR_{load}) \cdot L \cdot i_{\min} - (s \cdot LC + CR_{load}) \cdot v_{\min}}{\left(s^2 LCR_{load} + s \cdot L + R_{load}\right)} \tag{5.38}$$

During mode 2 (*off* mode), the voltage source provides zero energy to the inductor. The flow of current is due to the collapsing magnetic field of the inductor, through the free-wheeling diode. Thus the s-domain circuit is source-free, presenting a decaying inductor current characteristic, as shown in Fig. 5.8.

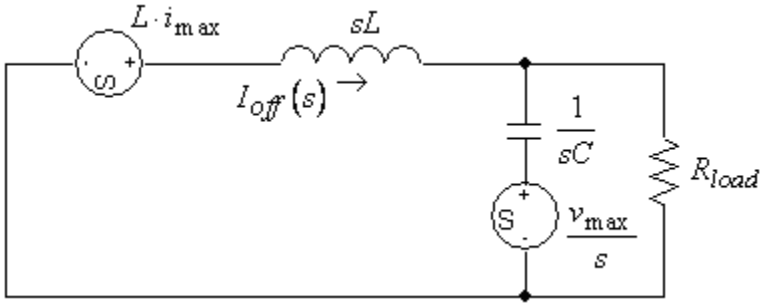

Figure 5.8: Buck converter, s-domain mode 2

The magnitude of initial current $i_{\max}$ for mode 2, is determined by the duty cycle k, as it relates to the *on-time* during mode 1. This current is the peak inductor current at the end of mode 1, and its value is essential in evaluating the inductor current waveform. Fig. 5.8 shows two sources that determine the flow of current during mode 2. The inductor current is:

$$I_{off}(s) = I_1(s) + I_2(s) \tag{5.39}$$

Partial currents $I_1(s)$ and $I_2(s)$ are given by:

$$I_1(s) = \frac{(s \cdot CR_{load} + 1) \cdot L \cdot i_{\max}}{\left(s^2 \cdot LCR_{load} + s \cdot L + R_{load}\right)} \tag{5.40}$$

$$I_2(s) = \frac{-(s \cdot LC + CR_{load}) \cdot v_{\max}}{\left(s^2 \cdot LCR_{load} + s \cdot L + R_{load}\right)} \tag{5.41}$$

Thus, the s-domain expression for inductor current, during mode 2, is:

$$I_2(s) = \frac{(s \cdot CR_{load} + 1) \cdot L \cdot i_{\max} - (s \cdot LC + CR_{load}) \cdot v_{\max}}{\left(s^2 \cdot LCR_{load} + s \cdot L + R_{load}\right)} \tag{5.42}$$

Inductor current time-domain expression, during mode 2, is determined only with prior knowledge of the duty cycle, maximum values of capacitor voltage and inductor current, and all component values.

5.4.2 Inductor current of boost converter

It is assumed that the boost converter is operating in steady-state mode. The inductor current and capacitor voltage alternate between minimum and maximum values, with a periodicity dictated by the converter switching frequency.

During mode 1 (*on* mode), the inductor current path shown in Fig. 5.9, consists of two sources and one reactive element.

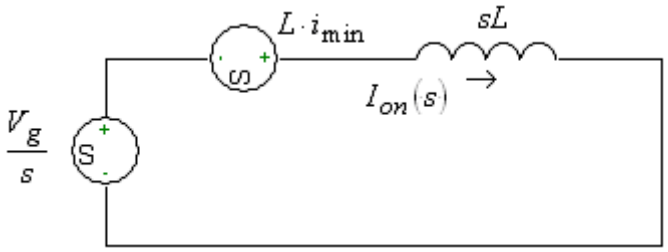

Figure 5.9: Boost converter, s-domain mode 1

Therefore, two partial currents contribute to the inductor current expression, according to the superposition method.

$$I_{on}(s) = I'(s) + I''(s) \tag{5.43}$$

where the expressions for the partial currents are:

$$I'(s) = \frac{V_g}{s^2 \cdot L} \tag{5.44}$$

$$I'(s) = \frac{L \cdot i_{\min}}{s \cdot L} = \frac{i_{\min}}{s} \tag{5.45}$$

Thus, the s-domain expression for inductor current during mode 1 is:

$$I_{on}(s) = \frac{V_g}{s^2 \cdot L} + \frac{i_{\min}}{s} \tag{5.46}$$

For mode 2 (*off* mode) the s-domain circuit, shown in Fig. 5.10, is similar to the mode 1 circuit for the buck converter.

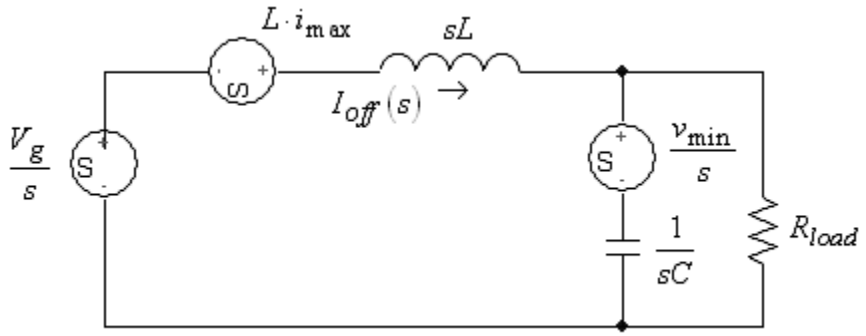

Figure 5.10: Boost converter, s-domain mode 2

Three sources drive the circuit, thus three partial currents describe the inductor current:

$$I_{off}(s) = I_1(s) + I_2(s) + I_3(s) \tag{5.47}$$

Employing superposition, the expressions for partial currents are determined:

$$I_1(s) = \frac{(R_{load} + 1) \cdot V_g}{\left(s^2 \cdot LCR_{load} + s \cdot L + R_{load}\right)} \tag{5.48}$$

$$I_2(s) = \frac{(s \cdot CR_{load} + 1) \cdot L \cdot i_{\max}}{\left(s^2 \cdot LCR_{load} + s \cdot L + R_{load}\right)} \tag{5.49}$$

$$I_3(s) = \frac{-(s \cdot LC + CR_{load}) \cdot v_{\min}}{\left(s^2 \cdot LCR_{load} + s \cdot L + R_{load}\right)} \tag{5.50}$$

The expression for s-domain inductor current, during mode 2 (*off* mode) is:

$$I_{off}(s) = \frac{(R_{load}+1)\cdot V_g + (s\cdot CR_{load}+1)\cdot L\cdot i_{\max} - (s\cdot LC + CR_{load})\cdot v_{\min}}{\left(s^2\cdot LCR_{load} + s\cdot L + R_{load}\right)} \qquad (5.51)$$

The inductor current waveform in time-domain is determined by applying the inverse Lapalce transform operator to Equations (5.46) and (5.51). This is possible only by knowing the peak and minimum values of inductor current and capacitor voltage, and the values of all components in the circuit.

5.4.3 Inductor current of buck-boost converter

During steady-state operation, the inductor current in buck-boost converter rises and decays exponentially about an average value. Finding the analytical expressions for inductor current during mode 1 and mode 2, determines an accurate Fourier-series model for the converter. The circuit complexity and variance from one mode to the other, requires analysis in the frequency domain. The s-domain circuit for mode 1 (*on* mode) is shown in Fig. 5.11, and is similar to mode 1 circuit for the boost converter. Hence, the s-domain expression for inductor current $I_{on}(s)$ during mode 1 is identical to that for boost converter:

$$I_{on}(s) = \frac{V_g}{s^2\cdot L} + \frac{i_{\min}}{s} \qquad (5.52)$$

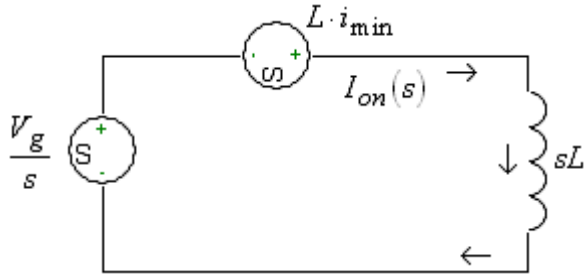

Figure 5.11: Buck-boost converter, s-domain mode 1

Mode 2 s-domain circuit is shown in Fig. 5.12, and is similar to that for the buck converter.

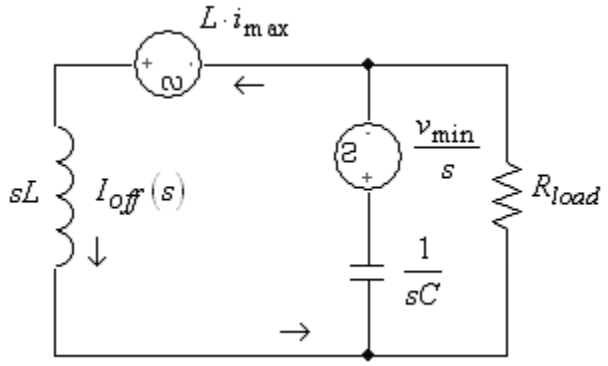

Figure 5.12: Buck-boost converter, s-domain mode 2

The expression for s-domain inductor current during mode 2, is similar to that of buck converter during the same mode:

$$I_2(s) = \frac{(s \cdot CR_{load} + 1) \cdot L \cdot i_{max} - (s \cdot LC + CR_{load}) \cdot v_{max}}{\left(s^2 \cdot LCR_{load} + s \cdot L + R_{load}\right)} \tag{5.53}$$

Determining the time-domain analytical expressions for inductor currents and converter output voltage is work intensive, requiring the aid of a computer, for a level of accuracy described by a higher-order harmonics. Thus, numerical analysis is accomplished through automatic computations of time-domain differential equations, using MATLAB.

5.5 Fourier-series Models of DC Power Systems

Impedances of NiCd batteries and DEFCs, covered in Chapter 7, are integrated in proposed models of DC power sources, and are shown in Figure 5.13 [77].

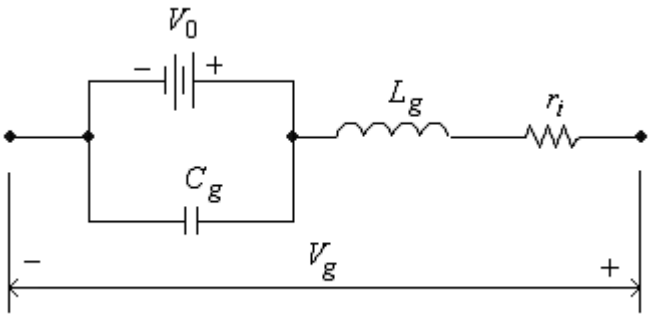

Figure 5.13: DC source equivalent circuit

The internal resistance of DC sources varies with frequency, and reaches a maximum at frequencies above 4 kHz. Below 4 kHz, the internal resistance of NiCd batteries varies nonlinearly from 0.1 Ω at 100 Hz, to 0.9 Ω at 4 kHz. The internal resistance of DEFCs varies nonlinearly over the entire frequency spectrum considered in this research. Approximate values of inductance and capacitance for NiCd battery and for DEFCs (mesh and foam), are derived in Sections 5.5.1 and 5.5.2, respectively.

5.5.1 Equivalent circuit of NiCd battery

The inductance of NiCd batteries is determined by applying a lower frequency signal (10 Hz) to the battery. The inductive reactance is approximately equal to the battery reactance at low frequencies, and was measured to be $X_L = 4.12\ m\Omega$. This value was used to calculate the inductive characteristic of the NiCd battery. At a frequency $f = 5.01\ kHz$, the NiCd battery reactance is zero. Thus the inductive reactance and capacitive reactance are equal. Thus, the battery capacitance is precisely determined.

$$L_{NiCd} = \frac{X_L}{2 \cdot \pi \cdot f} = \frac{4.12 \cdot 10^{-3}}{2 \cdot 3.14 \cdot 10} = 65.57 \quad \mu H$$

$$X_C = X_L \Rightarrow C_{NiCd} = \frac{1}{(2 \cdot \pi \cdot f)^2 \cdot L} = \frac{1}{(2 \cdot 3.14 \cdot 5010)^2 \cdot 65.57 \cdot 10^{-6}} = 15.4 \quad \mu F$$

5.5.2 Equivalent circuit of DEFC

Low frequency signal (10 Hz) is used to determine the DEFC inductive reactance, while high frequency signal is used to determine its capacitive reactance. Thus, both the inductance and capacitance of the DEFC can be evaluated. It is assumed that neither the capacitance, nor the inductance is a variable function of the applied-signal frequency. The internal resistance of DEFC varies with frequency, and is predicted by (2.8). The impedance data presented in Chapter 7 shows that DEFCs are characterized by internal capacitance, due to the dielectric properties of the electrolyte and/or fuel cell membranes, and by electrodes inductance.

$$L_{mesh} = \frac{X_L}{2 \cdot \pi \cdot f} = \frac{6.34 \cdot 10^{-3}}{2 \cdot 3.14 \cdot 10} = 100.9 \quad \mu H$$

$$L_{foam} = \frac{X_L}{2 \cdot \pi \cdot f} = \frac{3.73 \cdot 10^{-3}}{2 \cdot 3.14 \cdot 10} = 59.3 \quad \mu H$$

Direct ethanol fuel cell (DEFC) is characterized by larger inductive reactance, X_L, than capacitive reactance, X_C. Thus, the fuel cell reactance is positive, for mesh- and foam-type DEFC, over the frequency range considered in this research, as shown in Figs. 7.7 and 7.8. Determining DEFC capacitance is preceded by finding the capacitive reactance of the fuel cell.

$$X_C(f) = X(f) - X_L(f) \tag{5.54}$$

$$C_{mesh} = \frac{-1}{\left(2 \cdot \pi \cdot 10^5\right) \cdot X_C(f)} = \frac{-1}{\left(2 \cdot \pi \cdot 10^5\right) \cdot \left(0.0133 - 2 \cdot \pi \cdot f \cdot 100.9 \cdot 10^{-6}\right)} = 251.5 \quad nF$$

$$C_{foam} = \frac{-1}{\left(2 \cdot \pi \cdot f\right) \cdot X_C(f)} = \frac{-1}{\left(2 \cdot \pi \cdot 10^5\right) \cdot \left(0.00779 - 2 \cdot \pi \cdot 10^5 \cdot 59.3 \cdot 10^{-6}\right)} = 42.7 \quad nF$$

The inductances and capacitances determined for the DEFC-mesh and DEFC-foam are approximate values. Due to their variations with frequency, precise values of either inductance or capacitance for the fuel cells are not possible.

5.5.3 Buck converter-driven DEFC system

Integrating the fuel cell model proposed in the buck converter system of Section 5.1.1, the corresponding s-domain circuit for mode 1 (*on* mode) is shown in Figure 5.14. The fuel cell voltage, $V_g(s)$, is a function of the output voltage, $V_C(s)$, and of the fuel cell impedance, represented by the variable resistor-inductor-capacitor, r_i, L_g, C_g, network. Time-domain expression of DEFC voltage during mode 1 is obtained from the inverse Laplace transformation of $V_g(s)$.

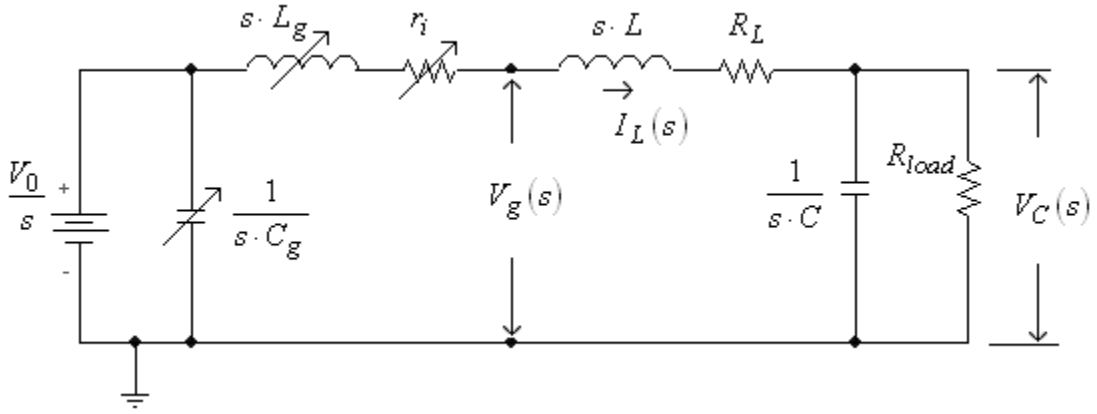

Figure 5.14: DEFC-buck converter mode 1

The s-domain circuit in Figure 5.14 is described by:

$$\frac{V_0}{s} = \left(s \cdot L_g + r_i + s \cdot L + R_L\right) \cdot I_L + V_C \tag{5.55}$$

Therefore, the s-domain expression for the inductor current during mode 1 is:

$$I_L(s) = \frac{V_0}{s} - \left(s \cdot L_g + r_i\right) \cdot \left[\frac{V_0}{s \cdot \left(s \cdot L_g + r_i + s \cdot L + R_L\right)} - \frac{V_C}{\left(s \cdot L_g + r_i + s \cdot L + R_L\right)} \right] \tag{5.56}$$

Knowing that the fuel cell output voltage is described by:

$$V_g(s) = \left(s \cdot L + R_L\right) \cdot I_L(s) + V_C \tag{5.57}$$

the s-domain expression for the fuel cell voltage is:

$$V_g(s) = \left(\frac{V_0}{s}\right) - \left(\frac{s \cdot L_g \cdot V_0}{s \cdot \left(s \cdot \left(L_g + L\right) + \left(r_i + R_L\right)\right)}\right) - \left(\frac{r_i \cdot V_0}{s \cdot \left(s \cdot \left(L_g + L\right) + \left(r_i + R_L\right)\right)}\right) + \left(\frac{s \cdot L_g \cdot V_C}{\left(s \cdot \left(L_g + L\right) + \left(r_i + R_L\right)\right)}\right) - \left(\frac{r_i \cdot V_C}{\left(s \cdot \left(L_g + L\right) + \left(r_i + R_L\right)\right)}\right) \quad (5.58)$$

The time-domain expression of fuel cell output voltage during mode 1 is obtained after substituting the numerical values in (5.60).

During mode 2 (*off* mode), the fuel-cell output of DEFC-buck converter system is equal to the fuel-cell open voltage, V_0, since there is no current associated with the internal resistance, inductance, and capacitance.

5.5.4 Boost converter-driven DEFC system

The s-domain circuit during mode 1 (*on* mode) is comprised by the fuel cell, switching transistor, and energy-storage inductor *L*, shown in Figure 5.15.

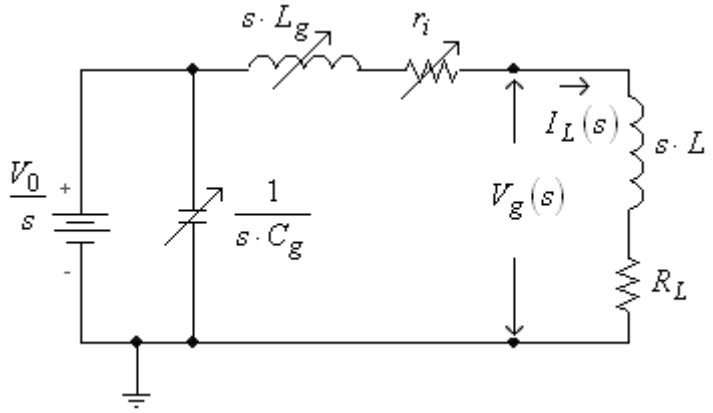

Figure 5.15: DEFC-boost converter mode 1

The equation describing the s-domain circuit is:

$$\frac{V_0}{s} = \left(s \cdot L_g + r_i + s \cdot L + R_L\right) \cdot I_L \quad (5.59)$$

The s-domain inductor current during mode 1 of the boost converter is:

$$I_L(s) = \frac{V_0}{s \cdot \left(s \cdot \left(L_g + L\right) + \left(r_i + R_L\right)\right)} \tag{5.60}$$

Thus, the fuel-cell output voltage in the s-domain during mode1 of the boost converter is:

$$V_g(s) = \left(s \cdot L + R_L\right) \cdot I_L(s) \tag{5.61}$$

$$V_g(s) = \frac{L \cdot V_0}{\left(s \cdot \left(L_g + L\right) + \left(r_i + R_L\right)\right)} + \frac{R_L \cdot V_0}{s \cdot \left(s \cdot \left(L_g + L\right) + \left(r_i + R_L\right)\right)} \tag{5.62}$$

The expression of fuel-cell output voltage during mode 2 (*off* mode) of the boost converter, is identical to the fuel-cell output voltage during mode 1 of the buck converter, and is presented in (5.60).

5.5.5 Buck-boost converter-driven DEFC system

Mode 1 (*on* mode) of DEFC-buck-boost converter system is identical to that of the DEFC-boost converter system. Thus, the s-domain equation (5.64) describes the fuel cell output voltage, V_g, during mode 1.

During mode 2 (*off* mode), the circuit of DEFC-buck-boost converter system is identical to that of DEFC-buck converter system. Thus, the output voltage of the fuel cell is:

$$V_g(s) = \frac{V_0}{s} \tag{5.63}$$

All output voltage expressions for DEFC, in any converter interface, are applicable to the NiCd battery systems. However, the internal resistance, inductance, and capacitance of DEFCs and NiCd battery, are variable and function of the switching frequency.

CHAPTER 6 - Fourier-Series Models of DC Systems

DC power sources are characterized by internal resistance and capacitance, quantities dependent on the frequency of the measuring signal. In practical applications, the electric power management, i.e., voltage and current regulation is accomplished through sequential switching of the DC power sources at variable switching frequencies. With the DC power source interfaced to a sequential switching circuit, a square wave pulse voltage is produced, thus a periodic current waveform is generated by the semiconductor switches through the inductor.

In this chapter, Fourier-series models of DC–DC converters are numerically evaluated through MATLAB simulations. Fourier-series models developed in Chapter 5 are expanded to include the DC power source characteristics, for two types of DC power systems: NiCd storage batteries and direct ethanol fuel cells. The MATLAB programs developed for nine types of DC converter-controlled systems are approximations of the actual DC systems. The MATLAB scripts implementing the Fourier-series models of DC systems in this chapter are shown in Appendix A.

6.1 Numerical evaluation of Fourier-series models for DC–DC converters

The Fourier-series models developed in Chapter 5 were evaluated numerically, and the average output voltage was compared to the expected value, as determined by the small-signal models in Chapter 4. Throughout section 6.1, the DC power source considered is an ideal voltage source.

6.1.1 *Numerical evaluation of buck converter model*

For an ideal voltage source V_g, with a nominal constant value of 2.6 V, the Fourier-series model for buck converter is evaluated at three distinct duty cycles: 50%, 65%, and 80%. The average output voltage is determined by (4.55), and is tabulated in Table 7.

Table 7: Buck converter output voltage

Duty cycle (%)	Input voltage (V)	Output voltage (V)
50	2.6	1.3
65	2.6	1.69
80	2.6	2.08

During transistor operation, the voltage drop across free wheeling diode is described by a square wave. Thus, the buck converter is a voltage-driven regulator. The peak diode voltage is equal to the voltage source magnitude, and the minimum diode voltage is zero, corresponding to the *off* status of switching transistor. The equivalent circuit for buck converter is shown in Fig. 6.1, where the voltage source and switching transistor were replace by a square-wave voltage source.

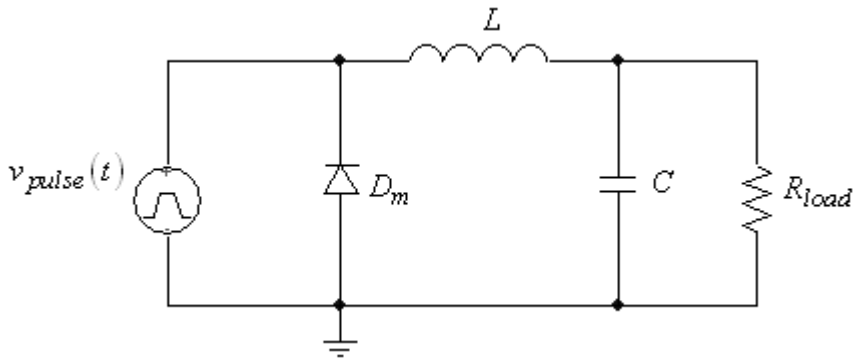

Figure 6.1: Fourier-series equivalent of buck converter

Shown in Figures 6.2 and 6.3, the output voltages, and inductor currents at duty cycles 50%, 65%, and 80% for a switching frequency of 200 Hz, are computed from the system of differential equations in (6.4).

$$\begin{cases} \dfrac{di_L(t)}{dt} = \dfrac{-R_{load}}{L} i_L(t) + \dfrac{C_0}{L} + \dfrac{C_1}{L}\sin(\omega_1 t + \varphi_1) + \ldots + \dfrac{C_{21}}{L}\sin(\omega_{21} t + \varphi_{21}) \\ \dfrac{dv_C(t)}{dt} = \dfrac{1}{C} i_L(t) - \dfrac{1}{R_{load} C} v_C(t) \end{cases} \tag{6.1}$$

The average capacitor voltage, v_C, is obtained by considering only the DC bias voltage, C_0, in the differential equation of system (6.1). However, for a good approximation, the voltage across diode is described by the DC bias and by a sum of 21 harmonics. Thus, the switching operation can be mathematically approximated as a square wave voltage across the free wheeling diode.

Figure 6.2 presents the output voltage of an ideal-source buck converter operating at a switching frequency of 200 Hz, and three distinct duty cycles: 50%, 65%, and 80%.

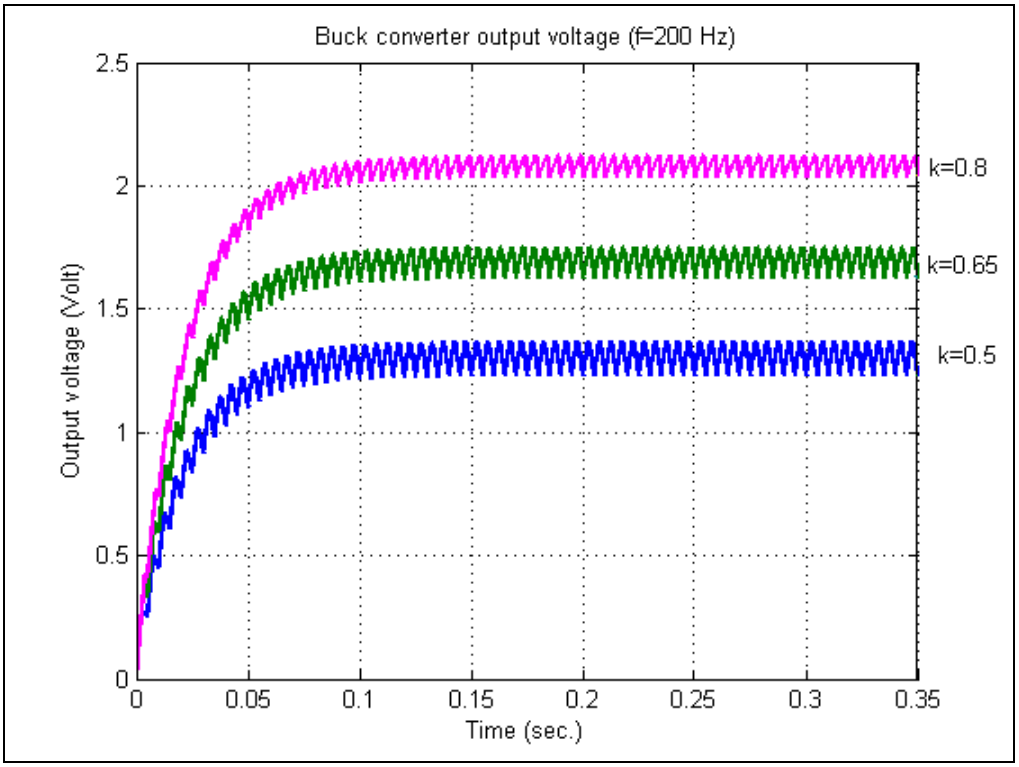

Figure 6.2: Buck converter output voltage

The output voltage ripple is characterized by a frequency equal to the switching frequency $f = 200\ Hz$ and of variable peak-to-peak amplitude. At a switching frequency of 200 Hz, the output voltage-ripple increases at 65% duty cycle as compared to the 50% duty cycle. This is due to the discontinuous conduction mode (DCM) of operation during both duty cycles, as shown in Fig. 6.2.

Buck converter operation at 200 Hz switching frequency, and 80% duty cycle, is characterized by continuous conduction mode (CCM) of operation, as shown by the purple trace in Fig. 6.3. Thus, the output voltage is characterized by lower ripple content at 80 % duty cycle as compared to 50% and 60% duty cycles. At switching frequency of 200 Hz, the output voltage and inductor current, for buck converter Fourier-series model, are in agreement with its large signal and small signal models.

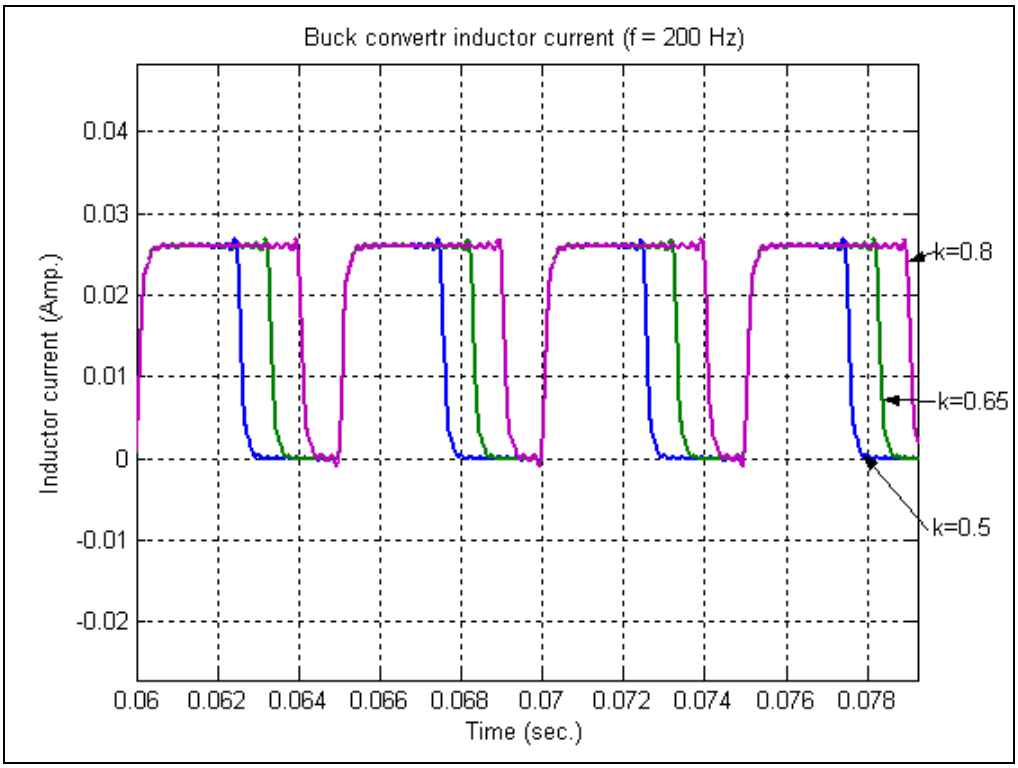

Figure 6.3: Buck converter, inductor current, f = 200 Hz

Increasing the switching frequency to 500 Hz and 1 kHz, respectively, the output voltage is characterized by lower ripple, as shown in Fig. 6.4 and Fig. 6.6. Altering switching frequency, while maintaining the duty cycle, has no effects on the average

output voltage. As predicted, and in agreement with the large signal and small signal models, the output ripple voltage decreases with the increase of switching frequency. Output voltages and inductor currents, described by the Fourier-series model of the buck converter are accurately represented for duty cycles of 50%, 65%, and 80%, at switching frequencies of 200 Hz, 500 Hz, and 1 kHz.

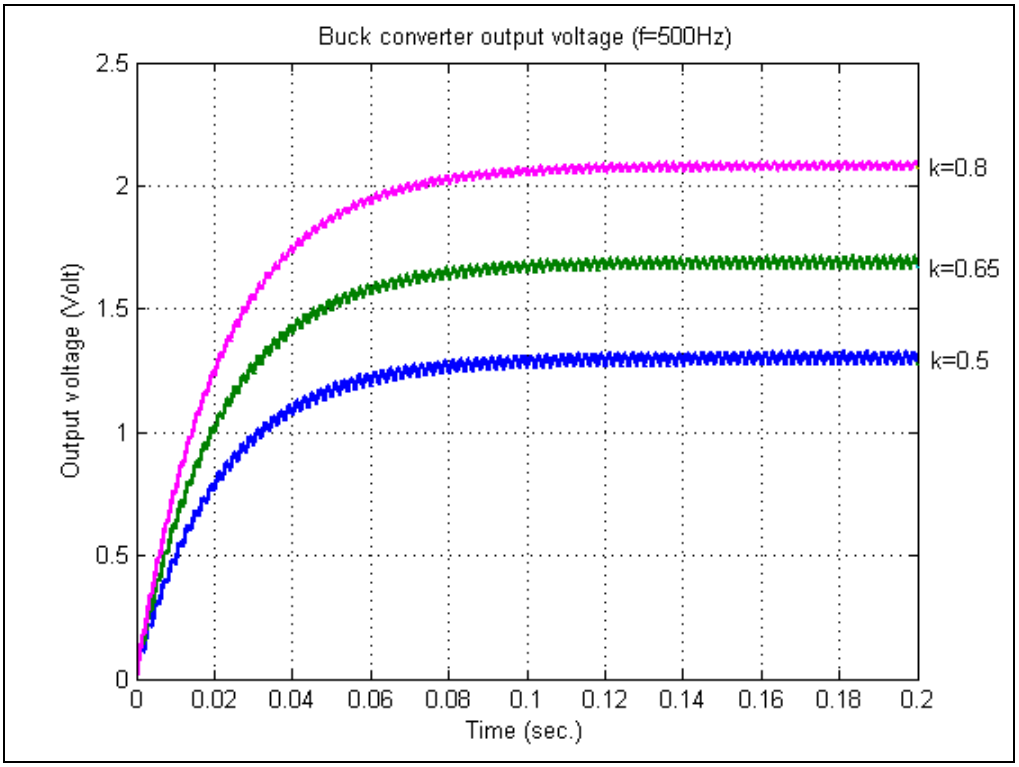

Figure 6.4: Buck converter output characteristics, f = 500Hz

Output voltage waveshapes, for buck converter Fourier-series model, at 500 Hz switching frequency, shown in Fig. 6.5, accurately describe the average output voltage and the AC ripple for all three duty cycles considered.

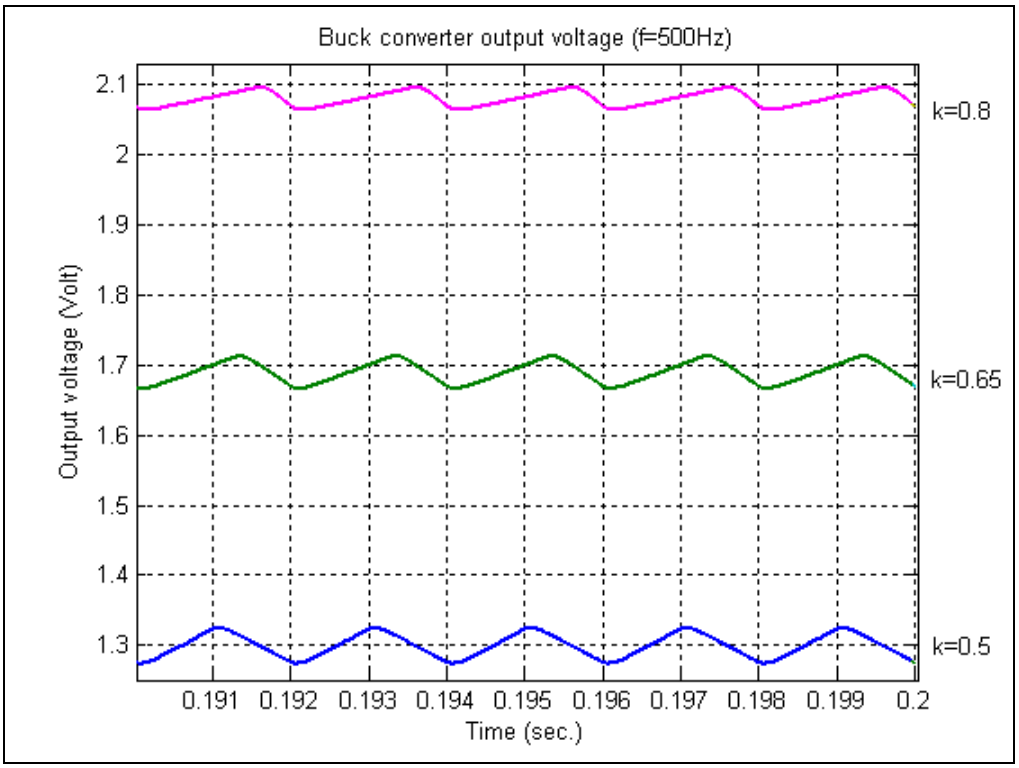

Figure 6.5: Buck converter output voltage waveshapes

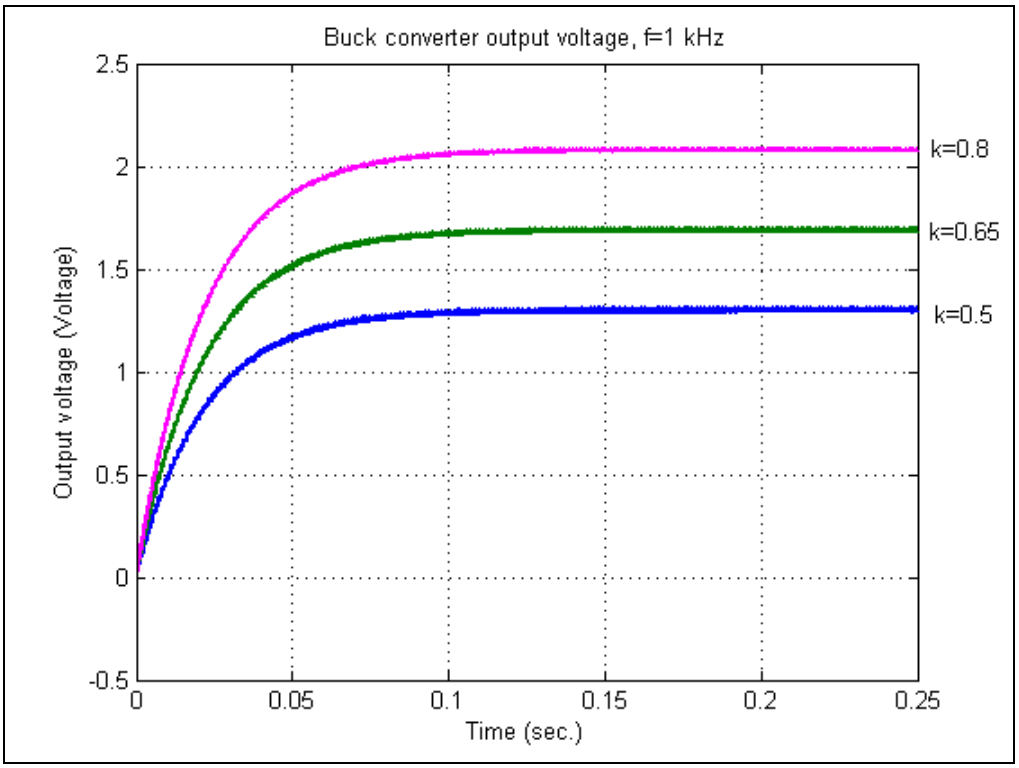

Figure 6.6: Buck converter output voltage, f=1 kHz

Increasing switching frequency parameter, in the MATLAB script, presented in Appendix A1, results in lower ripple voltage, as predicted. Inductor current, for switching frequency of 1 kHz, at 50%, 65%, and 80% duty cycle ,shown in Fig. 6.7, describes a continuous conduction mode (CCM) for all three duty cycles, as compared with the case of 200 Hz switching frequency, Fig. 6.3. Thus, the Fourier-series model of buck converter accurately describes the conduction mode of a particular buck converter, i.e., CCM or DCM.

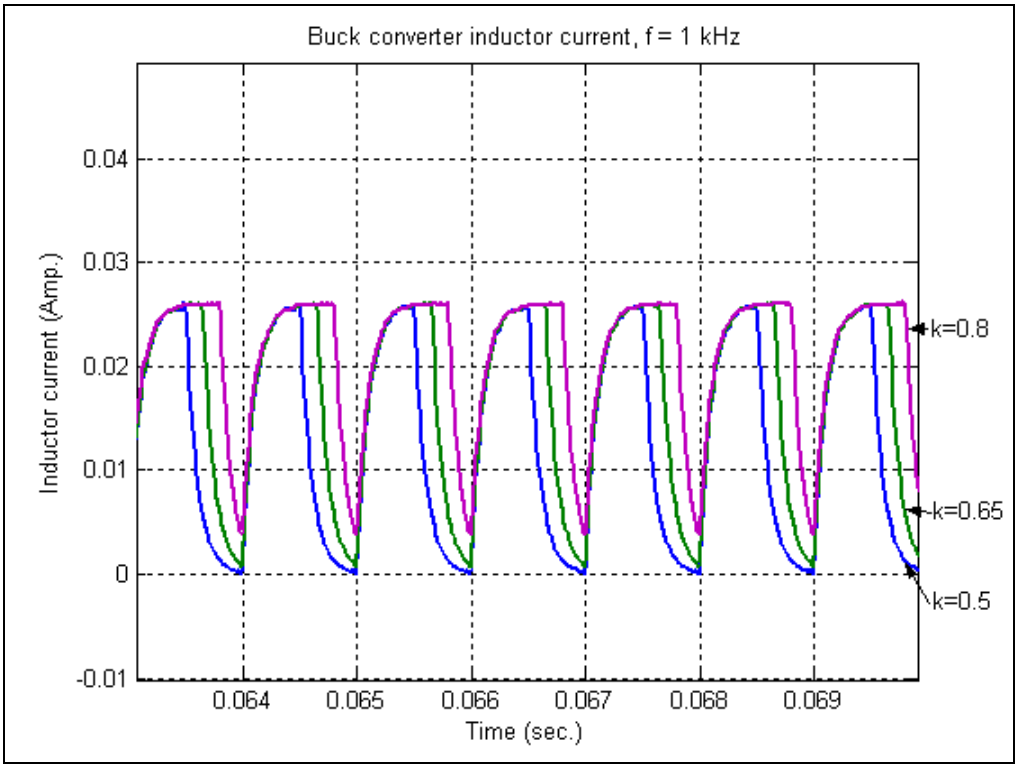

Figure 6.7: Buck converter, inductor current, f = 1 kHz

6.1.2 Numerical evaluation of boost converter model

For an ideal voltage source V_g, with a nominal constant value of 2.6 V, the Fourier-series model for boost converter is evaluated at three distinct duty cycles: 50%,

65%, and 80%. The average output voltage is determined by (4.55), and is tabulated in Table 8.

Table 8: Boost converter output voltage

Duty cycle (%)	Input voltage (V)	Output voltage (V)
50	2.6	5.2
65	2.6	7.428
80	2.6	13.0

Boost converter model is simulated with identical value components as used in section 6.1.1. The evaluation of boost converter Fourier-series model is accomplished at switching frequencies: 200 Hz, 500 Hz, and 1 kHz. As compared to buck converter equivalent circuit (Fig. 6.1), in the boost converter equivalent circuit, the switching transistor, and free wheeling diode operation is emulated by a pulse-current source, as shown in Fig. 6. 8.

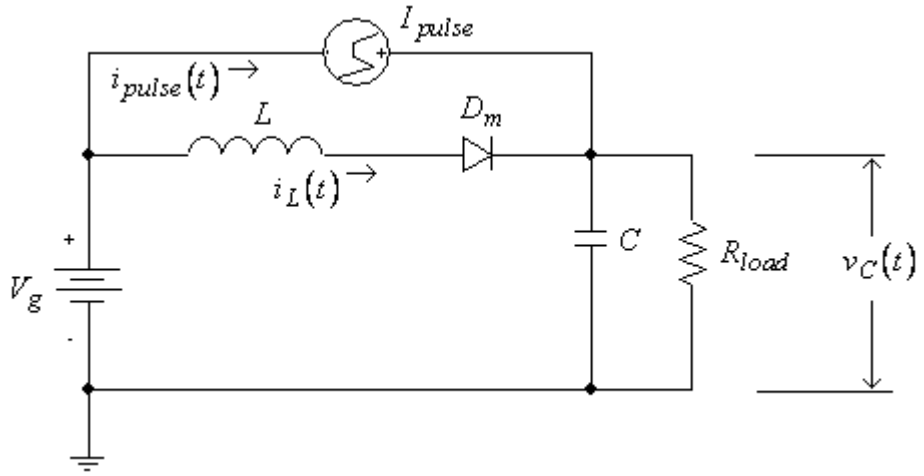

Figure 6.8: Fourier-series equivalent of boost converter

Boost converter output voltage is determined by the diode current, and by the voltage source value. Thus, the boost converter is a voltage-and-current driven regulator. While the voltage input remains constant, the current waveshape varies with the duty cycle and with switching frequency. Inductor current of the boost convert does not decrease to a zero value. Figure 6.9 shows the output voltage of the boost converter

operating at a switching frequency f =*200 Hz*, for the selected duty cycles. The corresponding inductor current waveshapes are shown in Fig. 6.10.

The input current waveshape is computed using *R-L* driven, and *R-L* natural response concepts. However, during *on* time, resistance *R* is equal to the inductor copper resistance, r_L, while during *off* time, resistance *R* is equal to the sum of inductor copper resistance and load resistance.

$$i_L(t_{on}) = \frac{1}{L} \cdot \left(V_g - r_L \cdot I(0)\right) \cdot e^{\left(\frac{-r_L}{L}\right) \cdot t} \tag{6.2}$$

$$i_L(t_{off}) = I_{\max} \cdot e^{\left(\frac{-R_{load}}{L}\right) \cdot t} \tag{6.3}$$

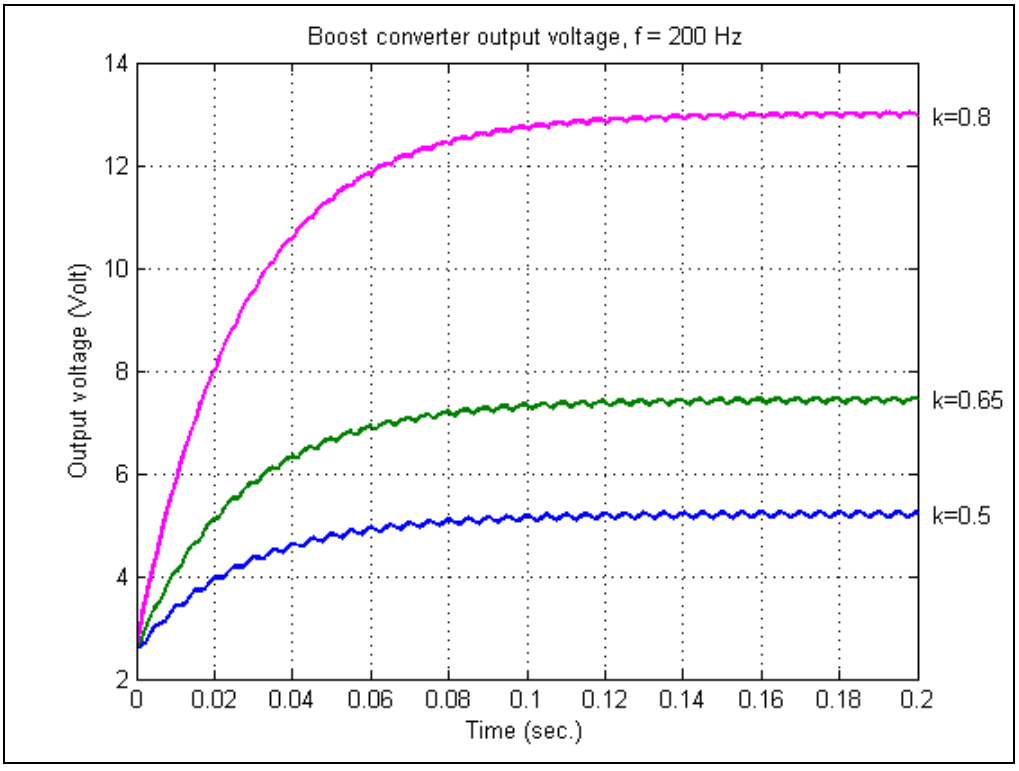

Figure 6.9: Boost converter output voltage, f =200 Hz

For a given duty cycle, boost converter output voltage has a smaller peak-to-peak ripple voltage, as compared to buck converter output voltage operating at identical duty cycle and switching frequency.

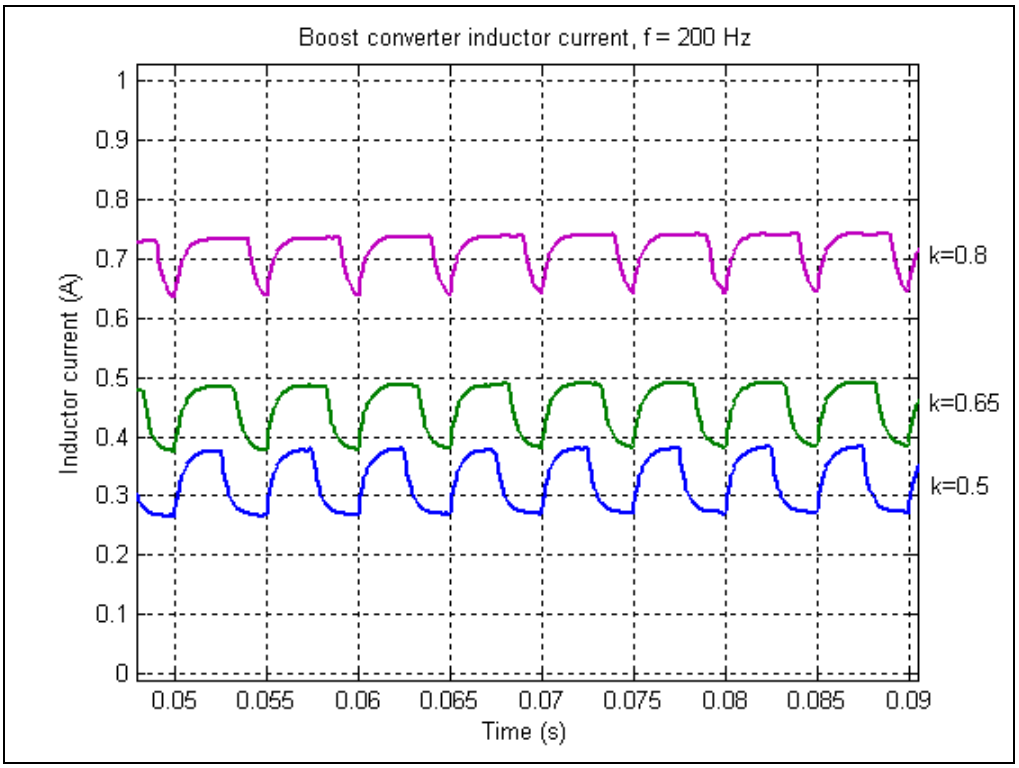

Figure 6.10: Inductor current of boost converter at f = 200 Hz

Figure 6.10 presents the inductor currents of a boost converter, modeled as Fourier-series, operating at 200 Hz switching frequency, and three distinct duty cycles: 50%, 65%, and 80%. Since none of the currents ever reaches a zero value, it is concluded that the boost converter operates in continuous conduction mode (CCM). At 50% duty cycle, the inductor current plot is symmetrical about an average value. It is determined, by inspection, that the average inductor currents are proportional to their respective duty cycle regimes.

Boost converter operation at a switching frequency of *1 kHz* is characterized by lower ripples, compared to operation at *200 Hz*, as shown in Fig. 6.11.

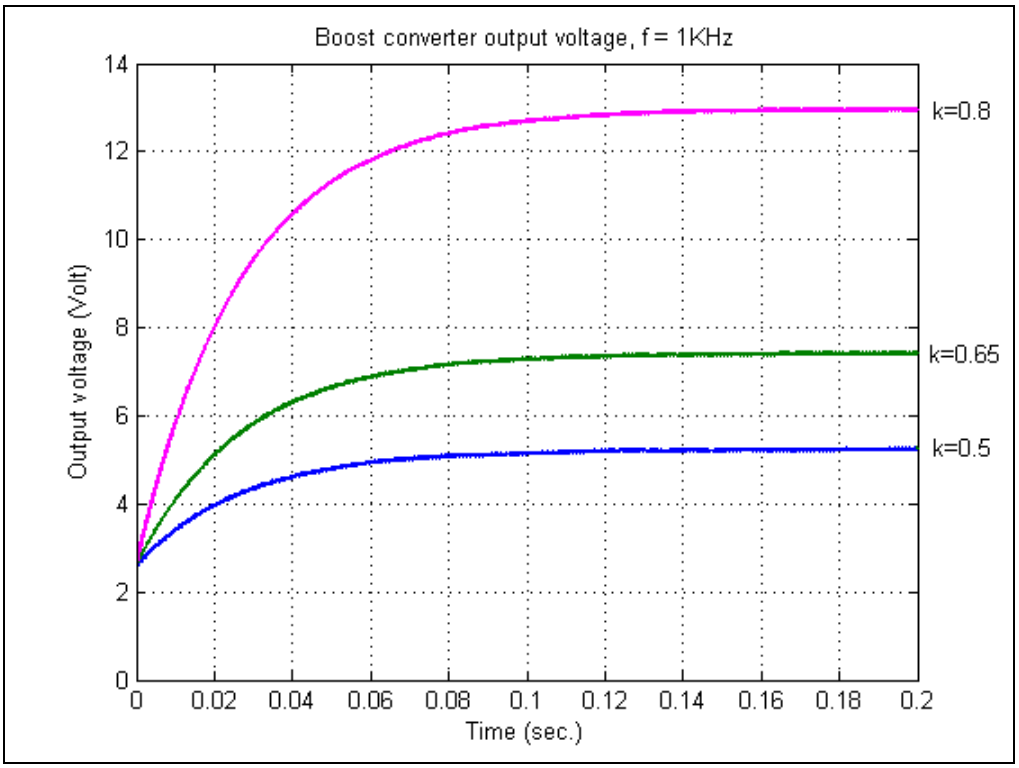

Figure 6.11: Boost converter output voltage, f = 1 kHz

6.1.3 Numerical evaluation of buck-boost converter model

Using the same component values employed in boost converter evaluations, the Fourier-series buck-boost converter model evaluation is performed at three duty cycles: 50%, 65%, and 80%, and at three switching frequencies: 200 Hz, 500 Hz, and 1 kHz. The average output voltage of buck-boost converter is determined by (4.78), and is recorded in Table 9.

Table 9: Buck-boost converter output voltage

Duty cycle (%)	Input voltage (V)	Output voltage (V)
50	2.6	−2.6
65	2.6	−3.9
80	2.6	−10.4

The equivalent circuit for the Fourier-series model of buck-boost converter is shown in Fig. 6.12, where the current source emulates the switching transistor operation.

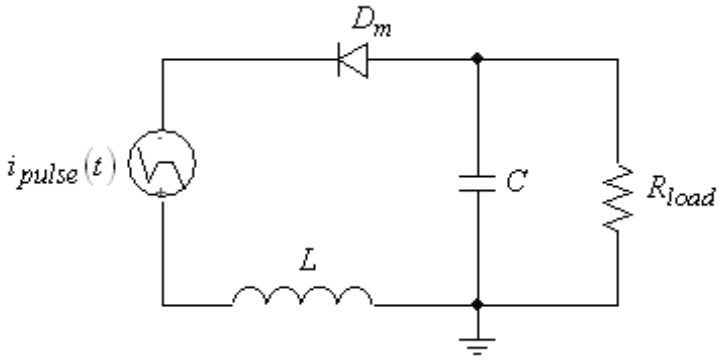

Figure 6.12: Fourier-series equivalent of buck-boost converter

Buck-boost converter operation is characterized by an inverted polarity of the output voltage. Shown in Fig. 6.13 and 6.16, the output voltage for buck-boost converter Fourier-series model, obtained through MATLAB simulations, exhibits the inverted polarity and the predicted average values. Graphical representations of the Fourier-series model output voltage, shown in Fig. 6.14, describe an increase of voltage ripple with the increase of duty cycle. Assuming continuous conduction mode of operation, the inductor current never reaches zero value, as shown in Fig. 6.15.

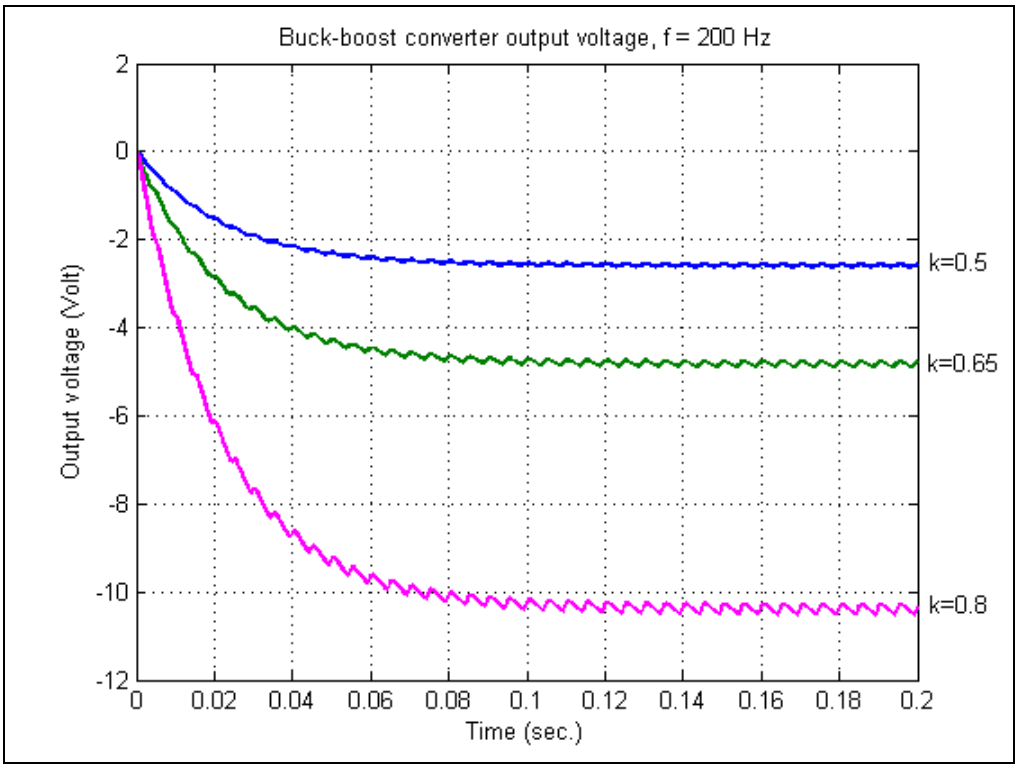

Figure 6.13: Buck-boost converter output voltage at f = 200 Hz

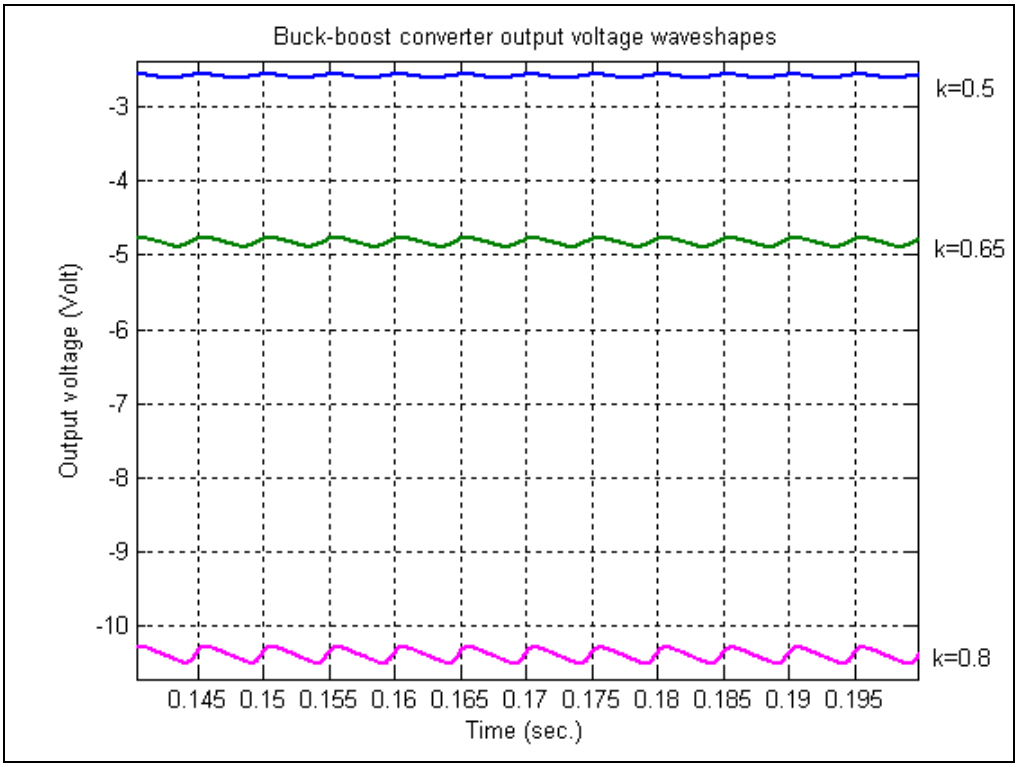

Figure 6.14: Output voltage waveshapes of buck-boost converter

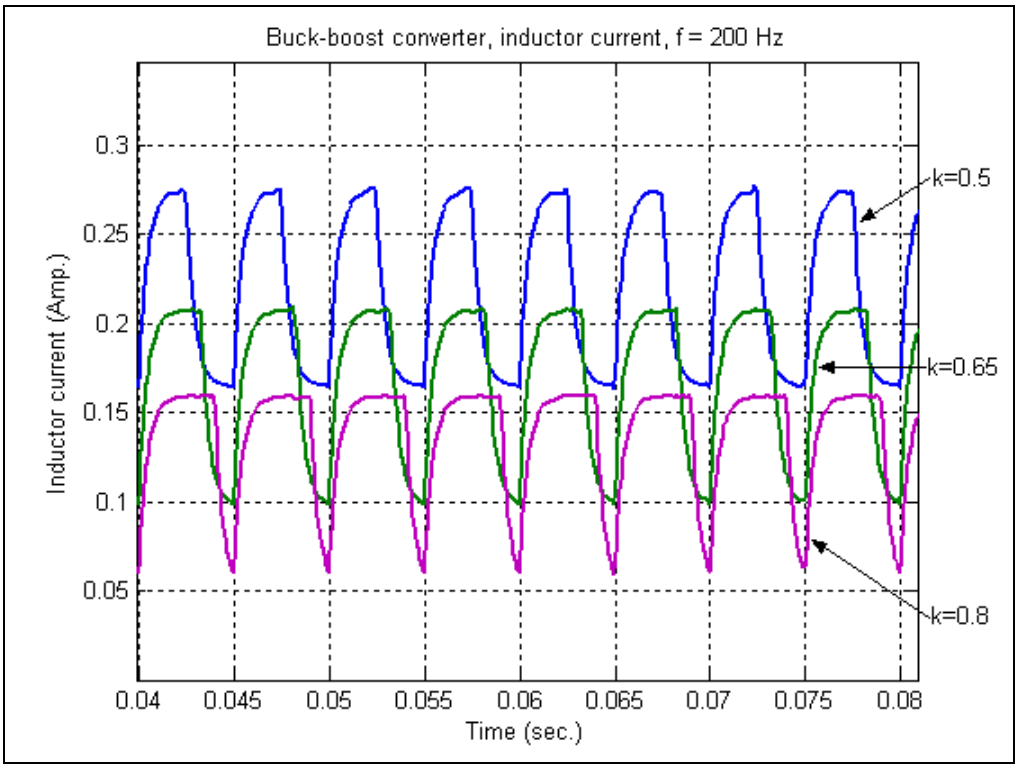

Figure 6.15: Inductor current waveshapes for buck-boost converter

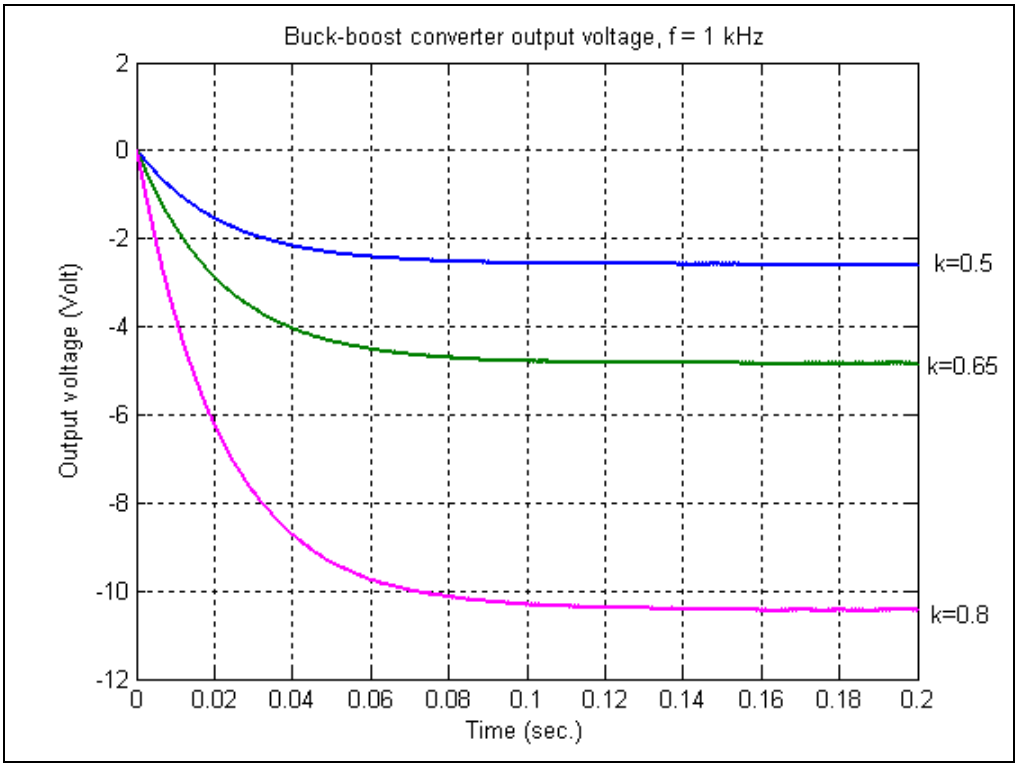

Figure 6.16: Output voltage of buck-boost converter at f = 1 kHz

6.2 DC–DC converter-driven power systems

The *I-V* characteristic of any DC power source contains information on the electrochemical process within the source. It relates the current delivered by the DC power source to its voltage, while under loading conditions. In general, the open-circuit voltage of a DC power source is larger than the load voltage. Due to the electrochemistry within a power source, the load current is not obtained by Ohm's law. The voltage at the power source terminals is not constant, and varies with the load current. The impedance of any DC power source is characterized by a real component, thus describing the ohmic internal resistance, and by an imaginary component, describing the reactance of the source. The real component, *Re(Z)*, and the imaginary component, *Im(Z)*, of DC sources impedance determine a phase angle between the source voltage and current through the source. Therefore, the Fourier-series representation of DC–DC converter-driven power systems, will account for the impedance of the DC source. The phase angle is given by:

$$\theta_n = \tan^{-1}\left(\frac{\mathrm{Im}(Z_n)}{\mathrm{Re}(Z_n)}\right) \tag{6.4}$$

Thus, each harmonic sine wave, in the Fourier-series representation, induces unique phase angles to the DC source impedance. Consequently, during sequential switching, the source impedance is "seen" by the converter as dependent on both the frequency and duty cycle.

6.2.1 Impedances of DC Power Sources

DC power sources convert chemical energy into electric energy through an electrochemical reaction. The space between anode and cathode is filled by the electrolyte. Due to electrolytes chemistry, size, and geometrical configuration of electrodes, each type of DC power source is characterized by particular internal

resistances. DC power sources, encountering AC conditions, exhibit variable impedances, function of signal frequency.

6.2.2 NiCd battery impedance

The impedances of three pairs of Ni-Cd battery, series connected, were measured. Within a frequency range of 0.1 Hz to approximately 3 kHz, the impedance of Ni-Cd battery is nonlinear, reaching a magnitude of 0.9 Ω. At frequency values exceeding 3 kHz, the impedance remains constant. Figure 6.17 shows the NiCd battery impedance, as a function of frequency, over a signal frequency range from *0.1 Hz* to *10 kHz*. Nickel-cadmium battery complex impedance: reactance, *Im(Z)*, as a function of resistance, *Re(Z)*, is shown in Fig 6.18.

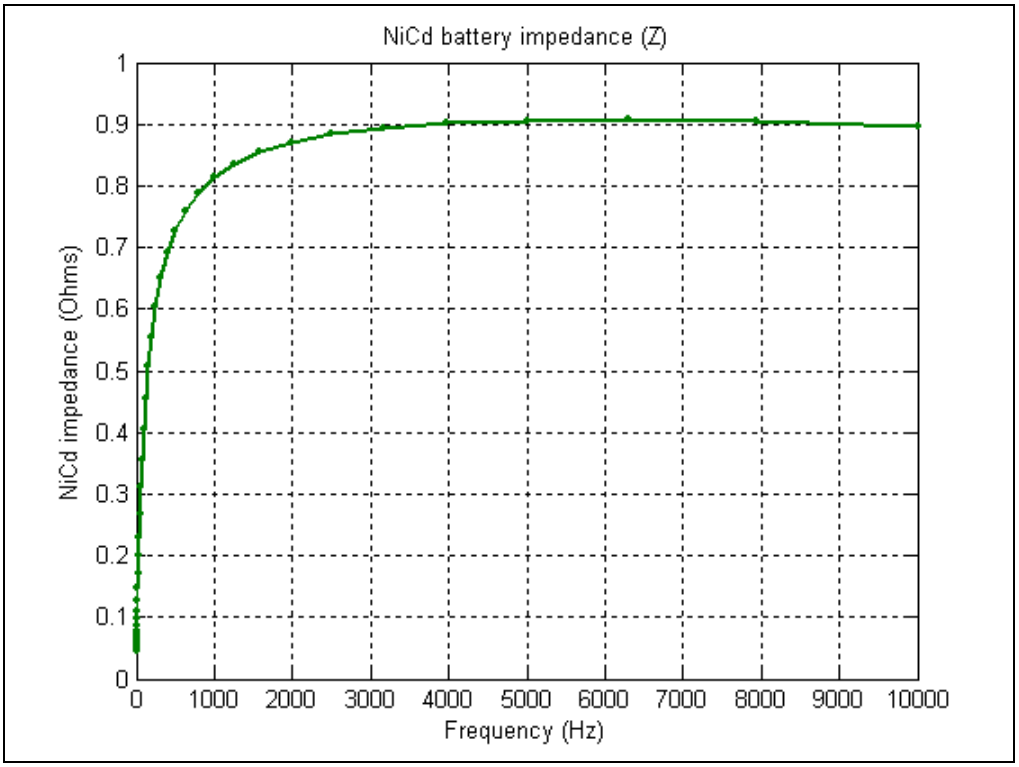

Figure 6.17: NiCd battery impedance (Z)

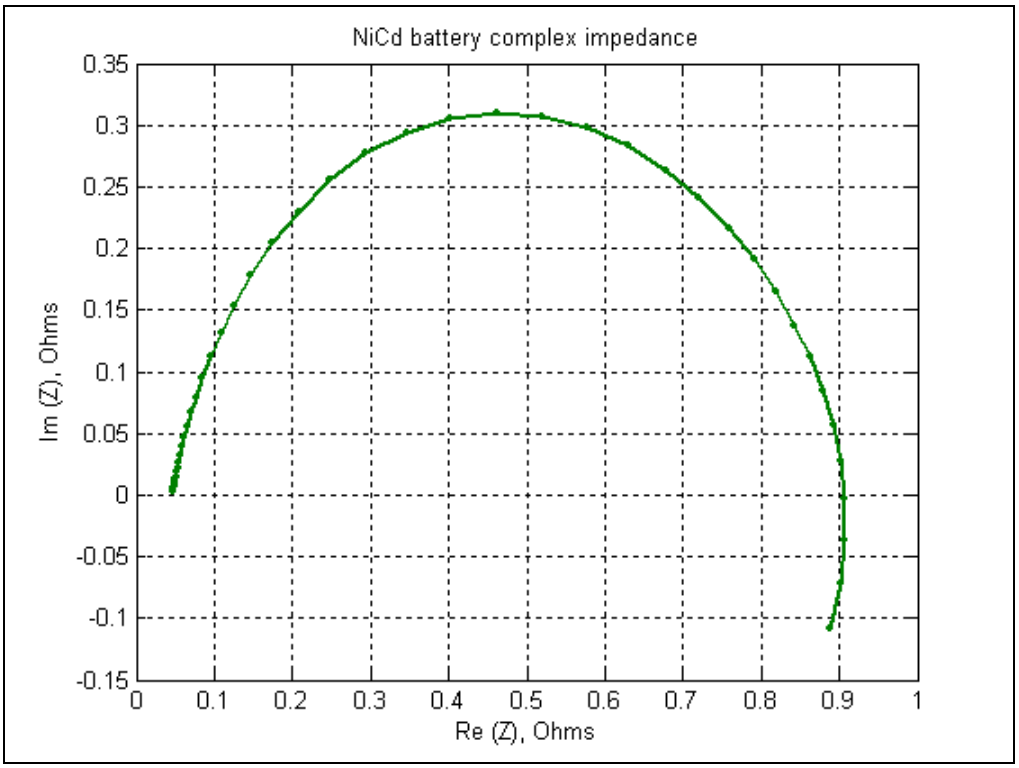

Figure 6.18: NiCd battery complex impedance

6.2.3 Direct Ethanol Fuel Cell Impedance

The impedances of DEFC-mesh and DEFC-foam were computed from the complex impedance values for each fuel cell. Measurements conducted at CAVS-Mississippi State University, using the Solartron equipment were compiled using MATLAB script.

Impedance plots for both DEFC-mesh and DEFC-foam in Fig. 6.19 show a nonlinearity dependence to signal frequency, and increasing dissimilarity of impedance magnitudes with the increase of frequency.

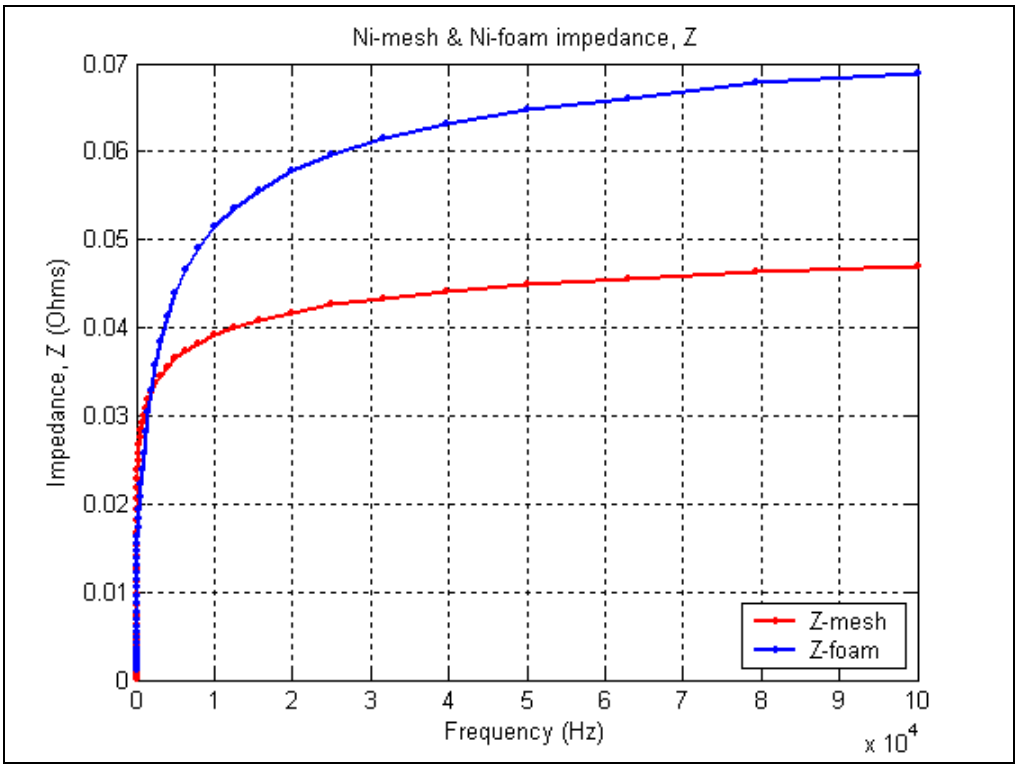

Figure 6.19: DEFC-mesh & foam impedances

Identical in size, DEFC-mesh and DEFC-foam are characterized by dissimilar complex impedances. The impedance plots of DEFC-mesh and DEFC-foam, shown in Fig. 6.20, suggest different responses to an AC signal of variable frequency. Impedance magnitudes, as a function of frequency, are different for the two fuel cells. The complex impedances of the two fuel cells, shown in Fig 6.21, determine inductor currents of magnitudes and phase angles different for the two DEFC power sources. As a consequence, the power transferred from DEFC source will exhibit different values at any particular switching frequency and duty cycle, for the two DEFC systems.

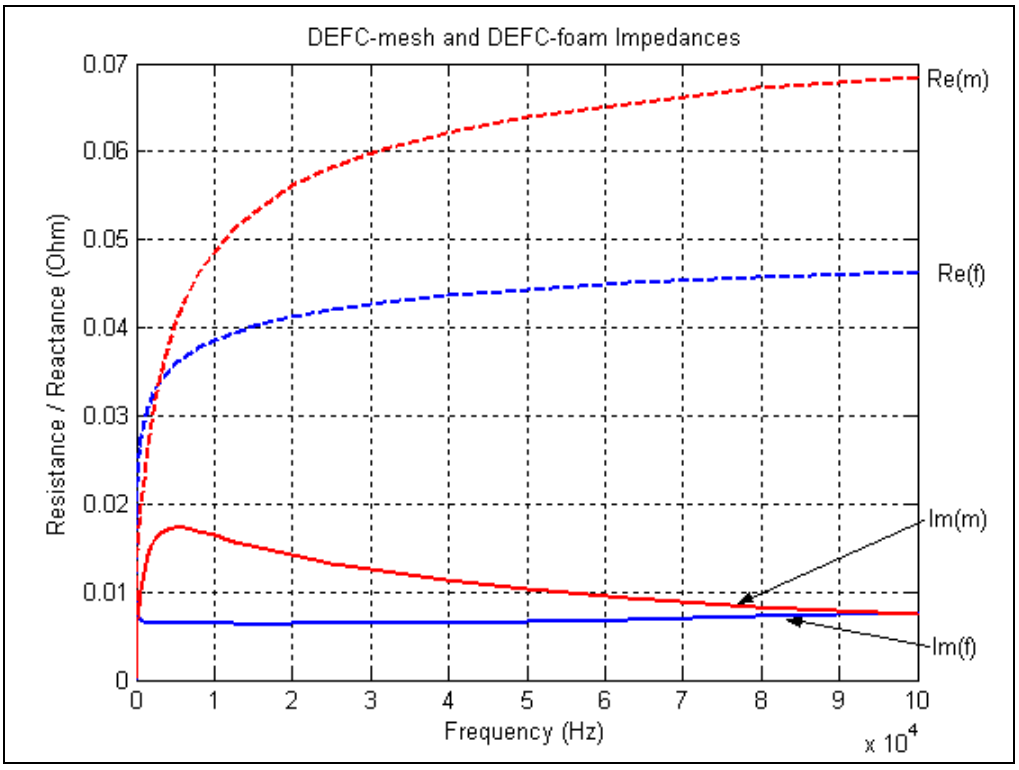

Figure 6.20: Impedances of DEFC-mesh and DEFC-foam

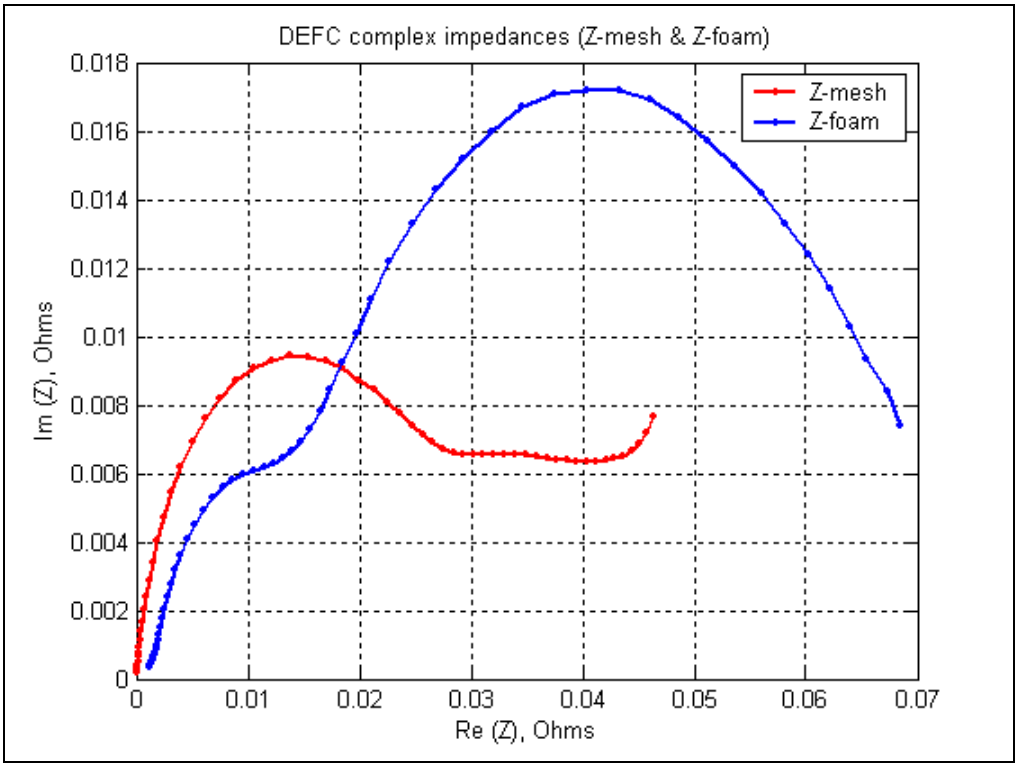

Figure 6.21: DEFC Ni-mesh & Ni-foam complex impedances

6.2.4 Buck converter-driven NiCd battery power systems

The polarization curve of Ni-Cd battery describing its voltage-current characteristics is shown in Fig. 6.22. From the polarization curve in Fig 6.22, the voltage-current characteristic of NiCd battery is described by the battery output voltage function of load current:

$$V_{NiCd} = 2.776 - 0.263 \cdot I_{NiCd} \tag{6.5}$$

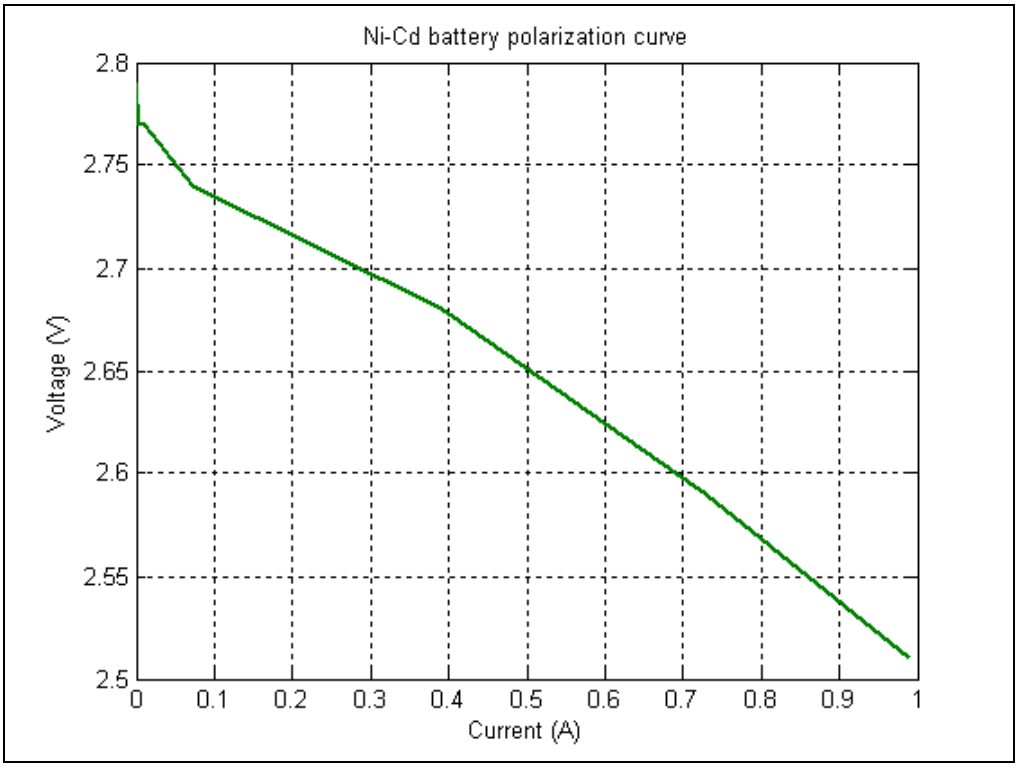

Figure 6.22: Ni-Cd battery polarization curve

Equation 6.5 expresses the voltage-current characteristics, where the current coefficient is the internal resistance of NiCd battery, and is 0.263 Ω.

During mode 1 (on) of the NiCd-buck converter system, the voltage at the battery terminals is equal to the open-circuit voltage, minus the voltage drop across NiCd battery internal resistance:

$$V_{on} = \left(1 - \frac{r_{source}}{Z_{Total}}\right) \cdot V_0 \tag{6.6}$$

where, the circuit impedance, Z_{Total}, during mode 1 (on) is:

$$Z_{Total} = \sqrt{\mathrm{Re}\left(Z_{Total}\right)^2 + \mathrm{Im}\left(Z_{Total}\right)^2} \tag{6.7}$$

Considering the source internal resistance only, the expressions for the real part and the imaginary part of the impedance are:

$$\mathrm{Re}\left(Z_{Total}\right) = r_{source} + r_L + \frac{R_{load} \cdot \left(\frac{1}{\omega_0 \cdot C}\right)}{\sqrt{R_{load}^2 + \left(\frac{1}{\omega_0 \cdot C}\right)^2}} \cdot \cos\left(-\frac{\pi}{2} + \arctan\left(\frac{1}{\omega_0 \cdot C \cdot R_{load}}\right)\right) \tag{6.8}$$

$$\mathrm{Im}\left(Z_{Total}\right) = X_{source} + \omega_0 \cdot L + \frac{R_{load} \cdot \left(\frac{1}{\omega_0 \cdot C}\right)}{\sqrt{R_{load}^2 + \left(\frac{1}{\omega_0 \cdot C}\right)^2}} \cdot \sin\left(-\frac{\pi}{2} + \arctan\left(\frac{1}{\omega_0 \cdot C \cdot R_{load}}\right)\right) \tag{6.9}$$

The Fourier-series model, approximating a NiCd battery-buck converter system, is described by a square-wave voltage-source, series connected to an *R-L-C* circuit, similar to the one shown in Fig. 6.1. The voltage magnitude of the square-wave voltage source is zero, during mode 2 (off), and is equal to the value described by equation (6.6), during mode 1 (on). To simulate a real NiCd battery, the concept of source internal resistance is implemented in the MATLAB script, shown in the Appendix A4. Thus, the battery will deliver power at different voltages, as the switching frequency is changed, as shown in Fig. 6.3. The simulation was done for three duty cycles: 50%, 65%, and 80%.

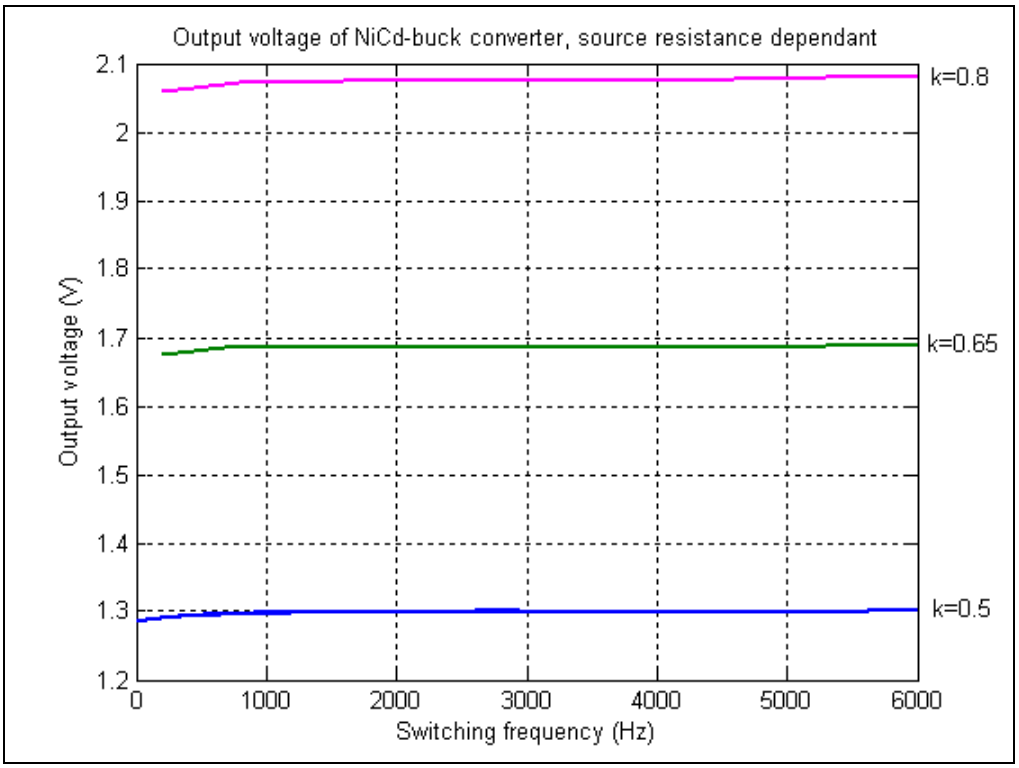

Figure 6.23: Output voltage of NiCd-buck converter, source resistance dependant

The effect of NiCd battery internal resistance, on the output voltage of the system at low frequencies, was observed. At frequencies above 1 kHz, the effect is negligible.

The set of simulations were repeated for the same duty cycles: 50%, 65%, and 80%, replacing the internal resistance with the measured NICd battery impedance, i.e., Re(Z) and Im(Z). Shown in Fig. 6.24, are the output voltage plots for the NiCd battery-buck converter system, where the battery impedance is considered.

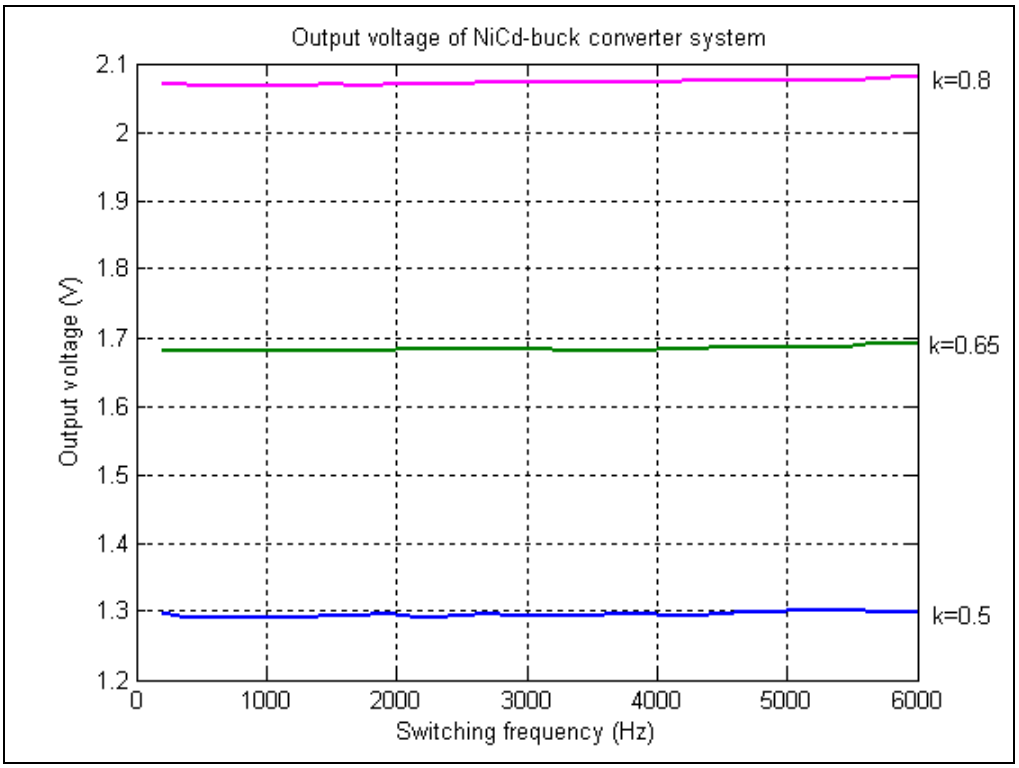

Figure 6.24: Output voltage of NiCd battery-buck converter, impedance dependant

The algorithm shown in the MATLAB script, of Appendix A5, was used to determine the effective voltage, and is given by:

$$V_{on} = \left(1 - \frac{Z_{source}}{Z_{Total}}\right) \cdot V_0 \tag{6.10}$$

Where, the source impedance magnitude is:

$$Z_{source} = \sqrt{\mathrm{Re}(Z)^2 + \mathrm{Im}(Z)^2} \tag{6.11}$$

The real and imaginary parts of the circuit impedance, during mode 1 (on) are:

$$\mathrm{Re}(Z_{Total}) = \mathrm{Re}(Z) + r_L + \frac{R_{load} \cdot \left(\frac{1}{\omega_0 \cdot C}\right)}{\sqrt{R_{load}^2 + \left(\frac{1}{\omega_0 \cdot C}\right)^2}} \cdot \cos\left(-\frac{\pi}{2} + \arctan\left(\frac{1}{\omega_0 \cdot C \cdot R_{load}}\right)\right) \tag{6.12}$$

$$\mathrm{Im}(Z_{Total}) = \mathrm{Im}(Z) + \omega_0 \cdot L + \frac{R_{load} \cdot \left(\frac{1}{\omega_0 \cdot C}\right)}{\sqrt{R_{load}^2 + \left(\frac{1}{\omega_0 \cdot C}\right)^2}} \cdot \sin\left(-\frac{\pi}{2} + \arctan\left(\frac{1}{\omega_0 \cdot C \cdot R_{load}}\right)\right) \tag{6.13}$$

The voltage magnitude of the square-wave voltage source, approximating the buck converter commutation, is zero, during mode 2 (off), and is equal to the value described by equation (6.10), during mode 1 (on). Different values of Re(Z) and Im(Z) are used for each of the switching frequencies. The output voltage characteristic of the simulated system shows a small decrease in output voltage, at frequencies below 3 kHz. At higher frequencies, the system output voltage is comparable to that of the ideal voltage source system.

6.2.5 Buck converter-driven, DEFC power systems

Figure 6.19 shows the phase angle dependency of signal frequency for Direct Ethanol Fuel Cells. Unlike NiCd batteries, DEFCs exhibit a positive phase angle over the considered frequency range, thus suggesting an inductive reactance associated with the inner workings of the cells.

From the polarization curve in Fig 6.24, the voltage-current characteristic of DEFC is described by the fuel-cell output voltage function of load current, and is:

$$V_{DEFC} = 0.966 - 1.44 \cdot I_{DEFC} \tag{6.14}$$

Equation 6.14 expresses the voltage-current characteristics of the DEFC, where the current coefficient is the internal resistance of the fuel cell, and is 1.44 Ω.

Due to predominant positive reactance, the equivalent circuit for DEFCs should consist of an inductive component series-connected to a resistive component. Particular to liquid electrolyte DC power sources, the flow of electric charges through electrolyte generates a magnetic field within the cell.

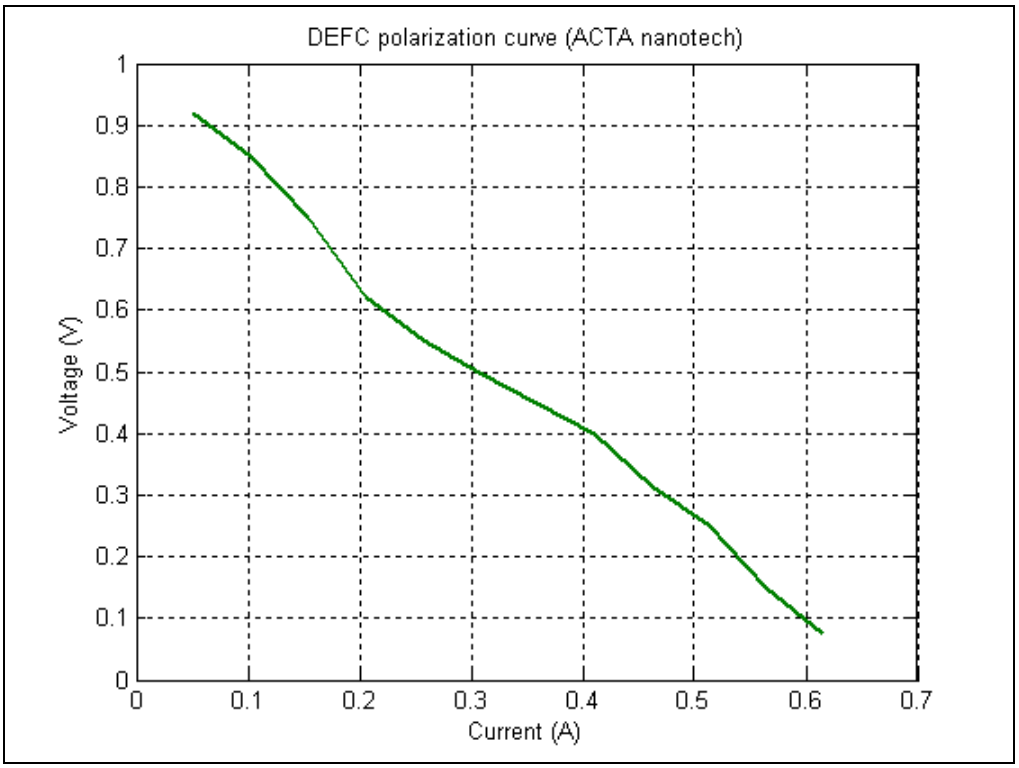

Figure 6.25: DEFC polarization curve

An approximation of the real DEFC-buck converter system is accomplished by implementing the internal resistance of the DEFC, determined from the polarization curve, in the MATLAB script, shown in Appendix A4. Both, DEFC mesh and DEFC foam exhibit identical voltage-current characteristics (information provided by ACTA nanotech). Thus, only one set of plots were generated for the DEFC mesh & foam-buck converter system, as shown in Fig. 6.26. The voltage magnitude of the square-wave voltage source, approximating the buck converter commutation, is zero, during mode 2 (off), and is equal to the value described by equation (6.6), during mode 1 (on). The effect of DEFC internal resistance on the system output voltage is greater at lower frequencies and at higher duty cycle.

To emulate realistic conditions, i.e., AC characteristics, the internal resistance of DEFCs was replaced with their measured impedances, Re(Z) and Im(Z). The voltage magnitude of the square-wave voltage source, approximating the buck converter commutation, is zero, during mode 2 (off), and is equal to the value described by equation (6.10), during mode 1 (on). The simulation was done using different values of

Re(Z) and Im(Z) for each one of DEFC, mesh and foam, over a frequency range of 200 Hz to 6 kHz. The MATLAB script in Appendix A5 was used, where the first set of simulations was done for the DEFC-mesh, and the second set for the DEFC-foam. The output voltage characteristics obtained for each system, DEFC mesh-buck converter, and DEFC foam-buck converter, are shown in Figs. 6.27 and 6.28.

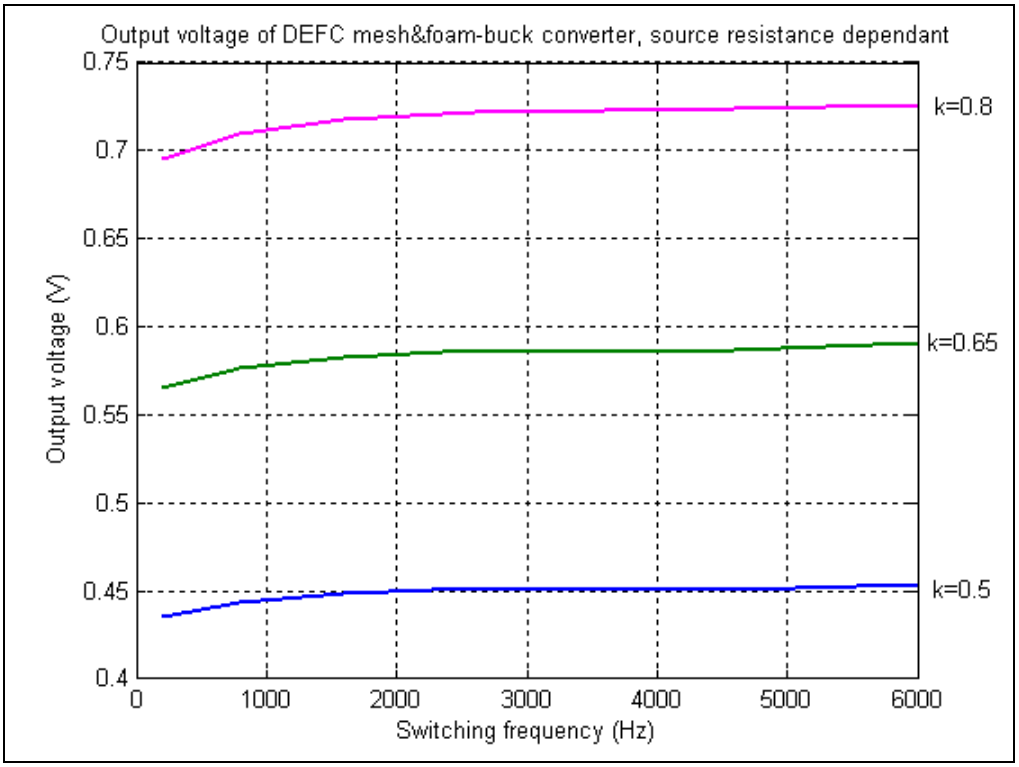

Figure 6.26: Output voltage of DEFC mesh & foam-buck converter, source resistance dependant

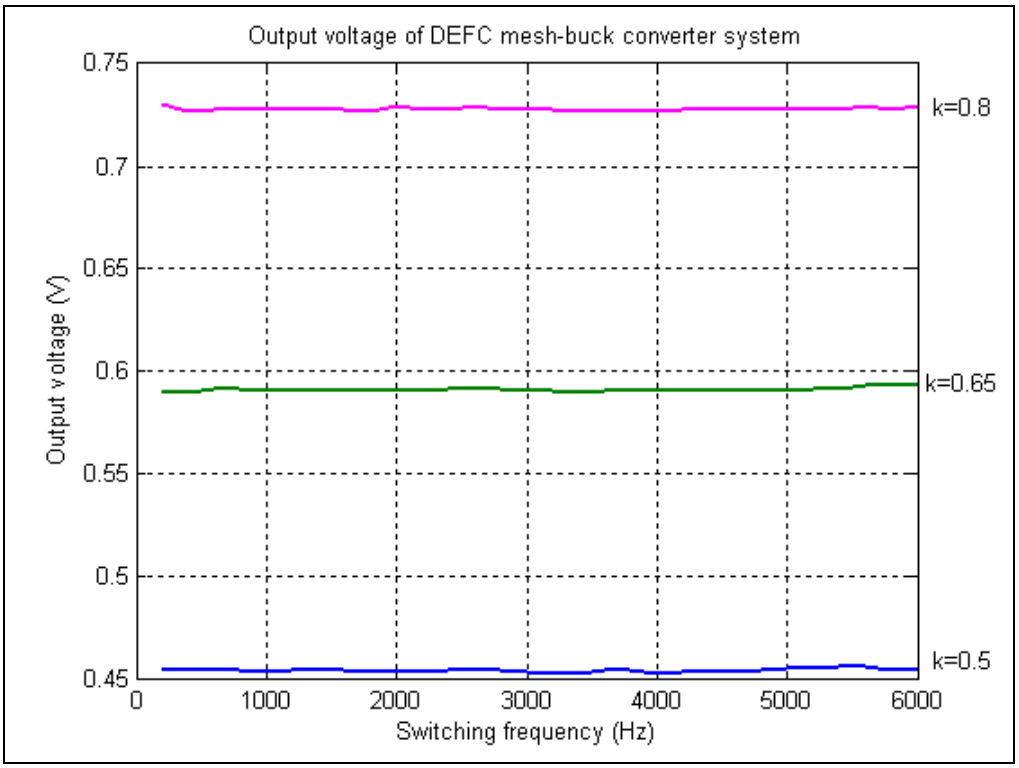

Figure 6.27: Output voltage of DEFC mesh-buck converter, impedance dependant

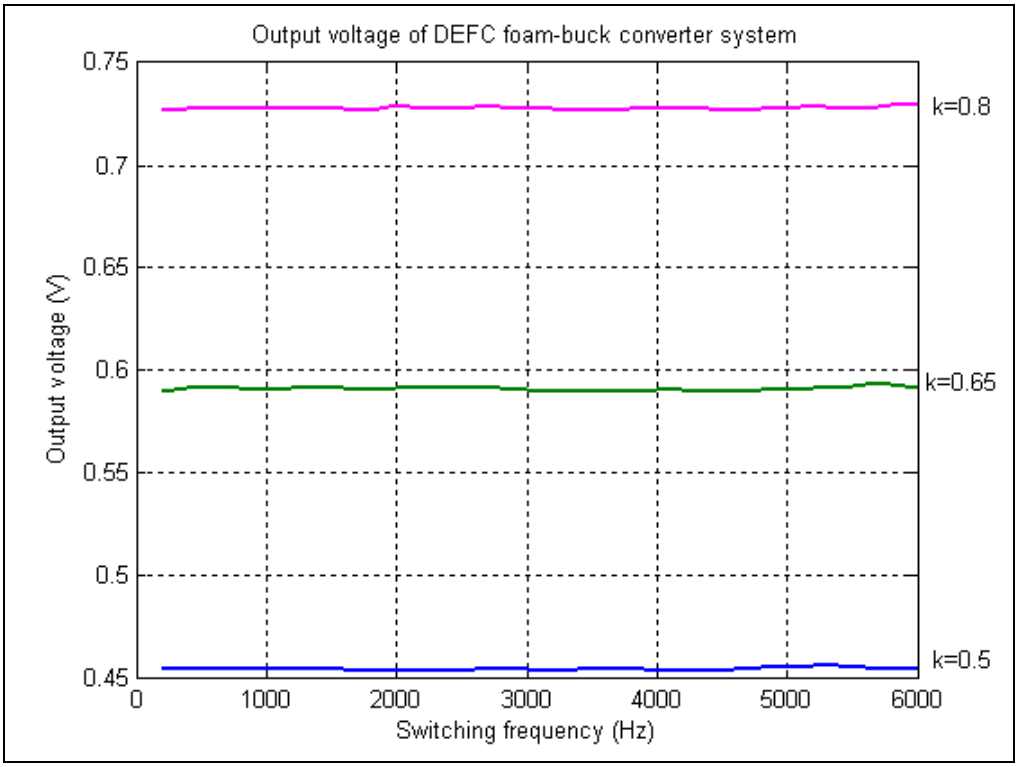

Figure 6.28: Output voltage of DEFC foam-buck converter, impedance dependant

The effect of DEFC-mesh impedance on the output voltage of the system is small, and dependent on the switching frequency and on the duty cycle. The system output voltage is nearly constant over the switching frequency range, for each duty cycle. The effect of DEFC-foam impedance on the output voltage of the system is small, and dependent on the switching frequency and the duty cycle.

6.2.6 Boost converter-driven NiCd battery power systems

During mode 1 (*on* mode), the inductor and NiCd battery are connected in series, via switching transistor Q_{switch}. During mode 2 (*off* mode), the NiCd battery is connected in series with inductor *L*, and parallel network $R_{load}C$. The impedance "seen" by the NiCd battery during mode 2 is larger, as compared to mode 1. Thus, the effective voltages during mode 1 (on) and 2 (off), are smaller than the source open circuit voltage. Their values are determined by:

$$V_{on} = \left(1 - \frac{r_{source}}{\sqrt{\left(r_{source} + r_L\right)^2 + \left(\omega_0 \cdot L\right)^2}} \right) \cdot V_0 \tag{6.15}$$

$$V_{off} = \left(1 - \frac{r_{source}}{Z_{Total}} \right) \cdot V_0 \tag{6.16}$$

Circuit impedance during mode 2 (off) Z_{Total} is determined by equations (6.7) to (6.9), when considering the source internal resistance only. The Fourier-series model, approximating a NiCd battery-boost converter system, is described by an independent voltage source, series connected to an *R-L-C* circuit, and a pulse-wave current source, connected to the circuit, as shown in Fig. 6.8. The current magnitude and wave-shape of the pulse-wave current source is implemented in the MATLAB script as two independent square-wave voltage sources, V_{on}, describing the boost converter system during mode 1 (on), and V_{off}, describing the boost converter system during mode 2 (off). The maximum voltage magnitudes of the square-wave voltage sources V_{on} and V_{off} is determined by equations (6.15) and (6.16) respectively. Their minimum values are zero. The Fourier-series model of NiCd-boost converter, under internal resistance approximation, was

simulated using MATLAB script, shown in Appendix A5, for three selected duty cycles, 50%, 65%, and 80%. The output voltage characteristic for all three duty cycles was plotted, as shown in Fig. 6.29.

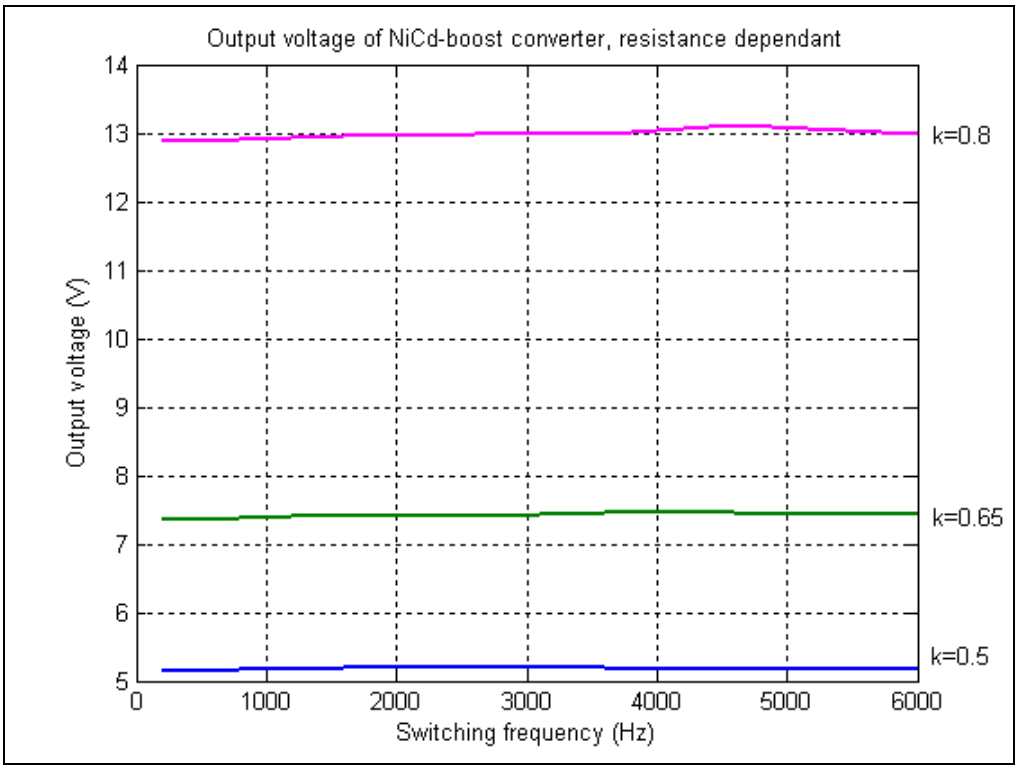

Figure 6.29: Output voltage of NiCd-boost converter, source resistance dependant

The effect of internal resistance of the NiCd battery is small, as compared to the estimated average output voltage of the system.

Under sequential switching conditions, DC sources are characterized by internal impedances, with varying magnitudes, and dependent to the switching frequency. Thus, the internal resistance of the NiCd battery was replaced by its impedance, in the MATLAB script, shown in Appendix A8.

The effective voltages during mode 1 (on) and 2 (off) are ratios of the open-circuit voltage of the NiCd battery, and are:

$$V_{on} = \left(1 - \frac{Z_{source}}{Z_{source} + Z_L}\right) \cdot V_0 \qquad (6.17)$$

$$V_{off} = \left(1 - \frac{Z_{source}}{Z_{Total}}\right) \cdot V_0 \tag{6.18}$$

The simulations, employing MATLAB script in Appendix A8, were done for three duty cycles, 50%, 65%, and 80%, emulating the NiCd battery impedance. The output voltage characteristics for the three duty cycles are shown in Fig. 6.30.

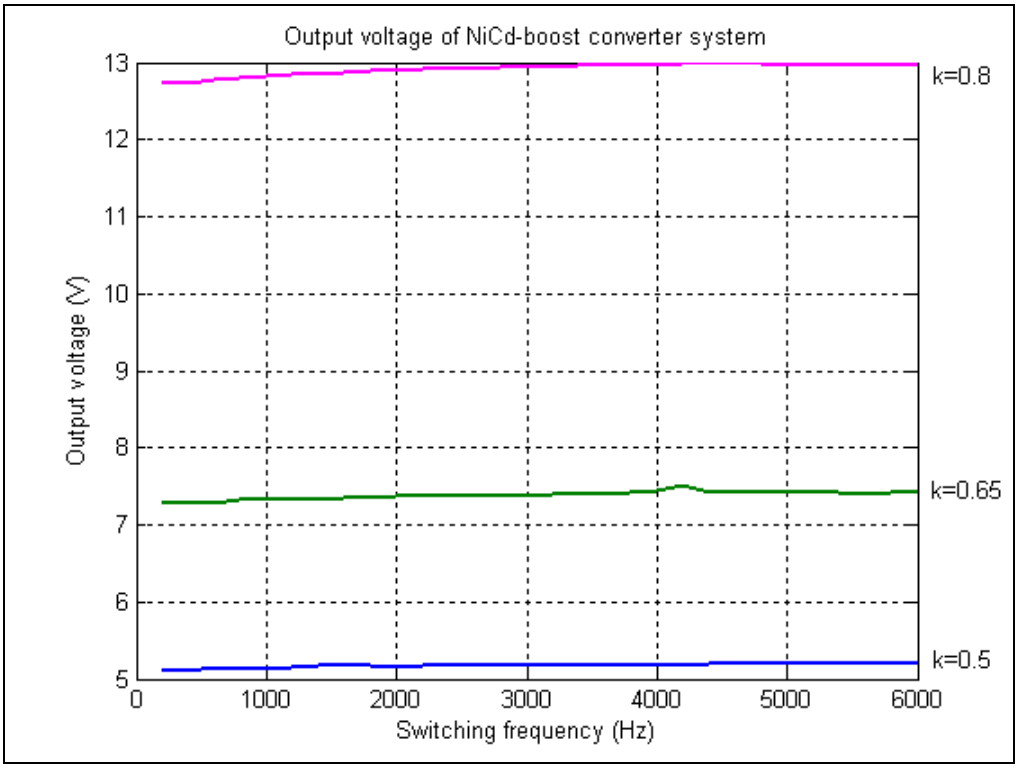

Figure 6.30: Output voltage of NiCd battery-boost converter, impedance dependant

6.2.7 Boost converter-driven DEFC power systems

The voltage-current characteristics of DEFC-mesh and DEFC-foam are identical. Thus, the internal resistance approximation for both DC sources is identical. Therefore, one set of plots is sufficient to describe the output voltage characteristics for the DEFC-boost converter system, when only the source internal resistance is considered. The Fourier-series model, approximating the DEFC-boost converter system, is described by an independent voltage source, series connected to an *R-L-C* circuit, and a pulse-wave

current source, connected to the circuit, as shown in Fig. 6.8. The current magnitude and wave-shape of the pulse-wave current source is implemented in the MATLAB script as the commutation of two independent square-wave voltage sources, V_{on}, describing the boost converter system during mode 1 (on), and V_{off}, describing the boost converter system during mode 2 (off). The maximum voltage magnitudes of the square-wave voltage sources V_{on} and V_{off} is determined by equations (6.15) and (6.16) respectively. Their minimum values are zero.

The output voltage characteristics, of DEFC-boost converter system, shown in Fig. 6.31, were obtained using MATLAB script in the Appendix A5. The internal resistance of the source is 1.44 Ω, and was computed from the polarization curve of DEFC mesh & foam, provided by ACTA nanotech. The converter was simulated for three duty cycles, 50%, 65%, and 80%.

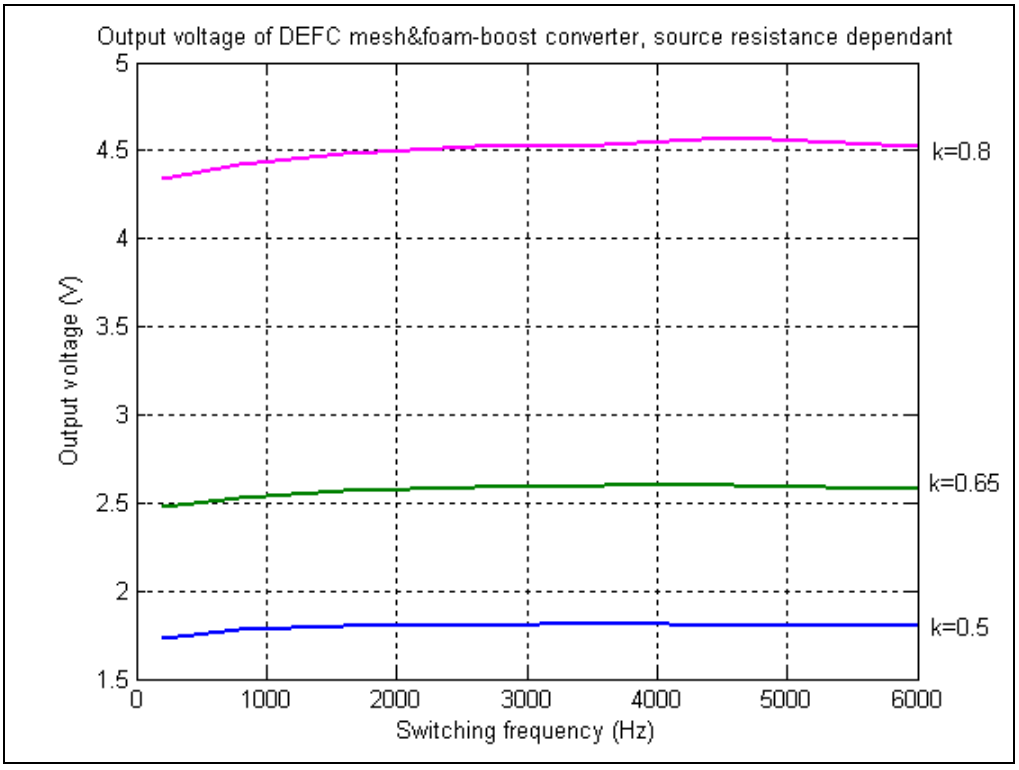

Figure 6.31: Output voltage of DEFC mesh & foam-boost converter, source resistance dependant

The effect of the internal resistance, at 50% and 65% duty cycle, on the output voltage for DEFC-boost converter is small, as compared to the predicted values. At 80%

duty cycle, the output voltage varies 0.24 V, from 200 Hz to 4600Hz switching frequency.

Ni-mesh and Ni-foam electrodes DEFCs exhibit different complex impedance characteristics. Thus, the response of each DEFC-boost converter system to the sequential switching process is predicted to be unique.

To emulate DEFC-mesh and DEFC-foam impedance characteristics, their internal resistance of 1.44 Ω was substituted with the respective DEFC impedance. The MATLAB script from Appendix A8 was used to simulate both, DEFC mesh & foam-boost converter systems. The output voltage characteristics of each system, is shown in Figs. 6.32 and 6.33.

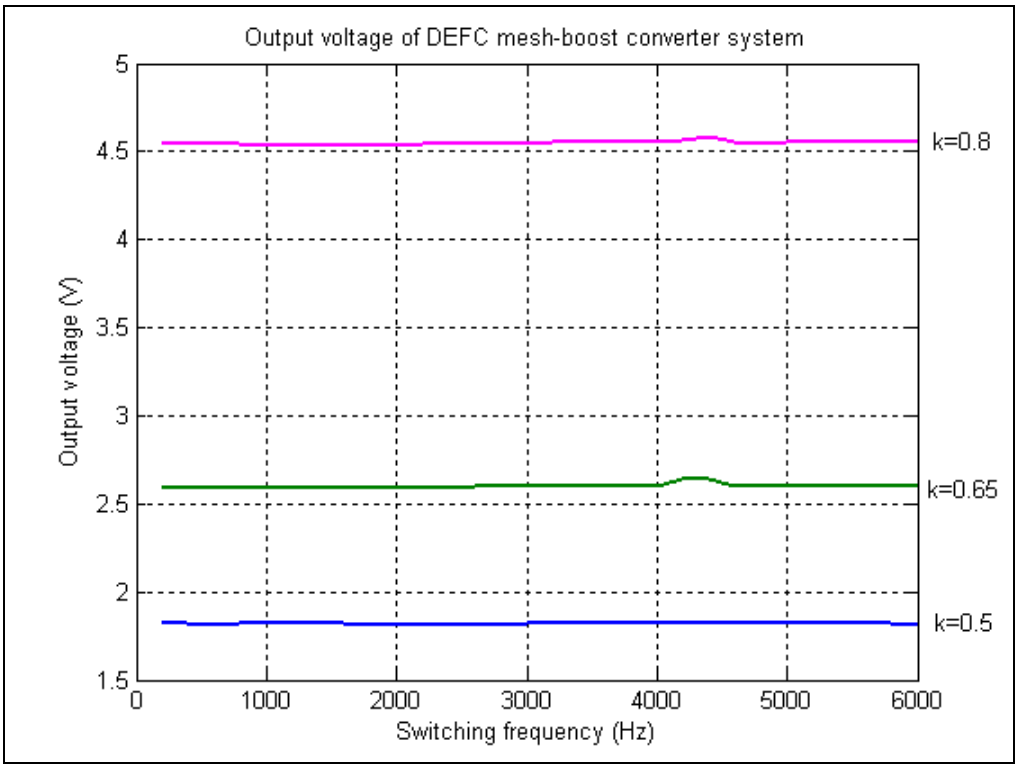

Figure 6.32: Output voltage of DEFC mesh-boost converter model

The effects of DEFC-mesh & foam impedances, on the output voltage characteristics of the systems are small, as compared to the predicted values, over the switching frequency range considered.

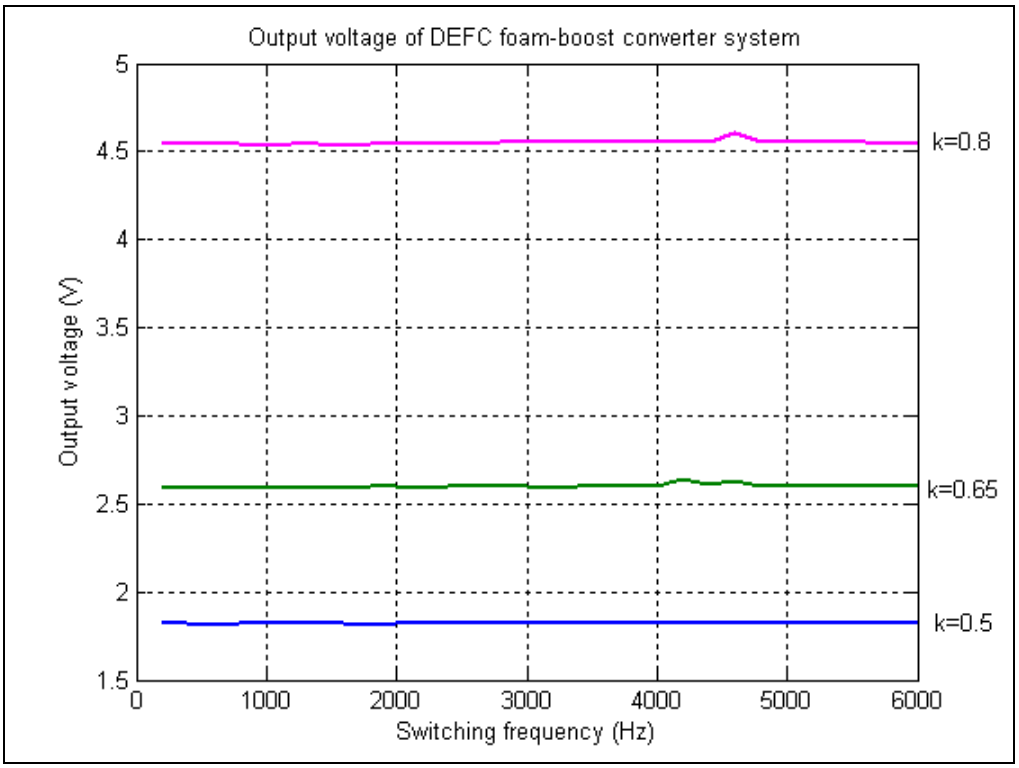

Figure 6.33: Output voltage of DEFC foam-boost converter model

6.2.8 Buck-boost converter driven NiCd battery power systems

During mode 1 (*on* mode), the inductor and NiCd battery are connected in series via switching transistor Q_{switch}. During mode 2 (*off* mode), the NiCd battery is not supplying power to the system. The Fourier-series model, approximating a NiCd battery-buck-boost converter system, is described by a pulse-wave current source, connected to an *R-L-C* circuit, as shown in Fig. 6.12. The current magnitude and wave-shape of the pulse-wave current source, during mode 2 (off), is determined, in the MATLAB script, by a square-wave voltage source, V_{on}, describing the buck-boost converter system during mode 1 (on). The voltage magnitude of the square-wave voltage source, approximating the buck-boost converter commutation, is zero, during mode 2 (off), and is equal to the value described by equation (6.15), during mode 1 (on). It is predicted a decrease of NiCd battery output voltage during mode 1, especially at low switching frequencies. The

effective voltage during mode 1 (on) is smaller than the source open circuit voltage. Approximating the NiCd battery as a DC source, series-connected to a resistor (NiCd battery internal resistance), the effective voltage at the battery terminals during mode 1 (on) is given by equation (6.15). During mode 2 (off), the voltage "seen" by the buck-boost converter is zero. Employing the MATLAB script A6, shown in the Appendix, and a source resistance of 0.263 Ω, simulations of the NiCd battery-buck-boost converter system were performed. Three duty cycles were considered, 50%, 65%, and 80%, and a switching frequency ranging from 200 Hz to 6 kHz. The output voltage characteristics of NiCd battery-buck-boost converter system is shown in Fig. 6.34.

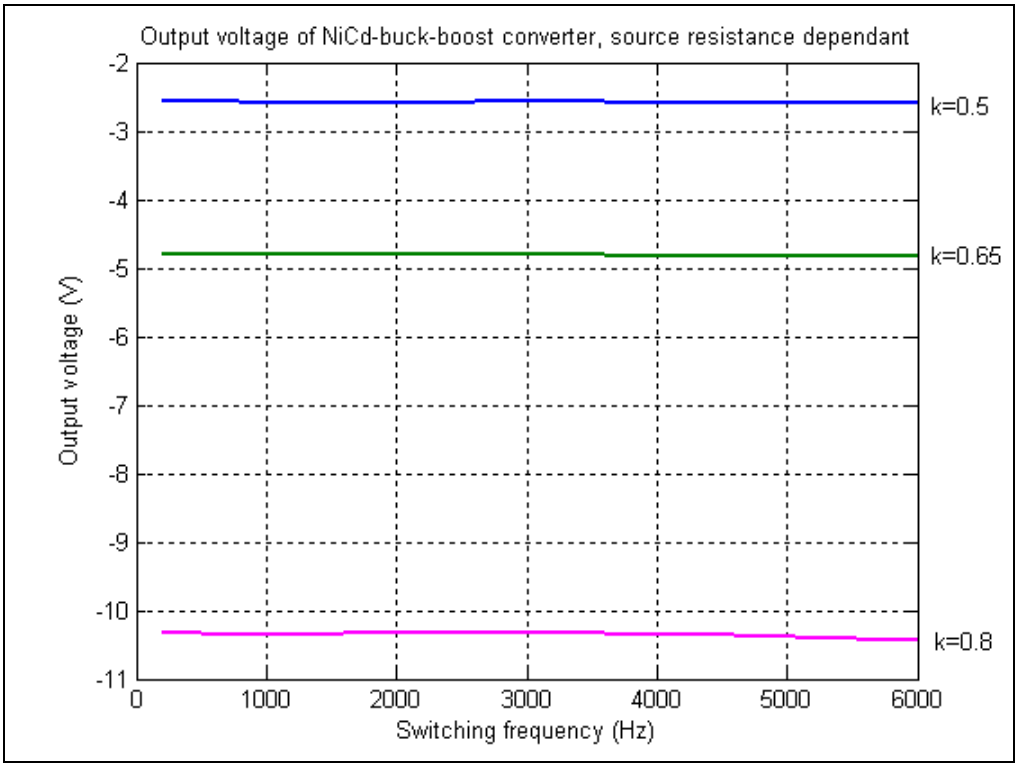

Figure 6.34: Output voltage of NiCd-buck-boost converter, source resistance dependant

The internal resistance of NiCd battery has a small effect on the output voltage characteristics of the system, over the switching frequency range, simulated at any of the three duty cycles.

Considering the effects of the NiCd battery impedance on the output voltage characteristics, the effective voltage at the battery terminals, during mode 1 (on) is given by equation (6.17). The simulation of NiCd battery-buck-boost system was done employing MATLAB script, shown in the Appendix A9. Three duty cycles were considered, 50%, 65%, and 80%, and a switching frequency ranging from 200 Hz to 6 kHz. The impedance values, Re(Z) and Im(Z), were corresponding to the switching frequency values used. The output voltage characteristics obtained through simulation, employing MATLAB script A9, are shown in Fig. 6.35.

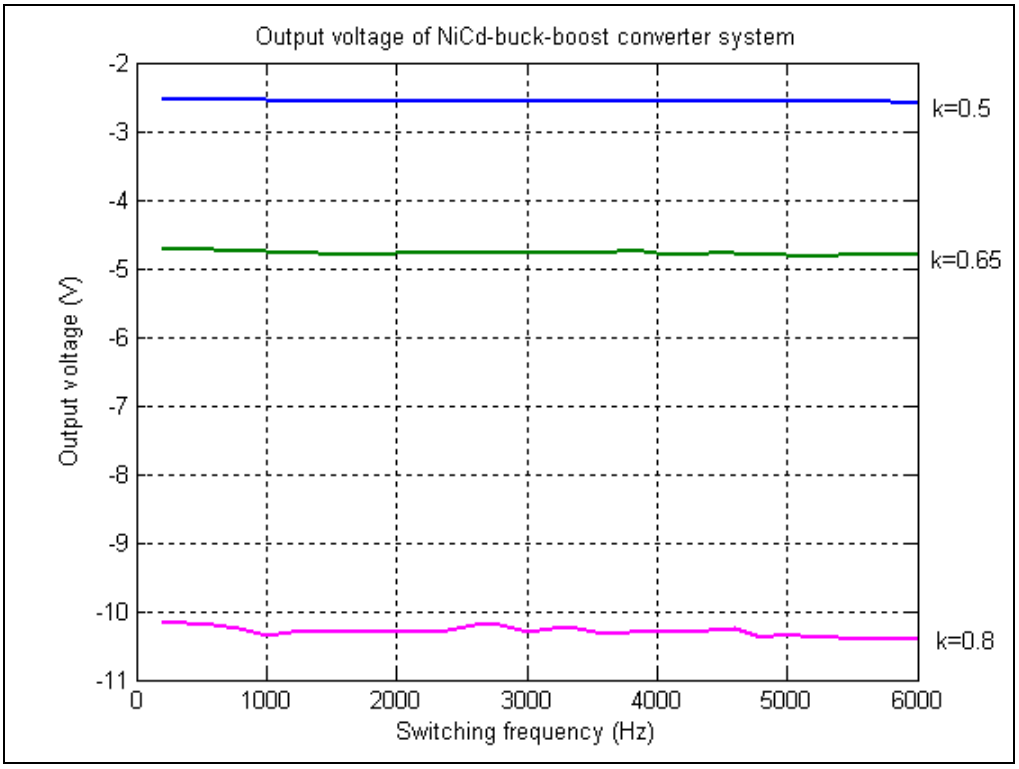

Figure 6.35: Output voltage of NiCd battery-buck-boost converter, source impedance dependent

The effects of NiCd battery impedance, on the output voltage characteristics of the system, are small, as compared to the predicted output voltage values.

6.2.9 Buck-boost converter driven DEFC power systems

The polarization curve of DEFC, shown in Fig. 6.24, and described by Equation (6.6), implies a decrease of fuel-cell output voltage during mode 1 (*on* mode), characteristic to an increase of inductor current. This voltage drop, at the input port of the buck-boost converter, alters the predicted operating parameters of the DEFC powered system. At low switching frequencies, mode 1 lasts for a longer time, as compared to higher frequencies, which determines a higher inductor current and a lower fuel-cell output voltage. Thus, the output voltage of the DEFC powered system is dependent on converter duty cycle, switching frequency, and the inductance of the circuit.

The internal resistance approximation for both DEFC-mesh and DEFC-foam is the same. Thus, one set of plots describes the output voltage characteristics for the DEFC mesh & foam-buck-boost converter system, when approximating the source internal resistance. The Fourier-series model, approximating a DEFC-buck-boost converter system, is described by a pulse-wave current source, connected to an *R-L-C* circuit, as shown in Fig. 6.12. The current magnitude and wave-shape of the pulse-wave current source, during mode 2 (off), is determined, in the MATLAB script, by a square-wave voltage source, V_{on}, describing the buck-boost converter system during mode 1 (on). The voltage magnitude of the square-wave voltage source, approximating the buck-boost converter commutation, is zero, during mode 2 (off), and is equal to the value described by equation (6.15), during mode 1 (on). The MATLAB script used in this simulation is shown in Appendix A6, and the internal resistance used is 1.44 Ω, as compiled from the polarization curve of the DEFC.

The output voltage characteristics, obtained through simulation of MATLAB script A6, for three selected duty cycles, 50%, 65%, and 80%, is shown in Fig. 6.36.

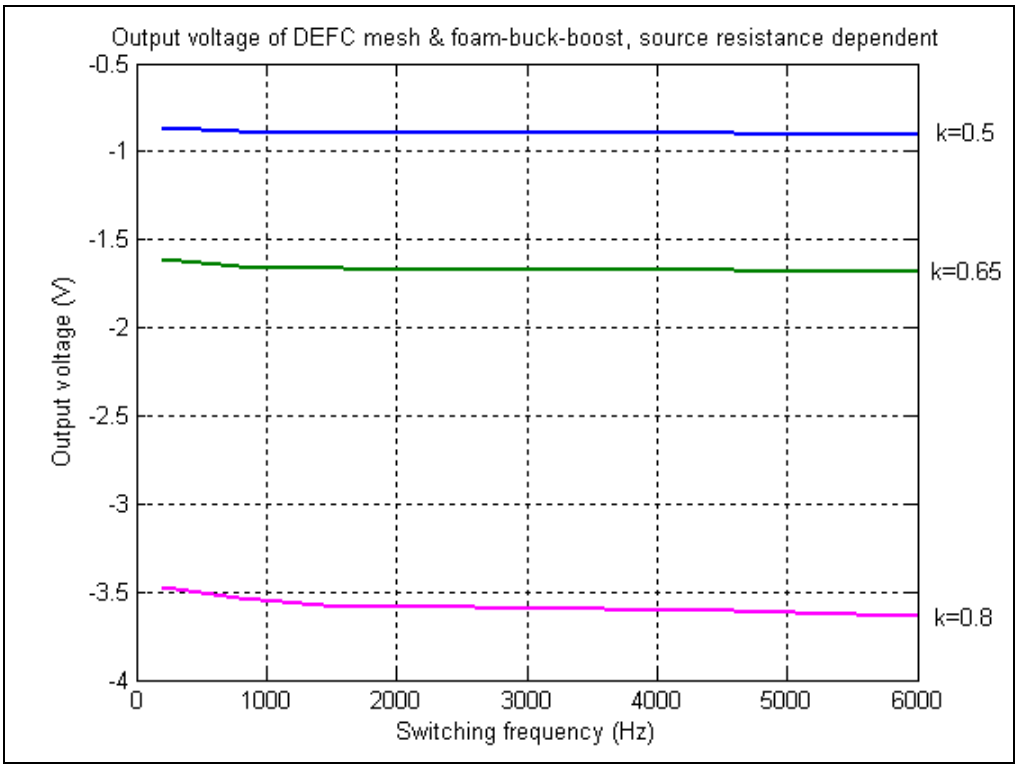

Figure 6.36: Output voltage of DEFC mesh & foam-buck-boost converter, source resistance dependant

System simulation at 80% duty cycle shows a decrease in its output voltage at lower frequencies, and is close to the predicted values, at higher frequencies. Simulations performed for 50% and 65% duty cycle yielded small deviations from the predicted output voltage values, over the entire switching frequency range.

MATLAB script A9, shown in the Appendix, is obtained from MATLAB script A6, by replacing the internal resistance of DEFCs with their respective impedances, and is an approximation of the DEFC-buck-boost converter system. The converter commutation is emulated by a square-wave voltage source. The effective voltage at the fuel cell terminals, during mode 1 (on), is determined by the equation (6.17). Thus, the voltage magnitude of the square-wave voltage source, approximating the buck-boost converter commutation, is zero, during mode 2 (off), and is equal to the value described by equation (6.17), during mode 1 (on). Each fuel cell impedance is described by a set of points, Re(Z) and Im(Z), corresponding to each switching frequency. Three duty cycles are considered for each DEFC simulation set. The output voltage characteristics obtained,

for DEFC-mesh and DEFC-foam-buck-boost converter systems, are shown in Figs.6.37 and 6.38.

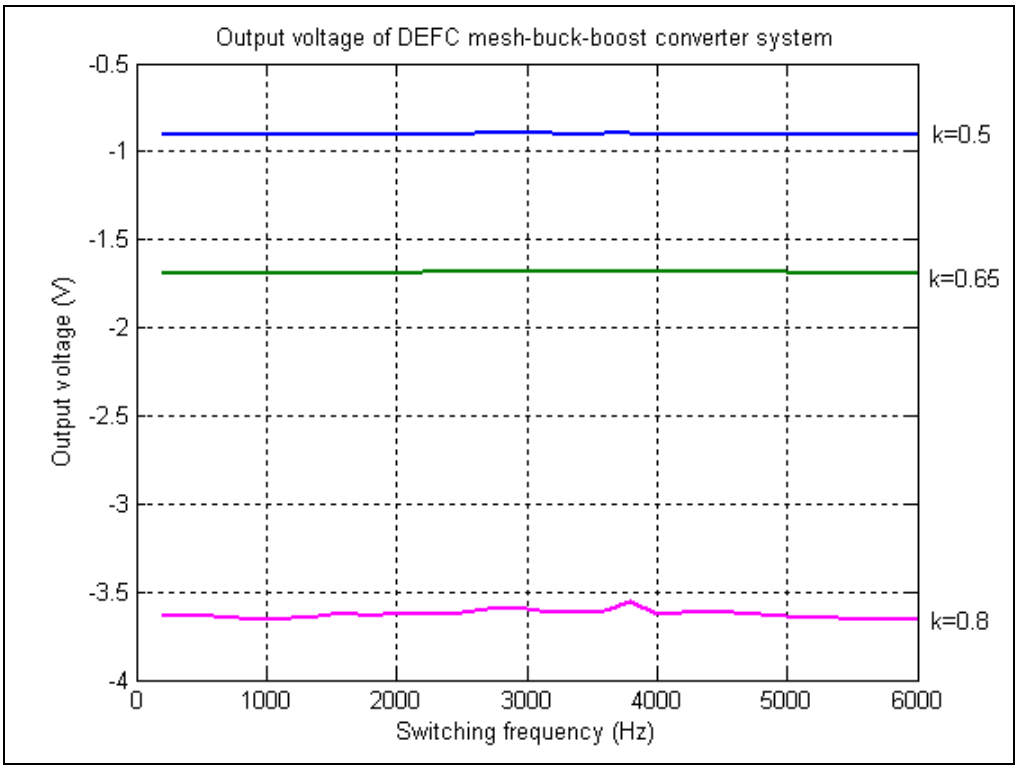

Figure 6.37: Output voltage of DEFC mesh-buck-boost converter, source impedance dependant

The plots in Figs. 6.37 and 6.38, obtained through simulations, and employing MATLAB script A9, show negligible effect of the DEFCs impedance on the output voltage of the system.

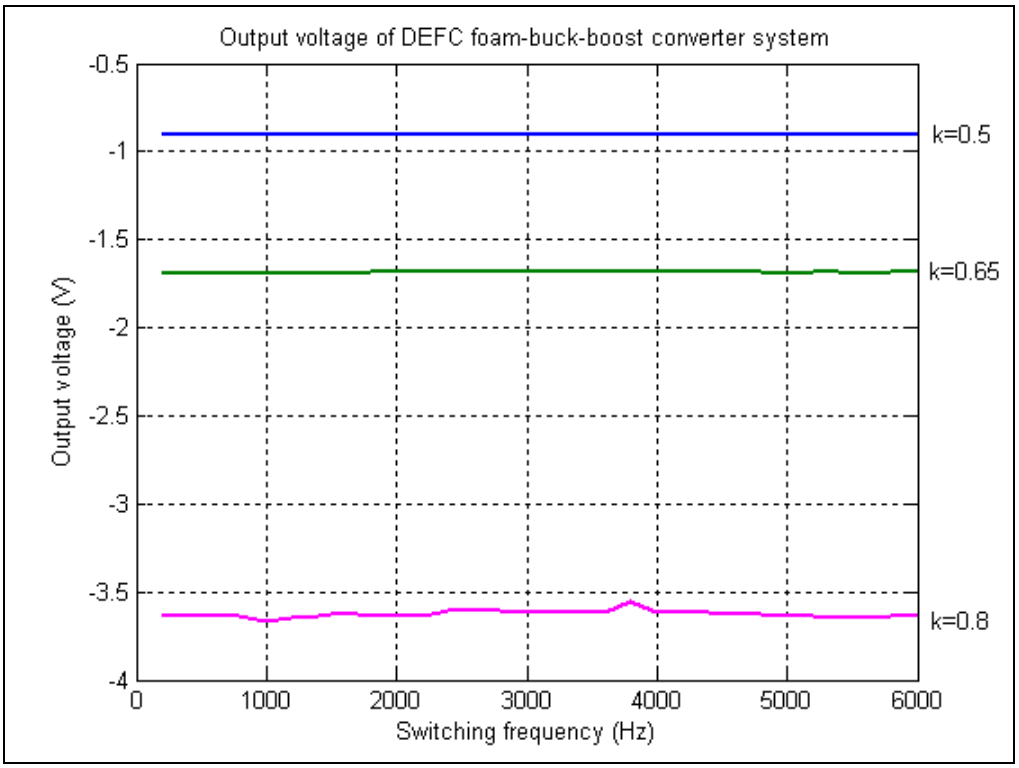

Figure 6.38: Output voltage of DEFC foam-buck-boost converter, source impedance dependant

CHAPTER 7 - Experimental Validation

Performance characteristics were experimentally determined for eight DC power systems in the lab, at different duty cycles and over selected switching frequency ranges. Measured and computed performances were compared to validate the Fourier-series models developed in this work. Steady-state output voltages at predetermined switching frequencies were measured and recorded on spreadsheet. Graphical representations of output voltage versus switching frequency are presented for eight DC power systems at three duty cycles. Waveforms of output voltages were recorded at low frequency through a digital storage oscilloscope. Good agreement between measured and simulated waveforms characteristics verifies analytical computations and validates the Fourier-series models developed.

7.1 Experimental Setting

All Impedance measurements were conducted at Center for Advanced Vehicular Systems (CAVS), of Mississippi State University. The impedances for Ni-Cd batteries, and Direct Ethanol fuel cells were determined using Solartron 1260 signal generator, interfaced to HP computer for data collection. The power systems characteristics measurements were conducted at Pittsburg State University in the Department of Engineering Technology.

7.1.1 Equipment and Software

- Digital Multimeter
- Bench Multimeter
- Dual channel digital storage oscilloscope Instek-GDS-820
- Axiom MC68HC12-B32 microcontroller and development board
- Personal computer
- NiCd AA-600 Intermatic batteries
- Direct Ethanol Fuel Cells, 20% Ethanol fuel.

For illustration purposes, the DEFC anode and cathode views are shown in Fig. 7.1. The DEFC assembly, including the fuel tank and fuel conduit is shown in fig. 7.2.

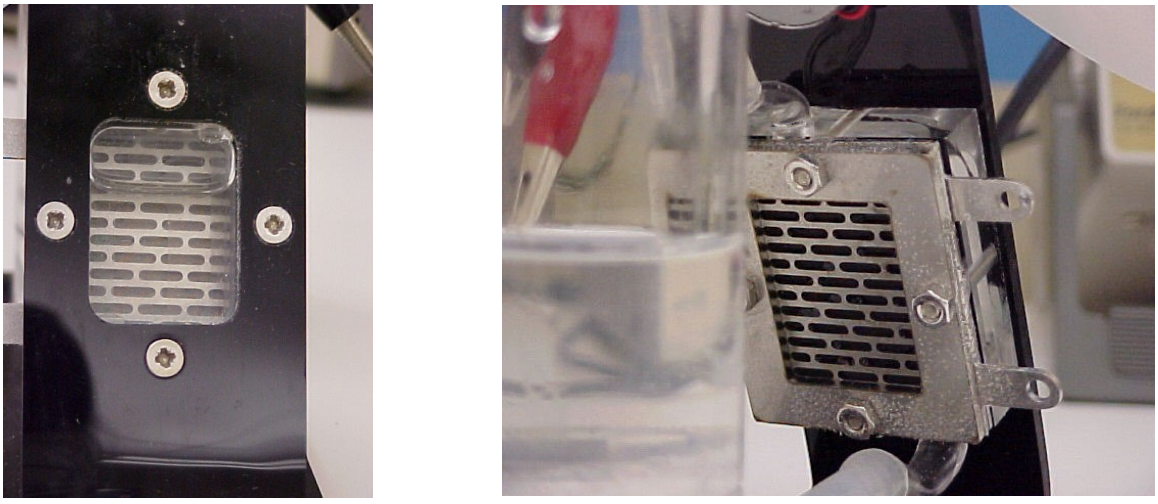

a. b.

Figure 7.1: a. Anode view, b. cathode view

Figure 7.2: DEFC assembly

7.1.2 Methodology

Three DC–DC discrete components buck converter, boost converter, and buck-boost converters, were constructed and interfaced to the DC power sources under consideration as shown in Figs. 7.3 through 7.5. For each DC power source, MOSFET gate signal switching frequency was increased from 200 Hz to 6 kHz, in increments of 200 Hz, at predetermined duty cycles. The pulse width and the switching frequency were generated by the microcontroller. The gate triggering characteristics were implemented

through assembly language algorithm, and altered manually through Mini IDE interfacing software. Three duty cycle values were selected, as the most practical choices in real applications: 50%, 65%, and 80%. For each duty cycle-switching frequency pair, the input voltage values (**A-GD**) and the output voltage values (**B-C**) were recorded. To compensate for the DEFC electrochemical response to change of frequency, five to ten minutes were allowed between consecutive measurements. This way, the electrochemical reaction reached equilibrium at the time of measurement. In the case of NiCd batteries, electrochemical equilibrium was reached within seconds. Thus, little time elapsed between consecutive measurements, condition that determined a nearly constant output voltage at the batteries terminals. Values of input voltage an output voltage, for each DC system configuration, were recorded in Excel-table format, and are included in Attachment B. Data analysis and graphical representations were performed using MATLAB 6.1.5 software.

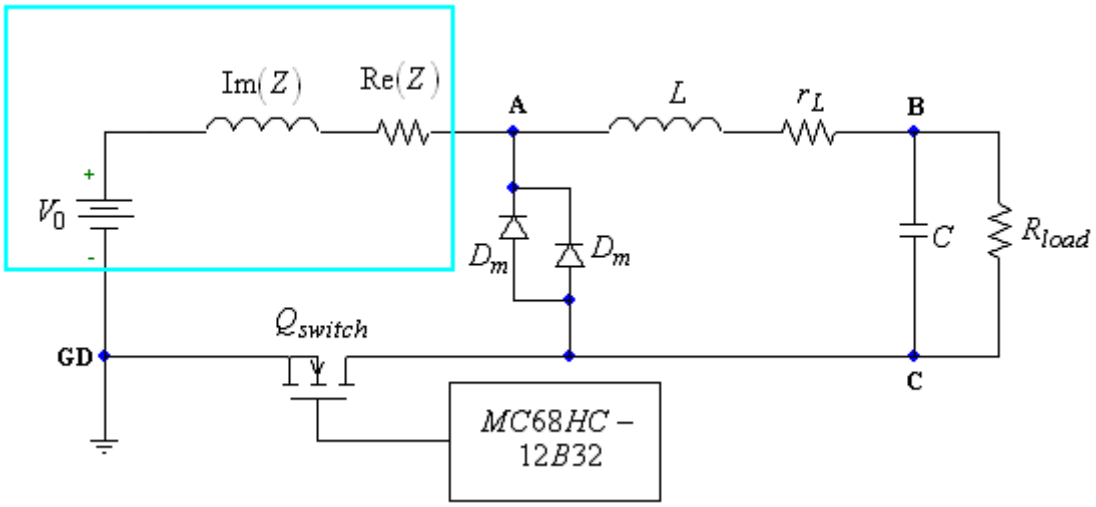

Figure 7.3: Experimental buck converter-driven DC system

DC power sources are represented in Figs. 7.3 through 7.5 as equivalent circuits, i.e., source potential + source impedance. Complex impedances are represented as parallel networks of a capacitor, accounting for the imaginary component, and a resistor, accounting for the real component of source impedance. All experimental DC–DC converters employed two parallel-connected switching diodes, thus minimizing the risk of diode burn-out. The forward-bias voltage drop across free-wheeling diode is 40 mV.

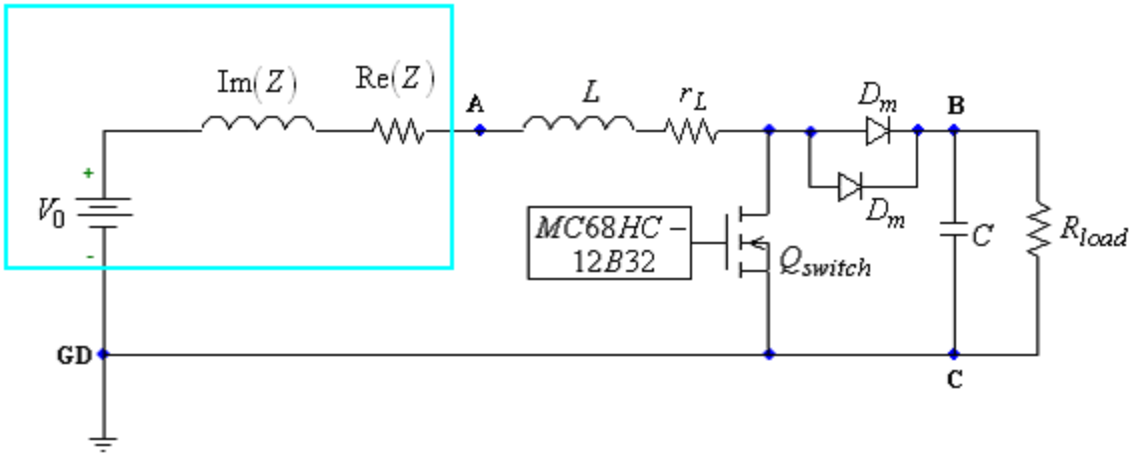

Figure 7.4: Experimental boost converter-driven DC system

An n-channel E-MOSFET was chosen for the switching transistor, of 10mV Drain-Source voltage drop.

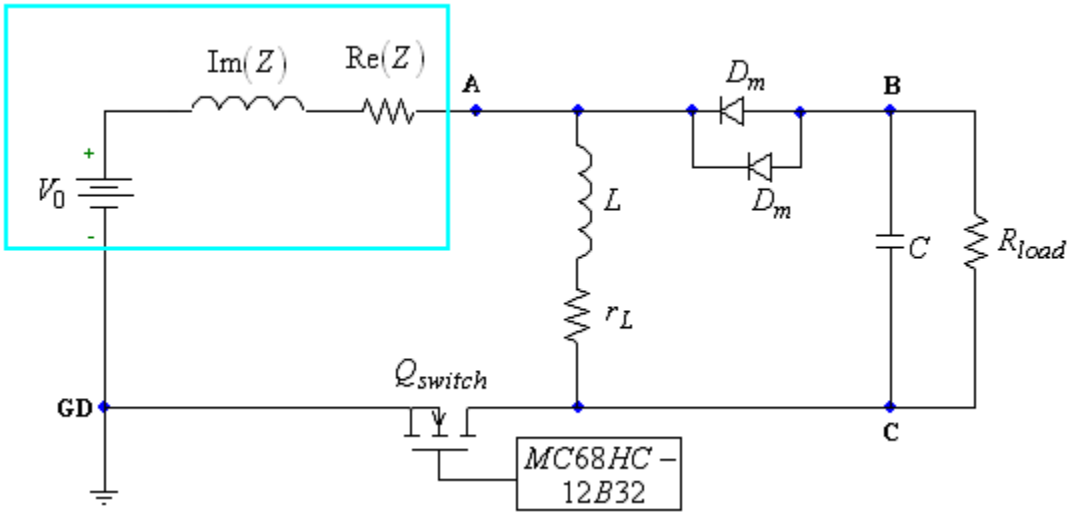

Figure 7.5: Experimental buck-boost converter-driven DC system

7.2 Buck Converter Driven Power Systems

For practicality reasons, buck converter topology was altered, such as to accommodate the E-MOSFET switching transistor and its triggering scheme. Thus, the switching transistor has the source terminal connected to the negative of the DC power source, which is grounded. This way, the Gate-Source voltage was easily triggered by a function generator, via R-G and R-GS resistive network, limiting MOSFET Gate current. A 220 μF (225 μF) electrolytic capacitor was used as the output filter, and a 10 mH (10.06 mH) inductor, of ohmic resistance 23.7 Ω, was employed as the energy storage device. A 100 Ω resistor was used as a load for the buck converter power system.

7.2.1 Ni-Cd Battery–Buck Converter System

Figure 7.6 shows that the output voltages of NiCd-buck system is within the predicted values, over the frequency range 200 Hz to 2.5 kHz, for all three duty cycles regimes.

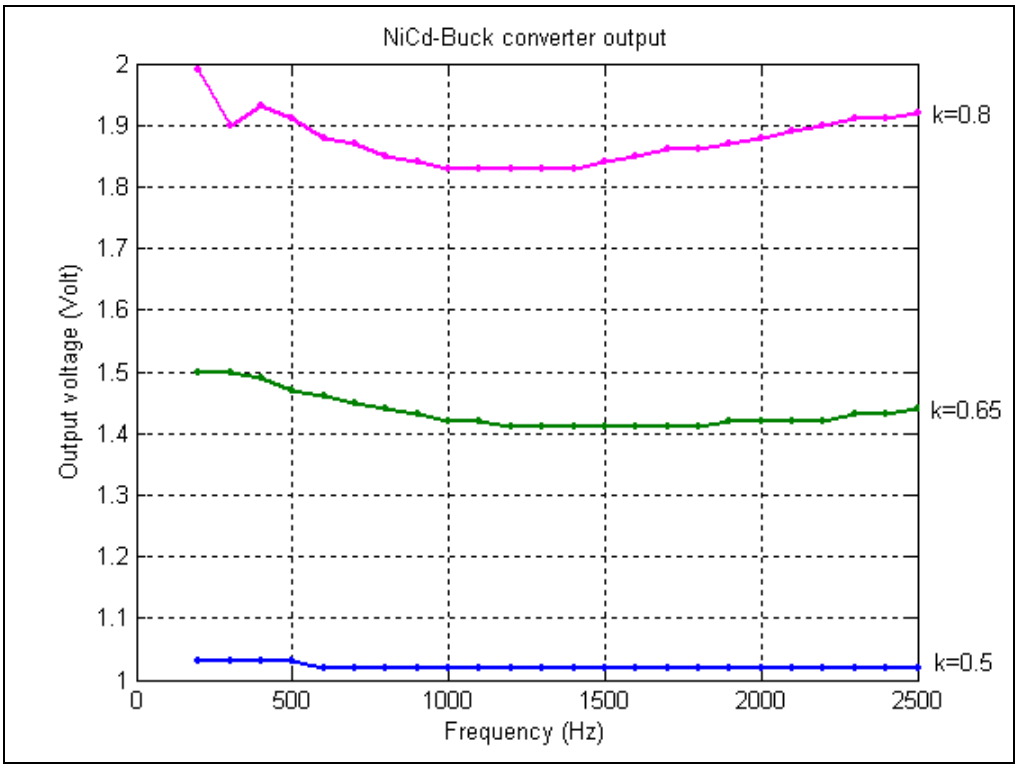

Figure 7.6: NiCd buck-converter output characteristics

7.2.2 DEFC–Buck Converter System

Measurements on DEFC-buck converter power system were performed for Ni-mesh electrode DEFC and for Ni-foam DEFC. Converter switching frequency ranged from 200 Hz to 6 kHz, in increments of 200 Hz.

Output voltages for DEFC-mesh and DEFC-foam are inversely proportional to the switching frequency for all three duty cycles. This decrease in output voltage value is due to the increasing reactance associated with inductor *L*, as shown in Figs. 7.7 and 7.8.

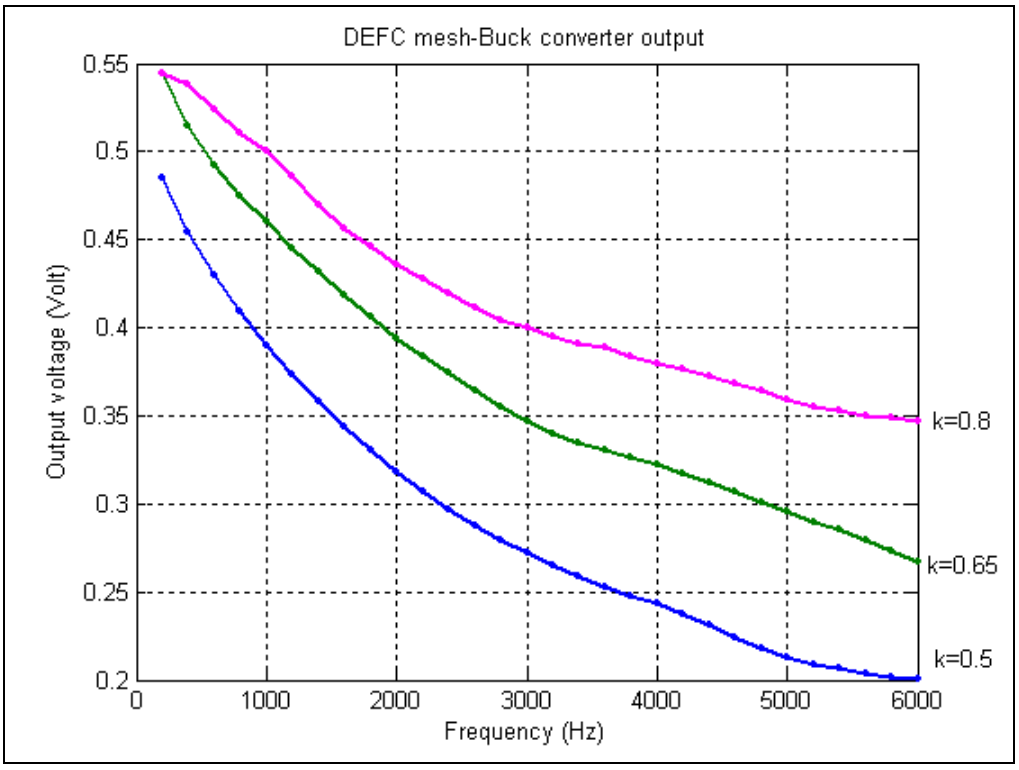

Figure 7.7: DEFC mesh buck-converter output characteristics

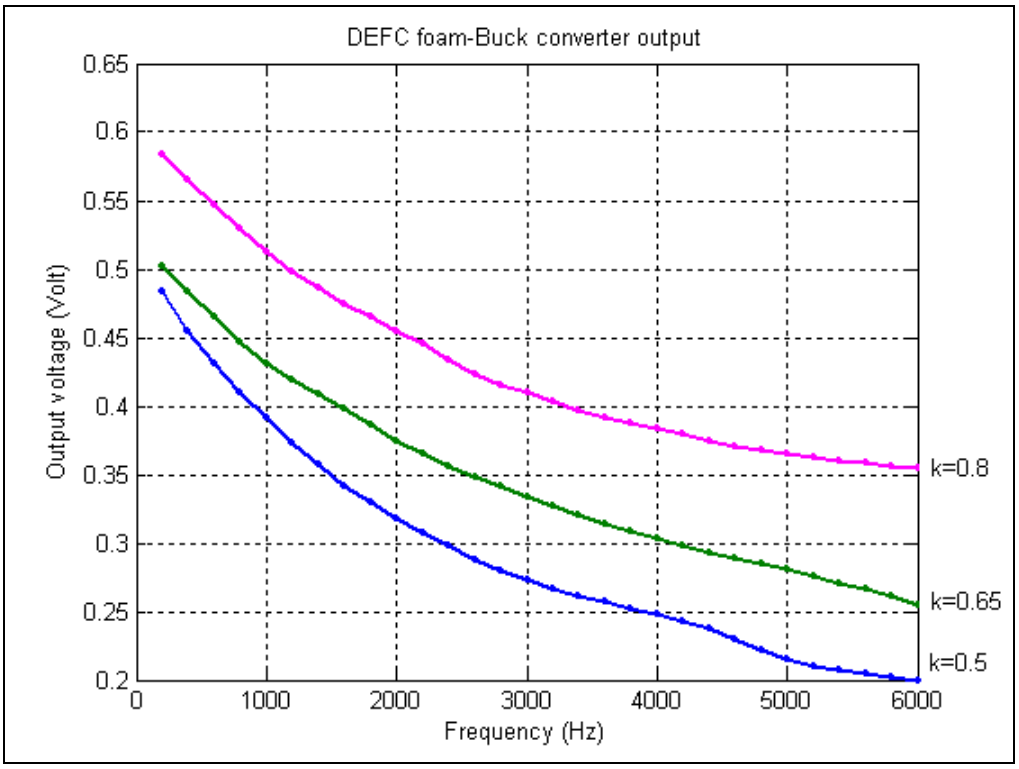

Figure 7.8: DEFC foam buck-converter output characteristics

While the output voltages are slightly smaller for DEFC mesh-buck converter, as compared to DEFC foam-buck converter, at 200 Hz switching frequency, both systems exhibit nearly identical output voltages at 6 kHz switching frequency.

7.3 Boost Converter-Driven Power Systems

A 10 kΩ resistance was used as the load for all boost converter driven DC systems. All other converter components were kept the same from the buck converter DC systems. A large resistance value for the load determines output voltage values larger than predicted by the duty cycle ratio. The choice for 10 kΩ load resistance resides in the need of avoiding premature discharge of the NiCd batteries, and the requirement of measurable output voltages over the selected frequency range.

7.3.1 Ni-Cd Battery Boost-Converter System

Interfaced to a boost converter, NiCd batteries exhibit a voltage drop at battery terminals dependent on the switching frequency and converter duty cycle. Accordingly, the average current delivered by the NiCd batteries increases, as predicted by the polarization curve. The increase of circuit current determines an increase of the output voltage, whose magnitude exceeds the predicted voltage, and is dependent on the switching frequency, as shown in Fig. 7.9.

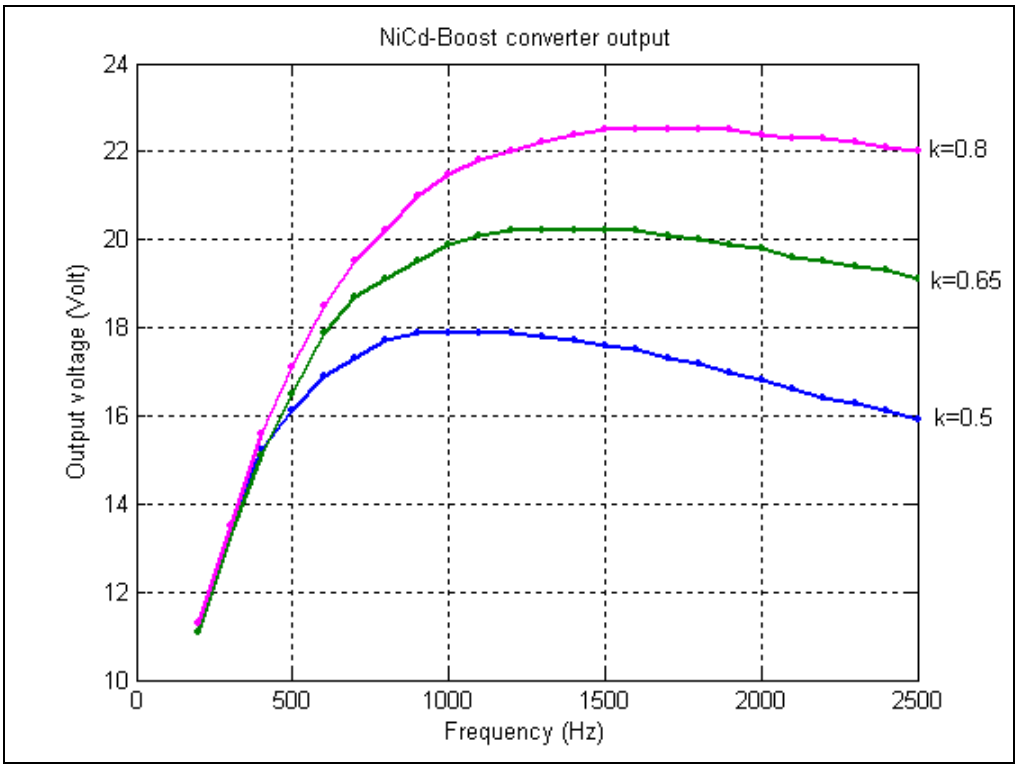

Figure 7.9: NiCd-boost converter output characteristics

7.3.2 DEFC–Boost Converter System

During switching transistor *on* time, the fuel cell stack is connected to inductor *L.* thus, as the inductor current reaches its maximum value, the fuel cell stack respond as it would be short-circuited. The values of output voltage, measured at selected frequencies and duty cycles, for DEFC mesh-boost converter system, are shown in Fig. 7.10. Comparison of conversion ratios for DEFC mesh-boost converter system, at 50%, 65%, and 80%, shown in Fig. 7.11, indicates a peak performance at switching frequencies 1400 Hz, 1400 Hz, and 1800Hz respectively, with peak conversion ratios of 5.7 at 50%, 6.92 at 65%, and 7.32 at 80% duty cycle. The expected conversion ratios are lower than the values obtain experimentally.

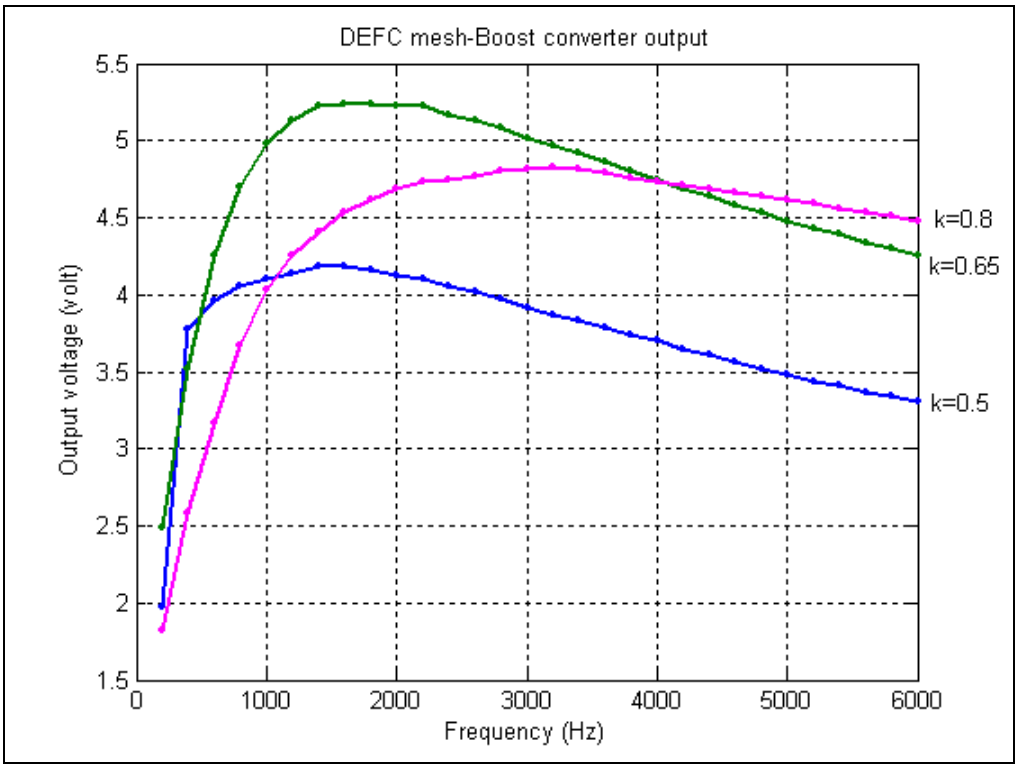

Figure 7.10: DEFC mesh boost-converter output characteristics

For frequency range 200 Hz to 4 kHz, the maximum output voltage delivered to the load is achieved at 65% duty cycle. System operation at 80% duty cycle achieves maximum output voltage characteristics at frequencies exceeding 4 kHz. For switching frequencies below 1 kHz, operation at duty cycle of 80% results in lower output voltage as compared to 50% and 65% duty cycle for the same switching frequency range.

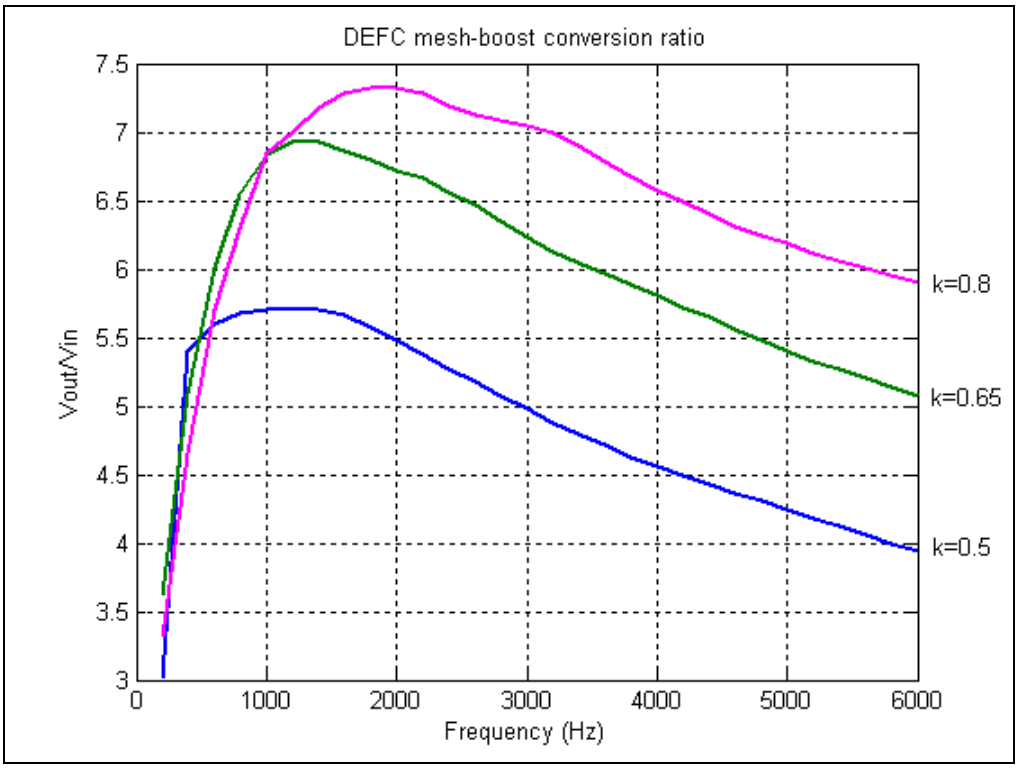

Figure 7.11: DEFC mesh-boost conversion ratio

DEFC mesh-boost converter system supplies power to a 10 kΩ load. Thus the maximum powers delivered to the load at respective duty cycle are: 1.755 mW at 50%, 2.74 mW at 65%, and 2.33 mW at 80% duty cycle. Thus, experimental results indicate that operation of DEFC mesh-boost converter system achieves greatest power transfer at 65% duty cycle, as the switching transistor operates at a switching frequency of 1400 Hz.

DEFC Nickel-foam electrodes exhibit different performances than DEFC Nickel-mesh electrodes. DEFC foam-boost converter system operation at 50% duty cycle assures the highest output voltage at switching frequencies below 2800 Hz, as shown in Fig. 7.12.

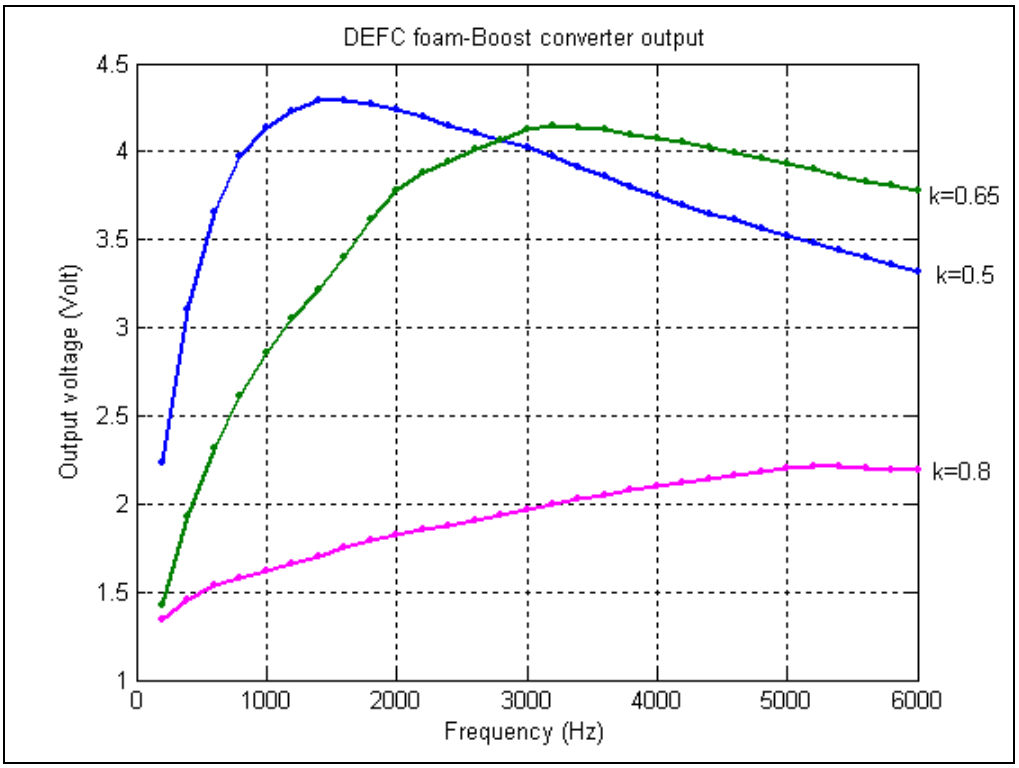

Figure 7.12: DEFC foam-Boost converter output characteristics

Switching frequencies above 2800 Hz and duty cycle of 65% operation determines maximum system output voltage. Unlike DEFC mesh-boost converter, system operation at 80% duty cycle yields lowest output voltage over the entire switching frequency range considered in this research.

Direct ethanol fuel cell foam-boost conversion ratio versus switching frequency characteristics exhibit maximum conversion ratios at lower frequencies, with highest conversion ratio at 80% duty cycle, as shown in Fig. 7.13.

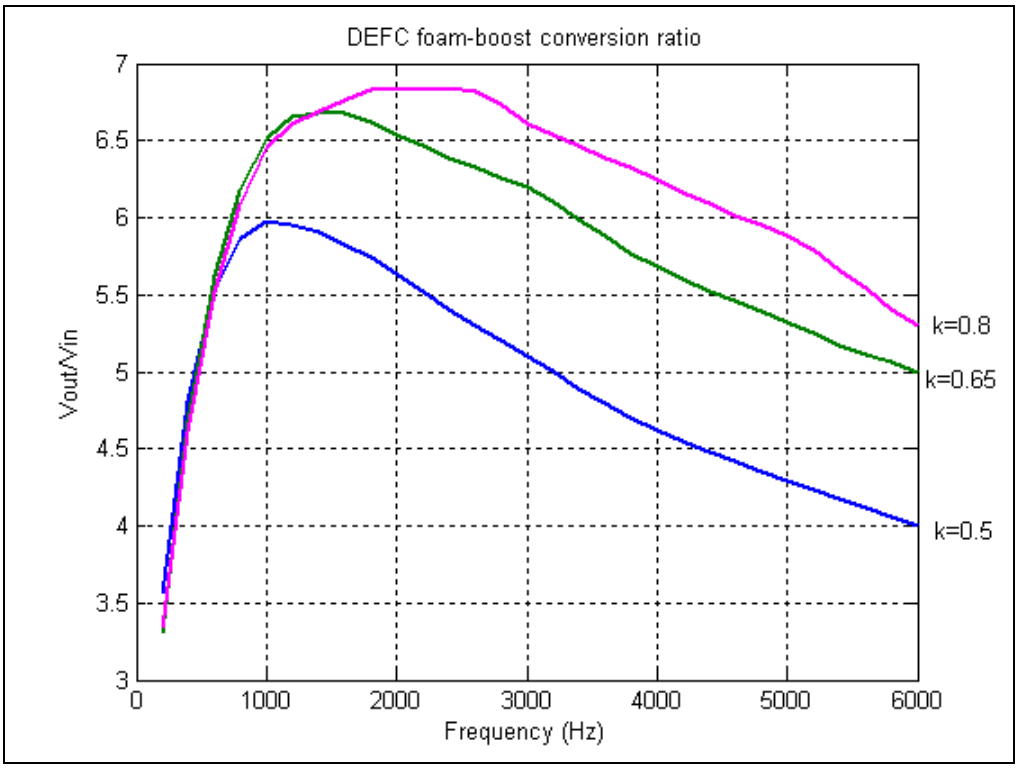

Figure 7.13: DEFC foam-boost conversion ratio

The DEFC-foam interfaced to a boost converter exhibits a transient regime that is dependent on the switching frequency, as shown in Figure 7.14 (for 50% duty cycle). The maximum output voltage is achieved few seconds after the converter starts its operation, then the system output voltage decays to a steady-state value. Different output voltages were measured for different switching frequencies at constant duty cycle, as shown in Figure 7.14.

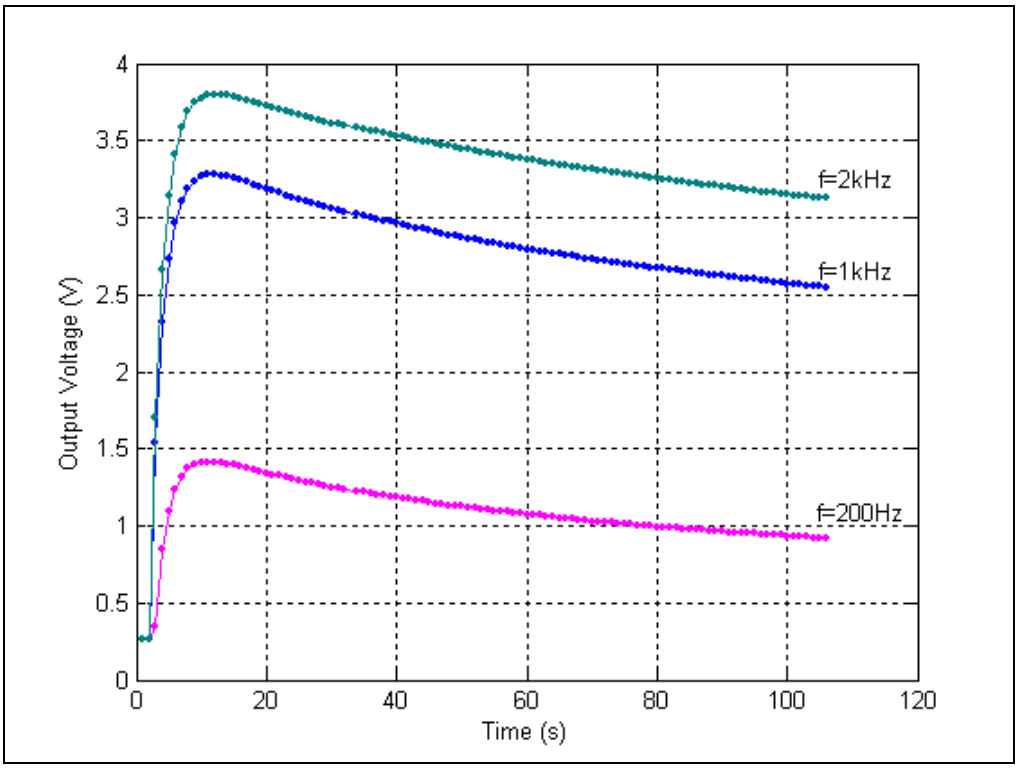

Figure 7.14: DEFC-foam-boost converter output at 50% duty cycle

Similar transients were observed for DEFC-boost converter operation at 65% and 80% duty cycles.

7.4 Buck-Boost Converter-Driven Power Systems

Buck-boost converter systems exhibit an inverted polarity of the output voltage, as compared to the input voltage. This particularity excludes the use of electrolytic capacitors for the output filter. For practicality purpose, a ceramic capacitor of 105.4 nF was used.

7.4.1 NiCd Battery–Buck-Boost Converter System

NiCd batteries terminals voltage is altered by the buck-boost converter duty cycle, and by the switching frequency at which the system operates. Therefore, the voltage output for NiCd-buck-boost converter system reaches peak values function of switching frequency and duty cycle operation regimes, as shown in Fig. 7.15.

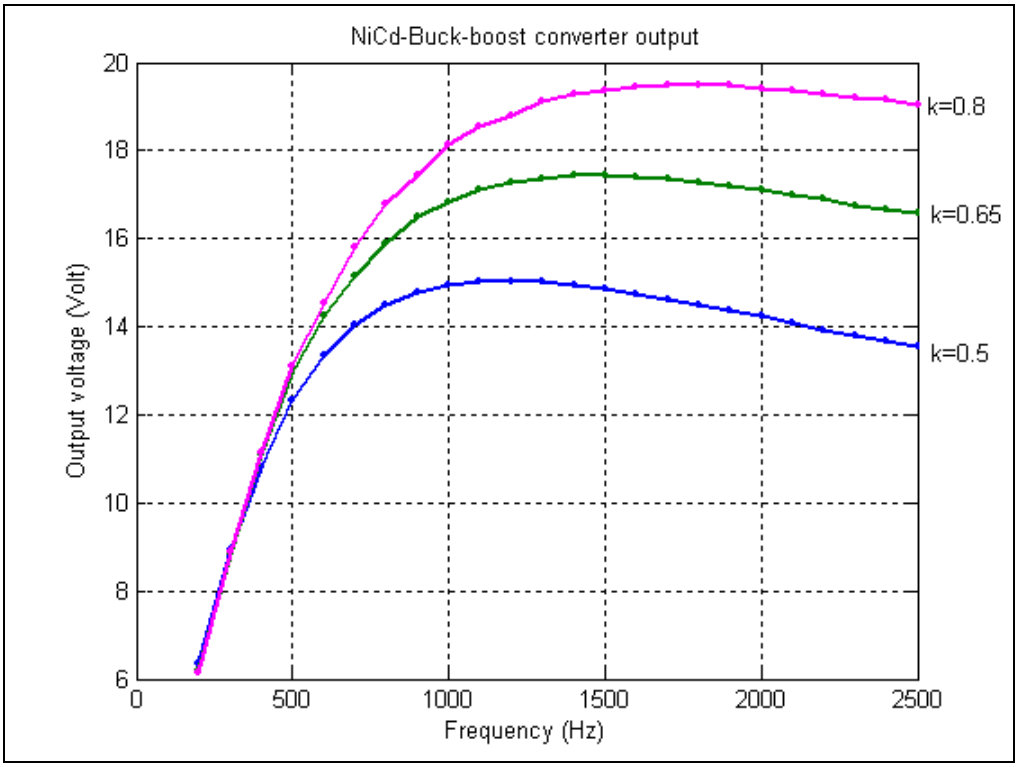

Figure 7.15: NiCd-Buck-boost converter output characteristics

NiCd-buck-boost system exhibit output voltages of varying values over the switching frequency range, and are always proportional to the duty cycle value, i.e., greater output voltage is obtained at greater duty cycle, provided the switching frequency is maintained constant.

7.4.2 DEFC–Buck-Boost Converter System

During switching transistor *time-on*, the current flows through inductor *L*, switching transistor Q_{switch}, and fuel cell. This increases the current drawn by the converter from the power source, which determines a decrease in the fuel cell voltage.

During converter sequential switching, the fuel cell output voltage is lower than the open circuit voltage. The electrochemistry within the fuel cell is dependent on circuit current, during *on* cycle. System output voltage, measured across load terminals, is dependent on the switching frequency, suggesting a direct dependence of fuel cell chemical activity to the switching frequency and duty cycle operation of the converter.

For switching frequencies in the range of 200 Hz to 1.8 kHz, DEFC mesh-buck-boost system operation at 50%, exhibits maximum voltage output, as shown in Fig. 7.16.

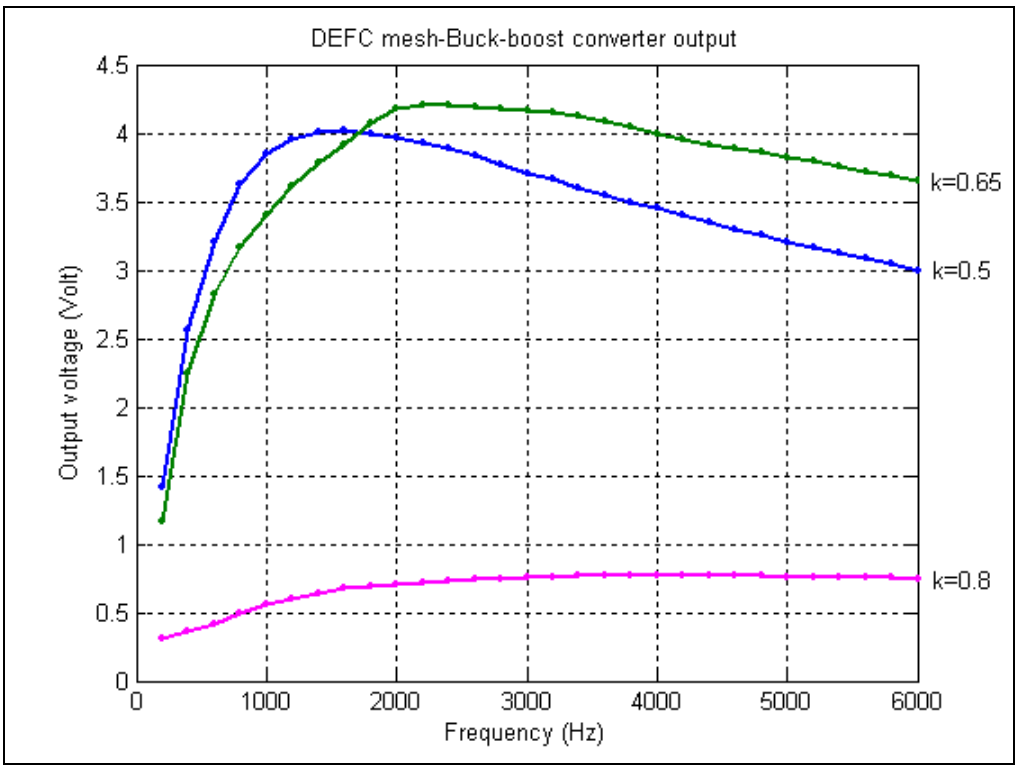

Figure 7.16: DEFC mesh-buck-boost converter output characteristics

System operation at switching frequencies beyond 1.8 kHz, achieves maximum voltage output when operating at 65% duty cycle. Unexpectedly, system operation at 80% duty cycle is characterized by lowest output voltage, as compared to 50% and 65% duty cycle regimes.

Figure 7.17 shows the input-output voltage conversion ratios for three duty cycles over a switching frequency range from 200 Hz to 6 kHz. Maximum conversion ratio, for DEFC mesh-buck-boost converter system, is achieved at 65% duty cycle, over the entire switching frequency range considered.

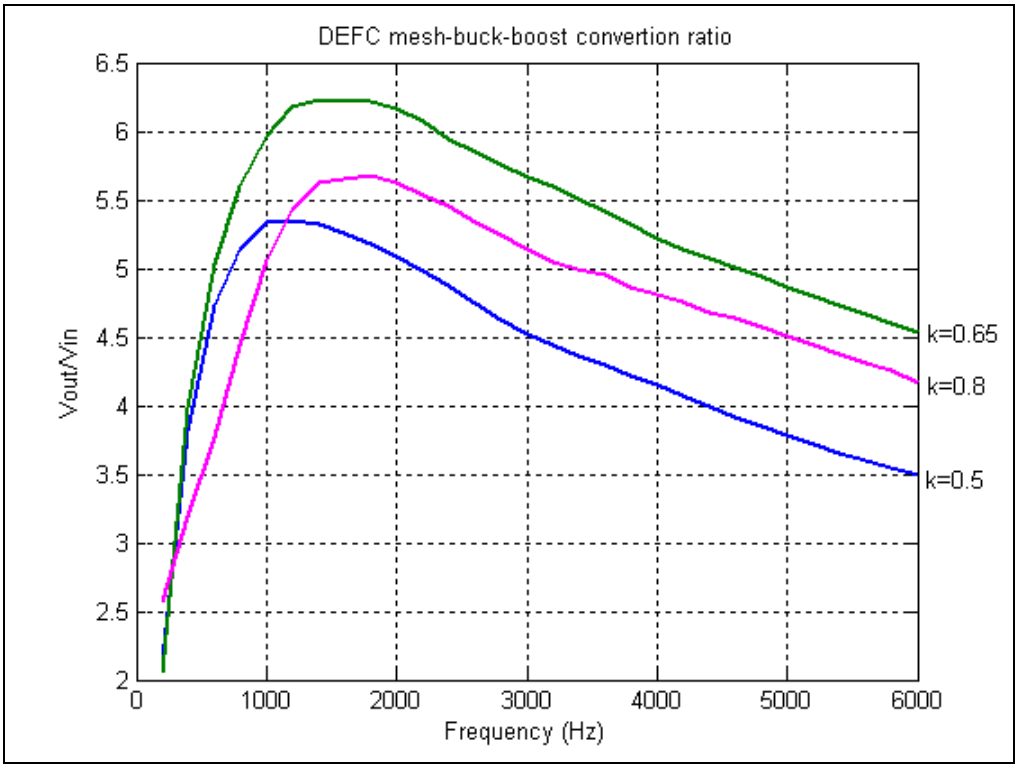

Figure 7.17: DEFC mesh-buck-boost conversion ratios

Maximum output voltage, and consequently maximum power transfer, is achieved by the DEFC foam-buck-boost converter system at 65% duty cycle, and 2.2 kHz switching frequency, as shown in Fig. 7.18.

System operation at 80% duty cycle resulted in lowest output voltage, and implicitly lowest power transfer, over the entire switching frequency range. System

operation at frequencies lower than 500 Hz, have yielded maximum output voltage for 50% duty cycle.

Overall, operation at 80% duty cycle was not characterized by maximum performance for DEFC foam-buck-boost system, at any switching frequency, as shown in Fig. 7.18

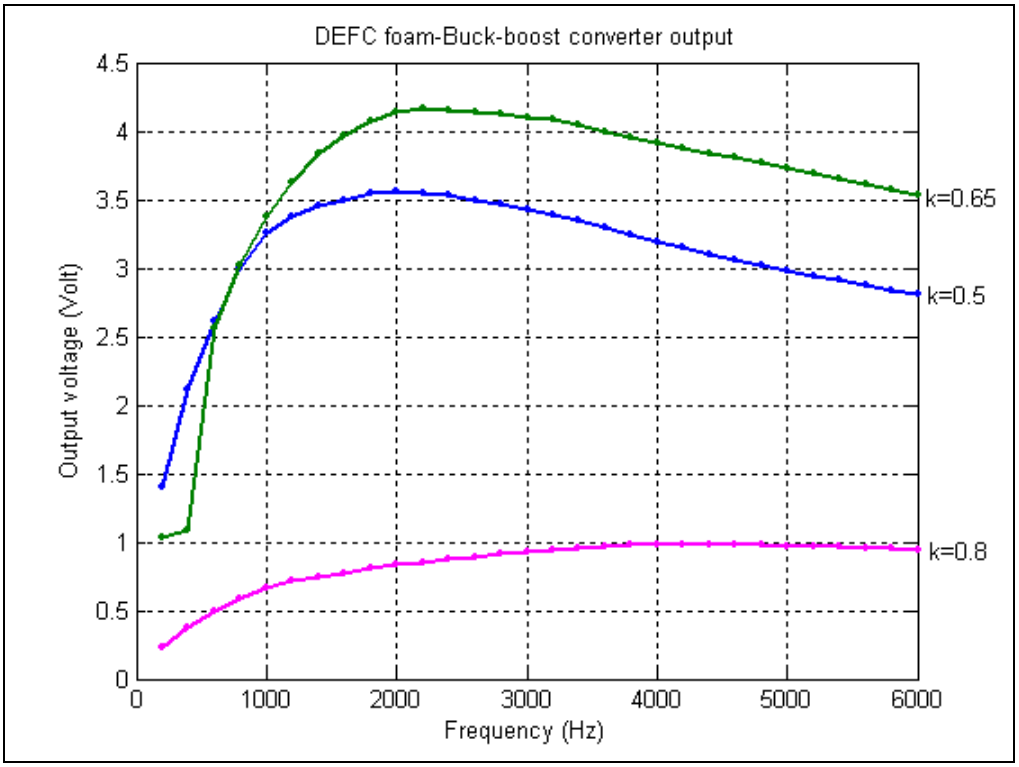

Figure 7.18: DEFC foam-buck-boost converter output characteristics

DEFC foam-buck-boost converter system exhibits input-output voltage maximum conversion ratio at 50% duty cycle, for switching frequencies below 500 Hz. Maximum conversion ratio for this system is dominated by a duty cycle of 65%, at frequencies in excess of 500 Hz. Figure 7.19hows that the conversion ratios, for 50%, 65%, and 80% duty cycles of the system, are plotted with respect to the switching frequency.

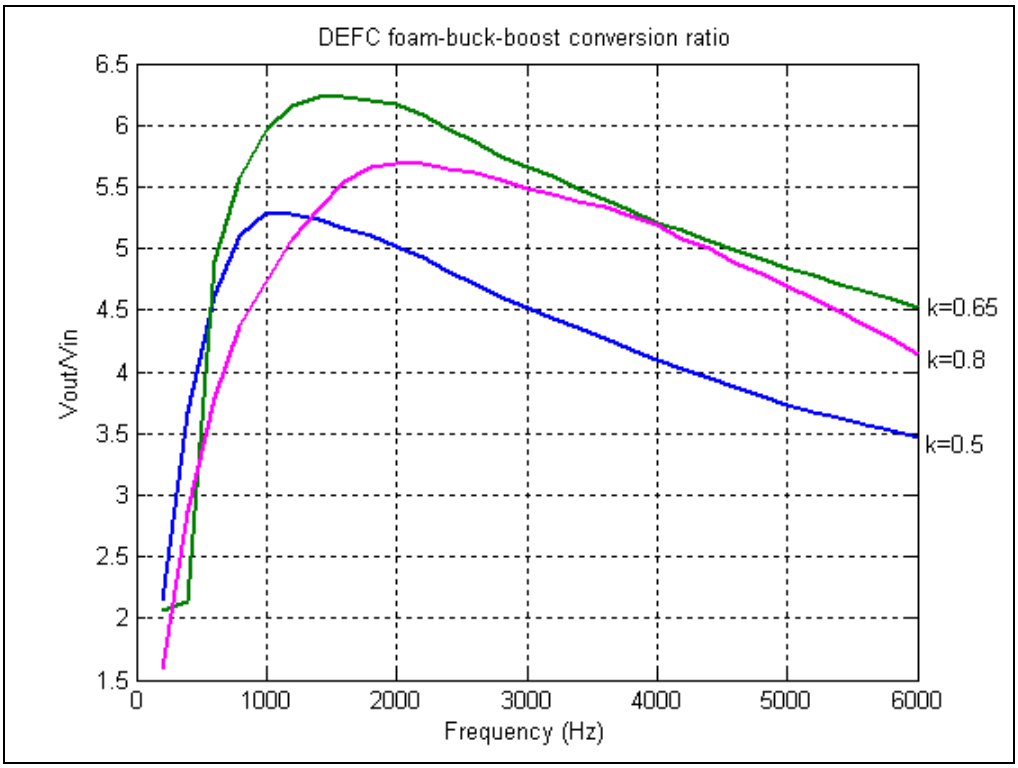

Figure 7.19: DEFC foam-buck-boost conversion ratios

CHAPTER 8 - Conclusions and Future Research

Development of Fourier-series models for DC–DC converters is presented in this research. Detailed analysis and modeling was performed, for buck, boost, and buck-boost converters, interfaced to ideal DC voltage sources. The DC power sources studied in this work are Nickel-Cadmium batteries (NiCd) and Direct Ethanol Fuel Cells (DEFC). Output voltages were measured for the three individual DC power sources, as interfaced to each type of DC–DC converter. Three different duty cycles, of triggering signal, were employed, over a predetermined switching frequency range. This work presented a novel approach in modeling DC–DC converters, and DC power systems.

8.1 Conclusions

The research included an extensive literature review of DC–DC converter models, and DC power source characteristics and modeling techniques. Results of literature review indicated the need of comprehensive models for DC power system, in general, and for DC–DC converters, in particular. The work introduces the electrochemistry, physics, and thermodynamics associated with DC power sources operation. Detailed discussion of NiCd batteries, fuel cells, and electrochemical equations describing their operation are included.

The development of Fourier-series models for DC–DC converters is given. The foundation of Fourier-series models consists of approximating any periodic wave, voltage and/or current, as a sum of sinusoidal harmonics. The frequencies and amplitudes of fundamental sinusoid and its harmonics were easily computed, based on fundamental frequency and amplitude of the considered wave. For an ideal voltage sources as the

input for a DC power system, the Fourier-series models were accurate in describing the average output voltages, the wave shapes of ripple voltages, and the inductor currents.

Employing real DC power sources, i.e., NiCd batteries, and direct ethanol fuel cells, the measured output voltages, for boost and buck-boost systems, were not in agreement with the Fourier-series models. Thus, the DC power source characteristics should be taken in consideration for accurate models. Complex impedances and polarization curves were determined for DC power sources employed in this research. Comparison of model predictions and experimental data suggests that the electrochemistry characteristic of each DC power source is altered by the electric current flow, and by the switching frequency at which DC–DC converters operate. Preliminary findings suggest an increase of electric current delivered by each cell, as the switching frequency increases. Visual observations indicate an increased electrochemical activity in the DEFC, for boost and buck-boost converter topologies. The increased electrochemical activity was represented by the excess of carbon-dioxide generation within the fuel cells, observed during switching transistor commutation. Concomitant with increased electrochemical activity, the voltage at fuel cells terminals dropped. Similar findings, with regard to terminals voltage drop, were noted for NiCd batteries in boost and/or buck-boost driven DC power systems. Based on these findings, Fourier-series models added an electrochemical–current coefficient to the current equation, thus accounting for the electrochemical processes within the DC power source. Fourier-series models developed in this work are beneficial to the designer of DC power systems, especially when employing fuel cells as DC power sources. The equivalent systems, developed through Fourier-series approach, are linear, time-invariant systems, thus system stability can be evaluated. Complex impedances and voltage-current characteristics vary for different types of DC power sources, which can alter the expected output voltages and currents, whenever under sequential switching operation regimes. Thus, the Fourier-series models presented require additional “tuning” of the DC power source considered by the designer. Electrochemical coefficients and/or impedance coefficients are determined empirically.

The work introduces Fourier-series models as a new method of DC–DC converters modeling. The research determines the output characteristics of DC power

systems employing sequential switching circuitry. Direct Ethanol Fuel Cells electrochemistry is altered by the sequential switching of DC–DC converters, in particular boost and buck-boost converters. The Fourier-series model can be applied to any sequential switching system.

8.2 Publications and Products

Part of this work has been presented at the 38th North American Power Symposium, Carbondale, IL, 2006, in one conference paper. Another paper has been presented at the 39th North American Power Symposium, Las Cruces, NM, 2007. A more comprehensive paper has been submitted to IEEE Transactions on Power Electronics. The Fourier-series models of DC power systems are under consideration as an interactive educational tool for power electronics courses at both Pittsburg State University and Mississippi Valley State University. The findings of this research are instrumental in the design of power systems for NASA-EPSCoR high altitude airplane project. ACTA-nanotech, the industry supporter of this research, will use the Fourier-series models and the collected data on DEFC converter-driven power systems to design the new generation of DEFC power systems for transportation and residential applications.

8.3 Future Work

The following research can be considered as an extension of the present work:

1) Development of DC-AC converter models through Fourier-series representation of sequential switching.
2) Investigate fuel-cell electrochemical activity enhancement, employing buck-boost converters to emulate short-circuit conditions of the power source.

3) Use the Fourier-series models, of DC power systems, to reduce the amount of Platinum-alloy catalyst for PEM fuel cells, thus reducing their cost.
4) Investigate the effectiveness of Fourier-series models as educational tools for power electronics courses.
5) Investigate the applicability of Fourier-series method in modeling DC motors electric commutation.
6) Investigate the correlation between the polarization curve and the complex impedance of electrochemical DC power sources.

References

[1] Fuel Cell Handbook, Office of Fossil Energy, U.S. Department of Energy, 4th Edition, November 1998.

[2] J. A. Smith, M. H. Nehrir, V. Gerez, S. R. Shaw, "A broad look at the workings, types, and applications of fuel cells," *Proc. IEEE Power Engineering Society,* pp. 70-75, 2002.

[3] S. Thomas and M. Zalbowitz, "Fuel Cells – Green Power," *Los Alamos Laboratory, Los Alamos, NM,* (online: http://education.lanl.gov/resources/fuelcells.

[4] N. M. Sammers and R. Boersma, "Small-scale fuel cells for residential use," *Journal of Power Sources,* vol. 86, pp. 98-110, 2000.

[5] C. Wang, M. H. Nehrir, and S. R. Shaw, "Dynamic models and model validation for PEM fuel cells using electrical circuits," *IEEE Transactions on Energy Conversion*, vol. 20, no. 2, pp. 442-451, June 2005.

[6] J.C. Amphlett, R.M. Baumert, R.F. Mann, B.A. Peppley, and P.R. Roberge, "Performance modeling of the Ballard Mark-IV solid polymer electrolyte fuel cell," *Journal of Electrochemical Society*, vol. 142, no. 1, pp. 1-8, January 1995.

[7] A. Rowe and X. Li, "Mathematical modeling of proton exchange membrane fuel cells," *Journal of Power Sources*, vol. 102, no. 1-2, pp. 82-96, December 2001.

[8] J.C. Amphlett, R.F. Mann, B.A. Peppley, P.R. Roberge, and A. Rodrigues, "A model predicting transient responses of proton exchange membrane fuel cells," *Journal of Power Sources*, vol. 61, no. 1-2, pp. 183-188, July/August 1996.

[9] R. Cowden, M. Nahon, and M.A. Rosen, "Modeling and analysis of a solid polymer fuel cell system for transportation applications," *International Journal of Hydrogen Energy*, vol. 26, no. 6, pp. 615-623, June 2001.

[10] C. E. Chamberlin, "Modeling of proton exchange membrane fuel cell performance with an empirical equation," *Journal of Electrochemical Society*, vol. 142, no. 8, August 1995.

[11] D. Bevers and M. Wöhr, "Simulation of polymer electrolyte fuel cell electrode," *Journal of Applied Electrochemistry*, vol. 27, no. 11, pp. 1254-1264, November 1997.

[12] J. Hamelin, K. Agbossou, A. Laperrière, F. Laurencelle, and T. K. Bose, "Dynamic behavior of a PEM fuel cell stack for stationary applications," *International Journal of Hydrogen Energy*, vol. 26, no. 6, pp. 625-629, June 2001.

[13] M. Wöhr, K. Bolwin, W. Schurnberger, M. Fischer, W. Neubrand, and G. Eigenberger, "Dynamic modeling and simulation of a polymer membrane fuel cell including mass transporting limitations," *International Journal of Hydrogen Energy*, vol. 23, no. 3, pp. 213-218, March 1998.

[14] H. P. van Bussel, F. G. Koene, and R. K. Mallant, "Dynamic model of solid polymer fuel cell water management," *Journal of Power Sources*, vol. 71, no. 1-2, pp. 218-222, March 1998.

[15] J. Laramine and A. Dicks. Fuel Systems, Explained. John Willey & Sons, 2003.

[16] A. Schneuwly, M. Bärtschi, V. Hermann, G. Sartorelli, R. Gallay, and R. Koetz, "BOOSTCAP double-layer capacitors for peak power automotive applications," *Proc. International Advanced Automotive Battery Conference*, Las Vegaas, NV, 2002.

[17] M. T. Iqbal, "Simulation of a small wind fuel cell hybrid energy system," *Renewable Energy*, vol. 28, no. 4, pp. 511-522, April 2003.

[18] W. Z. Black and J. G. Hartley. Thermodynamics. Harper-Collins, 3rd Edition, 1996.

[19] W. Vielstich, A. Lamm, and H. A. Gastaiger. Handbook of Fuel Cells, Fundamentals, Technology, and Applications. John Wiley & Sons, 2003.

[20] P. M. Gomadan, and J. W. Weidner, "Analysis of electrochemical impedance spectroscopy in proton exchange membrane fuel cells," *International Journal of Energy Research*, vol. 29, pp. 1133-1151, March 2005.

[21] A. Lasia, "Electrochemical impedance spectroscopy and its applications," *Modern Aspects of Electrochemistry*, vol. 32, pp. 143-248, Academic/Plenum, New York, 1999.

[22] O. Antoine, Y. Bultel, and R. Durand, "Oxygen reduction reaction kinetics and mechanism on platinum nanoparticles inside Nafion," *Journal of Electroanalytical Chemistry*, vol. 499, pp. 85-94, 2001.

[20] J. T. Pukrushpan, H. Peng, and A. G. Stefanopoulus, "Simulation and analysis of transient fuel cell system performance based on a dynamic reactant flow model," *ASME-Proceedings of IMECE,* New Orleans, LA, 2002.

[21] W. C. Yang, B. Bates, N. Fletcher, R. Pow, "Control Challenges and Methodologies in Fuel Cell Vehicle Development," *Proc. International Conference on Transportation Electronics*, Dearborn, MI, 1998.

[22] W. Friede, S. Raël, and B. Davat, "Mathematical model and characterization of the transient behavior of a PEM fuel cell," *IEEE Transactions on Power Electronics*, vol. 19, no. 5, pp. 1234-1241, September 2004.

[23] G. Maggio, V. Recupero, and L. Pino, "Modeling polymer electrolyte fuel cells: An innovative approach," *Journal of Power Sources*, vol. 101, pp. 275-286, October 2001.

[24] A. P. Saab, F. H. Garzon, and T. A. Zawodzinski, "Determination of ionic and electronic resistivities in carbon/polyelectrolyte fuel-cell composite electrodes," *Journal of the Electrochemical Society*, vol. 149, no. 12, pp. A1541-A1546, 2002.

[25] H. A. Gasteiger and M. F. Mathias, "Fundamental research and development challenges in polymer electrolyte fuel cell technology," *Proc. Electrochemical Society Meeting*, Salt Lake City, UT, 2003.

[26] T. Abe, H Shima, W. Kuniaki, and Y. Ito, "Study of PEFCs by AC impedance, current interrupt, and Dew point measurements," *Journal of the Electrochemical Society*, vol. 151, no. 1, pp. A101-A105, 2004.

[27] M. Ciureanu and H. Wang, "Electrochemical independence study of electrode-membrane assemblies in PEM fuel cells," *Journal of the Electrochemical Society*, vol. 146, no. 11, pp. 4031-4040, 1999.

[28] A. P. Saab, F. H. Garzon, and T. A. Zawodzinski, "The effects of processing conditions and chemical composition on electronic and ionic resistivities of fuel cell

electrode composites," *Journal of the Electrochemical Society*, vol. 150, no. 2, pp. A214-A218, 2003.

[29] G. Li and P. G. Pickup, "Ionic conductivity of PEMFC electrodes: Effect of Nafion loading," *Journal of the Electrochemical Society*, vol. 150, no. 11, pp. C745-C752, 2003.

[30] G. Chen, C. C. Waraksa, H. Cho, D. D. Mcdonald, and T. Mallouk, "EIS studies of porous oxygen electrodes with discrete particles: I. Impedance of oxide catalyst supports," *Journal of the Electrochemical Society*, vol. 150, no. 9, pp: E423-E428, 2003.

[31] Q. Guo and R. E. White, "A steady-state impedance model for a PEM cathode," *Journal of the Electrochemical Society*, vol. 151, no. 4, pp. E133-E139, 2004.

[32] F. Jouen, G. Lindbergh, and K. Wiezell, "Transient techniques for investigation mass-transport limitations in gas diffusion electrodes: I. Experimental characterization of the PEFC cathode," *Journal of the Electrochemical Society*, vol. 150, no. 12, pp. A1711-A1717, 2003.

[33] F. Jouen and G. Lindbergh, "Transient techniques for investigation mass-transport limitations in gas diffusion electrodes: I. Modeling the PEFC cathode," *Journal of the Electrochemical Society*, vol. 150, no. 12, pp. A1699-A1710.

[34] Q. G. Yan, Q. Y. Liu, and J. X. Wu, "Experiments Toward Fundamental Validation of PEM Fuel Cell Models," *Proc. International Conference on Fuel Cell Science, Engineering and Technology*, 2005, Ypsilanti, MI.

[35] J. X. Wu and Q. Y. Liu "Simulation-aided PEM fuel cell design and performance evaluation," *Transactions of ASME*, vol. 2, pp. 20-28, February 2005.

[36] M. P. Kennedy and L.O. Chua, "Van der Pol and chaos," *IEEE Transactions on Circuits and Systems*, vol. 33, no. 10, pp. 974-980, October 1986.

[37] D. C. Hamill, "Learning about chaotic circuits with SPICE," *IEEE Transactions on Education*, vol. 36, no. 1, pp. 28-35, February 1993.

[38] R. D. Middlebrook and S. Cuk, "A general unified approach to modeling switching converter power stages," *Power Processing and Electronics Specialists Conference*, pp. 18-34, Cleveland, OH, 1976.

[39] J. Baillieul, R.W. Brockett, and R.B. Washburn, "Chaotic motion in nonlinear feedback systems," *IEEE Transactions on Circuits and Systems*, vol. 27, no. 11, pp. 990-997, November 1980.

[40] G. W. Wester and R. D. Middlebrook, "Low-frequency characterization of switched dc-to-dc converters," *Power Processing and Electronics Specialists Conference*, pp. 9-20, Atlantic City, NJ, May 1972.

[41] R.W. Brockett and J.R. Wood, "Understanding power converter chaotic behavior in protective and abnormal modes," *Powercon 11*, 1984.

[42] D.C. Hamill and D.J. Jefferies, "Subharmonics and chaos in a controlled switched-mode power converter," *IEEE Transactions on Circuits and Systems*, vol 35, no. 8, pp. 1059-1061, August 1988.

[43] J.H. Deane and D.C. Hamil, "Instability, subharmonics and chaos in power electronic systems," *IEEE Transactions on Power Electronics*, vol. 5, no. 3, pp. 260-268, July 1990.

[44] J.H. Deane and D.C. Hamil, "Analysis, simulation and experimental study of chaos in the buck converter," *Power Electronics Specialists Conference*, pp. 491-498, San Antonio TX, June 1990.

[45] J.H. Deane and D.C. Hamil, "Chaotic behavior in current-mode controlled dc-dc converter," *Electronics Letters*, vol. 27, no. 13, pp. 1172-1173, June 1991.

[46] D.C. Hamill, J.H. Deane and D.J. Jefferies, "Modeling of chaotic dc-dc converters by iterated nonlinear mapping," *IEEE Transactions on Power Electronics*, vol. 7, no. 1, pp. 25-36, January 1992.

[47] J.H. Deane, "Chaos in a current-mode controlled boost dc-dc converter," *IEEE Transactions on Circuits and Systems*, vol.39, no. 8, pp. 680-683, August 1992.

[48] D.C. Hamill, "Chaos in dc-dc converters," *IEE Digest*, no. 203, pp. 5.1-5.4, London, November 1992.

[49] J. Chen, D. Maksimovic, and R. Erickson, "A new low-stress buck-boost converter for universal-input PFC applications," *Proc. Applied Power Electronics Conference*, vol. 1, pp. 343-349, 2001.

[50] J. Chen, D. Maksimovic, and R. Erickson, "Buck-Boost PWM converters having two independently controlled switches," *Proc. IEEE Power Electronics Specialists Conference*, vol. 2, pp. 736-741, 2001.

[51] V. Vorperian, "Simplified analysis of PWM converters using model of PWM switch–Part 1: continuous conduction mode," *IEEE Transactions on Aeronautical and Electrical Systems*, vol. 26, no. 3, pp. 490-496, May 1990.

[52] V. Vorperian, "Simplified analysis of PWM converters using model of PWM switch–Part 2: discontinuous conduction mode," *IEEE Transactions on Aeronautical and Electrical Systems*, vol. 26, no. 3, pp. 497-505, May 1990.

[53] B. Johansson, "A comparison and an improvement of two continuous-time models for current-mode control," *IEEE International Telecommunication Energy Conference*, pp. 552-559, Montreal, Canada, 2002.

[54] S.P. Hsu, A. Brown, L. Rensink, and R.D. Middlebrook, "Modeling and analysis of switching DC-to-DC converters in constant frequency current-programmed mode," *IEEE Power Electronics Specialists Conference Record*, pp. 284-301, 1979.

[55] S. Pavljašević and D. Macsimović, "Using a discrete-time model for large-signal analysis of a current-programmed Boost converter," *IEEE Power Electronics Specialists Conference Record*, pp. 715-721, 1991.

[56] Yan-Fei Liu and Paresh C. Sen, "A General Unified Large Signal Model for Current Programmed DC-to-DC Converters," *IEEE Transactions on Power Electronics*, vol. 9, no. 4, pp. 414-424, July 1994.

[57] R.B. Ridley, "A new, continuous-time model for current-mode control," *IEEE Transactions on Power Electronics*, vol. 6, no. 2, pp. 271-280, 1991.

[58] R. Tymersky and D. Li, "State-space models for current programmed, pulse width-modulated converters," *IEEE Transactions on Power Electronics*, vol. 8, no. 3, pp. 271-278, 1993.

[59] R. Tymersky, "Application of the time-varying transfer function for exact small-signal analysis," *IEEE Transactions on Power Electronics*, vol. 9, no. 2, pp. 196-205, 1994.

[60] E. Gietl, “Space-shuttle 120-V/28-V fuel cell power system model”, *Private Communication,”* 2006.

[61] G. H. Xu, C. Chen, J. Wang, and D. D. Li, “Nonlinear control for AC/DC power system with nonlinear loads,” *International Conference on Power Systems Technology*, vol. 1, pp. 361-366, Singapore, 2004.

[62] Z. Yulin, and J. Jinguo, “Model and applications for harmonics analysis of AC/DC power electronic converters in high-power industrial drives,” *Canadian Conference on Electrical and Computer Engineering*, vol. 1, pp. 369-373, Toronto, Canada, 2001.

[63] N. Fernandopulle and R. T. Alden “Domain of stability of AC/DC power systems,” *Canadian Conference on Electrical and Computer Engineering*, vol. 1, pp. 433-438, Niagara Falls, Canada, 2004.

[64] E. W. Gholdston, K. Karimi, F. C. Lee, J. Rajagopalan, Y. Panov, and B. Manners, “Stability of large DC power systems using switching converters, with applications to the International Space Station,” *Proc. Intersociety Conference on Energy Conversion Engineering*, vol. 1, pp. 166-171, Canoga Park, CA, 1996.

[65] S. Mazumder, M. Alfayyoummi, A. H. Nayfeh, and D. Borojevic, “A theoretical and experimental investigationof the nonlinear dynamics of DC–DC converters,” *Proc. Power Electronics Specialists Conference*, vol.2, pp. 729-734, Galway, Ireland, 2000.

[66] K. Ogata. Modern Control Engineering. 4th Edition, Prentice-Hall, Inc., 2002.

[67] H. Kobayashi and P. M. Asbeck, “Active cancellation of switching noise for DC–DC converter-driven RF power amplifiers,” *IEEE MTT-S International Microwave Symposium*, vol. 3, pp. 1647-1650, Seattle, WA, 2002.

[68] J. H. Ly and K. Siri, "Frequency response analysis for DC–DC converters without small-signal linearization," *Proc. Applied Power Electronics Conference and Exposition*, vol. 2, pp. 1008-1013, Miami Beach, FL, 2003.

[69] R. L. Meade and R. Diffenderfer. Foundations of Electronics, Circuits and Devices. 4th Edition, Thomson-Delmar Learning, 2003.

[70] L. Zhijiong, S. Shapira, and K. Stiles, "Correlations of MOSFET transconductance: Its physical origins and relevance to analog MOSFET modeling and operation," *IEEE Transactions on Electron Devices*, vol. 50, no.3, pp. 853-858, 2003.

[71] M. Dogruel, "Input linearization of nonlinear systemsvia pulse-width control," *IEEE Transactions on Automatic Control*, vol. 48, no. 4, pp. 635-638, 2003.

[72] Z. Hu, B. Zhang, and W. Deng, "Output controllability of switched power converters as switched linear systems," *Proc. Power Electronics and Motion Control Conference*, vol. 3, pp. 1665-1668, Riga, Latvia, 2004.

[73] J. P. Hespanha, D. Liberzon, D. Angeli and E.D. Sontag, "Nonlinear-norm observability notions and stability of switched systems," *IEEE Transactions on Automatic Control*, vol. 50, no. 2, pp. 154-168, 2005.

[74] N. F. Marcia and G. J. Thaler. Modeling & Control of Dynamic Systems. Thomson Delmar Learning, 2005.

[75] R. A. Guineee, C. Lyden "A novel Fourier series time function for modeling and simulation of PWM," *IEEE Transactions on Circuits and Systems*, vol. 52, no. 11, pp. 2427-2435, 2005.

[76] F. Mişoc, M. M. Morcos, and J. Lookadoo, "Fourier-Series Models of DC–DC Converters," *38th North American Power Symposium*, pp. 233-240, Carbondale, IL, 2006.

[77] G. Fontes, C. Turpin, S. Astire, and T. A. Meynard, "Interactions Between Fuel Cells and Power Converters: Influence of Current Harmonics on a Fuel Cell Stack," *IEEE Transactions on Power Electronics*, vol. 22, no. 2, pp. 670-678, 2007.

Appendix A - MATLAB m-Files

MATLAB Implementation of Fourier-series Models

Graphical representations of Fourier-series models for of DC–DC converters are obtained through MATLAB instructions scripts particular to each type of converter, developed in Chapter 6. MATLAB program sources for each DC–DC converter model are shown.

A1: MATLAB instruction set for buck converter, ideal source

```
function buck6

%-------------------------------------------------------------------------
% This script evaluates the output voltage of a buck converter
% Author:    Florian Misoc
% Date:      October 15, 2006
% Version:   5, fsw = switching frequency (Hz)
% Copyright: Florian Misoc 2006
%-------------------------------------------------------------------------
tspan=[0 0.12]; % Time span of the simulation
xz0=[0; 0]; % Initial conditions for the two variables: zx(1)=iL, zx(2)=vC
% The equation is solved using ode45
ode45(@func6,tspan,xz0);
%-------------------------------------------------------------------------
function dxzdt=func6(t,xz)
R=100;
L=0.01;
C=0.0002;
M=2.6; %Voltage amplitude: 2.6 Volts <<< VOLTAGE-SOURCE
fsw=800; %Switching frequency: 200 Hz <<< FREQUENCY
W0=2*pi*fsw; %fundamental angular-frequency
N=21; %number of harmonics considered
K=0.65; % Duty cycle: K=20% (K=0.20) <<< DUTY CYCLE
for m=1
   for n=1:N
      Wn(m,n)=n*W0; %harmonics angular-frequencies
   end
end
[Wn];
```

```
W=[W0 Wn];
Mn0=M;
Co=K*M;
for n=1:N
    An(:,n)=(M/(n*pi))*sin(2*pi*n*K);
    Bn(:,n)=(-M/(n*pi))*(cos(2*pi*n*K)-1);
    Cn(:,n)=((An(:,n)^2)+(Bn(:,n)^2))^0.5;
    ph(:,n)=atan(Bn(:,n)\An(:,n));
end
[Cn];
[ph];
Vn=[Co Cn];
a11=-R/L;
a12=-1/L;
a21=1/C;
a22=-1/(R*C);
b11=(1/L);
b21=1/R*C;
B=ones(1,N+1);
Vg=[Vn(:,1);Vn(:,2)*sin(2*pi*fsw*t+ph(:,1));Vn(:,3)*sin(2*pi*2*fsw*t+ph(:,2));Vn(:,4)*sin(2*
pi*3*fsw*t+ph(:,3));Vn(:,5)*sin(2*pi*4*fsw*t+ph(:,4));Vn(:,6)*sin(2*pi*5*fsw*t+ph(:,5));Vn(:,
7)*sin(2*pi*6*fsw*t+ph(:,6));Vn(:,8)*sin(2*pi*7*fsw*t+ph(:,7));Vn(:,9)*sin(2*pi*8*fsw*t+ph(:
,8));Vn(:,10)*sin(2*pi*9*fsw*t+ph(:,9));Vn(:,11)*sin(2*pi*10*fsw*t+ph(:,10));Vn(:,12)*sin(2*
pi*11*fsw*t+ph(:,11));Vn(:,13)*sin(2*pi*12*fsw*t+ph(:,12));Vn(:,14)*sin(2*pi*13*fsw*t+ph(:
,13));Vn(:,15)*sin(2*pi*14*fsw*t+ph(:,14));Vn(:,16)*sin(2*pi*15*fsw*t+ph(:,15));Vn(:,17)*si
n(2*pi*16*fsw*t+ph(:,16));Vn(:,18)*sin(2*pi*17*fsw*t+ph(:,17));Vn(:,19)*sin(2*pi*18*fsw*t+
ph(:,18));Vn(:,20)*sin(2*pi*19*fsw*t+ph(:,19));Vn(:,21)*sin(2*pi*20*fsw*t+ph(:,20));Vn(:,22
)*sin(2*pi*21*fsw*t+ph(:,21))]; % Input voltage Fourier-series representation
Vfg=B*Vg;
%-------------------------------------------------------------------------
dxzdt=[a11*xz(1)+b11*Vfg;
    a21*xz(1)+a22*xz(2)];
```

A2: MATLAB instruction set for boost converter, ideal source

```
function boost6

%-------------------------------------------------------------------------
% This script evaluates the output voltage of a boost converter
% Author:    Florian Misoc
% Date:      October 25, 2006
% Version:   2
% Copyright: Florian Misoc 2006
%-------------------------------------------------------------------------
tspan=[0 0.2];
x0=[0.026; 2.6];
% The equation is solved using ode45
```

```
ode45(@fuct,tspan,x0);
%-------------------------------------------------------------------------
function dxdt=fuct(t,x)
R=100;
L=0.01;
rL=23.7;
C=0.0002;
M=2.6; %Voltage amplitude: 2.6 Volts <<< VOLTAGE-SOURCE
fsw=500; %Switching frequency: 200 Hz <<< FREQUENCY
per=1/fsw;
W0=2*pi*fsw; %fundamental angular-frequency
N=21; %number of harmonics considered
K=0.8; % Duty cycle: K=20% (K=0.20) <<< DUTY CYCLE
for m=1
   for n=1:N
      Wn(m,n)=n*W0; %harmonics angular-frequencies
   end
end
[Wn];
W=[W0 Wn];
Con=M/K;
for n=1:N
   An(:,n)=(M/(n*pi))*sin(2*pi*n*K);
   Bn(:,n)=(-M/(n*pi))*(cos(2*pi*n*K)-1);
   Cn(:,n)=((An(:,n)^2)+(Bn(:,n)^2))^0.5;
   ph(:,n)=atan(Bn(:,n)\An(:,n));
end
[Cn];
[ph];
Vn=[Con Cn];
a11=-rL/L;
a12=(1-K)/L;
a21=0;
a22=-1/(R*C);
b11=(1/L);
b21=1/(R*C);
B=ones(1,N+1);
Vfn=[Vn(:,1);Vn(:,2)*sin(W0*t+ph(:,1));Vn(:,3)*sin(2*W0*t+ph(:,2));Vn(:,4)*sin(3*W0*t+ph(
:,3));Vn(:,5)*sin(4*W0*t+ph(:,4));Vn(:,6)*sin(5*W0*t+ph(:,5));Vn(:,7)*sin(6*W0*t+ph(:,6));
Vn(:,8)*sin(7*W0*t+ph(:,7));Vn(:,9)*sin(8*W0*t+ph(:,8));Vn(:,10)*sin(9*W0*t+ph(:,9));Vn(:,
11)*sin(10*W0*t+ph(:,10));Vn(:,12)*sin(11*W0*t+ph(:,11));Vn(:,13)*sin(12*W0*t+ph(:,12))
;Vn(:,14)*sin(13*W0*t+ph(:,13));Vn(:,15)*sin(14*W0*t+ph(:,14));Vn(:,16)*sin(15*W0*t+ph(
:,15));Vn(:,17)*sin(16*W0*t+ph(:,16));Vn(:,18)*sin(17*W0*t+ph(:,17));Vn(:,19)*sin(18*W0
*t+ph(:,18));Vn(:,20)*sin(19*W0*t+ph(:,19));Vn(:,21)*sin(20*W0*t+ph(:,20));Vn(:,22)*sin(2
1*W0*t+ph(:,21))];
Von=B*Vfn; % Fourier-series representation of mode-1 input voltage
Cof=M/(1-K);
for m=1:N
   Am(:,m)=(M/(m*pi))*sin(2*pi*m*(1-K));
   Bm(:,m)=(-M/(m*pi))*(cos(2*pi*m*(1-K))-1);
   Cm(:,m)=((Am(:,m)^2)+(Bm(:,m)^2))^0.5;
```

```
    pm(:,m)=atan(Bm(:,m)\Am(:,m));
end
[Cm];
[pm];
Vm=[Cof Cm];
tau=W0*K*per;
Vfm=[Vm(:,1);Vm(:,2)*sin(W0*t+tau+pm(:,1));Vm(:,3)*sin(2*W0*t+tau+pm(:,2));Vm(:,4)*si
n(3*W0*t+tau+pm(:,3));Vm(:,5)*sin(4*W0*t+tau+pm(:,4));Vm(:,6)*sin(5*W0*t+tau+pm(:,5)
);Vm(:,7)*sin(6*W0*t+tau+pm(:,6));Vm(:,8)*sin(7*W0*t+tau+pm(:,7));Vm(:,9)*sin(8*W0*t+
tau+pm(:,8));Vm(:,10)*sin(9*W0*t+tau+ph(:,9));Vm(:,11)*sin(10*W0*t+tau+pm(:,10));Vm(:
,12)*sin(11*W0*t+tau+pm(:,11));Vm(:,13)*sin(12*W0*t+tau+pm(:,12));Vm(:,14)*sin(13*W
0*t+tau+pm(:,13));Vm(:,15)*sin(14*W0*t+tau+pm(:,14));Vm(:,16)*sin(15*W0*t+tau+pm(:,
15));Vm(:,17)*sin(16*W0*t+tau+pm(:,16));Vm(:,18)*sin(17*W0*t+tau+pm(:,17));Vm(:,19)*
sin(18*W0*t+tau+pm(:,18));Vm(:,20)*sin(19*W0*t+tau+pm(:,19));Vm(:,21)*sin(20*W0*t+t
au+pm(:,20));Vm(:,22)*sin(21*W0*t+tau+pm(:,21))];
Vof=B*Vfm; % Fourier-series representation of mode-2 input voltage
%-------------------------------------------------------------------------------
dxdt=[a11*x(1)+a12*x(2)+b11*Von
    a21*x(1)+a22*x(2)+b21*Vof];
```

A3: MATLAB instruction set for buck-boost converter, ideal source

```
function bubo

%-------------------------------------------------------------------------
% This script evaluates the output voltage of a buck-boost converter
% Author:    Florian Misoc
% Date:      October 25, 2006
% Version:   2
% Copyright: Florian Misoc 2006
%-------------------------------------------------------------------------
tspan=[0 0.25];
y0=[0; 0];
% The equation is solved using ode45
ode45(@funct,tspan,y0);
%-------------------------------------------------------------------------
function dydt=funct(t,y)
R=100;
L=0.01;
rL=23.7;
C=0.0002;
M=2.6; %Voltage amplitude: 2.6 Volts <<< VOLTAGE-SOURCE
fsw=500; %Switching frequency: 200 Hz <<< FREQUENCY
W0=2*pi*fsw; %fundamental angular-frequency
per=1/fsw;
N=21; %number of harmonics considered
K=0.8; % Duty cycle (in decimal format) <<< DUTY CYCLE
gama5=0.118;
gama6=0.286;
```

```
gama8=0.758;
for m=1
   for n=1:N
      Wn(m,n)=n*W0; %harmonics angular-frequencies
   end
end
[Wn];
W=[W0 Wn];
a11=-rL/L;
a12=0;
a21=0;
a22=-1/(R*C);
b11=(1/L);
b21=-gama8/C;
B=ones(1,N+1);
[Wn];
W=[W0 Wn];
Con=M/K;
for n=1:N
   An(:,n)=(M/(n*pi))*sin(2*pi*n*K);
   Bn(:,n)=(-M/(n*pi))*(cos(2*pi*n*K)-1);
   Cn(:,n)=((An(:,n)^2)+(Bn(:,n)^2))^0.5;
   ph(:,n)=atan(Bn(:,n)\An(:,n));
end
[Cn];
[ph];
Vn=[Con Cn];
B=ones(1,N+1);
Vfn=[Vn(:,1);Vn(:,2)*sin(W0*t+ph(:,1));Vn(:,3)*sin(2*W0*t+ph(:,2));Vn(:,4)*sin(3*W0*t+ph(
:,3));Vn(:,5)*sin(4*W0*t+ph(:,4));Vn(:,6)*sin(5*W0*t+ph(:,5));Vn(:,7)*sin(6*W0*t+ph(:,6));
Vn(:,8)*sin(7*W0*t+ph(:,7));Vn(:,9)*sin(8*W0*t+ph(:,8));Vn(:,10)*sin(9*W0*t+ph(:,9));Vn(:,
11)*sin(10*W0*t+ph(:,10));Vn(:,12)*sin(11*W0*t+ph(:,11));Vn(:,13)*sin(12*W0*t+ph(:,12))
;Vn(:,14)*sin(13*W0*t+ph(:,13));Vn(:,15)*sin(14*W0*t+ph(:,14));Vn(:,16)*sin(15*W0*t+ph(
:,15));Vn(:,17)*sin(16*W0*t+ph(:,16));Vn(:,18)*sin(17*W0*t+ph(:,17));Vn(:,19)*sin(18*W0
*t+ph(:,18));Vn(:,20)*sin(19*W0*t+ph(:,19));Vn(:,21)*sin(20*W0*t+ph(:,20));Vn(:,22)*sin(2
1*W0*t+ph(:,21))];
Von=B*Vfn;
dydt=[a11*y(1)+a12*y(2)+b11*Von;
    a21*y(1)+a22*y(2)+b21*(y(1))];
```

A4: MATLAB instruction set for buck converter, source resistance dependent

```
function buck568R
%--------------------------------------------------------------------------
% This script evaluates the output voltage of a buck converter, accounting
% for the source internal resistance, rs. Three sources are considered:
% NiCd battery, DEFC-mesh, and DEFC-foam
% Author:    Florian Misoc
% Date:      October 15, 2006
% Version:   5, fsw = switching frequency (Hz)
% Copyright: Florian Misoc 2006
%--------------------------------------------------------------------------
tspan=[0 0.2]; % Time span of the simulation
x568z0=[0; 0; 0; 0; 0; 0]; % Initial conditions for the two variables: zx(1)=iL, zx(2)=vC
% The equation is solved using ode45
ode45(@func568,tspan,x568z0);
%--------------------------------------------------------------------------
function dx568zdt=func568(t,x568z)
R=100; % Load resistance, 100 Ohms
L=0.01; % Inductor impedance, 10 mH
rL=23.7; % Inductor copper resistance, 23.7 Ohms
C=0.00022; % Filtering capacitor, 220 uF
M0=2.6; %Voltage amplitude: open-circuit voltage<<< VOLTAGE-SOURCE:
NiCd=2.6, DEFC=0.91
fsw=200; %Switching frequency: 200 Hz-6 kHz <<< FREQUENCY
W0=2*pi*fsw; %fundamental angular-frequency
N=21; %number of harmonics considered
K5=0.5; % Duty cycle: K=50% (K=0.50) <<< DUTY CYCLE
K6=0.65; % Duty cycle: K=65% (K=0.65) <<< DUTY CYCLE
K8=0.8; % Duty cycle: K=80% (K=0.80) <<< DUTY CYCLE
for m=1
   for n=1:N
      Wn(m,n)=n*W0; %harmonics angular-frequencies
   end
end
[Wn];
W=[W0 Wn];
NiCd=0.263; % internal resistance of NiCd battery, from the polarization curve
DEFC=1.44; % internal resistance of DEFC, from the polarization curve
rs=NiCd; % internal resistance of the source, rs=NiCd, or rs=DEFC
XC=(1/(W0*C)); %XC is the filtering capacitor reactance
ReZT=rs+rL+(R*XC/(R^2+XC^2)^0.5)*cos(-pi/2+atan(XC/R));
```

```
ImZT=W0*L+(R*XC/(R^2+XC^2)^0.5)*sin(-pi/2+atan(XC/R));
ZT=((ReZT^2+ImZT^2)^0.5); % total impedance during mode 1, (on)
MD=(rs/ZT)*M0; % MD is the voltage drop across source's internal resistance
M=M0-MD; % M is the effective voltage at source terminals
Co5=K5*M;
for n=1:N
   An5(:,n)=(M/(n*pi))*sin(2*pi*n*K5);
   Bn5(:,n)=(-M/(n*pi))*(cos(2*pi*n*K5)-1);
   Cn5(:,n)=((An5(:,n)^2)+(Bn5(:,n)^2))^0.5;
   ph5(:,n)=atan(Bn5(:,n)\An5(:,n));
end
[Cn5];
[ph5];
Vn5=[Co5 Cn5];
a11=-R/L;
a12=0;
a21=1/C;
a22=-1/(R*C);
b11=(1/L);
b21=0;
B=ones(1,N+1);
Vg5=[Vn5(:,1);Vn5(:,2)*sin(2*pi*fsw*t+ph5(:,1));Vn5(:,3)*sin(2*pi*2*fsw*t+ph5(:,2));
Vn5(:,4)*sin(2*pi*3*fsw*t+ph5(:,3));Vn5(:,5)*sin(2*pi*4*fsw*t+ph5(:,4));Vn5(:,6)*sin(
2*pi*5*fsw*t+ph5(:,5));Vn5(:,7)*sin(2*pi*6*fsw*t+ph5(:,6));Vn5(:,8)*sin(2*pi*7*fsw*
t+ph5(:,7));Vn5(:,9)*sin(2*pi*8*fsw*t+ph5(:,8));Vn5(:,10)*sin(2*pi*9*fsw*t+ph5(:,9));
Vn5(:,11)*sin(2*pi*10*fsw*t+ph5(:,10));Vn5(:,12)*sin(2*pi*11*fsw*t+ph5(:,11));Vn5(:
,13)*sin(2*pi*12*fsw*t+ph5(:,12));Vn5(:,14)*sin(2*pi*13*fsw*t+ph5(:,13));Vn5(:,15)*
sin(2*pi*14*fsw*t+ph5(:,14));Vn5(:,16)*sin(2*pi*15*fsw*t+ph5(:,15));Vn5(:,17)*sin(2
*pi*16*fsw*t+ph5(:,16));Vn5(:,18)*sin(2*pi*17*fsw*t+ph5(:,17));Vn5(:,19)*sin(2*pi*1
8*fsw*t+ph5(:,18));Vn5(:,20)*sin(2*pi*19*fsw*t+ph5(:,19));Vn5(:,21)*sin(2*pi*20*fs
w*t+ph5(:,20));Vn5(:,22)*sin(2*pi*21*fsw*t+ph5(:,21))];
Vfg5=B*Vg5;
Co6=K6*M;
for n=1:N
   An6(:,n)=(M/(n*pi))*sin(2*pi*n*K6);
   Bn6(:,n)=(-M/(n*pi))*(cos(2*pi*n*K6)-1);
   Cn6(:,n)=((An6(:,n)^2)+(Bn6(:,n)^2))^0.5;
   ph6(:,n)=atan(Bn6(:,n)\An6(:,n));
end
[Cn6];
[ph6];
Vn6=[Co6 Cn6];
Vg6=[Vn6(:,1);Vn6(:,2)*sin(2*pi*fsw*t+ph6(:,1));Vn6(:,3)*sin(2*pi*2*fsw*t+ph6(:,2));
Vn6(:,4)*sin(2*pi*3*fsw*t+ph6(:,3));Vn6(:,5)*sin(2*pi*4*fsw*t+ph6(:,4));Vn6(:,6)*sin(
2*pi*5*fsw*t+ph6(:,5));Vn6(:,7)*sin(2*pi*6*fsw*t+ph6(:,6));Vn6(:,8)*sin(2*pi*7*fsw*
t+ph6(:,7));Vn6(:,9)*sin(2*pi*8*fsw*t+ph6(:,8));Vn6(:,10)*sin(2*pi*9*fsw*t+ph6(:,9));
```

```
Vn6(:,11)*sin(2*pi*10*fsw*t+ph6(:,10));Vn6(:,12)*sin(2*pi*11*fsw*t+ph6(:,11));Vn6(:
,13)*sin(2*pi*12*fsw*t+ph6(:,12));Vn6(:,14)*sin(2*pi*13*fsw*t+ph6(:,13));Vn6(:,15)*
sin(2*pi*14*fsw*t+ph6(:,14));Vn6(:,16)*sin(2*pi*15*fsw*t+ph6(:,15));Vn6(:,17)*sin(2
*pi*16*fsw*t+ph6(:,16));Vn6(:,18)*sin(2*pi*17*fsw*t+ph6(:,17));Vn6(:,19)*sin(2*pi*1
8*fsw*t+ph6(:,18));Vn6(:,20)*sin(2*pi*19*fsw*t+ph6(:,19));Vn6(:,21)*sin(2*pi*20*fs
w*t+ph6(:,20));Vn6(:,22)*sin(2*pi*21*fsw*t+ph6(:,21))];
Vfg6=B*Vg6;
Co8=K8*M;
for n=1:N
    An8(:,n)=(M/(n*pi))*sin(2*pi*n*K8);
    Bn8(:,n)=(-M/(n*pi))*(cos(2*pi*n*K8)-1);
    Cn8(:,n)=((An8(:,n)^2)+(Bn8(:,n)^2))^0.5;
    ph8(:,n)=atan(Bn8(:,n)\An8(:,n));
end
[Cn8];
[ph8];
Vn8=[Co8 Cn8];
Vg8=[Vn8(:,1);Vn8(:,2)*sin(2*pi*fsw*t+ph8(:,1));Vn8(:,3)*sin(2*pi*2*fsw*t+ph8(:,2));
Vn8(:,4)*sin(2*pi*3*fsw*t+ph8(:,3));Vn8(:,5)*sin(2*pi*4*fsw*t+ph8(:,4));Vn8(:,6)*sin(
2*pi*5*fsw*t+ph8(:,5));Vn8(:,7)*sin(2*pi*6*fsw*t+ph8(:,6));Vn8(:,8)*sin(2*pi*7*fsw*
t+ph8(:,7));Vn8(:,9)*sin(2*pi*8*fsw*t+ph8(:,8));Vn8(:,10)*sin(2*pi*9*fsw*t+ph8(:,9));
Vn8(:,11)*sin(2*pi*10*fsw*t+ph8(:,10));Vn8(:,12)*sin(2*pi*11*fsw*t+ph8(:,11));Vn8(:
,13)*sin(2*pi*12*fsw*t+ph8(:,12));Vn8(:,14)*sin(2*pi*13*fsw*t+ph8(:,13));Vn8(:,15)*
sin(2*pi*14*fsw*t+ph8(:,14));Vn8(:,16)*sin(2*pi*15*fsw*t+ph8(:,15));Vn8(:,17)*sin(2
*pi*16*fsw*t+ph8(:,16));Vn8(:,18)*sin(2*pi*17*fsw*t+ph8(:,17));Vn8(:,19)*sin(2*pi*1
8*fsw*t+ph8(:,18));Vn8(:,20)*sin(2*pi*19*fsw*t+ph8(:,19));Vn8(:,21)*sin(2*pi*20*fs
w*t+ph8(:,20));Vn8(:,22)*sin(2*pi*21*fsw*t+ph8(:,21))];
Vfg8=B*Vg8;
dx568zdt=[a11*x568z(1)+b11*Vfg5;
    a21*x568z(1)+a22*x568z(2);
    a11*x568z(3)+b11*Vfg6;
    a21*x568z(3)+a22*x568z(4);
    a11*x568z(5)+b11*Vfg8;
    a21*x568z(5)+a22*x568z(6)];
 grid on
```

A5: MATLAB instruction set for boost converter, source resistance dependent

```
function boost568R
%-------------------------------------------------------------------------
% This script evaluates the output voltage of a boost converter, accounting
% for the source internal resistance, rs. Three sources are considered:
% NiCd battery, DEFC-mesh, and DEFC-foam
% Author:    Florian Misoc
% Date:      October 25, 2006
% Version:   3
% Copyright: Florian Misoc 2006
%-------------------------------------------------------------------------
tspan=[0 0.24];
x568x0=[0.0091; 0.91; 0.0091; 0.91; 0.0091; 0.91];
% The equation is solved using ode45
ode45(@fuct568,tspan,x568x0);
%-------------------------------------------------------------------------
function dx568xdt=fuct568(t,x568x)
R=100; % Load resistance, 100 Ohms
L=0.01; % Inductor impedance, 10 mH
rL=23.7; % Inductor copper resistance, 23.7 Ohms
C=0.00022; % Filtering capacitor, 220 uF
M0=0.91; %Voltage amplitude: open-circuit voltage<<< VOLTAGE-SOURCE:
NiCd=2.6, DEFC=0.91
fsw=6000; %Switching frequency: 200 Hz-6 kHz <<< FREQUENCY
per=1/fsw;
W0=2*pi*fsw; %fundamental angular-frequency
N=21; %number of harmonics considered
K5=0.5; % Duty cycle: in decimal format <<< DUTY CYCLE
K6=0.65; % Duty cycle: in decimal format <<< DUTY CYCLE
K8=0.8; % Duty cycle: in decimal format <<< DUTY CYCLE
for m=1
   for n=1:N
      Wn(m,n)=n*W0; %harmonics angular-frequencies
   end
end
[Wn];
W=[W0 Wn];
NiCd=0.263; % internal resistance of NiCd battery, from the polarization curve
DEFC=1.44; % internal resistance of DEFC, from the polarization curve
rs=NiCd; % internal resistance of the source, rs=NiCd, or rs=DEFC
MDon=(rs/((rs+rL)^2+(W0*L)^2)^0.5)*M0; % MD is the voltage drop across source's
internal resistance during ON time
Mon=M0-MDon; % M is the effective voltage at source terminals during ON time
XC=(1/(W0*C)); %XC is the filtering capacitor reactance
```

```
ReZT=rs+rL+(R*XC/(R^2+XC^2)^0.5)*cos(-pi/2+atan(XC/R));
ImZT=W0*L+(R*XC/(R^2+XC^2)^0.5)*sin(-pi/2+atan(XC/R));
ZT=((ReZT^2+ImZT^2)^0.5); % total impedance during mode 2, (off)
MDoff=(rs/ZT)*M0; % MD is the voltage drop across source's internal resistance during
OFF time
Moff=M0-MDoff; % M is the effective voltage at source terminals during OFF time
C05=Mon/(1-K5);
for n=1:N
   An5(:,n)=(Mon/(n*pi))*sin(2*pi*n*K5);
   Bn5(:,n)=(-Mon/(n*pi))*(cos(2*pi*n*K5)-1);
   Con5(:,n)=((An5(:,n)^2)+(Bn5(:,n)^2))^0.5;
   ph5(:,n)=atan(Bn5(:,n)\An5(:,n));
end
[Con5];
[ph5];
Vn5=[C05 Con5];
B=ones(1,N+1);
Vg5=[Vn5(:,1);Vn5(:,2)*sin(2*pi*fsw*t+ph5(:,1));Vn5(:,3)*sin(2*pi*2*fsw*t+ph5(:,2));
Vn5(:,4)*sin(2*pi*3*fsw*t+ph5(:,3));Vn5(:,5)*sin(2*pi*4*fsw*t+ph5(:,4));Vn5(:,6)*sin(
2*pi*5*fsw*t+ph5(:,5));Vn5(:,7)*sin(2*pi*6*fsw*t+ph5(:,6));Vn5(:,8)*sin(2*pi*7*fsw*
t+ph5(:,7));Vn5(:,9)*sin(2*pi*8*fsw*t+ph5(:,8));Vn5(:,10)*sin(2*pi*9*fsw*t+ph5(:,9));
Vn5(:,11)*sin(2*pi*10*fsw*t+ph5(:,10));Vn5(:,12)*sin(2*pi*11*fsw*t+ph5(:,11));Vn5(:
,13)*sin(2*pi*12*fsw*t+ph5(:,12));Vn5(:,14)*sin(2*pi*13*fsw*t+ph5(:,13));Vn5(:,15)*
sin(2*pi*14*fsw*t+ph5(:,14));Vn5(:,16)*sin(2*pi*15*fsw*t+ph5(:,15));Vn5(:,17)*sin(2
*pi*16*fsw*t+ph5(:,16));Vn5(:,18)*sin(2*pi*17*fsw*t+ph5(:,17));Vn5(:,19)*sin(2*pi*1
8*fsw*t+ph5(:,18));Vn5(:,20)*sin(2*pi*19*fsw*t+ph5(:,19));Vn5(:,21)*sin(2*pi*20*fs
w*t+ph5(:,20));Vn5(:,22)*sin(2*pi*21*fsw*t+ph5(:,21))];
Von5=B*Vg5;
Cof5=Moff/(1-K5);
for m=1:N
   Am5(:,m)=(Moff/(m*pi))*sin(2*pi*m*(1-K5));
   Bm5(:,m)=(-Moff/(m*pi))*(cos(2*pi*m*(1-K5))-1);
   Cm5(:,m)=((Am5(:,m)^2)+(Bm5(:,m)^2))^0.5;
   pm5(:,m)=atan(Bm5(:,m)\Am5(:,m));
end
[Cm5];
[pm5];
Vm5=[Cof5 Cm5];
tau5=W0*K5*per;
Vfm5=[Vm5(:,1);Vm5(:,2)*sin(W0*t+tau5+pm5(:,1));Vm5(:,3)*sin(2*W0*t+tau5+pm5(
:,2));Vm5(:,4)*sin(3*W0*t+tau5+pm5(:,3));Vm5(:,5)*sin(4*W0*t+tau5+pm5(:,4));Vm5(
:,6)*sin(5*W0*t+tau5+pm5(:,5));Vm5(:,7)*sin(6*W0*t+tau5+pm5(:,6));Vm5(:,8)*sin(7
*W0*t+tau5+pm5(:,7));Vm5(:,9)*sin(8*W0*t+tau5+pm5(:,8));Vm5(:,10)*sin(9*W0*t+t
au5+pm5(:,9));Vm5(:,11)*sin(10*W0*t+tau5+pm5(:,10));Vm5(:,12)*sin(11*W0*t+tau5
+pm5(:,11));Vm5(:,13)*sin(12*W0*t+tau5+pm5(:,12));Vm5(:,14)*sin(13*W0*t+tau5+p
m5(:,13));Vm5(:,15)*sin(14*W0*t+tau5+pm5(:,14));Vm5(:,16)*sin(15*W0*t+tau5+pm5
```

```
(:,15));Vm5(:,17)*sin(16*W0*t+tau5+pm5(:,16));Vm5(:,18)*sin(17*W0*t+tau5+pm5(:,
17));Vm5(:,19)*sin(18*W0*t+tau5+pm5(:,18));Vm5(:,20)*sin(19*W0*t+tau5+pm5(:,19
));Vm5(:,21)*sin(20*W0*t+tau5+pm5(:,20));Vm5(:,22)*sin(21*W0*t+tau5+pm5(:,21))];
Vof5=B*Vfm5;
C06=Mon/(1-K6);
for n=1:N
   An6(:,n)=(Mon/(n*pi))*sin(2*pi*n*K6);
   Bn6(:,n)=(-Mon/(n*pi))*(cos(2*pi*n*K6)-1);
   Con6(:,n)=((An6(:,n)^2)+(Bn6(:,n)^2))^0.5;
   ph6(:,n)=atan(Bn6(:,n)\An6(:,n));
end
[Con6];
[ph6];
Vn6=[C06 Con6];
B=ones(1,N+1);
Vg6=[Vn6(:,1);Vn6(:,2)*sin(2*pi*fsw*t+ph6(:,1));Vn6(:,3)*sin(2*pi*2*fsw*t+ph6(:,2));
Vn6(:,4)*sin(2*pi*3*fsw*t+ph6(:,3));Vn6(:,5)*sin(2*pi*4*fsw*t+ph6(:,4));Vn6(:,6)*sin(
2*pi*5*fsw*t+ph6(:,5));Vn6(:,7)*sin(2*pi*6*fsw*t+ph6(:,6));Vn6(:,8)*sin(2*pi*7*fsw*
t+ph6(:,7));Vn6(:,9)*sin(2*pi*8*fsw*t+ph6(:,8));Vn6(:,10)*sin(2*pi*9*fsw*t+ph6(:,9));
Vn6(:,11)*sin(2*pi*10*fsw*t+ph6(:,10));Vn6(:,12)*sin(2*pi*11*fsw*t+ph6(:,11));Vn6(:
,13)*sin(2*pi*12*fsw*t+ph6(:,12));Vn6(:,14)*sin(2*pi*13*fsw*t+ph6(:,13));Vn6(:,15)*
sin(2*pi*14*fsw*t+ph6(:,14));Vn6(:,16)*sin(2*pi*15*fsw*t+ph6(:,15));Vn6(:,17)*sin(2
*pi*16*fsw*t+ph6(:,16));Vn6(:,18)*sin(2*pi*17*fsw*t+ph6(:,17));Vn6(:,19)*sin(2*pi*1
8*fsw*t+ph6(:,18));Vn6(:,20)*sin(2*pi*19*fsw*t+ph6(:,19));Vn6(:,21)*sin(2*pi*20*fs
w*t+ph6(:,20));Vn6(:,22)*sin(2*pi*21*fsw*t+ph6(:,21))];
Von6=B*Vg6;
Cof6=Moff/(1-K6);
for m=1:N
   Am6(:,m)=(Moff/(m*pi))*sin(2*pi*m*(1-K6));
   Bm6(:,m)=(-Moff/(m*pi))*(cos(2*pi*m*(1-K6))-1);
   Cm6(:,m)=((Am6(:,m)^2)+(Bm6(:,m)^2))^0.5;
   pm6(:,m)=atan(Bm6(:,m)\Am6(:,m));
end
[Cm6];
[pm6];
Vm6=[Cof6 Cm6];
tau6=W0*K6*per;
Vfm6=[Vm6(:,1);Vm6(:,2)*sin(W0*t+tau6+pm6(:,1));Vm6(:,3)*sin(2*W0*t+tau6+pm6(
:,2));Vm6(:,4)*sin(3*W0*t+tau6+pm6(:,3));Vm6(:,5)*sin(4*W0*t+tau6+pm6(:,4));Vm6(
:,6)*sin(5*W0*t+tau6+pm6(:,5));Vm6(:,7)*sin(6*W0*t+tau6+pm6(:,6));Vm6(:,8)*sin(7
*W0*t+tau6+pm6(:,7));Vm6(:,9)*sin(8*W0*t+tau6+pm6(:,8));Vm6(:,10)*sin(9*W0*t+t
au6+pm6(:,9));Vm6(:,11)*sin(10*W0*t+tau6+pm6(:,10));Vm6(:,12)*sin(11*W0*t+tau6
+pm6(:,11));Vm6(:,13)*sin(12*W0*t+tau6+pm6(:,12));Vm6(:,14)*sin(13*W0*t+tau6+p
m6(:,13));Vm6(:,15)*sin(14*W0*t+tau6+pm6(:,14));Vm6(:,16)*sin(15*W0*t+tau6+pm6
(:,15));Vm6(:,17)*sin(16*W0*t+tau6+pm6(:,16));Vm6(:,18)*sin(17*W0*t+tau6+pm6(:,
```

```
17));Vm6(:,19)*sin(18*W0*t+tau6+pm6(:,18));Vm6(:,20)*sin(19*W0*t+tau6+pm6(:,19
));Vm6(:,21)*sin(20*W0*t+tau6+pm6(:,20));Vm6(:,22)*sin(21*W0*t+tau6+pm6(:,21))];
Vof6=B*Vfm6;
C08=Mon/(1-K8);
for n=1:N
   An8(:,n)=(Mon/(n*pi))*sin(2*pi*n*K8);
   Bn8(:,n)=(-Mon/(n*pi))*(cos(2*pi*n*K8)-1);
   Con8(:,n)=((An8(:,n)^2)+(Bn8(:,n)^2))^0.5;
   ph8(:,n)=atan(Bn8(:,n)\An8(:,n));
end
[Con8];
[ph8];
Vn8=[C08 Con8];
B=ones(1,N+1);
Vg8=[Vn8(:,1);Vn8(:,2)*sin(2*pi*fsw*t+ph8(:,1));Vn8(:,3)*sin(2*pi*2*fsw*t+ph8(:,2));
Vn8(:,4)*sin(2*pi*3*fsw*t+ph8(:,3));Vn8(:,5)*sin(2*pi*4*fsw*t+ph8(:,4));Vn8(:,6)*sin(
2*pi*5*fsw*t+ph8(:,5));Vn8(:,7)*sin(2*pi*6*fsw*t+ph8(:,6));Vn8(:,8)*sin(2*pi*7*fsw*
t+ph8(:,7));Vn8(:,9)*sin(2*pi*8*fsw*t+ph8(:,8));Vn8(:,10)*sin(2*pi*9*fsw*t+ph8(:,9));
Vn8(:,11)*sin(2*pi*10*fsw*t+ph8(:,10));Vn8(:,12)*sin(2*pi*11*fsw*t+ph8(:,11));Vn8(:
,13)*sin(2*pi*12*fsw*t+ph8(:,12));Vn8(:,14)*sin(2*pi*13*fsw*t+ph8(:,13));Vn8(:,15)*
sin(2*pi*14*fsw*t+ph8(:,14));Vn8(:,16)*sin(2*pi*15*fsw*t+ph8(:,15));Vn8(:,17)*sin(2
*pi*16*fsw*t+ph8(:,16));Vn8(:,18)*sin(2*pi*17*fsw*t+ph8(:,17));Vn8(:,19)*sin(2*pi*1
8*fsw*t+ph8(:,18));Vn8(:,20)*sin(2*pi*19*fsw*t+ph8(:,19));Vn8(:,21)*sin(2*pi*20*fs
w*t+ph8(:,20));Vn8(:,22)*sin(2*pi*21*fsw*t+ph8(:,21))];
Von8=B*Vg8;
Cof8=Moff/(1-K8);
for m=1:N
   Am8(:,m)=(Moff/(m*pi))*sin(2*pi*m*(1-K8));
   Bm8(:,m)=(-Moff/(m*pi))*(cos(2*pi*m*(1-K8))-1);
   Cm8(:,m)=((Am8(:,m)^2)+(Bm8(:,m)^2))^0.5;
   pm8(:,m)=atan(Bm8(:,m)\Am8(:,m));
end
[Cm8];
[pm8];
Vm8=[Cof8 Cm8];
tau8=W0*K8*per;
Vfm8=[Vm8(:,1);Vm8(:,2)*sin(W0*t+tau8+pm8(:,1));Vm8(:,3)*sin(2*W0*t+tau8+pm8(
:,2));Vm8(:,4)*sin(3*W0*t+tau8+pm8(:,3));Vm8(:,5)*sin(4*W0*t+tau8+pm5(:,4));Vm8(
:,6)*sin(5*W0*t+tau8+pm8(:,5));Vm8(:,7)*sin(6*W0*t+tau8+pm8(:,6));Vm8(:,8)*sin(7
*W0*t+tau8+pm8(:,7));Vm8(:,9)*sin(8*W0*t+tau8+pm8(:,8));Vm8(:,10)*sin(9*W0*t+t
au8+pm8(:,9));Vm8(:,11)*sin(10*W0*t+tau8+pm8(:,10));Vm8(:,12)*sin(11*W0*t+tau8
+pm8(:,11));Vm8(:,13)*sin(12*W0*t+tau8+pm8(:,12));Vm8(:,14)*sin(13*W0*t+tau8+p
m8(:,13));Vm8(:,15)*sin(14*W0*t+tau8+pm8(:,14));Vm8(:,16)*sin(15*W0*t+tau8+pm8
(:,15));Vm8(:,17)*sin(16*W0*t+tau8+pm8(:,16));Vm8(:,18)*sin(17*W0*t+tau8+pm8(:,
17));Vm8(:,19)*sin(18*W0*t+tau8+pm8(:,18));Vm8(:,20)*sin(19*W0*t+tau8+pm8(:,19
));Vm8(:,21)*sin(20*W0*t+tau8+pm8(:,20));Vm8(:,22)*sin(21*W0*t+tau8+pm8(:,21))];
```

```
Vof8=B*Vfm8;
a11=-rL/L;
a125=K5/L;
a126=K6/L;
a128=K8/L;
a21=0;
a22=-1/((rL+R)*C);
b11=(1/L);
b21=1/((rL+R)*C);
dx568xdt=[a11*x568x(1)+a125*x568x(2)+b11*Von5
   a21*x568x(1)+a22*x568x(2)+b21*Vof5;
   a11*x568x(3)+a126*x568x(2)+b11*Von6
   a21*x568x(3)+a22*x568x(4)+b21*Vof6;
   a11*x568x(5)+a128*x568x(2)+b11*Von8
   a21*x568x(5)+a22*x568x(6)+b21*Vof8];
grid on
```

A6: MATLAB instruction set for buck-boost converter, source resistance dependent

```
function bubo568R
%-------------------------------------------------------------------------
% This script evaluates the output voltage of a buck-boost converter, accounting
% for the source internal resistance, rs. Three sources are considered:
% NiCd battery, DEFC-mesh, and DEFC-foam
% Author:    Florian Misoc
% Date:      October 25, 2006
% Version:   2
% Copyright: Florian Misoc 2006
%-------------------------------------------------------------------------
tspan=[0 0.14];
y568y0=[0; 0; 0; 0; 0; 0];
% The equation is solved using ode45
ode45(@funct568,tspan,y568y0);
%-------------------------------------------------------------------------
function dy568ydt=funct568(t,y568y)
R=100; % Load resistance, 100 Ohms
L=0.01; % Inductor impedance, 10 mH
rL=23.7; % Inductor copper resistance, 23.7 Ohms
C=0.00022; % Filtering capacitor, 220 uF
```

```
M0=0.91; %Voltage amplitude: open-circuit voltage<<< VOLTAGE-SOURCE:
NiCd=2.6, DEFC=0.91
fsw=6000; %Switching frequency: 200 Hz-6 kHz <<< FREQUENCY
W0=2*pi*fsw; %fundamental angular-frequency
per=1/fsw;
N=21; %number of harmonics considered
K5=0.5; % Duty cycle (in decimal format) <<< DUTY CYCLE
K6=0.65; % Duty cycle (in decimal format) <<< DUTY CYCLE
K8=0.8; % Duty cycle (in decimal format) <<< DUTY CYCLE
gama5=0.118; % ratio of inductor total current during off-mode at 50% duty cycle
gama6=0.286; % ratio of inductor total current during off-mode at 65% duty cycle
gama8=0.758; % ratio of inductor total current during off-mode at 80% duty cycle
for m=1
   for n=1:N
      Wn(m,n)=n*W0; %harmonics angular-frequencies
   end
end
[Wn];
W=[W0 Wn];
NiCd=0.263; % internal resistance of NiCd battery, from the polarization curve
DEFC=1.44; % internal resistance of DEFC, from the polarization curve
rs=NiCd; % internal resistance of the source, rs=NiCd, or rs=DEFC
ZT=(((rs+rL)^2+(W0*L)^2)^0.5); % total impedance during mode 1, (on)
MD=(rs/ZT)*M0; % MD is the voltage drop across source's internal resistance
M=M0-MD; % M is the effective voltage at source terminals
C05=M/K5;
for n=1:N
   An5(:,n)=(M/(n*pi))*sin(2*pi*n*K5);
   Bn5(:,n)=(-M/(n*pi))*(cos(2*pi*n*K5)-1);
   Cn5(:,n)=((An5(:,n)^2)+(Bn5(:,n)^2))^0.5;
   ph5(:,n)=atan(Bn5(:,n)\An5(:,n));
end
[Cn5];
[ph5];
Vn5=[C05 Cn5];
B=ones(1,N+1);
Vg5=[Vn5(:,1);Vn5(:,2)*sin(2*pi*fsw*t+ph5(:,1));Vn5(:,3)*sin(2*pi*2*fsw*t+ph5(:,2));
Vn5(:,4)*sin(2*pi*3*fsw*t+ph5(:,3));Vn5(:,5)*sin(2*pi*4*fsw*t+ph5(:,4));Vn5(:,6)*sin(
2*pi*5*fsw*t+ph5(:,5));Vn5(:,7)*sin(2*pi*6*fsw*t+ph5(:,6));Vn5(:,8)*sin(2*pi*7*fsw*
t+ph5(:,7));Vn5(:,9)*sin(2*pi*8*fsw*t+ph5(:,8));Vn5(:,10)*sin(2*pi*9*fsw*t+ph5(:,9));
Vn5(:,11)*sin(2*pi*10*fsw*t+ph5(:,10));Vn5(:,12)*sin(2*pi*11*fsw*t+ph5(:,11));Vn5(:
,13)*sin(2*pi*12*fsw*t+ph5(:,12));Vn5(:,14)*sin(2*pi*13*fsw*t+ph5(:,13));Vn5(:,15)*
sin(2*pi*14*fsw*t+ph5(:,14));Vn5(:,16)*sin(2*pi*15*fsw*t+ph5(:,15));Vn5(:,17)*sin(2
*pi*16*fsw*t+ph5(:,16));Vn5(:,18)*sin(2*pi*17*fsw*t+ph5(:,17));Vn5(:,19)*sin(2*pi*1
8*fsw*t+ph5(:,18));Vn5(:,20)*sin(2*pi*19*fsw*t+ph5(:,19));Vn5(:,21)*sin(2*pi*20*fs
w*t+ph5(:,20));Vn5(:,22)*sin(2*pi*21*fsw*t+ph5(:,21))];
```

```
Von5=B*Vg5;
Cof5=1/(1-K5);
for m=1:N
   Am5(:,m)=(1/(m*pi))*sin(2*pi*m*(1-K5));
   Bm5(:,m)=(-1/(m*pi))*(cos(2*pi*m*(1-K5))-1);
   Cm5(:,m)=((Am5(:,m)^2)+(Bm5(:,m)^2))^0.5;
   pm5(:,m)=atan(Bm5(:,m)\Am5(:,m));
end
[Cm5];
[pm5];
Vm5=[Cof5 Cm5];
tau5=W0*K5*per;
Vfm5=[Vm5(:,1);Vm5(:,2)*sin(W0*t+tau5+pm5(:,1));Vm5(:,3)*sin(2*W0*t+tau5+pm5(
:,2));Vm5(:,4)*sin(3*W0*t+tau5+pm5(:,3));Vm5(:,5)*sin(4*W0*t+tau5+pm5(:,4));Vm5(
:,6)*sin(5*W0*t+tau5+pm5(:,5));Vm5(:,7)*sin(6*W0*t+tau5+pm5(:,6));Vm5(:,8)*sin(7
*W0*t+tau5+pm5(:,7));Vm5(:,9)*sin(8*W0*t+tau5+pm5(:,8));Vm5(:,10)*sin(9*W0*t+t
au5+pm5(:,9));Vm5(:,11)*sin(10*W0*t+tau5+pm5(:,10));Vm5(:,12)*sin(11*W0*t+tau5
+pm5(:,11));Vm5(:,13)*sin(12*W0*t+tau5+pm5(:,12));Vm5(:,14)*sin(13*W0*t+tau5+p
m5(:,13));Vm5(:,15)*sin(14*W0*t+tau5+pm5(:,14));Vm5(:,16)*sin(15*W0*t+tau5+pm5
(:,15));Vm5(:,17)*sin(16*W0*t+tau5+pm5(:,16));Vm5(:,18)*sin(17*W0*t+tau5+pm5(:,
17));Vm5(:,19)*sin(18*W0*t+tau5+pm5(:,18));Vm5(:,20)*sin(19*W0*t+tau5+pm5(:,19
));Vm5(:,21)*sin(20*W0*t+tau5+pm5(:,20));Vm5(:,22)*sin(21*W0*t+tau5+pm5(:,21))];
Vof5=B*Vfm5;
C06=M/K6;
for n=1:N
   An6(:,n)=(M/(n*pi))*sin(2*pi*n*K6);
   Bn6(:,n)=(-M/(n*pi))*(cos(2*pi*n*K6)-1);
   Cn6(:,n)=((An6(:,n)^2)+(Bn6(:,n)^2))^0.5;
   ph6(:,n)=atan(Bn6(:,n)\An6(:,n));
end
[Cn6];
[ph6];
Vn6=[C06 Cn6];
B=ones(1,N+1);
Vg6=[Vn6(:,1);Vn6(:,2)*sin(2*pi*fsw*t+ph6(:,1));Vn6(:,3)*sin(2*pi*2*fsw*t+ph6(:,2));
Vn6(:,4)*sin(2*pi*3*fsw*t+ph6(:,3));Vn6(:,5)*sin(2*pi*4*fsw*t+ph6(:,4));Vn6(:,6)*sin(
2*pi*5*fsw*t+ph6(:,5));Vn6(:,7)*sin(2*pi*6*fsw*t+ph6(:,6));Vn6(:,8)*sin(2*pi*7*fsw*
t+ph6(:,7));Vn6(:,9)*sin(2*pi*8*fsw*t+ph6(:,8));Vn6(:,10)*sin(2*pi*9*fsw*t+ph6(:,9));
Vn6(:,11)*sin(2*pi*10*fsw*t+ph6(:,10));Vn6(:,12)*sin(2*pi*11*fsw*t+ph6(:,11));Vn6(:
,13)*sin(2*pi*12*fsw*t+ph6(:,12));Vn6(:,14)*sin(2*pi*13*fsw*t+ph6(:,13));Vn6(:,15)*
sin(2*pi*14*fsw*t+ph6(:,14));Vn6(:,16)*sin(2*pi*15*fsw*t+ph6(:,15));Vn6(:,17)*sin(2
*pi*16*fsw*t+ph6(:,16));Vn6(:,18)*sin(2*pi*17*fsw*t+ph6(:,17));Vn6(:,19)*sin(2*pi*1
8*fsw*t+ph6(:,18));Vn6(:,20)*sin(2*pi*19*fsw*t+ph6(:,19));Vn6(:,21)*sin(2*pi*20*fs
w*t+ph6(:,20));Vn6(:,22)*sin(2*pi*21*fsw*t+ph6(:,21))];
Von6=B*Vg6;
Cof6=1/(1-K6);
```

```
for m=1:N
   Am6(:,m)=(1/(m*pi))*sin(2*pi*m*(1-K6));
   Bm6(:,m)=(-1/(m*pi))*(cos(2*pi*m*(1-K6))-1);
   Cm6(:,m)=((Am6(:,m)^2)+(Bm6(:,m)^2))^0.5;
   pm6(:,m)=atan(Bm6(:,m)\Am6(:,m));
end
[Cm6];
[pm6];
Vm6=[Cof6 Cm6];
tau6=W0*K6*per;
Vfm6=[Vm6(:,1);Vm6(:,2)*sin(W0*t+tau6+pm6(:,1));Vm6(:,3)*sin(2*W0*t+tau6+pm6(
:,2));Vm6(:,4)*sin(3*W0*t+tau6+pm6(:,3));Vm6(:,5)*sin(4*W0*t+tau6+pm6(:,4));Vm6(
:,6)*sin(5*W0*t+tau6+pm6(:,5));Vm6(:,7)*sin(6*W0*t+tau6+pm6(:,6));Vm6(:,8)*sin(7
*W0*t+tau6+pm6(:,7));Vm6(:,9)*sin(8*W0*t+tau6+pm6(:,8));Vm6(:,10)*sin(9*W0*t+t
au6+pm6(:,9));Vm6(:,11)*sin(10*W0*t+tau6+pm6(:,10));Vm6(:,12)*sin(11*W0*t+tau6
+pm6(:,11));Vm6(:,13)*sin(12*W0*t+tau6+pm6(:,12));Vm6(:,14)*sin(13*W0*t+tau6+p
m6(:,13));Vm6(:,15)*sin(14*W0*t+tau6+pm6(:,14));Vm6(:,16)*sin(15*W0*t+tau6+pm6
(:,15));Vm6(:,17)*sin(16*W0*t+tau6+pm6(:,16));Vm6(:,18)*sin(17*W0*t+tau6+pm6(:,
17));Vm6(:,19)*sin(18*W0*t+tau6+pm6(:,18));Vm6(:,20)*sin(19*W0*t+tau6+pm6(:,19
));Vm6(:,21)*sin(20*W0*t+tau6+pm6(:,20));Vm6(:,22)*sin(21*W0*t+tau6+pm6(:,21))];
Vof6=B*Vfm6;
C08=M/K8;
for n=1:N
   An8(:,n)=(M/(n*pi))*sin(2*pi*n*K8);
   Bn8(:,n)=(-M/(n*pi))*(cos(2*pi*n*K8)-1);
   Cn8(:,n)=((An8(:,n)^2)+(Bn8(:,n)^2))^0.5;
   ph8(:,n)=atan(Bn8(:,n)\An8(:,n));
end
[Cn8];
[ph8];
Vn8=[C08 Cn8];
B=ones(1,N+1);
Vg8=[Vn8(:,1);Vn8(:,2)*sin(2*pi*fsw*t+ph8(:,1));Vn8(:,3)*sin(2*pi*2*fsw*t+ph8(:,2));
Vn8(:,4)*sin(2*pi*3*fsw*t+ph8(:,3));Vn8(:,5)*sin(2*pi*4*fsw*t+ph8(:,4));Vn8(:,6)*sin(
2*pi*5*fsw*t+ph8(:,5));Vn8(:,7)*sin(2*pi*6*fsw*t+ph8(:,6));Vn8(:,8)*sin(2*pi*7*fsw*
t+ph8(:,7));Vn8(:,9)*sin(2*pi*8*fsw*t+ph8(:,8));Vn8(:,10)*sin(2*pi*9*fsw*t+ph8(:,9));
Vn8(:,11)*sin(2*pi*10*fsw*t+ph8(:,10));Vn8(:,12)*sin(2*pi*11*fsw*t+ph8(:,11));Vn8(:
,13)*sin(2*pi*12*fsw*t+ph8(:,12));Vn8(:,14)*sin(2*pi*13*fsw*t+ph8(:,13));Vn8(:,15)*
sin(2*pi*14*fsw*t+ph8(:,14));Vn8(:,16)*sin(2*pi*15*fsw*t+ph8(:,15));Vn8(:,17)*sin(2
*pi*16*fsw*t+ph8(:,16));Vn8(:,18)*sin(2*pi*17*fsw*t+ph8(:,17));Vn8(:,19)*sin(2*pi*1
8*fsw*t+ph8(:,18));Vn8(:,20)*sin(2*pi*19*fsw*t+ph8(:,19));Vn8(:,21)*sin(2*pi*20*fs
w*t+ph8(:,20));Vn8(:,22)*sin(2*pi*21*fsw*t+ph8(:,21))];
Von8=B*Vg8;
Cof8=1/(1-K8);
for m=1:N
   Am8(:,m)=(1/(m*pi))*sin(2*pi*m*(1-K8));
```

```
    Bm8(:,m)=(-1/(m*pi))*(cos(2*pi*m*(1-K8))-1);
    Cm8(:,m)=((Am8(:,m)^2)+(Bm8(:,m)^2))^0.5;
    pm8(:,m)=atan(Bm8(:,m)\Am8(:,m));
end
[Cm8];
[pm8];
Vm8=[Cof8 Cm8];
tau8=W0*K8*per;
Vfm8=[Vm8(:,1);Vm8(:,2)*sin(W0*t+tau8+pm8(:,1));Vm8(:,3)*sin(2*W0*t+tau8+pm8(
:,2));Vm8(:,4)*sin(3*W0*t+tau8+pm8(:,3));Vm8(:,5)*sin(4*W0*t+tau8+pm8(:,4));Vm8(
:,6)*sin(5*W0*t+tau8+pm8(:,5));Vm8(:,7)*sin(6*W0*t+tau8+pm8(:,6));Vm8(:,8)*sin(7
*W0*t+tau8+pm8(:,7));Vm8(:,9)*sin(8*W0*t+tau8+pm8(:,8));Vm8(:,10)*sin(9*W0*t+t
au8+pm8(:,9));Vm8(:,11)*sin(10*W0*t+tau8+pm8(:,10));Vm8(:,12)*sin(11*W0*t+tau8
+pm8(:,11));Vm8(:,13)*sin(12*W0*t+tau8+pm8(:,12));Vm8(:,14)*sin(13*W0*t+tau8+p
m8(:,13));Vm8(:,15)*sin(14*W0*t+tau8+pm8(:,14));Vm8(:,16)*sin(15*W0*t+tau8+pm8
(:,15));Vm8(:,17)*sin(16*W0*t+tau8+pm8(:,16));Vm8(:,18)*sin(17*W0*t+tau8+pm8(:,
17));Vm8(:,19)*sin(18*W0*t+tau8+pm8(:,18));Vm8(:,20)*sin(19*W0*t+tau8+pm8(:,19
));Vm8(:,21)*sin(20*W0*t+tau8+pm8(:,20));Vm8(:,22)*sin(21*W0*t+tau8+pm8(:,21))];
Vof8=B*Vfm8;
a11=-rL/L;
a12=0;
a21=0;
a22=-1/(R*C);
b11=(1/L);
b215=-gama5/C;
b216=-gama6/C;
b218=-gama8/C;
dy568ydt=[a11*y568y(1)+a12*y568y(2)+b11*Von5;
    a21*y568y(1)+a22*y568y(2)+b215*y568y(1);
    a11*y568y(3)+a12*y568y(4)+b11*Von6;
    a21*y568y(3)+a22*y568y(4)+b216*y568y(3);
    a11*y568y(5)+a12*y568y(6)+b11*Von8;
    a21*y568y(5)+a22*y568y(6)+b218*y568y(5)];
 grid on
```

A7: MATLAB instruction set for buck converter, source impedance dependent

```
function buck568Z
%-------------------------------------------------------------------------
% This script evaluates the output voltage of a buck converter, accounting
% for the source impedance (Re(Z) and Im(Z). Three sources are considered:
% NiCd battery, DEFC-mesh, and DEFC-foam
% Author:    Florian Misoc
% Date:      October 15, 2006
% Version:   5, fsw = switching frequency (Hz)
% Copyright: Florian Misoc 2006
%-------------------------------------------------------------------------
tspan=[0 0.2]; % Time span of the simulation
x568z0=[0; 0; 0; 0; 0; 0]; % Initial conditions for the two variables: zx(1)=iL, zx(2)=vC
% The equation is solved using ode45 function
ode45(@func568,tspan,x568z0);
%-------------------------------------------------------------------------
function dx568zdt=func568(t,x568z)
R=100; % Load resistance, 100 Ohms
L=0.01; % Inductor impedance, 10 mH
rL=23.7; % Inductor copper resistance, 23.7 Ohms
C=0.00022; % Filtering capacitor, 220 uF
M0=0.91; %Voltage amplitude: <<< VOLTAGE-SOURCE: NiCd=2.6 V, DEFC=0.91 V
frequency=[200 400 600 800 1000 1200 1400 1600 1800 2000 2200 2400 2600 2800
3000 3200 3400 3600 3800 4000 ...
      4200 4400 4600 4800 5000 5200 5400 5600 5800 6000];
% NiCd complex impedance, Re(ZNiCd) and Im(ZNiCd)---------------------------
ReNiCd=[0.461 0.631 0.712 0.76 0.791 0.813 0.831 0.844 0.855 0.863 0.87 0.876 0.881
0.886 0.889 0.893 0.895 0.898 0.9 0.901 0.903 0.904 0.905 0.906 0.906 0.906 0.906
0.906 0.906 0.906];
ImNiCd=[0.31 0.283 0.246 0.215 0.191 0.171 0.152 0.137 0.124 0.112 0.101 0.0903
0.0807 0.0718 0.0635 0.0555 0.048 0.0408 0.0339 0.0272 0.0208 0.0146 0.0085 0.0027 -
0.0029 -0.0084 -0.0137 -0.0189 -0.024 -0.0289];
%-------------------------------------------------------------------------
% DEFC-mesh complex impedance, Re(DEFC-mesh) and Im(DEFC-mesh)-------------
ReDEFCm=[0.0225 0.0257 0.0273 0.0284 0.0293 0.03 0.0306 0.0311 0.0316 0.032
0.0324 0.0328 0.0331 0.0334 0.0337 0.034 0.0342 0.0345 0.0347 0.0349 0.0351 0.0353
0.0355 0.0357 0.0359 0.036 0.0362 0.0363 0.0365 0.0366];
ImDEFCm=[0.00809 0.00711 0.00676 0.0066 0.00656 0.00653 0.00653 0.00653
0.00654 0.00654 0.00654 0.00654 0.00654 0.00654 0.00655 0.00655 0.00655 0.00654
0.00653 0.00652 0.00651 0.00651 0.0065 0.00649 0.00648 0.00648 0.00648 0.00647
0.00647 0.00647];
%-------------------------------------------------------------------------
% DEFC-foam complex impedance, Re(DEFC-foam) and Im(DEFC-foam)-------------
```

```
ReDEFCf=[0.0148 0.0174 0.0194 0.0211 0.0227 0.0243 0.0257 0.0269 0.0281 0.0292
0.0303 0.0314 0.0323 0.0332 0.034 0.0348 0.0355 0.0362 0.0369 0.0376 0.0382 0.0388
0.0393 0.0399 0.0404 0.0409 0.0413 0.0418 0.0422 0.0427];
ImDEFCf=[0.00692 0.00848 0.0099 0.0111 0.0122 0.0131 0.0138 0.0144 0.0148 0.0152
0.0155 0.0159 0.0161 0.0164 0.0166 0.0167 0.0169 0.017 0.0171 0.0171 0.0171 0.0172
0.0172 0.0172 0.0172 0.0172 0.0172 0.0172 0.0172 0.0172];
%-------------------------------------------------------------------------
nn=1;% nn takes values from 1 to 30, there are 30 values of switching frequency
fsw=frequency(:,nn); %Switching frequency: 200 Hz-6 kHz <<< FREQUENCY
Re=ReDEFCm(:,nn);
Im=ImDEFCm(:,nn);
W0=2*pi*fsw; %fundamental angular-frequency
N=21; %number of harmonics considered
K5=0.5; % Duty cycle: K=50% (K=0.50) <<< DUTY CYCLE
K6=0.65; % Duty cycle: K=65% (K=0.65) <<< DUTY CYCLE
K8=0.8; % Duty cycle: K=80% (K=0.80) <<< DUTY CYCLE
for m=1
   for n=1:N
      Wn(m,n)=n*W0; %harmonics angular-frequencies
   end
end
[Wn];
W=[W0 Wn];
XC=(1/(W0*C));
ZS=(Re^2+Im^2)^0.5; % DC source impedance
ReZT=Re+rL+(R*XC/(R^2+XC^2)^0.5)*cos(-pi/2+atan(XC/R));
ImZT=Im+W0*L+(R*XC/(R^2+XC^2)^0.5)*sin(-pi/2+atan(XC/R));
ZT=((ReZT^2+ImZT^2)^0.5); % total impedance during mode 1, (on)
MD=(ZS/ZT)*M0; % MD is the voltage drop across source impedance
M=M0-MD; % M is the effective voltage at source terminals. For ideal sources, M=M0
Co5=K5*M;
for n=1:N
   An5(:,n)=(M/(n*pi))*sin(2*pi*n*K5);
   Bn5(:,n)=(-M/(n*pi))*(cos(2*pi*n*K5)-1);
   Cn5(:,n)=((An5(:,n)^2)+(Bn5(:,n)^2))^0.5;
   ph5(:,n)=atan(Bn5(:,n)\An5(:,n));
end
[Cn5];
[ph5];
Vn5=[Co5 Cn5];
a11=-R/L;
a12=0;
a21=1/C;
a22=-1/(R*C);
b11=(1/L);
b21=0;
```

```
B=ones(1,N+1);
Vg5=[Vn5(:,1);Vn5(:,2)*sin(2*pi*fsw*t+ph5(:,1));Vn5(:,3)*sin(2*pi*2*fsw*t+ph5(:,2));
Vn5(:,4)*sin(2*pi*3*fsw*t+ph5(:,3));Vn5(:,5)*sin(2*pi*4*fsw*t+ph5(:,4));Vn5(:,6)*sin(
2*pi*5*fsw*t+ph5(:,5));Vn5(:,7)*sin(2*pi*6*fsw*t+ph5(:,6));Vn5(:,8)*sin(2*pi*7*fsw*
t+ph5(:,7));Vn5(:,9)*sin(2*pi*8*fsw*t+ph5(:,8));Vn5(:,10)*sin(2*pi*9*fsw*t+ph5(:,9));.
..Vn5(:,11)*sin(2*pi*10*fsw*t+ph5(:,10));Vn5(:,12)*sin(2*pi*11*fsw*t+ph5(:,11));Vn5
(:,13)*sin(2*pi*12*fsw*t+ph5(:,12));Vn5(:,14)*sin(2*pi*13*fsw*t+ph5(:,13));Vn5(:,15)
*sin(2*pi*14*fsw*t+ph5(:,14));Vn5(:,16)*sin(2*pi*15*fsw*t+ph5(:,15));Vn5(:,17)*sin(
2*pi*16*fsw*t+ph5(:,16));Vn5(:,18)*sin(2*pi*17*fsw*t+ph5(:,17));Vn5(:,19)*sin(2*pi*
18*fsw*t+ph5(:,18));Vn5(:,20)*sin(2*pi*19*fsw*t+ph5(:,19));Vn5(:,21)*sin(2*pi*20*fs
w*t+ph5(:,20));Vn5(:,22)*sin(2*pi*21*fsw*t+ph5(:,21))];
Vfg5=B*Vg5;
Co6=K6*M;
for n=1:N
   An6(:,n)=(M/(n*pi))*sin(2*pi*n*K6);
   Bn6(:,n)=(-M/(n*pi))*(cos(2*pi*n*K6)-1);
   Cn6(:,n)=((An6(:,n)^2)+(Bn6(:,n)^2))^0.5;
   ph6(:,n)=atan(Bn6(:,n)\An6(:,n));
end
[Cn6];
[ph6];
Vn6=[Co6 Cn6];
Vg6=[Vn6(:,1);Vn6(:,2)*sin(2*pi*fsw*t+ph6(:,1));Vn6(:,3)*sin(2*pi*2*fsw*t+ph6(:,2));
Vn6(:,4)*sin(2*pi*3*fsw*t+ph6(:,3));Vn6(:,5)*sin(2*pi*4*fsw*t+ph6(:,4));Vn6(:,6)*sin(
2*pi*5*fsw*t+ph6(:,5));Vn6(:,7)*sin(2*pi*6*fsw*t+ph6(:,6));Vn6(:,8)*sin(2*pi*7*fsw*
t+ph6(:,7));Vn6(:,9)*sin(2*pi*8*fsw*t+ph6(:,8));Vn6(:,10)*sin(2*pi*9*fsw*t+ph6(:,9));.
..Vn6(:,11)*sin(2*pi*10*fsw*t+ph6(:,10));Vn6(:,12)*sin(2*pi*11*fsw*t+ph6(:,11));Vn6
(:,13)*sin(2*pi*12*fsw*t+ph6(:,12));Vn6(:,14)*sin(2*pi*13*fsw*t+ph6(:,13));Vn6(:,15)
*sin(2*pi*14*fsw*t+ph6(:,14));Vn6(:,16)*sin(2*pi*15*fsw*t+ph6(:,15));Vn6(:,17)*sin(
2*pi*16*fsw*t+ph6(:,16));Vn6(:,18)*sin(2*pi*17*fsw*t+ph6(:,17));Vn6(:,19)*sin(2*pi*
18*fsw*t+ph6(:,18));Vn6(:,20)*sin(2*pi*19*fsw*t+ph6(:,19));Vn6(:,21)*sin(2*pi*20*fs
w*t+ph6(:,20));Vn6(:,22)*sin(2*pi*21*fsw*t+ph6(:,21))];
Vfg6=B*Vg6;
Co8=K8*M;
for n=1:N
   An8(:,n)=(M/(n*pi))*sin(2*pi*n*K8);
   Bn8(:,n)=(-M/(n*pi))*(cos(2*pi*n*K8)-1);
   Cn8(:,n)=((An8(:,n)^2)+(Bn8(:,n)^2))^0.5;
   ph8(:,n)=atan(Bn8(:,n)\An8(:,n));
end
[Cn8];
[ph8];
Vn8=[Co8 Cn8];
Vg8=[Vn8(:,1);Vn8(:,2)*sin(2*pi*fsw*t+ph8(:,1));Vn8(:,3)*sin(2*pi*2*fsw*t+ph8(:,2));
Vn8(:,4)*sin(2*pi*3*fsw*t+ph8(:,3));Vn8(:,5)*sin(2*pi*4*fsw*t+ph8(:,4));Vn8(:,6)*sin(
2*pi*5*fsw*t+ph8(:,5));Vn8(:,7)*sin(2*pi*6*fsw*t+ph8(:,6));Vn8(:,8)*sin(2*pi*7*fsw*
```

```
t+ph8(:,7));Vn8(:,9)*sin(2*pi*8*fsw*t+ph8(:,8));Vn8(:,10)*sin(2*pi*9*fsw*t+ph8(:,9));.
..Vn8(:,11)*sin(2*pi*10*fsw*t+ph8(:,10));Vn8(:,12)*sin(2*pi*11*fsw*t+ph8(:,11));Vn8
(:,13)*sin(2*pi*12*fsw*t+ph8(:,12));Vn8(:,14)*sin(2*pi*13*fsw*t+ph8(:,13));Vn8(:,15)
*sin(2*pi*14*fsw*t+ph8(:,14));Vn8(:,16)*sin(2*pi*15*fsw*t+ph8(:,15));Vn8(:,17)*sin(
2*pi*16*fsw*t+ph8(:,16));Vn8(:,18)*sin(2*pi*17*fsw*t+ph8(:,17));Vn8(:,19)*sin(2*pi*
18*fsw*t+ph8(:,18));Vn8(:,20)*sin(2*pi*19*fsw*t+ph8(:,19));Vn8(:,21)*sin(2*pi*20*fs
w*t+ph8(:,20));Vn8(:,22)*sin(2*pi*21*fsw*t+ph8(:,21))];
Vfg8=B*Vg8;
dx568zdt=[a11*x568z(1)+b11*Vfg5;
    a21*x568z(1)+a22*x568z(2);
    a11*x568z(3)+b11*Vfg6;
    a21*x568z(3)+a22*x568z(4);
    a11*x568z(5)+b11*Vfg8;
    a21*x568z(5)+a22*x568z(6)];
grid on
```

A8: MATLAB instruction set for boost converter, source impedance dependent

```
function boost568Z
%-------------------------------------------------------------------------
% This script evaluates the output voltage of a boost converter, accounting
% for the source impedance (Re(Z) and Im(Z). Three sources are considered:
% NiCd battery, DEFC-mesh, and DEFC-foam
% Author:    Florian Misoc
% Date:      October 25, 2006
% Version:   2
% Copyright: Florian Misoc 2006
%-------------------------------------------------------------------------
tspan=[0 0.24];
x568x0=[0.0091; 0.91; 0.0091; 0.91; 0.0091; 0.91];
% The equation is solved using ode45
ode45(@fuct568,tspan,x568x0);
%-------------------------------------------------------------------------
function dx568xdt=fuct568(t,x568x)
R=100;
L=0.01;
rL=23.7;
C=0.00022;
```

```
M0=0.91; %Voltage amplitude: 0.91 Volts <<< VOLTAGE-SOURCE: NiCd=2.6 V,
DEFC=0.91 V
frequency=[200 400 600 800 1000 1200 1400 1600 1800 2000 2200 2400 2600 2800
3000 3200 3400 3600 3800 4000 4200 4400 4600 4800 5000 5200 5400 5600 5800
6000];
% NiCd complex impedance, Re(ZNiCd) and Im(ZNiCd)--------------------------
ReNiCd=[0.461 0.631 0.712 0.76 0.791 0.813 0.831 0.844 0.855 0.863 0.87 0.876 0.881
0.886 0.889 0.893 0.895 0.898 0.9 0.901 0.903 0.904 0.905 0.906 0.906 0.906 0.906
0.906 0.906 0.906];
ImNiCd=[0.31 0.283 0.246 0.215 0.191 0.171 0.152 0.137 0.124 0.112 0.101 0.0903
0.0807 0.0718 0.0635 0.0555 0.048 0.0408 0.0339 0.0272 0.0208 0.0146 0.0085 0.0027 -
0.0029 -0.0084 -0.0137 -0.0189 -0.024 -0.0289];
%-------------------------------------------------------------------------
% DEFC-mesh complex impedance, Re(DEFC-mesh) and Im(DEFC-mesh)-------------
ReDEFCm=[0.0225 0.0257 0.0273 0.0284 0.0293 0.03 0.0306 0.0311 0.0316 0.032
0.0324 0.0328 0.0331 0.0334 0.0337 0.034 0.0342 0.0345 0.0347 0.0349 0.0351 0.0353
0.0355 0.0357 0.0359 0.036 0.0362 0.0363 0.0365 0.0366];
ImDEFCm=[0.00809 0.00711 0.00676 0.0066 0.00656 0.00653 0.00653 0.00653
0.00654 0.00654 0.00654 0.00654 0.00654 0.00654 0.00655 0.00655 0.00655 0.00654
0.00653 0.00652 0.00651 0.00651 0.0065 0.00649 0.00648 0.00648 0.00648 0.00647
0.00647 0.00647];
%-------------------------------------------------------------------------
% DEFC-foam complex impedance, Re(DEFC-foam) and Im(DEFC-foam)-------------
ReDEFCf=[0.0148 0.0174 0.0194 0.0211 0.0227 0.0243 0.0257 0.0269 0.0281 0.0292
0.0303 0.0314 0.0323 0.0332 0.034 0.0348 0.0355 0.0362 0.0369 0.0376 0.0382 0.0388
0.0393 0.0399 0.0404 0.0409 0.0413 0.0418 0.0422 0.0427];
ImDEFCf=[0.00692 0.00848 0.0099 0.0111 0.0122 0.0131 0.0138 0.0144 0.0148 0.0152
0.0155 0.0159 0.0161 0.0164 0.0166 0.0167 0.0169 0.017 0.0171 0.0171 0.0171 0.0172
0.0172 0.0172 0.0172 0.0172 0.0172 0.0172 0.0172 0.0172];
%-------------------------------------------------------------------------
nn=30;% nn takes values from 1 to 30, there are 30 values of switching frequency
fsw=frequency(:,nn); %Switching frequency: 200 Hz-6 kHz <<< FREQUENCY
Re=ReDEFCf(:,nn);
Im=ImDEFCf(:,nn);
per=1/fsw;
W0=2*pi*fsw; %fundamental angular-frequency
N=21; %number of harmonics considered
K5=0.5; % Duty cycle: in decimal format <<< DUTY CYCLE
K6=0.65; % Duty cycle: in decimal format <<< DUTY CYCLE
K8=0.8; % Duty cycle: in decimal format <<< DUTY CYCLE
for m=1
   for n=1:N
      Wn(m,n)=n*W0; %harmonics angular-frequencies
   end
end
[Wn];
```

```
W=[W0 Wn];
ZS=(Re^2+Im^2)^0.5; % DC source impedance
ZTon=(((Re+rL)^2+(Im+W0*L)^2)^0.5); % total impedance during mode 1, (on)
MDon=(ZS/ZTon)*M0; % MD is the voltage drop across source impedance
Mon=M0-MDon; % M is the effective voltage at source terminals during ON time, for
ideal sources, M=M0
XC=(1/(W0*C)); %XC is the filtering capacitor reactance
ReZToff=Re+rL+(R*XC/(R^2+XC^2)^0.5)*cos(-pi/2+atan(XC/R));
ImZToff=Im+W0*L+(R*XC/(R^2+XC^2)^0.5)*sin(-pi/2+atan(XC/R));
ZToff=((ReZToff^2+ImZToff^2)^0.5); % total impedance during mode 2, (off)
MDoff=(ZS/ZToff)*M0; % MD is the voltage drop across source's internal resistance
during OFF time
Moff=M0-MDoff; % M is the effective voltage at source terminals during OFF time
C05=Mon/(1-K5);
for n=1:N
   An5(:,n)=(Mon/(n*pi))*sin(2*pi*n*K5);
   Bn5(:,n)=(-Mon/(n*pi))*(cos(2*pi*n*K5)-1);
   Con5(:,n)=((An5(:,n)^2)+(Bn5(:,n)^2))^0.5;
   ph5(:,n)=atan(Bn5(:,n)\An5(:,n));
end
[Con5];
[ph5];
Vn5=[C05 Con5];
B=ones(1,N+1);
Vg5=[Vn5(:,1);Vn5(:,2)*sin(2*pi*fsw*t+ph5(:,1));Vn5(:,3)*sin(2*pi*2*fsw*t+ph5(:,2));
Vn5(:,4)*sin(2*pi*3*fsw*t+ph5(:,3));Vn5(:,5)*sin(2*pi*4*fsw*t+ph5(:,4));Vn5(:,6)*sin(
2*pi*5*fsw*t+ph5(:,5));Vn5(:,7)*sin(2*pi*6*fsw*t+ph5(:,6));Vn5(:,8)*sin(2*pi*7*fsw*
t+ph5(:,7));Vn5(:,9)*sin(2*pi*8*fsw*t+ph5(:,8));Vn5(:,10)*sin(2*pi*9*fsw*t+ph5(:,9));.
..Vn5(:,11)*sin(2*pi*10*fsw*t+ph5(:,10));Vn5(:,12)*sin(2*pi*11*fsw*t+ph5(:,11));Vn5
(:,13)*sin(2*pi*12*fsw*t+ph5(:,12));Vn5(:,14)*sin(2*pi*13*fsw*t+ph5(:,13));Vn5(:,15)
*sin(2*pi*14*fsw*t+ph5(:,14));Vn5(:,16)*sin(2*pi*15*fsw*t+ph5(:,15));Vn5(:,17)*sin(
2*pi*16*fsw*t+ph5(:,16));Vn5(:,18)*sin(2*pi*17*fsw*t+ph5(:,17));Vn5(:,19)*sin(2*pi*
18*fsw*t+ph5(:,18));Vn5(:,20)*sin(2*pi*19*fsw*t+ph5(:,19));Vn5(:,21)*sin(2*pi*20*fs
w*t+ph5(:,20));Vn5(:,22)*sin(2*pi*21*fsw*t+ph5(:,21))];
Von5=B*Vg5;
Cof5=Moff/(1-K5);
for m=1:N
   Am5(:,m)=(Moff/(m*pi))*sin(2*pi*m*(1-K5));
   Bm5(:,m)=(-Moff/(m*pi))*(cos(2*pi*m*(1-K5))-1);
   Cm5(:,m)=((Am5(:,m)^2)+(Bm5(:,m)^2))^0.5;
   pm5(:,m)=atan(Bm5(:,m)\Am5(:,m));
end
[Cm5];
[pm5];
Vm5=[Cof5 Cm5];
tau5=W0*K5*per;
```

```
Vfm5=[Vm5(:,1);Vm5(:,2)*sin(W0*t+tau5+pm5(:,1));Vm5(:,3)*sin(2*W0*t+tau5+pm5(
:,2));Vm5(:,4)*sin(3*W0*t+tau5+pm5(:,3));Vm5(:,5)*sin(4*W0*t+tau5+pm5(:,4));Vm5(
:,6)*sin(5*W0*t+tau5+pm5(:,5));Vm5(:,7)*sin(6*W0*t+tau5+pm5(:,6));Vm5(:,8)*sin(7
*W0*t+tau5+pm5(:,7));Vm5(:,9)*sin(8*W0*t+tau5+pm5(:,8));Vm5(:,10)*sin(9*W0*t+t
au5+pm5(:,9));Vm5(:,11)*sin(10*W0*t+tau5+pm5(:,10));Vm5(:,12)*sin(11*W0*t+tau5
+pm5(:,11));Vm5(:,13)*sin(12*W0*t+tau5+pm5(:,12));Vm5(:,14)*sin(13*W0*t+tau5+p
m5(:,13));Vm5(:,15)*sin(14*W0*t+tau5+pm5(:,14));Vm5(:,16)*sin(15*W0*t+tau5+pm5
(:,15));Vm5(:,17)*sin(16*W0*t+tau5+pm5(:,16));Vm5(:,18)*sin(17*W0*t+tau5+pm5(:,
17));Vm5(:,19)*sin(18*W0*t+tau5+pm5(:,18));Vm5(:,20)*sin(19*W0*t+tau5+pm5(:,19
));Vm5(:,21)*sin(20*W0*t+tau5+pm5(:,20));Vm5(:,22)*sin(21*W0*t+tau5+pm5(:,21))];
Vof5=B*Vfm5;
C06=Mon/(1-K6);
for n=1:N
   An6(:,n)=(Mon/(n*pi))*sin(2*pi*n*K6);
   Bn6(:,n)=(-Mon/(n*pi))*(cos(2*pi*n*K6)-1);
   Con6(:,n)=((An6(:,n)^2)+(Bn6(:,n)^2))^0.5;
   ph6(:,n)=atan(Bn6(:,n)\An6(:,n));
end
[Con6];
[ph6];
Vn6=[C06 Con6];
B=ones(1,N+1);
Vg6=[Vn6(:,1);Vn6(:,2)*sin(2*pi*fsw*t+ph6(:,1));Vn6(:,3)*sin(2*pi*2*fsw*t+ph6(:,2));
Vn6(:,4)*sin(2*pi*3*fsw*t+ph6(:,3));Vn6(:,5)*sin(2*pi*4*fsw*t+ph6(:,4));Vn6(:,6)*sin(
2*pi*5*fsw*t+ph6(:,5));Vn6(:,7)*sin(2*pi*6*fsw*t+ph6(:,6));Vn6(:,8)*sin(2*pi*7*fsw*
t+ph6(:,7));Vn6(:,9)*sin(2*pi*8*fsw*t+ph6(:,8));Vn6(:,10)*sin(2*pi*9*fsw*t+ph6(:,9));.
..Vn6(:,11)*sin(2*pi*10*fsw*t+ph6(:,10));Vn6(:,12)*sin(2*pi*11*fsw*t+ph6(:,11));Vn6
(:,13)*sin(2*pi*12*fsw*t+ph6(:,12));Vn6(:,14)*sin(2*pi*13*fsw*t+ph6(:,13));Vn6(:,15)
*sin(2*pi*14*fsw*t+ph6(:,14));Vn6(:,16)*sin(2*pi*15*fsw*t+ph6(:,15));Vn6(:,17)*sin(
2*pi*16*fsw*t+ph6(:,16));Vn6(:,18)*sin(2*pi*17*fsw*t+ph6(:,17));Vn6(:,19)*sin(2*pi*
18*fsw*t+ph6(:,18));Vn6(:,20)*sin(2*pi*19*fsw*t+ph6(:,19));Vn6(:,21)*sin(2*pi*20*fs
w*t+ph6(:,20));Vn6(:,22)*sin(2*pi*21*fsw*t+ph6(:,21))];
Von6=B*Vg6;
Cof6=Moff/(1-K6);
for m=1:N
   Am6(:,m)=(Moff/(m*pi))*sin(2*pi*m*(1-K6));
   Bm6(:,m)=(-Moff/(m*pi))*(cos(2*pi*m*(1-K6))-1);
   Cm6(:,m)=((Am6(:,m)^2)+(Bm6(:,m)^2))^0.5;
   pm6(:,m)=atan(Bm6(:,m)\Am6(:,m));
end
[Cm6];
[pm6];
Vm6=[Cof6 Cm6];
tau6=W0*K6*per;
Vfm6=[Vm6(:,1);Vm6(:,2)*sin(W0*t+tau6+pm6(:,1));Vm6(:,3)*sin(2*W0*t+tau6+pm6(
:,2));Vm6(:,4)*sin(3*W0*t+tau6+pm6(:,3));Vm6(:,5)*sin(4*W0*t+tau6+pm6(:,4));Vm6(
```

```
:,6)*sin(5*W0*t+tau6+pm6(:,5));Vm6(:,7)*sin(6*W0*t+tau6+pm6(:,6));Vm6(:,8)*sin(7
*W0*t+tau6+pm6(:,7));Vm6(:,9)*sin(8*W0*t+tau6+pm6(:,8));Vm6(:,10)*sin(9*W0*t+t
au6+pm6(:,9));Vm6(:,11)*sin(10*W0*t+tau6+pm6(:,10));Vm6(:,12)*sin(11*W0*t+tau6
+pm6(:,11));Vm6(:,13)*sin(12*W0*t+tau6+pm6(:,12));Vm6(:,14)*sin(13*W0*t+tau6+p
m6(:,13));Vm6(:,15)*sin(14*W0*t+tau6+pm6(:,14));Vm6(:,16)*sin(15*W0*t+tau6+pm6
(:,15));Vm6(:,17)*sin(16*W0*t+tau6+pm6(:,16));Vm6(:,18)*sin(17*W0*t+tau6+pm6(:,
17));Vm6(:,19)*sin(18*W0*t+tau6+pm6(:,18));Vm6(:,20)*sin(19*W0*t+tau6+pm6(:,19
));Vm6(:,21)*sin(20*W0*t+tau6+pm6(:,20));Vm6(:,22)*sin(21*W0*t+tau6+pm6(:,21))];
Vof6=B*Vfm6;
C08=Mon/(1-K8);
for n=1:N
   An8(:,n)=(Mon/(n*pi))*sin(2*pi*n*K8);
   Bn8(:,n)=(-Mon/(n*pi))*(cos(2*pi*n*K8)-1);
   Con8(:,n)=((An8(:,n)^2)+(Bn8(:,n)^2))^0.5;
   ph8(:,n)=atan(Bn8(:,n)\An8(:,n));
end
[Con8];
[ph8];
Vn8=[C08 Con8];
B=ones(1,N+1);
Vg8=[Vn8(:,1);Vn8(:,2)*sin(2*pi*fsw*t+ph8(:,1));Vn8(:,3)*sin(2*pi*2*fsw*t+ph8(:,2));
Vn8(:,4)*sin(2*pi*3*fsw*t+ph8(:,3));Vn8(:,5)*sin(2*pi*4*fsw*t+ph8(:,4));Vn8(:,6)*sin(
2*pi*5*fsw*t+ph8(:,5));Vn8(:,7)*sin(2*pi*6*fsw*t+ph8(:,6));Vn8(:,8)*sin(2*pi*7*fsw*
t+ph8(:,7));Vn8(:,9)*sin(2*pi*8*fsw*t+ph8(:,8));Vn8(:,10)*sin(2*pi*9*fsw*t+ph8(:,9));.
..Vn8(:,11)*sin(2*pi*10*fsw*t+ph8(:,10));Vn8(:,12)*sin(2*pi*11*fsw*t+ph8(:,11));Vn8
(:,13)*sin(2*pi*12*fsw*t+ph8(:,12));Vn8(:,14)*sin(2*pi*13*fsw*t+ph8(:,13));Vn8(:,15)
*sin(2*pi*14*fsw*t+ph8(:,14));Vn8(:,16)*sin(2*pi*15*fsw*t+ph8(:,15));Vn8(:,17)*sin(
2*pi*16*fsw*t+ph8(:,16));Vn8(:,18)*sin(2*pi*17*fsw*t+ph8(:,17));Vn8(:,19)*sin(2*pi*
18*fsw*t+ph8(:,18));Vn8(:,20)*sin(2*pi*19*fsw*t+ph8(:,19));Vn8(:,21)*sin(2*pi*20*fs
w*t+ph8(:,20));Vn8(:,22)*sin(2*pi*21*fsw*t+ph8(:,21))];
Von8=B*Vg8;
Cof8=Moff/(1-K8);
for m=1:N
   Am8(:,m)=(Moff/(m*pi))*sin(2*pi*m*(1-K8));
   Bm8(:,m)=(-Moff/(m*pi))*(cos(2*pi*m*(1-K8))-1);
   Cm8(:,m)=((Am8(:,m)^2)+(Bm8(:,m)^2))^0.5;
   pm8(:,m)=atan(Bm8(:,m)\Am8(:,m));
end
[Cm8];
[pm8];
Vm8=[Cof8 Cm8];
tau8=W0*K8*per;
Vfm8=[Vm8(:,1);Vm8(:,2)*sin(W0*t+tau8+pm8(:,1));Vm8(:,3)*sin(2*W0*t+tau8+pm8(
:,2));Vm8(:,4)*sin(3*W0*t+tau8+pm8(:,3));Vm8(:,5)*sin(4*W0*t+tau8+pm5(:,4));Vm8(
:,6)*sin(5*W0*t+tau8+pm8(:,5));Vm8(:,7)*sin(6*W0*t+tau8+pm8(:,6));Vm8(:,8)*sin(7
*W0*t+tau8+pm8(:,7));Vm8(:,9)*sin(8*W0*t+tau8+pm8(:,8));Vm8(:,10)*sin(9*W0*t+t
```

```
au8+pm8(:,9));Vm8(:,11)*sin(10*W0*t+tau8+pm8(:,10));Vm8(:,12)*sin(11*W0*t+tau8
+pm8(:,11));Vm8(:,13)*sin(12*W0*t+tau8+pm8(:,12));Vm8(:,14)*sin(13*W0*t+tau8+p
m8(:,13));Vm8(:,15)*sin(14*W0*t+tau8+pm8(:,14));Vm8(:,16)*sin(15*W0*t+tau8+pm8
(:,15));Vm8(:,17)*sin(16*W0*t+tau8+pm8(:,16));Vm8(:,18)*sin(17*W0*t+tau8+pm8(:,
17));Vm8(:,19)*sin(18*W0*t+tau8+pm8(:,18));Vm8(:,20)*sin(19*W0*t+tau8+pm8(:,19
));Vm8(:,21)*sin(20*W0*t+tau8+pm8(:,20));Vm8(:,22)*sin(21*W0*t+tau8+pm8(:,21))];
Vof8=B*Vfm8;
a11=-rL/L;
a125=K5/L;
a126=K6/L;
a128=K8/L;
a21=0;
a22=-1/((rL+R)*C);
b11=(1/L);
b21=1/((rL+R)*C);
dx568xdt=[a11*x568x(1)+b11*Von5
   a21*x568x(1)+a22*x568x(2)+b21*Vof5;
   a11*x568x(3)+b11*Von6
   a21*x568x(3)+a22*x568x(4)+b21*Vof6;
   a11*x568x(5)+b11*Von8
   a21*x568x(5)+a22*x568x(6)+b21*Vof8];
grid on
```

A9: MATLAB instruction set for buck-boost converter, source impedance dependent

```
function bubo568Z
%-------------------------------------------------------------------------
% This script evaluates the output voltage of a buck-boost converter, accounting
% for the source impedance (Re(Z) and Im(Z). Three sources are considered:
% NiCd battery, DEFC-mesh, and DEFC-foam
% Author:    Florian Misoc
% Date:      October 25, 2006
% Version:   2
% Copyright: Florian Misoc 2006
%-------------------------------------------------------------------------
tspan=[0 0.14];
y568y0=[0; 0; 0; 0; 0; 0];
% The equation is solved using ode45
ode45(@funct568,tspan,y568y0);
%-------------------------------------------------------------------------
function dy568ydt=funct568(t,y568y)
```

```
R=100;
L=0.01;
rL=23.7;
C=0.00022;
M0=0.91; %Voltage amplitude: 0.91 Volts <<< VOLTAGE-SOURCE: DEFC
frequency=[200 400 600 800 1000 1200 1400 1600 1800 2000 2200 2400 2600 2800
3000 3200 3400 3600 3800 4000 4200 4400 4600 4800 5000 5200 5400 5600 5800
6000];
% NiCd complex impedance, Re(ZNiCd) and Im(ZNiCd)----------------------------
ReNiCd=[0.461 0.631 0.712 0.76 0.791 0.813 0.831 0.844 0.855 0.863 0.87 0.876 0.881
0.886 0.889 0.893 0.895 0.898 0.9 0.901 0.903 0.904 0.905 0.906 0.906 0.906 0.906
0.906 0.906 0.906];
ImNiCd=[0.31 0.283 0.246 0.215 0.191 0.171 0.152 0.137 0.124 0.112 0.101 0.0903
0.0807 0.0718 0.0635 0.0555 0.048 ...
      0.0408 0.0339 0.0272 0.0208 0.0146 0.0085 0.0027 -0.0029 -0.0084 -0.0137 -
0.0189 -0.024 -0.0289];
%-------------------------------------------------------------------------
% DEFC-mesh complex impedance, Re(DEFC-mesh) and Im(DEFC-mesh)-------------
ReDEFCm=[0.0225 0.0257 0.0273 0.0284 0.0293 0.03 0.0306 0.0311 0.0316 0.032
0.0324 0.0328 0.0331 0.0334 0.0337 0.034 0.0342 0.0345 0.0347 0.0349 0.0351 0.0353
0.0355 0.0357 0.0359 0.036 0.0362 0.0363 0.0365 0.0366];
ImDEFCm=[0.00809 0.00711 0.00676 0.0066 0.00656 0.00653 0.00653 0.00653
0.00654 0.00654 0.00654 0.00654 0.00654 0.00654 0.00655 0.00655 0.00655 0.00654
0.00653 0.00652 0.00651 0.00651 0.0065 0.00649 0.00648 0.00648 0.00648 0.00647
0.00647 0.00647];
%-------------------------------------------------------------------------
% DEFC-foam complex impedance, Re(DEFC-foam) and Im(DEFC-foam)-------------
ReDEFCf=[0.0148 0.0174 0.0194 0.0211 0.0227 0.0243 0.0257 0.0269 0.0281 0.0292
0.0303 0.0314 0.0323 0.0332 0.034 0.0348 0.0355 0.0362 0.0369 0.0376 0.0382 0.0388
0.0393 0.0399 0.0404 0.0409 0.0413 0.0418 0.0422 0.0427];
ImDEFCf=[0.00692 0.00848 0.0099 0.0111 0.0122 0.0131 0.0138 0.0144 0.0148 0.0152
0.0155 0.0159 0.0161 0.0164 0.0166 0.0167 0.0169 0.017 0.0171 0.0171 0.0171 0.0172
0.0172 0.0172 0.0172 0.0172 0.0172 0.0172 0.0172 0.0172];
%-------------------------------------------------------------------------
nn=1;% nn takes values from 1 to 30, there are 30 values of switching frequency
fsw=frequency(:,nn); %Switching frequency: 200 Hz-6 kHz <<< FREQUENCY
Re=ReNiCd(:,nn);
Im=ImNiCd(:,nn);
W0=2*pi*fsw; %fundamental angular-frequency
per=1/fsw;
N=21; %number of harmonics considered
K5=0.5; % Duty cycle (in decimal format) <<< DUTY CYCLE
K6=0.65; % Duty cycle (in decimal format) <<< DUTY CYCLE
K8=0.8; % Duty cycle (in decimal format) <<< DUTY CYCLE
gama5=0.118; % ratio of inductor total current during off-mode at 50% duty cycle
gama6=0.286; % ratio of inductor total current during off-mode at 65% duty cycle
```

```
gama8=0.758; % ratio of inductor total current during off-mode at 80% duty cycle
for m=1
   for n=1:N
      Wn(m,n)=n*W0; %harmonics angular-frequencies
   end
end
[Wn];
W=[W0 Wn];
ZS=(Re^2+Im^2)^0.5; % DC source impedance
ZT=(((Re+rL)^2+(W0*L)^2)^0.5); % total impedance during mode 1, (on)
MD=(ZS/ZT)*M0; % MD is the voltage drop across source impedance
M=M0-MD; % M is the effective voltage at source terminals, for ideal sources, M=M0
C05=M/K5;
for n=1:N
   An5(:,n)=(M/(n*pi))*sin(2*pi*n*K5);
   Bn5(:,n)=(-M/(n*pi))*(cos(2*pi*n*K5)-1);
   Cn5(:,n)=((An5(:,n)^2)+(Bn5(:,n)^2))^0.5;
   ph5(:,n)=atan(Bn5(:,n)\An5(:,n));
end
[Cn5];
[ph5];
Vn5=[C05 Cn5];
B=ones(1,N+1);
Vg5=[Vn5(:,1);Vn5(:,2)*sin(2*pi*fsw*t+ph5(:,1));Vn5(:,3)*sin(2*pi*2*fsw*t+ph5(:,2));
Vn5(:,4)*sin(2*pi*3*fsw*t+ph5(:,3));Vn5(:,5)*sin(2*pi*4*fsw*t+ph5(:,4));Vn5(:,6)*sin(
2*pi*5*fsw*t+ph5(:,5));Vn5(:,7)*sin(2*pi*6*fsw*t+ph5(:,6));Vn5(:,8)*sin(2*pi*7*fsw*
t+ph5(:,7));Vn5(:,9)*sin(2*pi*8*fsw*t+ph5(:,8));Vn5(:,10)*sin(2*pi*9*fsw*t+ph5(:,9));.
..Vn5(:,11)*sin(2*pi*10*fsw*t+ph5(:,10));Vn5(:,12)*sin(2*pi*11*fsw*t+ph5(:,11));Vn5
(:,13)*sin(2*pi*12*fsw*t+ph5(:,12));Vn5(:,14)*sin(2*pi*13*fsw*t+ph5(:,13));Vn5(:,15)
*sin(2*pi*14*fsw*t+ph5(:,14));Vn5(:,16)*sin(2*pi*15*fsw*t+ph5(:,15));Vn5(:,17)*sin(
2*pi*16*fsw*t+ph5(:,16));Vn5(:,18)*sin(2*pi*17*fsw*t+ph5(:,17));Vn5(:,19)*sin(2*pi*
18*fsw*t+ph5(:,18));Vn5(:,20)*sin(2*pi*19*fsw*t+ph5(:,19));Vn5(:,21)*sin(2*pi*20*fs
w*t+ph5(:,20));Vn5(:,22)*sin(2*pi*21*fsw*t+ph5(:,21))];
Von5=B*Vg5;
Cof5=1/(1-K5);
for m=1:N
   Am5(:,m)=(1/(m*pi))*sin(2*pi*m*(1-K5));
   Bm5(:,m)=(-1/(m*pi))*(cos(2*pi*m*(1-K5))-1);
   Cm5(:,m)=((Am5(:,m)^2)+(Bm5(:,m)^2))^0.5;
   pm5(:,m)=atan(Bm5(:,m)\Am5(:,m));
end
[Cm5];
[pm5];
Vm5=[Cof5 Cm5];
tau5=W0*K5*per;
```

```
Vfm5=[Vm5(:,1);Vm5(:,2)*sin(W0*t+tau5+pm5(:,1));Vm5(:,3)*sin(2*W0*t+tau5+pm5(
:,2));Vm5(:,4)*sin(3*W0*t+tau5+pm5(:,3));Vm5(:,5)*sin(4*W0*t+tau5+pm5(:,4));Vm5(
:,6)*sin(5*W0*t+tau5+pm5(:,5));Vm5(:,7)*sin(6*W0*t+tau5+pm5(:,6));Vm5(:,8)*sin(7
*W0*t+tau5+pm5(:,7));Vm5(:,9)*sin(8*W0*t+tau5+pm5(:,8));Vm5(:,10)*sin(9*W0*t+t
au5+pm5(:,9));Vm5(:,11)*sin(10*W0*t+tau5+pm5(:,10));Vm5(:,12)*sin(11*W0*t+tau5
+pm5(:,11));Vm5(:,13)*sin(12*W0*t+tau5+pm5(:,12));Vm5(:,14)*sin(13*W0*t+tau5+p
m5(:,13));Vm5(:,15)*sin(14*W0*t+tau5+pm5(:,14));Vm5(:,16)*sin(15*W0*t+tau5+pm5
(:,15));Vm5(:,17)*sin(16*W0*t+tau5+pm5(:,16));Vm5(:,18)*sin(17*W0*t+tau5+pm5(:,
17));Vm5(:,19)*sin(18*W0*t+tau5+pm5(:,18));Vm5(:,20)*sin(19*W0*t+tau5+pm5(:,19
));Vm5(:,21)*sin(20*W0*t+tau5+pm5(:,20));Vm5(:,22)*sin(21*W0*t+tau5+pm5(:,21))];
Vof5=B*Vfm5;
C06=M/K6;
for n=1:N
   An6(:,n)=(M/(n*pi))*sin(2*pi*n*K6);
   Bn6(:,n)=(-M/(n*pi))*(cos(2*pi*n*K6)-1);
   Cn6(:,n)=((An6(:,n)^2)+(Bn6(:,n)^2))^0.5;
   ph6(:,n)=atan(Bn6(:,n)\An6(:,n));
end
[Cn6];
[ph6];
Vn6=[C06 Cn6];
B=ones(1,N+1);
Vg6=[Vn6(:,1);Vn6(:,2)*sin(2*pi*fsw*t+ph6(:,1));Vn6(:,3)*sin(2*pi*2*fsw*t+ph6(:,2));
Vn6(:,4)*sin(2*pi*3*fsw*t+ph6(:,3));Vn6(:,5)*sin(2*pi*4*fsw*t+ph6(:,4));Vn6(:,6)*sin(
2*pi*5*fsw*t+ph6(:,5));Vn6(:,7)*sin(2*pi*6*fsw*t+ph6(:,6));Vn6(:,8)*sin(2*pi*7*fsw*
t+ph6(:,7));Vn6(:,9)*sin(2*pi*8*fsw*t+ph6(:,8));Vn6(:,10)*sin(2*pi*9*fsw*t+ph6(:,9));.
..Vn6(:,11)*sin(2*pi*10*fsw*t+ph6(:,10));Vn6(:,12)*sin(2*pi*11*fsw*t+ph6(:,11));Vn6
(:,13)*sin(2*pi*12*fsw*t+ph6(:,12));Vn6(:,14)*sin(2*pi*13*fsw*t+ph6(:,13));Vn6(:,15)
*sin(2*pi*14*fsw*t+ph6(:,14));Vn6(:,16)*sin(2*pi*15*fsw*t+ph6(:,15));Vn6(:,17)*sin(
2*pi*16*fsw*t+ph6(:,16));Vn6(:,18)*sin(2*pi*17*fsw*t+ph6(:,17));Vn6(:,19)*sin(2*pi*
18*fsw*t+ph6(:,18));Vn6(:,20)*sin(2*pi*19*fsw*t+ph6(:,19));Vn6(:,21)*sin(2*pi*20*fs
w*t+ph6(:,20));Vn6(:,22)*sin(2*pi*21*fsw*t+ph6(:,21))];
Von6=B*Vg6;
Cof6=1/(1-K6);
for m=1:N
   Am6(:,m)=(1/(m*pi))*sin(2*pi*m*(1-K6));
   Bm6(:,m)=(-1/(m*pi))*(cos(2*pi*m*(1-K6))-1);
   Cm6(:,m)=((Am6(:,m)^2)+(Bm6(:,m)^2))^0.5;
   pm6(:,m)=atan(Bm6(:,m)\Am6(:,m));
end
[Cm6];
[pm6];
Vm6=[Cof6 Cm6];
tau6=W0*K6*per;
Vfm6=[Vm6(:,1);Vm6(:,2)*sin(W0*t+tau6+pm6(:,1));Vm6(:,3)*sin(2*W0*t+tau6+pm6(
:,2));Vm6(:,4)*sin(3*W0*t+tau6+pm6(:,3));Vm6(:,5)*sin(4*W0*t+tau6+pm6(:,4));Vm6(
```

```
:,6)*sin(5*W0*t+tau6+pm6(:,5));Vm6(:,7)*sin(6*W0*t+tau6+pm6(:,6));Vm6(:,8)*sin(7
*W0*t+tau6+pm6(:,7));Vm6(:,9)*sin(8*W0*t+tau6+pm6(:,8));Vm6(:,10)*sin(9*W0*t+t
au6+pm6(:,9));Vm6(:,11)*sin(10*W0*t+tau6+pm6(:,10));Vm6(:,12)*sin(11*W0*t+tau6
+pm6(:,11));Vm6(:,13)*sin(12*W0*t+tau6+pm6(:,12));Vm6(:,14)*sin(13*W0*t+tau6+p
m6(:,13));Vm6(:,15)*sin(14*W0*t+tau6+pm6(:,14));Vm6(:,16)*sin(15*W0*t+tau6+pm6
(:,15));Vm6(:,17)*sin(16*W0*t+tau6+pm6(:,16));Vm6(:,18)*sin(17*W0*t+tau6+pm6(:,
17));Vm6(:,19)*sin(18*W0*t+tau6+pm6(:,18));Vm6(:,20)*sin(19*W0*t+tau6+pm6(:,19
));Vm6(:,21)*sin(20*W0*t+tau6+pm6(:,20));Vm6(:,22)*sin(21*W0*t+tau6+pm6(:,21))];
Vof6=B*Vfm6;
C08=M/K8;
for n=1:N
   An8(:,n)=(M/(n*pi))*sin(2*pi*n*K8);
   Bn8(:,n)=(-M/(n*pi))*(cos(2*pi*n*K8)-1);
   Cn8(:,n)=((An8(:,n)^2)+(Bn8(:,n)^2))^0.5;
   ph8(:,n)=atan(Bn8(:,n)\An8(:,n));
end
[Cn8];
[ph8];
Vn8=[C08 Cn8];
B=ones(1,N+1);
Vg8=[Vn8(:,1);Vn8(:,2)*sin(2*pi*fsw*t+ph8(:,1));Vn8(:,3)*sin(2*pi*2*fsw*t+ph8(:,2));
Vn8(:,4)*sin(2*pi*3*fsw*t+ph8(:,3));Vn8(:,5)*sin(2*pi*4*fsw*t+ph8(:,4));Vn8(:,6)*sin(
2*pi*5*fsw*t+ph8(:,5));Vn8(:,7)*sin(2*pi*6*fsw*t+ph8(:,6));Vn8(:,8)*sin(2*pi*7*fsw*
t+ph8(:,7));Vn8(:,9)*sin(2*pi*8*fsw*t+ph8(:,8));Vn8(:,10)*sin(2*pi*9*fsw*t+ph8(:,9));.
..Vn8(:,11)*sin(2*pi*10*fsw*t+ph8(:,10));Vn8(:,12)*sin(2*pi*11*fsw*t+ph8(:,11));Vn8
(:,13)*sin(2*pi*12*fsw*t+ph8(:,12));Vn8(:,14)*sin(2*pi*13*fsw*t+ph8(:,13));Vn8(:,15)
*sin(2*pi*14*fsw*t+ph8(:,14));Vn8(:,16)*sin(2*pi*15*fsw*t+ph8(:,15));Vn8(:,17)*sin(
2*pi*16*fsw*t+ph8(:,16));Vn8(:,18)*sin(2*pi*17*fsw*t+ph8(:,17));Vn8(:,19)*sin(2*pi*
18*fsw*t+ph8(:,18));Vn8(:,20)*sin(2*pi*19*fsw*t+ph8(:,19));Vn8(:,21)*sin(2*pi*20*fs
w*t+ph8(:,20));Vn8(:,22)*sin(2*pi*21*fsw*t+ph8(:,21))];
Von8=B*Vg8;
Cof8=1/(1-K8);
for m=1:N
   Am8(:,m)=(1/(m*pi))*sin(2*pi*m*(1-K8));
   Bm8(:,m)=(-1/(m*pi))*(cos(2*pi*m*(1-K8))-1);
   Cm8(:,m)=((Am8(:,m)^2)+(Bm8(:,m)^2))^0.5;
   pm8(:,m)=atan(Bm8(:,m)\Am8(:,m));
end
[Cm8];
[pm8];
Vm8=[Cof8 Cm8];
tau8=W0*K8*per;
Vfm8=[Vm8(:,1);Vm8(:,2)*sin(W0*t+tau8+pm8(:,1));Vm8(:,3)*sin(2*W0*t+tau8+pm8(
:,2));Vm8(:,4)*sin(3*W0*t+tau8+pm8(:,3));Vm8(:,5)*sin(4*W0*t+tau8+pm8(:,4));Vm8(
:,6)*sin(5*W0*t+tau8+pm8(:,5));Vm8(:,7)*sin(6*W0*t+tau8+pm8(:,6));Vm8(:,8)*sin(7
*W0*t+tau8+pm8(:,7));Vm8(:,9)*sin(8*W0*t+tau8+pm8(:,8));Vm8(:,10)*sin(9*W0*t+t
```

```
au8+pm8(:,9));Vm8(:,11)*sin(10*W0*t+tau8+pm8(:,10));Vm8(:,12)*sin(11*W0*t+tau8
+pm8(:,11));Vm8(:,13)*sin(12*W0*t+tau8+pm8(:,12));Vm8(:,14)*sin(13*W0*t+tau8+p
m8(:,13));Vm8(:,15)*sin(14*W0*t+tau8+pm8(:,14));Vm8(:,16)*sin(15*W0*t+tau8+pm8
(:,15));Vm8(:,17)*sin(16*W0*t+tau8+pm8(:,16));Vm8(:,18)*sin(17*W0*t+tau8+pm8(:,
17));Vm8(:,19)*sin(18*W0*t+tau8+pm8(:,18));Vm8(:,20)*sin(19*W0*t+tau8+pm8(:,19
));Vm8(:,21)*sin(20*W0*t+tau8+pm8(:,20));Vm8(:,22)*sin(21*W0*t+tau8+pm8(:,21))];
Vof8=B*Vfm8;
a11=-rL/L;
a12=0;
a21=0;
a22=-1/(R*C);
b11=(1/L);
b215=-gama5/C;
b216=-gama6/C;
b218=-gama8/C;
dy568ydt=[a11*y568y(1)+a12*y568y(2)+b11*Von5;
    a21*y568y(1)+a22*y568y(2)+b215*y568y(1);
    a11*y568y(3)+a12*y568y(4)+b11*Von6;
    a21*y568y(3)+a22*y568y(4)+b216*y568y(3);
    a11*y568y(5)+a12*y568y(6)+b11*Von8;
    a21*y568y(5)+a22*y568y(6)+b218*y568y(5)];
 grid on
```

Appendix B - DC Power Systems I/O Characteristics

Table B. 1: NiCd-Buck converter I/O

	k = 0.5			**k =0.65**			**k = 0.8**		
Buck	2.54-V	2.67-V	2.67-V	2.55-V	2.67-V	2.68-V	2.54-V	2.60-V	2.66-V
Freq. (Hz)	Vout (1)	Vout (2)	Vout (3)	Vout (1)	Vout (2)	Vout (3)	Vout (1)	Vout (2)	Vout (3)
200	1.03	1.03	1.03	1.5	1.52	1.52	1.99	1.98	2
300	1.03	1.03	1.04	1.5	1.51	1.51	1.96	1.96	1.97
400	1.03	1.04	1.04	1.49	1.48	1.5	1.93	1.94	1.95
500	1.03	1.04	1.04	1.47	1.48	1.49	1.91	1.91	1.92
600	1.02	1.04	1.04	1.46	1.47	1.48	1.88	1.89	1.9
700	1.02	1.04	1.04	1.45	1.46	1.47	1.87	1.87	1.89
800	1.02	1.04	1.04	1.44	1.45	1.46	1.85	1.85	1.87
900	1.02	1.04	1.04	1.43	1.44	1.45	1.84	1.84	1.86
1000	1.02	1.03	1.04	1.42	1.43	1.44	1.83	1.83	1.85
1100	1.02	1.03	1.04	1.42	1.43	1.44	1.83	1.82	1.85
1200	1.02	1.03	1.04	1.41	1.43	1.43	1.83	1.82	1.85
1300	1.02	1.03	1.04	1.41	1.42	1.43	1.83	1.82	1.85
1400	1.02	1.03	1.04	1.41	1.42	1.42	1.83	1.82	1.85
1500	1.02	1.03	1.04	1.41	1.42	1.42	1.84	1.83	1.86
1600	1.02	1.03	1.04	1.41	1.42	1.43	1.85	1.83	1.86
1700	1.02	1.03	1.04	1.41	1.42	1.43	1.86	1.84	1.87
1800	1.02	1.03	1.04	1.41	1.42	1.43	1.86	1.85	1.88
1900	1.02	1.03	1.04	1.42	1.42	1.43	1.87	1.86	1.89
2000	1.02	1.03	1.04	1.42	1.43	1.44	1.88	1.87	1.9
2100	1.02	1.03	1.04	1.42	1.43	1.44	1.89	1.87	1.9
2200	1.02	1.03	1.04	1.42	1.44	1.44	1.9	1.89	1.91
2300	1.02	1.03	1.04	1.43	1.44	1.45	1.91	1.89	1.92
2400	1.02	1.03	1.04	1.43	1.44	1.45	1.91	1.9	1.93
2500	1.02	1.03	1.04	1.44	1.45	1.46	1.92	1.91	1.94

Table B. 2: NiCd-Boost converter I/O

	k = 0.5			**k = 0.65**			**k = 0.8**		
Boost	2.77-V	2.68-V	2.66-V	2.77-V	2.79-V	2.60-V	2.79-V	2.75-V	2.73-V
Freq. (Hz)	Vout (1)	Vout (2)	Vout (3)	Vout (1)	Vout (2)	Vout (3)	Vout (1)	Vout (2)	Vout (3)
200	11.3	10.4	10.8	11.1	11.4	10.5	11.3	11	10.9
300	13.5	12.2	12.6	13.3	13.5	12.6	13.5	13.3	13.1
400	15.2	13.8	14.1	15.1	15.4	14.3	15.6	15.5	14.9
500	16.1	14.7	15.2	16.5	16.8	15.7	17.1	16.8	16.5
600	16.9	15.5	16	17.9	17.9	16.6	18.5	18.1	17.9
700	17.3	15.9	16.4	18.7	18.8	17.4	19.5	19.1	18.8
800	17.7	16.3	16.7	19.1	19.3	17.9	20.2	20	19.7
900	17.9	16.4	16.8	19.5	19.7	18.4	21	20.7	19.7
1000	17.9	16.5	17	19.9	20	18.7	21.5	21.1	20.2
1100	17.9	16.5	17	20.1	20.2	18.9	21.8	21.5	20.8
1200	17.9	16.5	16.9	20.2	20.4	19	22	21.7	21.1
1300	17.8	16.4	16.8	20.2	20.4	19.1	22.2	21.9	21.3
1400	17.7	16.3	16.8	20.2	20.4	19.1	22.4	22.1	21.6
1500	17.6	16.2	16.6	20.2	20.4	19.1	22.5	22.2	21.7
1600	17.5	16.1	16.5	20.2	20.3	19.1	22.5	22.2	21.8
1700	17.3	16	16.4	20.1	20.2	19	22.5	22.3	21.9
1800	17.2	15.8	16.2	20	20.1	18.9	22.5	22.2	21.9
1900	17	15.6	16.1	19.9	20.1	18.8	22.5	22.2	21.9
2000	16.8	15.6	16	19.8	19.9	18.7	22.4	22.2	21.8
2100	16.6	15.2	15.6	19.6	19.8	18.6	22.3	22	21.7
2200	16.4	15.1	15.5	19.5	19.6	18.5	22.3	22	21.6
2300	16.3	15	15.4	19.4	19.5	18.4	22.2	21.9	21.6
2400	16.1	14.8	15.3	19.3	19.4	18.3	22.1	21.8	21.4
2500	15.9	14.7	15.2	19.1	19.3	18.1	22	21.7	21.3

Table B. 3: NiCd-Buck-Boost I/O

	k = 0.5			**k = 0.65**			**k = 0.8**		
Buck-Boost	2.63-V	2.69-V	2.65-V	2.63-V	2.69-V	2.64-V	2.63-V	2.69-V	2.64-V
Freq. (Hz)	Vout (1)	Vout (2)	Vout (3)	Vout (1)	Vout (2)	Vout (3)	Vout (1)	Vout (2)	Vout (3)
200	6.33	6.43	6.3	6.18	6.38	6.07	6.15	6.17	6.24
300	8.94	8.98	9.18	8.83	9.02	9.02	8.88	9.05	8.78
400	10.8	11.16	11.11	11.09	11.35	11.18	11.15	11.28	11.19
500	12.31	12.67	12.45	12.94	13.11	12.91	13.1	13.43	13.2
600	13.33	13.69	13.44	14.23	14.64	14.21	14.55	14.98	14.58
700	14.04	14.39	14.09	15.15	15.56	15.32	15.82	16.06	15.79
800	14.48	14.82	14.57	15.89	16.22	15.94	16.78	17.09	16.77
900	14.78	15.13	14.86	16.48	16.88	16.53	17.46	17.77	17.63
1000	14.93	15.31	15.02	16.81	17.24	16.93	18.12	18.46	18.17
1100	15.02	15.39	15.11	17.11	17.5	17.17	18.53	18.87	18.55
1200	15.04	15.41	15.14	17.28	17.69	17.34	18.81	19.26	18.86
1300	15.01	15.37	15.11	17.38	17.77	17.44	19.12	19.52	19.11
1400	14.95	15.3	15.05	17.43	17.83	17.49	19.29	19.63	19.25
1500	14.87	15.22	14.95	17.44	17.83	17.5	19.38	19.74	19.38
1600	14.75	15.12	14.86	17.42	17.81	17.48	19.43	19.82	19.44
1700	14.62	15.01	14.75	17.35	17.77	17.41	19.48	19.87	19.47
1800	14.5	14.87	14.57	17.29	17.71	17.34	19.48	19.87	19.47
1900	14.38	14.73	14.44	17.21	17.6	17.25	19.48	19.86	19.45
2000	14.26	14.61	14.33	17.1	17.5	17.17	19.42	19.81	19.41
2100	14.08	14.44	14.19	17.01	17.38	17.09	19.37	19.76	19.36
2200	13.94	14.3	14.02	16.89	17.29	16.91	19.3	19.68	19.28
2300	13.78	14.15	13.91	16.74	17.2	16.82	19.21	19.64	19.18
2400	13.69	13.99	13.77	16.65	17.05	16.71	19.15	19.53	19.08
2500	13.55	13.85	13.58	16.58	16.94	16.61	19.03	19.41	19.02

Table B. 4: DEFC-Buck converter I/O

	k = 0.5	**k = 0.5**	**k = 0.65**	**k = 0.65**	**k = 0.8**	**k = 0.8**
Buck	2.03-V	2.03-V	2.52-V	2.52-V	2.27-V	2.27-V
Freq. (Hz)	Theor	Vout (1)	Theor	Vout (2)	Theor	Vout (3)
200	0.965	1	1.573	1.54	1.736	1.94
300	0.965	0.98	1.573	1.52	1.736	1.94
400	0.965	0.98	1.573	1.51	1.736	1.93
500	0.965	0.98	1.573	1.5	1.736	1.91
600	0.965	0.97	1.573	1.49	1.736	1.9
700	0.965	0.98	1.573	1.48	1.736	1.88
800	0.965	0.98	1.573	1.48	1.736	1.88
900	0.965	0.99	1.573	1.48	1.736	1.87
1000	0.965	0.99	1.573	1.47	1.736	1.87
1100	0.965	1	1.573	1.48	1.736	1.86
1200	0.965	1	1.573	1.47	1.736	1.86
1300	0.965	1	1.573	1.47	1.736	1.87
1400	0.965	1.01	1.573	1.48	1.736	1.88
1500	0.965	1.02	1.573	1.49	1.736	1.89
1600	0.965	1.03	1.573	1.49	1.736	1.89
1700	0.965	1.03	1.573	1.49	1.736	1.9
1800	0.965	1.03	1.573	1.49	1.736	1.91
1900	0.965	1.04	1.573	1.5	1.736	1.92
2000	0.965	1.04	1.573	1.5	1.736	1.93
2100	0.965	1.05	1.573	1.51	1.736	1.94
2200	0.965	1.06	1.573	1.52	1.736	1.95
2300	0.965	1.07	1.573	1.52	1.736	1.96
2400	0.965	1.07	1.573	1.53	1.736	1.96
2500	0.965	1.07	1.573	1.54	1.736	1.97

Table B. 5: DEFC mesh-Boost converter I/O

Boost-mesh	**k =0.5**		**k =0.65**		**k = 0.8**	
Freq. (Hz)	Vin	Vout	Vin	Vout	Vin	Vout
200	0.654	1.97	0.69	2.49	0.55	1.82
400	0.698	3.77	0.692	3.52	0.555	2.58
600	0.708	3.96	0.707	4.25	0.556	3.17
800	0.713	4.05	0.718	4.7	0.583	3.67
1000	0.719	4.1	0.728	4.98	0.589	4.03
1200	0.726	4.14	0.74	5.13	0.608	4.25
1400	0.733	4.18	0.754	5.22	0.614	4.41
1600	0.74	4.19	0.764	5.24	0.622	4.53
1800	0.746	4.16	0.771	5.24	0.631	4.62
2000	0.753	4.13	0.778	5.23	0.641	4.69
2200	0.762	4.1	0.783	5.22	0.65	4.73
2400	0.77	4.06	0.788	5.17	0.66	4.75
2600	0.776	4.02	0.793	5.13	0.67	4.77
2800	0.782	3.97	0.8	5.08	0.677	4.8
3000	0.788	3.92	0.806	5.02	0.684	4.82
3200	0.793	3.87	0.811	4.97	0.691	4.83
3400	0.799	3.83	0.813	4.92	0.699	4.82
3600	0.804	3.79	0.815	4.86	0.706	4.79
3800	0.808	3.74	0.816	4.8	0.713	4.76
4000	0.811	3.7	0.818	4.75	0.72	4.73
4200	0.813	3.65	0.82	4.69	0.726	4.71
4400	0.815	3.61	0.822	4.64	0.732	4.69
4600	0.816	3.56	0.824	4.58	0.738	4.66
4800	0.818	3.52	0.827	4.53	0.743	4.64
5000	0.82	3.48	0.829	4.48	0.747	4.62
5200	0.823	3.44	0.832	4.43	0.751	4.59
5400	0.827	3.41	0.834	4.39	0.753	4.56
5600	0.831	3.37	0.835	4.34	0.756	4.54
5800	0.836	3.34	0.837	4.3	0.758	4.51
6000	0.841	3.31	0.839	4.26	0.76	4.48

Table B. 6: DEFC foam-Boost converter I/O

	k = 0.5		**k = 0.65**		**k = 0.8**	
Freq. (Hz)	Vin	Vout	Vin	Vout	Vin	Vout
200	0.628	2.23	0.431	1.42	0.402	1.34
400	0.645	3.1	0.413	1.93	0.317	1.46
600	0.661	3.66	0.412	2.32	0.279	1.54
800	0.677	3.97	0.423	2.61	0.26	1.58
1000	0.693	4.14	0.439	2.86	0.251	1.62
1200	0.71	4.23	0.458	3.05	0.251	1.66
1400	0.726	4.29	0.482	3.22	0.254	1.7
1600	0.736	4.29	0.509	3.4	0.259	1.75
1800	0.744	4.27	0.545	3.61	0.262	1.79
2000	0.752	4.24	0.578	3.78	0.266	1.82
2200	0.76	4.2	0.6	3.88	0.271	1.85
2400	0.768	4.15	0.617	3.94	0.275	1.88
2600	0.775	4.11	0.634	4.01	0.28	1.91
2800	0.782	4.07	0.651	4.07	0.288	1.94
3000	0.788	4.02	0.666	4.13	0.298	1.97
3200	0.793	3.97	0.68	4.15	0.306	2
3400	0.799	3.91	0.691	4.14	0.314	2.03
3600	0.804	3.86	0.702	4.13	0.321	2.05
3800	0.808	3.8	0.711	4.1	0.329	2.08
4000	0.811	3.75	0.718	4.08	0.336	2.1
4200	0.813	3.7	0.723	4.05	0.344	2.12
4400	0.815	3.65	0.728	4.02	0.351	2.14
4600	0.817	3.61	0.731	3.99	0.359	2.16
4800	0.819	3.56	0.735	3.96	0.366	2.18
5000	0.82	3.52	0.738	3.93	0.374	2.2
5200	0.822	3.48	0.742	3.9	0.382	2.21
5400	0.824	3.44	0.746	3.86	0.39	2.21
5600	0.826	3.4	0.749	3.83	0.397	2.2
5800	0.828	3.36	0.753	3.81	0.405	2.19
6000	0.83	3.32	0.757	3.78	0.413	2.19

Table B. 7: DEFC mesh-Buck-boost converter I/O

	k = 0.5		**k = 0.65**		**k = 0.8**	
Freq. (Hz)	Vin	Vout	Vin	Vout	Vin	Vout
200	0.659	1.41	0.572	1.17	0.12	0.308
400	0.672	2.56	0.562	2.24	0.112	0.357
600	0.678	3.21	0.56	2.82	0.11	0.415
800	0.704	3.62	0.564	3.16	0.11	0.488
1000	0.721	3.85	0.57	3.4	0.11	0.556
1200	0.738	3.95	0.584	3.61	0.111	0.603
1400	0.754	4.01	0.607	3.78	0.114	0.642
1600	0.765	4.02	0.63	3.92	0.119	0.672
1800	0.773	4	0.654	4.07	0.122	0.693
2000	0.78	3.97	0.678	4.18	0.126	0.708
2200	0.789	3.93	0.694	4.21	0.13	0.72
2400	0.798	3.89	0.707	4.2	0.134	0.731
2600	0.807	3.83	0.717	4.19	0.139	0.741
2800	0.815	3.77	0.726	4.18	0.143	0.749
3000	0.82	3.71	0.734	4.16	0.147	0.756
3200	0.823	3.66	0.741	4.15	0.151	0.761
3400	0.825	3.6	0.748	4.12	0.153	0.764
3600	0.827	3.55	0.753	4.08	0.155	0.767
3800	0.829	3.5	0.759	4.04	0.158	0.769
4000	0.831	3.45	0.764	3.99	0.16	0.77
4200	0.835	3.4	0.768	3.95	0.162	0.77
4400	0.839	3.35	0.773	3.92	0.164	0.768
4600	0.842	3.3	0.777	3.89	0.165	0.766
4800	0.846	3.26	0.782	3.86	0.167	0.764
5000	0.849	3.21	0.786	3.82	0.169	0.761
5200	0.852	3.17	0.79	3.79	0.171	0.759
5400	0.854	3.12	0.794	3.76	0.173	0.757
5600	0.856	3.08	0.798	3.72	0.175	0.755
5800	0.858	3.04	0.802	3.69	0.177	0.753
6000	0.86	3.00	0.805	3.65	0.18	0.75

Table B. 8: DEFC foam-Buck-boost I/O

	k = 0.5		**k = 0.65**		**k = 0.8**	
Freq. (Hz)	Vin (V)	Vout (V)	Vin	Vout	Vin	Vout
200	0.657	1.4	0.499	1.03	0.142	0.225
400	0.574	2.11	0.509	1.09	0.132	0.379
600	0.564	2.61	0.522	2.56	0.13	0.493
800	0.588	3	0.542	3.02	0.134	0.585
1000	0.616	3.26	0.565	3.37	0.139	0.659
1200	0.638	3.37	0.59	3.63	0.14	0.711
1400	0.659	3.45	0.617	3.84	0.14	0.746
1600	0.678	3.5	0.638	3.97	0.14	0.775
1800	0.694	3.54	0.656	4.07	0.142	0.804
2000	0.709	3.56	0.671	4.14	0.146	0.83
2200	0.721	3.55	0.684	4.16	0.15	0.853
2400	0.733	3.53	0.696	4.15	0.155	0.874
2600	0.744	3.5	0.706	4.14	0.159	0.894
2800	0.753	3.47	0.716	4.12	0.164	0.912
3000	0.76	3.43	0.724	4.1	0.169	0.927
3200	0.765	3.39	0.731	4.08	0.173	0.94
3400	0.769	3.35	0.737	4.04	0.177	0.953
3600	0.772	3.3	0.741	4	0.181	0.966
3800	0.775	3.24	0.745	3.96	0.185	0.975
4000	0.778	3.19	0.75	3.91	0.189	0.98
4200	0.782	3.15	0.754	3.88	0.193	0.98
4400	0.786	3.1	0.758	3.84	0.196	0.979
4600	0.79	3.06	0.763	3.81	0.2	0.977
4800	0.794	3.02	0.767	3.77	0.203	0.975
5000	0.798	2.98	0.77	3.73	0.207	0.972
5200	0.801	2.94	0.772	3.69	0.211	0.969
5400	0.803	2.91	0.775	3.65	0.215	0.965
5600	0.805	2.87	0.777	3.61	0.219	0.959
5800	0.807	2.84	0.778	3.57	0.223	0.952
6000	0.809	2.81	0.78	3.53	0.228	0.944